OXIDATION KINETICS OF PURE AND BLENDED METHYL OCTANOATE/n-NONANE/METHYLCYCLOHEXANE: MEASUREMENTS AND MODELING OF OH*/CH* CHEMILUMINESCENCE, IGNITION DELAY TIMES AND LAMINAR FLAME SPEEDS

A Dissertation

by

BRANDON MICHAEL ROTAVERA

Submitted to the Office of Graduate Studies of
Texas A&M University
in partial fulfillment of the requirements for the degree of

DOCTOR OF PHILOSOPHY

May 2012

Major Subject: Interdisciplinary Engineering

OXIDATION KINETICS OF PURE AND BLENDED METHYL OCTANOATE/n-NONANE/METHYLCYCLOHEXANE: MEASUREMENTS AND MODELING OF OH*/CH* CHEMILUMINESCENCE, IGNITION DELAY TIMES AND LAMINAR FLAME SPEEDS

A Dissertation

by

BRANDON MICHAEL ROTAVERA

Submitted to the Office of Graduate Studies of
Texas A&M University
in partial fulfillment of the requirements for the degree of

DOCTOR OF PHILOSOPHY

Approved by:

Chair of Committee,	Eric L. Petersen
Committee Members,	Simon W. North
	Timothy J. Jacobs
	Rodney D. W. Bowersox
	M. Sam Mannan
Coordinator of Graduate Programs,	Robin Autenrieth

May 2012

Major Subject: Interdisciplinary Engineering

ABSTRACT

Oxidation Kinetics of Pure and Blended Methyl Octanoate/n-Nonane/Methylcyclohexane:

Measurements and Modeling of OH*/CH* Chemiluminescence,

Ignition Delay Times and Laminar Flame Speeds. (May 2012)

Brandon Michael Rotavera, B.S., University of Central Florida; M.S., Texas A&M University

Chair of Advisory Committee: Dr. Eric L. Petersen

The focus of the present work is on the empirical characterization and modeling of ignition trends of ternary blends of three distinct hydrocarbon classes, namely a methyl ester ($C_9H_{18}O_2$), a linear alkane (n-C_9H_{20}), and a cycloalkane (MCH). Numerous surrogate biofuel formulations have been proposed in the literature, yet specific blending of these species has not been studied. Moreover, the effects of blending biofuel compounds with conventional hydrocarbons are not widely studied and a further point is the lack of studies paying specific attention to the effects of fuel variation within a given blended biofuel. To this end, a statistical Design of Experiments L9 array, comprised of 4 parameters (%MO, %MCH, pressure, and equivalence ratio) with 3 levels of variation, constructed in order to systematically study the effects of relative fuel concentrations within the ternary blend enabled variations in fuel concentration for methyl octanoate and MCH of 10% – 30% and 20% – 40%, respectively. Variation in pressure of 1 atm, 5 atm, and 10 atm and in equivalence ratio of 0.5, 1.0, and 2.0 were used, respectively. The fuel-volume percentage of n-nonane varied from 30% – 70%. In total, 10 ternary blends were studied.

Ignition delay times for the ternary blends and for the three constituents were obtained by monitoring excited-state OH or CH transitions, $A^2\Sigma^+ \rightarrow X^2\Pi$ or $A^2\Delta \rightarrow X^2\Pi$, respectively, behind reflected shock waves using a heated shock tube facility. Dilute conditions of 99% Ar (vol.) were maintained in all shock tube experiments with the exception of a separate series of n-nonane and MCH experiments under stoichiometric conditions which used 4% oxygen (corresponding to ~ 95% Ar dilution). Temperatures behind reflected shock waves were varied over the range $1243 < T\,(K) < 1672$. From over 450 shock tube experiments, empirical ignition delay time correlations were constructed for all three pure fuels and a

master correlation equation for the blended fuels. Ignition experiments conducted on the pure fuels at 1.5 atm indicated the following ignition delay time order, from shortest to longest: methyl octanoate < n-nonane < MCH. With increased pressure to 10 atm (nominal) the order remained, in general, consistent. Under fuel-lean conditions, ignition trends between methyl octanoate and n-nonane exhibited overlap at temperatures below 1350 K, below which the trends diverged with methyl octanoate having shorter ignition delay times. Similar behavior was observed under fuel-rich conditions, yet with the overlap occurring above 1450 K. Stoichiometric ignition trends did not display overlapping behavior under either 1.5 atm or 10 atm pressure. Laminar flame speed measurements were performed at 1 atm and an initial temperature of 443 K on the pure fuel constituents. Additional flame speed measurements of MCH were conducted at 403 K to compare with literature values and were shown to agree strongly with experiments conducted in a constant-volume apparatus. The experiments conducted herein, for the first time, measure laminar flame speeds methyl octanoate.

A detailed chemical kinetics mechanism was compiled from three independent, well-validated models for the constituent fuels, where the sub-mechanisms for methyl octanoate and MCH were extracted for integration into a base n-nonane model. The compiled mechanism in the present study (4785 reactions and 1082 species) enables modeling of oxidation processes of the ternary fuel blends of interest. Calculations were performed using the compiled model relative to the base models to assess the impact of utilizing different base chemistry sets. In general, results were reproduced well relative to base models for both n-nonane and MCH, however results for methyl octanoate from both the compiled model and the base model are in disagreement with the results measured herein. Ignition delay times of the fuel blends are well-predicted for several conditions, specifically for blends at lean/high-pressure and stoichiometric/high-pressure conditions, however are not accurately modeled at fuel-rich, high-pressure conditions.

NOMENCLATURE

Abbreviations	*Definition*
FT	Fischer-Tropsch
FWHM	Full-Width Half-Maximum
HC	Hydrocarbon
H/C	Hydrogen-to-Carbon Ratio
ISW	Incident Shock Wave
L/D	Length-to-Diameter Ratio
LVP	Low Vapor Pressure
NTC	Negative Temperature Coefficient
RSW	Reflected Shock Wave
STP	(101325 Pa, 295 K)
UHP	Ultra High Purity (> 99.999%)
UV	Ultraviolet
VIS	Visible

Symbols	*Definition*	*Units*
A	Arrhenius Pre-Exponential, Frequency Factor	
a	Local Acoustic Speed	m/s
c	Speed of Light (in Vacuum)	m/s ($2.998 \cdot 10^8$ m/s)
c_P	Constant-Pressure Specific Heat	J/kg·K, kJ/kg·K
c_V	Constant-Volume Specific Heat	J/kg·K, kJ/kg·K
d	Diameter	m, cm, mm, μm
h	Planck Constant	J·s ($6.626 \cdot 10^{-34}$ J·s)
M	Mach Number	(Dimensionless)
M_W	Molecular Weight	kg/kmol
n	Arrhenius Non-Linearity Factor	(Dimensionless)
P	Pressure	torr, Pa, atm
R_u	Universal Gas Constant	J/mol·K, kJ/kmol·K
s	Entropy	J/kg·K, kJ/kg·K
T	Temperature	K
$\mathcal{V}$	Velocity	m/s, μm/ms
y	Mole Fraction	(Dimensionless)

Greek Symbols

Δ	Change (Final – Initial)	(Dimensionless)
γ	Specific Heat Ratio (c_P / c_V)	(Dimensionless)
λ	Wavelength	nm
ν	Frequency	s^{-1}
ρ	Density	kg/m^3
$\tau_{Ignition}$	Ignition Delay Time	μs

Subscripts	*Definition*
1	Initial State within Low-Pressure Section of Shock Tube
2	Conditions within Incident Shock Wave
3	Conditions within Expansion Fan
4	Initial State within High-Pressure Section of Shock Tube
5	Conditions behind Reflected Shock Wave
∞	Free-Stream Condition
R	Reflected

TABLE OF CONTENTS

Page

Page

LIST OF FIGURES

Page

Page

Page

Page

Page

Page

Page

Page

Page

Page

Page

Page

LIST OF TABLES

1. INTRODUCTION

Increasing global population and rising economies place heavy demands on requirements for power generation from non-renewable energy resources such as fuels produced from crude oil. The impetus for the use of distillate hydrocarbons from crude oil is due largely to the lower cost associated with such fuels as compared to other energy sources, including fuel cells, compressed natural gas, and hydrogen; the latter also possessing an inherent, large-scale infrastructure requirement which adversely contributes to the production economics. Further, coupled with economic growth in developing countries is the demand for powered transportation which leads to the immediate need for petroleum-based hydrocarbon fuels, the finite sources of which are depleting.

Transportation fuels derived from imported oil such as gasoline, diesel, and aviation fuels constitute a significant amount of the energy needs in the United States and combustion research serves to develop new means by which alternative transportation fuels can be tested, modeled, and developed in an attempt to palliate the consumption of fuels distilled from imported crude oil. One such method is the development of bio-derived fuels, including biodiesel, bio-alcohols and others which incorporate a percentage of renewable fuel derived from biomass sources. These fuels will be used in conjunction, as supplements, with petroleum-based transportation fuels currently in use (e.g. gasoline, diesel fuels). The key, then, to developing fuels which help address the needs of higher fuel efficiency, in terms of energy generation within the combustion chamber of an engine, and a low-impact net carbon cycle lies in the understanding of the chemical interplay between fuels produced from biological sources and fuels produced from conventional sources, namely crude oil. Corresponding to these needs, the emphasis of the present work revolves around the immediate demand for fundamental combustion measurements of topical, bio-derived fuels.

This dissertation follows the style of Combustion and Flame.

1.1 The role and impact of biofuels

Viable, long-term transportation fuel solutions to satisfy the growing energy needs of the United States must make use of an integrated approach which utilizes existing fuels, namely gasoline, diesel, and jet fuels, in conjunction with fuels derived from biological sources (biomass, algae, endophytes…) that are not intrusive on natural resources intended for human consumption. The impetus for the use of biofuels, such as ethanol, stems largely from the desire to reduce foreign-oil dependence and the interest in offsetting anthropogenic pollutants and greenhouse gas emissions. Issues related to biofuel sustainability, economic and sociological impacts have been the subject of several books [1 – 8]. One issue related to present biofuels is the high production cost; corn-based ethanol, without government subsidies, is not economically feasible [9, 10]. Thus, there is a strong need for an economical and compatible biofuel source. While there are many aspects required to fully assess the viability of a bio-derived fuel, concomitant with this need is a research program designed to assess the chemical influence of a given bio-derived fuel blended with gasoline and/or diesel with respect to processes such as ignition and pollutant formation.

Transportation fuels consume a significant amount of world energy needs, and research has aimed at methods of developing new means by which transportation fuels can be developed to mitigate the consumption of crude oil. One such method is the development of bio-derived fuels, including bio-diesel, bio-alcohol and others. There is a need for understanding the fundamental chemistry and combustion properties of fuels which are being tapped as replacements or supplements to current petroleum-based fuels. This need is enhanced by the desire to reduce or eliminate the toll taken on agriculture to produce fuels for transportation. Therefore, the goal of the present work is to compile a chemical kinetics model for a ternary fuel blend to study the chemical interactions of the three fuels which are representative of those found in bio-fuel and petroleum-based fuels in terms of both fundamental chemical kinetics and practical combustion phenomena. The tasks which are undertaken to achieve this goal include making fundamental measurements of species time histories and practical measurements of ignition delay times and laminar flame speeds at known thermodynamic conditions. The results are then compared to model predictions

from the compiled model which provides insight into reaction pathways, rates of production, and time histories of important reaction intermediates.

As of 2009, light-duty vehicles (cars and light trucks) account for nearly 50% of total petroleum consumption, over 2 billion barrels annually. Accordingly, addressing the fuel needs of such vehicles through improvements in combustion processes and production of alternative fuel sources could dramatically reduce the amount of oil consumed by this sector. Recently, the current Administration announced an agreement (within the National Vehicle Program) with thirteen major automakers, who supply 90% of the automobile market in the United States, to produce vehicles with increased fuel economy of 54.5 miles per gallon (mpg) for cars and light-duty trucks by Model Year 2025 [11]. In addition to improvements in thermal and mechanical engine efficiencies, fuel chemistry plays a significant role towards both increased fuel economy and in the reduction of carbon dioxide and pollutant emissions. Correspondingly, in the interest of favorable economics associated with conventional fuels and current interests in bio-derived fuels, measurements on the effects of blending bio-derived fuels with gasoline, diesel, and jet fuel components are imperative for predictive simulation of clean combustion engines that can meet rising fuel economy standards and reduce net greenhouse emissions.

The Fuel Economy Standards program set forth by the current Administration in agreement with industrial automaker partners was designed foremost as a bold initiative to reduce the dependence of the United States economy on foreign oil and, by extension, increase national security. Fuel efficiency standards, prior to the program recently put in place by the Administration, remained stagnant since the mid 1980's with requirements hovering near 28 mpg for passenger cars and near 20 mpg for light trucks [11]. Due to its ambitious design, the progress Fuel Economy Standards initiative set forth will receive significant national attention, and bio-derived fuels will undoubtedly be instrumental in reaching the engine standards on emissions and fuel consumption.

Dependence on foreign oil remains a prominent, nationally important issue, the solution to which provides increased economic strength, increased national security from a reduced reliance on foreign nations whose primary export is crude oil, and lasting technological developments. Stemming from advances in biofuel formulation and advanced fuel-flexible engines, there is an immediate need for understanding the interplay chemistry among bio-derived fuel molecules and traditional petroleum-based hydrocarbon fuels such as higher-order normal, branched, and cyclic alkanes and aromatics. National security is inextricably tied to the reliance on and importing of foreign crude oil. Instigated by unrest in some OPEC nations and the Middle East, which collectively produce of over 70% of the crude oil imported into the United States [12], significant interest in increased energy independence has spurred drastic improvements in fuel efficiency and coupled reduction in total petroleum consumption. Required from the standpoint of combustion chemistry to meet the high fuel-efficiency standards recently set forth by the Administration is a detailed knowledgebase of fuels that can be used to supplement or completely replace crude oil distillate fuels (i.e. biofuels). Combustion experiments on biofuels are therefore required to establish such a valuable database.

To develop and improve fuel-flexible internal combustion engines, engine designers make use of chemistry models which simulate chemical reactions within a specified set of engine conditions (temperature, pressure, compression time…) to predict the type and quantity of products yielded from the combustion process and properties such as ignition delay times. Chemical kinetics models combine quantitative information on elementary reactions of a wide range of molecules involved in the combustion process. Presently, models exist for a large number petroleum-based fuels commonly found as constituents within gasoline, diesel, or aviation fuels, such as higher-order n-alkanes [13 – 21], iso-octane [22, 23], and methylcyclohexane [24, 25], representing linear alkanes, branched alkanes, and cycloalkanes, respectively.

A large number of chemical kinetics models and computational studies also exist for oxygenated fuels and fuels derived from biological sources [26 – 43], owing to an increase in available experimental data on such fuels. Despite significant advances in detailed modeling of fuel chemistry for conventional fuels and

of alternative fuels, there remains a strong and persistent need for fundamental data as to the effects of blending. Requisite for accurate modeling of fuel chemistry under practical engine conditions is a wide range of measured combustion data including species profiles, autoignition behavior, pollutant species, and mechanisms of pollutant formation. Autoignition behavior (ignition delay times, ignition activation energy…) provides an important, global metric for detailed mechanism development. Therefore, the principal focus of the work is the development of a broad and coordinated series of ignition delay time measurements on biofuel compounds blended with conventional, petroleum-based fuels. A supporting objective was the compilation of a detailed chemical kinetics mechanism capable of modeling ignition trends of blended biofuel.

1.2 Scope of present work

There is a necessity for understanding the fundamental chemistry and combustion properties of fuels which are being tapped as replacements and/or supplements to current petroleum-based fuels. This need is immediately coupled to the requirement of blending effects of biologically derived fuels with conventional hydrocarbons. The interest in biofuels is enhanced by the desire to reduce or eliminate the toll taken on agriculture to produce fuels for transportation (e.g. ethanol, soy-based diesel) and increase the energy independence of the United States. Therefore, efforts are needed to provide vital fundamental combustion data needed to model biofuel combustion in advanced, high-fuel-efficiency engines within the United States in the interest of energy security and independence. The present effort aims to characterize blended biofuel combustion with respect to ignition behavior of 10 ternary blends and the three constituent fuels which comprise the blends and represents a first step beyond simple blending towards assessing the impact of hydrocarbon class variation on combustion phenomena.

The understanding of biofuel combustion by studying blending effects in detail is essential because practical utilization of biofuels will almost always be as a blend with petroleum distillate fuels. Although alternative and petroleum-based fuels have been studied individually, the behavior of biofuel blends cannot be captured simply through combination of the pure-fuel combustion behaviors. Therefore,

measurements of blended biofuel combustion are needed. Furthermore, a chemical kinetics model capable of describing blending effects on ignition behavior is necessary for engine designers to include biofuels in the development of next-generation, fuel-flexible engines.

To date, shock-tube experiments have involved only single-component studies of the species of interest in the current work. The measurements and modeling herein focused on blending effects of higher-order linear alkanes with cycloalkanes and a methyl ester, measured for the first time under shock-tube conditions. Oxidation of the constituent species and of ternary blends of a methyl ester (methyl octanoate, $C_9H_{18}O_2$), a normal alkane (n-nonane, n-C_9H_{20}), and a branched cycloalkane (methylcyclohexane, MCH/C_7H_{14}) were studied herein using shock tubes primarily, with supporting measurements for the constituent species from a laminar flame-speed device where, respectively, species time histories and laminar burning velocities were measured. In total, 10 compositions of blends were studied. A statistical approach was taken to design the series of experiments to cover the range of fuel variation of interest. Specifically, the study employed an L9 array to elucidate the effects of variation of two of the three fuels and on pressure an equivalence ratio on the aforementioned combustion phenomena. The relative proportion (volume fraction) of the conventional fuel constituents was varied in accordance with established parameters for common transportation fuels [44 – 46] including jet fuel and diesel fuel which are made up of hundreds of hydrocarbon species.

The primary focus of the present work was strictly to study the effect of relative concentrations of higher-order hydrocarbon species with three distinct bond structures (Fig. 1.1) to gain insight into the effects of blending on ignition chemistry and radical production/consumption pathways over varying thermodynamic conditions, rather than the proposition of a particular surrogate fuel or class of fuel blends for practical use. Noting that the typical composition of transportation fuels used in either aviation or internal combustion engines consists only of hydrocarbons (i.e. no oxygenated species), the presence of the methyl ester in the blends was intended to replicate a type of biofuel with the potential for use in transportation applications. Specifically, integration of the species allowed for determination of the effects

of such an oxygenated fuel with respect to ignition of the ternary blend (methyl ester/n-alkane/cycloalkane).

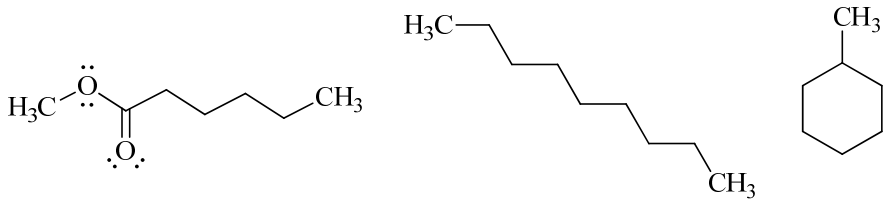

Fig. 1.1. Bond structure of methyl octanoate, n-nonane, and methylcyclohexane molecules.

The present work can be categorized as serving four primary purposes:

(1) Extend the range of experimental data on neat n-nonane and methylcyclohexane combustion

(2) Present the first fundamental shock-tube ignition measurements of neat methyl octanoate combustion

(3) Present the first laminar flame speed measurements of methyl octanoate

(4) Report the first shock-tube data from experiments on ternary blends of three distinct hydrocarbon classes using relative variation in the constituents using an efficient, statistical approach

(5) Compilation of a first-generation chemical kinetics mechanism for modeling of blending effects, based on existing chemical kinetics mechanisms in the literature

Largely due to the high volumetric percentage (40% – 60%) of higher-order normal alkanes in transportation fuels relative to more-complex fuel molecules, a relatively larger amount of experimental combustion data are available for this hydrocarbon class. It is generally accepted in the literature [47] that ignition delay times of higher-order n-alkanes above C_7 are similar at high temperatures. Therefore, for purposes of ignition delay time modeling, n-nonane is a suitable species to represent the linear alkane class and has received experimental and modeling attention on this parameter by the author [16, 48] and by Davidson et al. [49]. Cyclic alkanes are also abundant in diesel and aviation fuels, ranging from 20% – 50% by volume, and species such as cyclohexane, methyl- and ethyl-cyclohexane have been the focus of

several experimental and complementary modeling studies [50 – 62]. Within this class, methylcyclohexane (MCH) has been paid significant attention as a representative in surrogate fuel modeling. Saturated methyl esters ($R{-}C(=O){-}OCH_3$) are of interest as a biofuel supplement to petroleum-based transportation fuels, and combustion measurements of higher-order species using engines [63, 64], diffusion flames [65, 66], shock tubes [67, 68], microgravity droplet-ignition [69], and jet-stirred reactors [36, 41, 42, 70] are reported in the literature. Methyl decanoate ($C_{11}H_{22}O_2$) has been the primary representative for the methyl ester class [65 – 68, 70], however methyl octanoate serves the same role for purposes of ignition delay time measurements and involves fewer species and reactions to include in modeling of the chemical kinetics.

Experimental and modeling studies have been conducted on surrogates for respective hydrocarbon classes, yet the chemical interplay of non-traditional species, such as methyl esters, with conventional fuels, such as linear alkanes, iso-alkanes, aromatics, and cycloalkanes, has yet to be studied in detail with respect to blending effects. The understanding of biofuel combustion by studying blending effects in detail is essential because practical utilization of biofuels will almost always be as a blend with petroleum distillate fuels. Although alternative and petroleum-based fuels have been studied individually, the behavior of biofuel blends cannot be captured simply through combination of the pure-fuel combustion behaviors. Therefore, measurements of blended biofuel combustion are needed. Furthermore, chemical kinetics models capable of describing blending effects on ignition behavior are necessary for engine designers to include biofuels in the development of next-generation, fuel-flexible engines.

Discussed in the present work are the experimental and modeling approaches undertaken to characterize ignition behavior of blended biofuel components. Results of ignition delay times and OH* time histories are the primary focus, with supporting measurements of laminar flame speed of the fuel constituents also being discussed. Ignition delay time correlations are presented for each species and for 10 ternary blends. The chosen blends use concentrations of 5% and 30% (vol.) of the methyl ester, which slightly extend the limits of addition to diesel fuel as discussed by Alptekin and Çanakçi [71] where concentrations up to 20%

were found not to compromise properties such as density and viscosity. A chemical kinetics mechanism, based on the n-nonane mechanism of Rotavera et al. [48], was compiled for modeling of species time histories, ignition delay times, and reaction kinetics of the ternary fuel blends. The experiments undertaken and model compiled herein are of the first kind for methyl ester/linear alkane/cycloalkane blends.

Section 2 provides relevant literature for biofuels in general and in greater detail, a discussion on experimental and modeling studies performed on the pure fuel species. Section 3 discusses in significant detail the experimental approach employed in shock-tube and laminar flame speed experiments conducted. Section 4 provides details on the construction of the chemical kinetics model and specifics on the variety of chemistry modeling tools employed for analysis of blending effects. Sections 5, 6, and 7 focus on shock tube results from experiments on the fuel constituents, methyl octanoate, n-nonane, and MCH, respectively. Section 8 provides the experimental shock-tube results of the ternary fuel blends with supporting model calculations on blending effects. Section 9 discusses experimental trends observed in the blended studies using an empirical ignition delay time correlation calculated from the blended fuel ignition experiments. Section 10 presents the laminar flame speed measurements obtained for the pure fuel constituents. Results of the present work are summarized and recommendations for further study towards blended biofuel combustion in Section 11.

2. BACKGROUND

Biofuels serve as supplements to offset the use of petroleum-based transportation fuels such as gasoline, diesel, and aviation fuels. The oxygenated fuel compounds present in biofuels are derived from a variety of sources, including agricultural crops (corn, sugar cane), vegetable oil, and tallow, among others, and intended to both mitigate the consumption of non-renewable resources (i.e. crude oil) and decrease combustion pollutants including soot and NO_x. Commercial use of biofuels is likely to rely on an integrated solution encompassing blending of a wide range of conventional hydrocarbon classes (linear alkanes, branched alkanes, cycloalkanes, aromatics) with oxygenated hydrocarbons (esters, ethers, alcohols) due to favorable economics with respect to infrastructure and production requirements of conventional fuels relative to biologically derived fuels.

Ignition properties of a blended fuel cannot be reproduced using linear blending rules. Several surrogate formulations have been used to study biofuel ignition and oxidation, however studies focusing on blended biofuel combustion reported in the literature are limited in number. To an even lesser degree, the effects of relative variation in hydrocarbon classes contained in a given biofuel surrogate of interest has not been well-studied in general, and for some species not at all. The sections below provide the relevant background of blended biofuel studies (Section 2.1), and literature reviews for combustion studies involving the fuel constituents of interest in the present work, namely methyl octanoate (Section 2.2), n-nonane (Section 2.3), and MCH (Section 2.4).

2.1 Studies on biofuel components and surrogates for transportation fuel

Surrogate fuels are comprised of a specified composition which is formulated to replicate the combustion properties of a more complex fuel with the intent of enabling more facile chemical kinetics modeling. In addition, since each parent fuel molecule has numerous decomposition and reaction pathways, modeling of a fuel blend comprised of only a few components, compared to several hundred, reduces the overall mechanism size from the smaller amount of additional species and requisite sub-mechanisms.

The benefit of a *reduced mechanism* is the reduction in computational demands when complex reacting flows are modeled using both fluid mechanics (i.e. the Navier-Stokes equations) and chemical kinetics. Solutions to each of these equation sets are independently demanding and, due to present computational limits, a balance-point is sought after wherein one of the mechanisms (fluid mechanics or chemistry) is reduced to capture global phenomena rather than detailed processes (e.g. vortices in the case of fluid mechanics, or short-lived radical species chemistry in the case of chemical kinetics). While detailed chemistry is important from the perspective of fundamental science for proper analysis of reaction pathways, nascent soot chemistry, and other important processes, reduced chemistry models are often used when coupled with a complex fluid flow environment such as high-speed flow through a combustor or the control volume of an internal combustion engine.

Prior to reducing chemical kinetics mechanisms, detailed chemistry is in fact required. To this end, out of interest in the development of petroleum-based fuel replacements, chemical kinetics modeling has been devoted to the area of surrogate fuel modeling, the modeling of single- or multi-component fuels chemically and/or physically representative of more complex fuels. Motivated in part by reducing foreign oil consumption, due to the restrictions imposed on the operation of jet engines such as stringent requirements on power production, energy density of the fuel, mass density, and cooling requirements, numerous efforts have been dedicated towards developing jet fuel surrogates [72 – 77]. Considering the length of time biofuels have received experimental interest, while individual biofuel components have received some modeling treatment, only recently have chemical kinetics models that describe blended biofuel combustion become more prevalent (Table 2.1). No studies on blended biofuel oxidation have included either cycloalkanes or iso-alkanes.

Table 2.1. Volume percentages of hydrocarbon classes utilized as representative formulations of biofuel surrogates. Numerical designations of 1 and 2 are assigned to experimental and modeling studies, respectively. No studies on blended biofuel oxidation have included either cycloalkanes or iso-alkanes.

n-Alkane	Aromatic	Distillate	Methyl Ester	Alcohol	Reference
74/26	-	-	-	-	1/2: [26]
74	-	-	26	-	1/2: [26]
49	21	-	30	-	1/2: [27]
50	-	-	50	-	2: [28]
-	-	Diesel	≤ 50	-	1: [78]
80/50	-	-	-	20/50	1/2: [29]
92/80/50/45	-	-	-	8/20/50/55	1/2: [41]
50	-	-	25/25	-	2: [30]

2.2 Literature review of combustion studies involving methyl octanoate, n-nonane, and methylcyclohexane

Literature reviews of the three constituent fuels comprising ternary fuel blends in the current study are provided in the sections below, including both experimental and modeling studies. While ignition delay time measurements for n-nonane and MCH are summarized from the literature, measurements for methyl octanoate are reported for the first time in the present work. MCH has received the most experimental and modeling work, followed by n-nonane and methyl octanoate.

2.2.1 Methyl octanoate

Due partly to the oxygen present in the molecule and to the numerous production sources (biomass, vegetable oils, tallow) methyl esters have been widely studied as a biofuel [34 – 39, 43, 66, 79 – 81]. Several low- to intermediate-temperature experimental and modeling studies on methyl esters have been performed [37 – 39]. The comparative reactivity over the temperature range 650 < T (K) < 850 of common-carbon-number methyl esters and n-alkanes was studied from 4- to 20-bar using a rapid

compression machine, where the carbon numbers ranged from C_5 to C_8: methyl butanoate ($C_5H_{10}O_2$), methyl pentanoate ($C_6H_{12}O_2$), methyl hexanoate ($C_7H_{14}O_2$), and methyl heptanoate ($C_8H_{16}O_2$) [37]. It was observed that the negative-temperature coefficient (NTC) region for methyl esters manifested at a lower temperature than that typical of linear alkanes.

Experimental data on higher-molecular-weight saturated methyl esters approaching those found in biological sources have more recently been reported, particularly from jet-stirred reactor [38, 42, 70] and diffusion-flame experiments [65, 66, 82]. Ignition delay time experiments using a rapid-compression machine (RCM) have also been performed [37]. Higher-order saturated methyl esters ranging from C_7 to C_{10} have been the subject of recent experiments, and several chemical kinetics models for these species have been developed [39, 83 – 85]. Automatic mechanism generation has been implemented to produce detailed chemical kinetics mechanisms for methyl hexanoate, methyl heptanoate, and methyl decanoate ($C_{11}H_{22}O_2$) [38] and extension to $C_{19}H_{38}O_2$ [39] where C_{13}, C_{15}, and C_{17} methyl esters were included. In both studies, oxidation chemistry near 1 bar pressure is presented with each using temperature-dependent species concentration profiles produced from jet-stirred reactor experiments as validation data; temperature is limited to approximately 1100 K.

Fuel properties (e.g. density, viscosity, pour point, distillation temperature, flash point) of diesel fuel were characterized as a function of methyl ester concentration (2% – 75% by vol.) using commercially available, plant-derived oils [71]. Transesterification using methanol (H_3COH) and potassium hydroxide (KOH) as a catalyst was employed to produce methyl esters from five different plant-derived oils which were blended with two types of diesel fuel: Shell Extra Diesel and Normal Diesel. Neither the atomic composition nor the molecular structure of the methyl esters used in the study was specified. Detailed analysis of pure- and blended-fuel properties resulted in an important blending rule for maintenance of diesel fuel properties. It was proposed that the consistency in diesel fuel properties were retained for up to 20% methyl ester addition by volume.

Battin-Leclerc performed a thorough analysis on elementary reactions involving ethers, esters, and other fuel species utilized in biofuel surrogates [86] and, more recently, has composed a seminal review concerning chemical kinetics modeling of biofuel combustion [87]. Biet et al. reported computational findings using automatic mechanism generation (EXGAS) in which saturated methyl esters above methyl octanoate (C_9:0) show strong similarity with respect to both low- and intermediate-temperature reactivity and ignition behavior above 1000 K [84]. Therefore, using this assessment, methyl octanoate can be used as a representative for the higher-order methyl ester species common to biological oils, tallow, and other biofuel sources, while placing a ceiling on the number of species and reactions requisite for a detailed mechanism.

In the interest of arriving at a methyl ester which appropriately represents the ester function and overall reactivity of larger methyl esters (e.g. methyl palmitate, $C_{17}H_{34}O_2$; methyl stearate, $C_{19}H_{38}O_2$) which are principal components of vegetable and other heavy bio-derived oils, smaller methyl esters have received experimental and modeling attention [40 – 42, 64, 65]. The interest in smaller methyl esters arises primarily out of the effort to minimize or limit the number of species and reactions present in a chemical kinetics mechanism and also in part due to the associated difficulty in studying gas-phase reactions of methyl esters due to extremely low room-temperature vapor pressures; vapor pressures of $C_{17}H_{34}O_2$ and $C_{19}H_{38}O_2$ are ~ 1 mtorr at 20 °C. Herbinet et al. have performed low-temperature jet-stirred reactor experiments and complementary modeling of temperature-dependent species concentration profiles from C_{11} to C_{19} methyl esters [39]. Fundamental high-temperature chemical kinetics measurements on high-carbon-number methyl esters (> ca. C_{11}) using shock tubes, which complement low-temperature data and modeling, require special consideration due to the imposed vapor pressure constraints and are therefore not found in the literature for methyl esters above C_{11} (methyl decanoate) [65], with the exception of methyl dodecanoate droplet ignition work in a microgravity chamber by Marchese et al. [69]. Opposed-flow flame and flow reactor experiments have however been performed on methyl decanoate at high temperatures [40, 65, 66] and HCCI engine tests were performed using n-heptane, methyl decanoate, and dimethyl ether (H_3COCH_3) [64].

Shock-tube studies on methyl esters have been performed on lower-molecular weight esters [79, 81, 88], yet data on species with carbon number greater than 9 are relatively scarce. Methyl octanoate (other names include: caprylic acid /octanoic acid /methyl caprylate) is a methyl ester with a high molecular weight yet a manageable vapor pressure (~ 0.3 torr, 20 °C; ~ 12.6 torr, 80 °C) and could serve as a balance-point between larger methyl esters where both low- and high-temperature studies may be performed using multiple facilities due to the similarity of methyl esters for alkyl chains larger than C_7. Jet-stirred reactor experiments have been performed on blends of methyl octanoate with bio-butanol [36] and ethanol [41] over a wide range of conditions of equivalence ratio (ϕ = 0.5 – 2.0), temperature (560 – 1190 K), and pressure (1, 10 bar), the results from which led to the development of a chemical kinetics model describing radical intermediate production and oxidation products. Mole fractions from the oxidation of pure methyl octanoate in air at 1 atm were measured for fuel-lean and fuel-rich equivalence ratios from 800 K to 1350 K using an opposed-flow diffusion flame apparatus and a jet-stirred reactor wherein species profiles were reported as a function of temperature and distance from the fuel port [42]. Pyrolysis and oxidation experiments on methyl octanoate have recently been the subject of experimental treatment with regards to NO formation [31, 32]. Using an extraction technique, stable species formed from reactions occurring behind reflected shock waves were removed from the shock tube and analyzed offline using thermal conductivity and flame-ionization detection in conjunction with gas-chromatography. A wide range of equivalence ratios and temperatures were covered, and high experimental pressures were used (27 atm – 52 atm) from which detailed analysis of reaction pathways [31], model structure and rate parameters [32] was given. Ignition delay times from methyl decanoate combustion in air near 15 atm have recently been reported [67].

2.2.2 n-Nonane

Fundamental chemistry measurements of higher-order n-alkanes are a necessity in developing adaptive chemical kinetics models which benefit from comprehensive studies spanning a large parameter space, including temperature, pressure, equivalence ratio, fuel concentration, and dilution level. Fundamental data on n-alkanes from methane to octane are abundant, and combustion-related measurements on n-

decane, n-dodecane, and other heavy hydrocarbons are also available, although to a lesser extent. Studies on n-nonane oxidation chemistry are, however, scarce. Normal alkanes make up a significant proportion of diesel and aviation fuels, with jet fuels containing alkanes at levels of 50-70% by volume [44 – 46]. n-Nonane is present in petroleum-based fuels [46], and it is thus of interest to treat the straight-chained alkane experimentally with the aim of building a comprehensive kinetics mechanism to describe its oxidation over a wide range of thermodynamic conditions.

Fundamental combustion studies on n-C_9H_{20} ignition, temperature- and pressure-dependent reactivity, and oxidation pathways are not abundant in the literature. A detailed chemical kinetics study on hydroxyl reactions with linear hydrocarbons focused mainly on OH rate coefficient measurement with ethane and for n-alkanes from C_6 to C_{10} [89]. Measurements of the rate coefficient of n-C_9H_{20} + OH were obtained at high temperature (1100 K) using a shock-tube facility, and a second-order rate coefficient for consumption of OH by n-nonane of $4.55 \cdot 10^{-11}$ $cm^3 \cdot molecule^{-1} \cdot s^{-1}$ resulted from a series of experiments near 1 atm spanning a wide range of n-nonane concentration. A pyrolysis study was conducted in a downflow reactor for C_9, C_{12}, C_{13}, C_{16}, and C_{22} straight-chain alkanes to determine the major yield products using gas chromatography [90]. n-Nonane, at 9.3% decomposition by weight, was observed to have decomposed into the following, predominantly 1-alkene species near 900 K (in descending weight percentage of combustion products): 1-heptene (1-C_7H_{14}), 1-hexene (1-C_6H_{12}), 1-pentene (1-C_5H_{10}), 1-butane (1-C_4H_8), and ethylene. Rate coefficients were also measured for thermal decomposition of n-nonane. Kunzru et al. performed a detailed study on the thermal decomposition of pure n-nonane using a flow reactor with pressure maintained at 1 atm and temperature varied from 920 K – 1020 K, reporting the frequency factor (Arrhenius pre-exponential, A), order of reaction, and activation energy for the decomposition reaction [91]. Product distributions were measured as a function of n-nonane conversion percentage and temperature using gas chromatography. Over the range of temperatures covered in the study, ethylene production from n-nonane decomposition was shown to be considerably higher than any other hydrocarbon species considered. In agreement with the work of Zhou et al. [90], the results of [91] also agreed with a model proposed by kinetic theories of Rice [92] and Kossiakoff and Rice [93].

n-Nonane served as a fuel for investigating the sooting dynamics and droplet morphology of single-droplet combustion where, using a low-gravity approach, spherical gas-phase combustion is promoted around 600-μm droplets of nonane [94]. The paper investigates the effect of pressure (10 atm – 30 atm) on the growth of soot clouds from combustion of the droplet and droplet morphology after ignition. A similar series of independent experiments was conducted wherein the droplet combustion dynamics of JP-8 jet fuel were compared against those of nonane [95, 96].

An expansive modeling study on n-alkane reactivity by Westbrook et al. covered hydrocarbons from C_8 to C_{16} in which a kinetics mechanism was developed using a plethora of experimental data [47]. The model is shown to agree well with n-nonane pyrolysis measurements of Zhou et al. [90]. Model computations were carried out for stoichiometric ignition delay times of the group of higher-order alkanes at 13.5 bar, where overlap was observed at temperatures higher than 1000 K. Due to differences in chain length, the hydrocarbons displayed some variation in ignition delay times over certain regions of temperature. Within the negative temperature coefficient region, 890 K – 960 K, variance in ignition times amongst the hydrocarbons of as much as 1 ms is reported. Near 800 K, the fuels differ in ignition delay time by at most a measure of 600 μs. Ignition delay times remained distinguishable as temperature decreased to ~ 700 K, below which the ignition behavior amongst the various fuels again overlaps.

A chemical kinetics model for constructed jet-fuel surrogate testing (JetSurF v1.0/1.1) includes n-nonane among the n-alkanes incorporated into the mechanism [97]. The initial version of JetSurF has been expanded to include n-alkanes up to n-dodecane, cyclohexane, and mono-alkylated cyclohexane up to n-butyl-cyclohexane [15]. The JetSurF model has been well validated against laminar flame speed measurements [98 – 102], shock tube measurements of ignition delay times [49, 103 – 106] and ground-state species profiles [107 – 110], and jet-stirred and flow reactors [111 – 113]. Ji et al. [99] utilized JetSurF for prediction of laminar flame speeds and extinction strain rates of C_5 – C_{12} n-alkanes in air. Model calculations were compared to experimental data at 1 atm, where deviation from flame speed

measurements was highest (2.5 cm/s) for n-nonane-air mixtures within $0.9 < \phi < 1.1$. Davidson et al. [49] reported measurements of n-nonane ignition delay times using a heated shock tube and compared the experimental results to the JetSurF model. Fuel-lean and stoichiometric conditions were utilized where oxygen concentration remained fixed at 4% and pressure was maintained near 2.0 atm or 3.5 atm. Ignition delay times were also reported for dilute conditions in Rotavera et al. [16]. Table 2.2 summarizes ignition delay time experiments on n-nonane.

Table 2.2. Summary of ignition delay time measurements of n-nonane. All studies were conducted using shock tubes.

P (atm)	ϕ	%n-Nonane	Inert	Diagnostic	Reference
1.5 – 3.5	0.5 – 1.0	0.14 – 0.29	Ar	Pressure	[49]
1.5 – 10.5	0.5 – 2.0	0.10	Ar	OH*	[16]
1.5 – 10.5	0.5 – 2.0	0.14 – 0.57	Ar	Pressure/OH*	Present Study

2.2.3 Methylcyclohexane

Volume-based percentages of cycloalkanes in jet and diesel fuels can reach up to 35% and 45%, respectively [44 – 46]. Methylcyclohexane (MCH) has been studied over a wide range of conditions using shock tubes [114 – 118], rapid compression machines [24, 25, 119], and non-premixed flames [120]. Three models for MCH oxidation chemistry are present in the literature [24, 25, 121], where Orme et al. [24] serves as the base for Pitz et al. [25]. Under highly diluted conditions in Ar, MCH decomposition rates were measure using initial concentrations ranging from 300 to 1500 ppm MCH. Infrared absorption measurements of MCH decomposition and ethylene production at 3.39 μm and 10.53 μm, respectively, were taken behind reflected shock waves during MCH pyrolysis near 2.5 atm from 1150 K to 1430 K, and rate coefficient measurements were deduced using absorption cross sections of the both the parent fuel and of the products, the latter used to account for absorption by other hydrocarbons [114]. Ground-state hydroxyl (OH) ring-dye laser absorption measurements during lean ($\phi = 0.5$) MCH oxidation near 15 atm

were performed using a shock tube [115]. Initial fuel concentrations were varied from 750 to 1000 ppm, and temperature was controlled from 1121 to 1332 K. Time-dependent OH concentration measurements were compared against three chemical kinetics mechanisms with the strongest agreement exhibited by the Ranzi et al. mechanism [121]. Excited-state OH and CH emission measurements were used to extract ignition delay time measurements for MCH/O_2/Ar and MCH/air mixtures behind reflected shock waves from 795 K to 1560 K over a wide range of pressure (1 – 50 atm), fuel concentration (0.25 – 2.0% vol.), and equivalence ratio (0.5 – 2.0) where agreement with previous rapid-compression machine (RCM) measurements was reported [116]. The range of pressure for ignition delay time measurements was extended beyond that reported in [116] by Vanderover et al. [117] to pre-ignition pressures near 70 atm. The study reported ignition times of MCH/air from 880 K to 1319 K under lean (ϕ = 0.25, 0.50) and stoichiometric conditions from 10.8 atm to 69.5 atm. The chemical kinetics model given in Pitz et al. [25] is validated using shock tube and RCM ignition delay times [24] and diffusion flames [120]. Table 2.3 summarizes ignition delay time studies on MCH.

Table 2.3. Summary of ignition delay time measurements of MCH.

P (atm)	ϕ	%MCH	Inert	Diagnostic	Reference
0.6, 1, 1.7	0.1, 0.2, 0.5, 1.0, 2.1	0.0094 – 0.374	Ar	VIS Emission	[118]
1.5, 3	0.5, 1.0	0.19 – 0.38	Ar	OH*, CH*, Pressure	[54]
1, 17, 50	0.5, 1.0, 2.0	0.25 – 1.96	Air, Ar	OH*, CH*, Pressure	[116]
15, 25	0.5, 1.0, 1.5	1.05	Air, Ar	Pressure	[119]
1, 2, 4	0.105, 0.5, 1.0, 2.0	0.099 – 1.0	Ar	VIS, CH*, Pressure	[24]
12, 70	0.25, 0.5, 1.0	0.498 – 1.962	Air	OH*, Pressure	[117]
15	0.5	0.075 – 0.100	Ar	OH	[115]
10, 15, 20	1.0	1.96	Ar, 50/50 Ar/N_2, N_2	Pressure	[25]

3. EXPERIMENTAL METHODOLOGY

Described below are details concerning the preparation of the liquid fuel blends, fuel-injection technique, composition of gas-phase reactive mixtures, and saturation conditions for the fuel blends. A description of the heated shock tube facility is then given, including the design and specifications of the heating system, shock-tube temperature profiles, measurement of thermodynamic test conditions, definition of test time, diagnostics used in the present work, definition of ignition delay time, and measurement uncertainties. Details on shock wave theory, shock-tube design, boundary layer effects, and uncertainties in shock-tube experiments have been covered to a considerable degree in the literature [122 – 130], therefore only facility-specific details are discussed herein. The first appearance of shock tubes in the literature is in the work of Vielle in 1899 [131] and since the middle of the 20th century the device has become a well-established, reliable means of measuring a wide range of physical phenomena of interest to physics, chemistry, astrophysics, and astronomy [122, 123].

The flame speed facility used in the present work is described in detail in the work of Krejci [132]. Discussed below, for the flame speed measurements performed herein, is the procedure for injection of the liquid fuel blends into the flame speed vessel, details on the optical diagnostic used for flame visualization and subsequent measurement, the analytical procedure for determination of laminar flame speed, and measurement uncertainties.

3.1 Composition and preparation of ternary liquid fuel blends and gas-phase reactants

Due to the inherently low vapor pressure of the fuel constituents studied herein, ternary liquid fuel blends comprised of methyl octanoate, n-nonane, and methylcyclohexane were prepared to syringe-inject the blend into a heated mixing chamber in the shock-tube experiments and, in separate experiments, directly into the flame speed vessel. Direct-injection of the liquid blends assures that the exact relative proportions present in the liquid-phase are present in the gas phase, thereby avoiding preferential vaporization wherein species within a blend with the highest vapor pressure occupy, with increasing temperature, larger percentages of the gaseous state under phase equilibrium. Using a Design of Experiments approach [133,

134], an L9 orthogonal array was assembled to systematically approach the effect of variation of equivalence ratio, pressure, and hydrocarbon class on species time histories and ignition delay times (Table 3.1). Only laminar flame speeds of pure fuel constituents are presented in the present study. The L9 array allows for testing of the influence of four different independent variables (chosen here to be P, ϕ, %$C_9H_{18}O_2$, and %MCH) with each variable having three assigned values. The independent variables and corresponding levels are outlined explicitly in Table 3.2. The concentration of n-nonane is excluded from the construction of the L9 array, yet is included in the test set using a molar balance of the fuel volume fractions from the relation: $1 = y_{C_9H_{18}O_2} + y_{n-C_9H_{20}} + y_{C_7H_{14}}$. Equivalence ratio is defined herein using fuel-to-oxidizer ratios (Eqn. 3.1).

$$\phi = \left(\frac{\mathrm{X_{Fuel}}}{\mathrm{X_{Oxidizer}}}\right) \Big/ \left(\frac{\mathrm{X_{Fuel}}}{\mathrm{X_{Oxidizer}}}\right)_{\mathrm{Stoichiometric}} \qquad (3.1)$$

Table 3.1. Relative proportions (fuel vol.) of ternary fuel blends and respective test pressures and equivalence ratios. n-Nonane percentage is not included in the L9 array.

Blend	P (atm)	ϕ	%$C_9H_{18}O_2$	%MCH	%n-C_9H_{20}
1	1.5	0.5	10	20	70
2	1.5	1.0	20	30	50
3	1.5	2.0	30	40	30
4	5.0	0.5	20	40	40
5	5.0	1.0	30	20	50
6	5.0	2.0	10	30	60
7	10.0	0.5	30	30	40
8	10.0	1.0	10	40	50
9	10.0	2.0	20	20	60

Table 3.2. Independent variables and associated levels included in the L9 array.

Independent Variable	Level 1	Level 2	Level 3
P (atm)	1.5	5.0	10.0
Equivalence Ratio (ϕ)	0.5	1.0	2.0
%Methyl Octanoate (Fuel Vol.)	10	20	30
%Methylcyclohexane (Fuel Vol.)	20	30	40

The volumetric proportions of the ternary fuel blend constituents were designed with the intent of spanning a large range in concentration, while maintaining levels which are consistent with common surrogate fuels reported in the literature. The chosen methyl ester concentration range from 5% to 30% (vol.) extends slightly beyond the limits of addition to diesel fuel as discussed by Alptekin and Çanakçi [71] where concentrations up to 20% were found not to compromise properties such as density and viscosity. The increase in the upper limit was chosen to identify whether the additional methyl ester concentration impacts combustion properties, namely ignition properties. Ideal mole fractions were assigned to the three constituents in a given liquid mixture, and from the volumetric relationships relative masses were calculated and used to prepare the blends. The individual masses of the liquids were measured on an Ohaus ARA520 scale with 10-mg precision. Calculations were performed during preparation to ensure that the ternary mixtures were comprised of the appropriate molar proportions. Relative errors were calculated for each constituent, and a weighted error was then determined for a given blend from the summation of the relative errors. Purity levels for each constituent were ≥ 99%: Methyl octanoate (Sigma Aldrich: W272809-1KG-K), n-Nonane (Sigma Aldrich: N29406), Methylcyclohexane (Sigma Aldrich: M37889). The procedure for preparing the liquid blends is provided in the steps below (Blend 7 is used in the example calculation). All calculations are based on relative volume percentages and methyl octanoate was chosen as the initial input. Tabulation of the liquid masses and volumes used for the ternary blends and temperature-dependent liquid densities are provided in Appendix A and Appendix B, respectively.

Step 1 – Inject an arbitrary mass of methyl octanoate into beaker (e.g. 58.51 g) depending on the total fuel-blend volume desired. The numerical value of mass is not significant, however it dictates the final mass (and volume) of the liquid fuel blend. Volume for methyl octanoate is then calculated using the density of the fuel at 295 K. $V_{\text{Methyl Octanoate, Blend 7}}$ = 66.8 mL.

Step 2 – The *ideal* volume of n-nonane is then calculated relative to the actual volume of methyl octanoate from Step 1 using the prescribed molar relationship. For Blend 7, $V_{\text{n-Nonane}} = (40\%/30\%)V_{\text{Methyl Octanoate, Blend 7}}$ = 89.1 mL. The *ideal* mass of n-nonane to be added to the methyl octanoate is then determined using the density of n-C_9H_{20} at room temperature: $m = V \cdot \rho_{n-nonane}(295\ K)$. $m_{\text{n-Nonane}}$ = 63.8 g.

Step 3 – n-Nonane is then introduced into the beaker with the target mass calculated in Step 2 (e.g. 63.80 g of n-Nonane ideally added to the 58.51 g of methyl octanoate for a combined mass of 122.33 g). Actual mass of n-nonane is determined by subtracting the mass of the methyl octanoate in the liquid blend from the measured mass of the combined fuels (e.g. 122.04 g). The actual n-nonane volume is then calculated using the measured mass (e.g. 63.53 g) and the density of n-C_9H_{20} at 295 K. $V_{\text{n-Nonane, Blend 7}}$ = 88.7 mL.

Step 4 – The *ideal* volume of methylcyclohexane (MCH) is then calculated relative to the actual volume of methyl octanoate from Step 1. The *ideal* mass of methylcyclohexane to be added to the methyl octanoate/n-nonane blend is then determined using the *ideal* volume of MCH based on the relative amount to methyl octanoate and the density of MCH at room temperature: $m = V_{Ideal,MCH} \cdot \rho_{MCH}(295\ K)$.

Step 5 – Methylcyclohexane is then introduced into the beaker containing methyl octanoate and n-nonane with the target mass calculated in Step 4 (e.g. 51.29 g of methylcyclohexane ideally added to the 122.04 g of methyl octanoate/n-nonane blend for a combined mass of 173.33 g). The actual mass of methylcyclohexane is determined by subtracting the mass of the combined fuels (e.g. 173.55 g) from the total mass of the liquid blend in Step 3. The actual MCH volume is then calculated using the measured mass (e.g. 173.55 g – 122.04 g = 51.51 g) and the density of MCH at 295 K. $V_{\text{MCH, Blend 7}}$ = 67.1 mL.

Step 6 – Total mixture volume is calculated using the individual volumes. For Mixture 7, using 58.51 g of methyl octanoate, a total mixture volume of 222.7 mL is produced as a result of the predefined relative mole fractions.

Step 7 – Error in the measured mole fractions is calculated and tabulated for each mixture and an overall, weighted error is assigned to each fuel blend. Relative errors are determined using absolute values by the product of the actual volume ratios in the blend and the individual errors in mole fractions (Eqn. 3.2). Weighted error for each blend is determined using Eqn. 3.3. Error results are provided in Table 3.3. Weighted errors of less than 0.3% were maintained for all liquid blends.

$$Relative\ Error \equiv y_{i,actual} \cdot \left[\left(y_{i,actual} - y_{i,ideal}\right)/y_{i,actual}\right] \cdot 100 \qquad (3.2)$$

$$Weighted\ Error \equiv \sum_{i=1}^{3} (Relative\ Error)_i \qquad (3.3)$$

Table 3.3. Measured mole fractions, relative and weighted errors for ternary liquid fuel blends. Blend x, from Rotavera and Petersen [135] uses 5% (fuel vol.) methyl octanoate, and is not included in the L9 array.

Blend	$C_9H_{18}O_2$	% Error	n-C_9H_{20}	% Error	MCH	% Error	Weighted Error
1	0.10	0.00	0.70	0.00	0.20	0.16	0.03
2	0.20	0.00	0.50	0.29	0.30	0.03	0.15
3	0.30	0.00	0.30	0.14	0.40	0.01	0.05
4	0.20	0.00	0.40	0.01	0.40	0.02	0.01
5	0.30	0.00	0.50	0.03	0.20	0.01	0.02
6	0.10	0.00	0.60	0.02	0.30	0.02	0.02
7	0.30	0.00	0.40	0.46	0.30	0.42	0.31
8	0.10	0.00	0.50	0.11	0.40	0.02	0.06
9	0.20	0.00	0.60	0.07	0.20	0.12	0.06
x	0.05	0.00	0.50	0.09	0.45	0.04	0.07

Characterization of the volatility of the liquid fuels is of significant importance to the study due to the aforementioned potential for condensation. Temperature-dependent vapor pressures were determined by applying an empirical expression for the Clapeyron equation along the liquid-vapor phase boundary. Antoine [136] extended the Clapeyron equation for vapor-liquid phase equilibrium by adding a third constant (Eqn. 3.4). The values of the (Antoine) constants A, B, and C were calculated using regression analysis from experimental data over a prescribed range of temperature and are listed for fuel constituent in Table 3. The Antioine constants from Rose and Supina [137] for methyl octanoate yield pressure in units of torr, while the constants for n-nonane and methylcyclohexane from [138] yield pressure in units of bar.

$$log_{10}\left(P_{Vapor}\right) = A - \frac{B}{T + C - 273.15} \qquad (3.4)$$

Table 3.4. Antoine constants for methyl octanoate [137], n-nonane [138], and methylcyclohexane [138].

Species	A	B	C	Units of Pressure
$C_9H_{18}O_2$	7.57031	1920.100	216.780	torr
n-C_9H_{20}	4.07356	1438.030	202.694	bar
C_7H_{14}	3.98232	1290.968	223.701	bar

Calculations of vapor pressure were performed over the possible range of initial (pre-shock) temperatures in the present study (Fig. 3.1), and it was identified that the limiting factor in terms of temperature requirements is the methyl ester species due to its larger molecular size and comparatively more complex structure relative to n-nonane or methylcyclohexane. Shock-tube experiments performed herein maintained a nominal initial temperature of 50 °C. The initial temperature of the flame speed experiments was maintained at 170 °C. In the latter experiments, methyl octanoate had the lowest saturation temperature (143.6 °C) at the maximum partial pressure required for performing fuel-rich experiments

(175.0 torr). Correspondingly, the 170 °C temperature was chosen to maintain partial pressures below 50% of the saturation pressure at 143.6 °C (175.0 torr). The saturation pressure of methyl octanoate at 170 °C, using the Antioine equation, is 406 torr.

Tables 3.5 and 3.6.a/.b detail the saturation pressures for the fuel constituents at these temperatures and partial pressures used in the experiments. Noting the diminutive quantity of fuel used in the highly dilute shock-tube experiments from Table 3.5, the saturation temperature for these pressures are below room temperature. The initial temperature of the shock tube of 50 °C is therefore sufficient to neglect concerns for condensation during the experiment (tests were performed to validate this assumption nonetheless, as described towards the end of the present section). In all cases, noting the ppm-level of fuel present in the experiments, temperature ceilings are lower than those required for non-dilute studies where the partial pressure of the fuel is significantly higher.

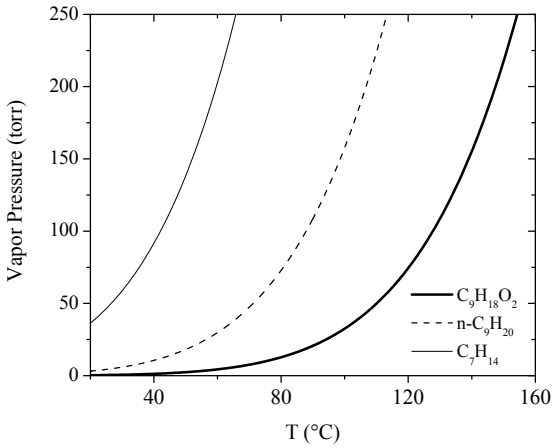

Fig. 3.1. Calculated vapor pressure curves for methyl octanoate, n-nonane, and methylcyclohexane as a function of temperature using the Antoine equation (Eqn. 3.4).

Table 3.5. Maximum partial pressures of fuel present in shock-tube experiments. Blend 7 was studied under lean, high-pressure conditions (ϕ = 0.5, 10 atm) which required the highest initial test pressure in the series and therefore the highest partial pressures. n-Nonane is not included since the ignition results presented herein for this species use the empirical correlation of Rotavera et al. [16].

Blend	$P_{C_9H_{18}O_2}$ (torr)	$P_{n\text{-}C_9H_{20}}$ (torr)	P_{MCH} (torr)
(Pure)	0.150	-	0.171
7	0.045	0.056	0.045

Table 3.6a. Maximum partial pressures of fuels present in laminar flame speed experiments. Only pure fuel (i.e. single component) tests were conducted in the present work. The maximum partial pressures are calculated at ϕ = 1.4, the terminal equivalence ratio for the flame speed measurements in the present work.

Fuel	$P_{C_9H_{18}O_2}$ (torr)	$P_{n\text{-}C_9H_{20}}$ (torr)	P_{MCH} (torr)
(Pure)	175.0	156.0	207.0

Table 3.6b. Saturation temperatures corresponding to the maximum partial pressures of fuels present in laminar flame speed experiments from Table 3.6.a. The initial temperature of the flame speed experiments was maintained at 170 °C.

Fuel	$T_{sat.,\,P,\,C_9H_{18}O_2}$	$T_{sat.,\,P,\,n\text{-}C_9H_{20}}$	$T_{sat.,\,P,\,MCH}$
(Pure)	143.6	99.7	60.6

3.1.1 Preparation of gas-phase reactants from liquid fuel blends for shock tube experiments

The stoichiometric reaction equation for the ternary blends is written according to Eqn. 3.5 to account for the three species in the blend, where the relative mole fractions are defined according to the L9 array. The oxygen content of methyl octanoate is included in the calculation of the number of oxygen moles, x.

$$y_1 C_9H_{18}O_2 + y_2 n\text{-}C_9H_{20} + y_3 C_7H_{14} + xO_2 \rightarrow aCO_2 + bH_2O \qquad (3.5)$$

A mole fraction calculator was developed to determine the partial pressures, for a given fuel blend and corresponding equivalence ratio, required to prepare gaseous mixtures. Appendix C contains an outline of the spreadsheet used. The details are summarized below.

Mole fractions of a given constituent depend on the relative amounts of fuel species in the blend, equivalence ratio, and level of dilution (99% Ar for the present study). Stoichiometric oxygen-to-fuel ratios, $(O{:}F)_{Stoich.,}$ were determined by solving Eqn. 3.5 for x based on 1 mole of total fuel (Eqn. 3.6).

$$(O{:}F)_{Stoich.} = 12.5y_{C_9H_{18}O_2} + 14y_{n\text{-}C_9H_{20}} + 10.5y_{MCH} \quad (3.6)$$

Fuel mole fractions were then calculated using Eqn. 3.7:

$$y_i = y_{i,\,Blend}\left(y_{O_2}/O{:}F\right) \quad (3.7)$$

Mole fraction of oxygen calculated using Eqn. 3.8.

$$y_{O_2} = (1 - y_{Ar})(O{:}F/1 + O{:}F) \quad (3.8)$$

Oxygen-to-fuel ratios depend on the composition of the blend and the corresponding equivalence ratio (Eqn. 3.9):

$$O{:}F = (O{:}F)_{Stoich}/\phi \quad (3.9)$$

The results of the calculations for fuel and oxygen mole fractions for each mixture are provided in Table 3.7. The balance of the sum of the mole fractions in Table 3.7 is the diluent (0.99 Ar). Over the range of mole fractions required for the particular blends, and corresponding stoichiometry, methyl octanoate, n-

nonane, and MCH concentrations were varied by factors of 12, 5, and 8, respectively. Oxygen concentration varied only 10% over the range of equivalence ratios due to the constraint of 99% Ar. The larger variation in fuel percentage affords the development of a well-constrained experimental correlation dependent on concentration (Section 3.2.5)

Table 3.7. Molar composition and stoichiometry of blends in shock tube experiments (balance: 0.99 Ar).

Blend	ϕ	Mole Fractions			
		$C_9H_{18}O_2$	n-C_9H_{20}	MCH	O_2
1	0.5	0.000037	0.000256	0.000073	0.009634
2	1.0	0.000147	0.000366	0.000220	0.009267
3	2.0	0.000424	0.000424	0.000565	0.008587
4	0.5	0.000078	0.000156	0.000156	0.009609
5	1.0	0.000217	0.000361	0.000144	0.009278
6	2.0	0.000135	0.000811	0.000405	0.008649
7	0.5	0.000115	0.000154	0.000115	0.009615
8	1.0	0.000074	0.000372	0.000297	0.009257
9	2.0	0.000267	0.000800	0.000267	0.008667
x	1.0	0.000040	0.000370	0.000340	0.009250

After the liquid mixtures were prepared a scientific-grade syringe, constructed of a borosilicate body with a stainless steel needle, was used to extract a specific volume of fuel for injection into either the shock tube or laminar flame speed vessel. For shock-tube experiments, only small amounts of fuel were used due to the high level of dilution (ratio of moles of Ar to moles of fuel ~ 100); the typical range of liquid fuel injected into the shock-tube mixing chamber was ca. 0.5 – 2.5 mL. For flame speed experiments where

fuel makes up approximately 2% of the total mixture by volume, ca. 5 – 15 mL were injected directly into the vessel. Mole fractions of fuel and oxygen were calculated for fixed Ar concentration (99% by vol.) using the desired equivalence ratio (Table 3.7).

The gas-phase mixtures were prepared in a chamber separate from the shock tube using the partial pressure method. Inside the mixing chamber, turbulent mixing is promoted through an internal multi-hole delivery tube where the 800-μm-diameter holes span the length of the chamber. High-purity research-grade (> 99.9995%) oxygen and Ar were employed. Precautions were taken to ensure mixture homogeneity and avoidance of condensation inside of the supply lines and in the mixing chamber. First, mixtures were made with the partial pressures below 20% of respective saturation pressures at the nominal 50 °C temperature of the system. During the addition of the other constituents (O_2 and Ar), pulses were used to further promote mixing during their individual injection.

A second precaution was taken whereby a minimum waiting time of 12 hours was adopted prior to using the mixture for experiments to allow for further mixing through diffusive processes. Since repeatability is of particular importance due to the low vapor-pressure of the fuel and corresponding concerns over fuel condensation, the issue being the potential for an inhomogeneous mixture, repeat mixtures were tested. Mixtures were repeated a minimum of two times, with some mixtures ($C_9H_{18}O_2$, $\phi = 1.0$) being repeated beyond the minimum to ensure repeatability of the mixing procedure and resulting measurements. Further, in the stoichiometric mixtures, fuel was intentionally left isolated in the mixing tank for 12 hrs., 18 hrs., and 24 hrs. during the repeat tests with varying amounts of fuel used in each case. Oxygen leakage into the mixing system over the longest time pereiod (24 hrs.), equal to 21% of total leak rate (ambient air sepage), was at most 50 mtorr, or less than 0.2% of the total oxygen content in the mixture.

A remaining uncertainty, and third precautionary measure taken due to the tendency of polar molecules to form temporary bonds with metal surfaces (ion-dipole bonding), was the use of passivation in experiments

involving methyl octanoate and the ternary blends. In the single-component methyl octanoate experiments, the shock tube was filled to the pressure used for the initial pressure in the experiment (ca. 50 torr for 1-atm experiments) and left to reside inside of the shock tube for approximately 1 min., after which the shock tube was evacuated and re-filled to the desired initial pressure. No differences in the ignition delay time results were observed with or without the use of passivation.

Lastly, the potential for fuel loss (through either condensation and/or ion-dipole bonding of the methyl ester) from expansion into the shock tube during filling was also monitored. Initial pressure levels in the shock tube were maintained for several minutes and no change in pressure was observed. Waiting time, filling rate, and initial pressures, in addition to the repeats provided confidence in the results. Given the diminutive quantities of fuel used in the present experiments, even a small change in fuel concentration from losses would strongly impact the results.

Consistent trends produced from a given mixture eliminate the concern of fuel loss during variation in waiting time (1 min. – 5 min.) and filling rate and provided confidence in repeatability for each individual mixture. Further, and repeatable trends from different mixtures supported the consistency of the measurement technique. Therefore, the four above precautions (partial pressures of fuels maintained below 20% of respective saturation pressures at 50 °C, 12-hr. waiting time for completed gas-phase mixtures to undergo diffusion processes and further enhance mixture homogeneity beyond that attained using induced turbulence, use of passivation to verify no loss in concentration of the polar species, and monitoring of pre-test pressure) provided assurance in the composition of the reactive mixture entering the shock tube, leading to repeatable measurements of species profiles and ignition times.

3.2 Description of heated shock tube facility

The heated shock-tube facility makes use of the 4.0-m long stainless steel driven section and a 2.0-m long driver section described in detail in Rotavera [139]. The internal dimensions for the circular driver and square driven sections are 7.6 cm and 10.8 cm, respectively. The driver section (L /D = 23.6) was supplied

He driver gas for the present experiments. Shock-front velocity is precisely measured through the use of four high-frequency piezoelectric pressure transducers (PCB 113A) mounted atop the driven section at locations toward the end of the shock tube in conjunction with 120-MHz counters /timers (Phillips P6666), using respective distances between pressure sensors and the recorded time intervals. For a given measurement of shock speed, two pressure transducers are employed to report an initial time and final time where the initial time indicates the arrival of the (incident) shock at the first transducer, and the final time indicates the arrival at the second. The 120-MHz sampling rate allows the timers to provide shock velocities on microsecond timescales. In total, the four pressure sensors make up a three-interval field within which velocities is measured. A linear extrapolation of the measured velocities is used to calculate the shock speed at the plane of the endwall where the reflected shock forms. An extrapolation is required due to physical limitations in positioning the pressure transducer directly at the endwall. Three measurements of shock speed are made, and a linear trend of the three data points is then calculated from which then the velocity of the shock at the arrival of the endwall is extracted.

3.2.1 Heating system and shock-tube temperature profiles

When performing gas-phase shock-tube experiments using high-molecular-weight hydrocarbons, due to the inherent low vapor pressure, heating is required to (i) raise the saturation pressure to levels which allow for preparation of a gas-phase reactive mixture and (ii) limit the potential for condensation. Modifications were implemented in the 4-m long, 117-cm^2 shock-tube facility described in Rotavera [139], wherein a series of heating systems were recently implemented as a part of the present study to allow for precise control over the initial temperature of both the system and reactive mixture. Feedback-controlled heating elements were installed over six regions along the shock tube to minimize axial temperature gradients, while the gas preparation system and mixing tank have additional, independent temperature control.

Figure 3.2 provides a detailed schematic of the shock tube facility. Figure 3.3 shows axial temperature measurements of heated atmospheric air along the shock-tube centerline at three nominal temperatures.

Temperature measurements were made using a K-type bead thermocouple mounted inside of an extended temperature probe. The probe was inserted through the endwall at prescribed, relative distances with measurements made along the shock-tube centerline at intervals of 15 cm. The thermocouple remained fixed at a given position for a time sufficiently long for the temperature reading to reach steady-state, which was roughly 30 s. As shown in Fig. 3.3, temperature along the shock tube remains highly uniform with a maximum ΔT relative to the average of ±0.6 °C, ±1.2 °C, and ±2.5 °C for the 52 °C, 82 °C, and 112 °C average temperatures, respectively. Temperature closer to the diaphragm station was measured to be outside the narrow deviation observed for the main part of the shock tube. However, average temperatures within 60 cm of the diaphragm were set higher than the saturation temperature of the condensable species. In addition, the region nearest the diaphragm station (the shock-formation region) passes undeveloped, highly turbulent flow which makes relatively slight temperature non-uniformities insignificant. Careful attention was paid to ensure a highly uniform temperature profile near the endwall region. The shock-tube facility utilized for the present work is temperature-controlled with heating capability up to 110 °C, which provides assurance in mixture composition in that low-vapor-pressure fuels remain in the vapor phase (i.e. mole fractions remain constant).

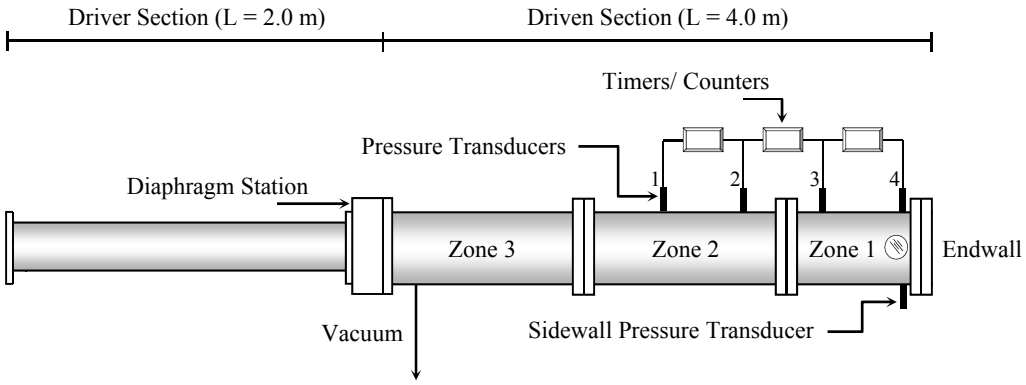

Fig. 3.2. Schematic of heated shock-tube facility. Feedback-controlled heating elements cover seven regions along the shock tube to minimize axial temperature gradients. Heating Zones 2 and 3 supplied with 1 kW, Zone 1 supplied with 0.5 kW. Supplementary heating elements and independent temperature controllers are placed around the diaphragm station, two connecting flanges, and endwall flange.

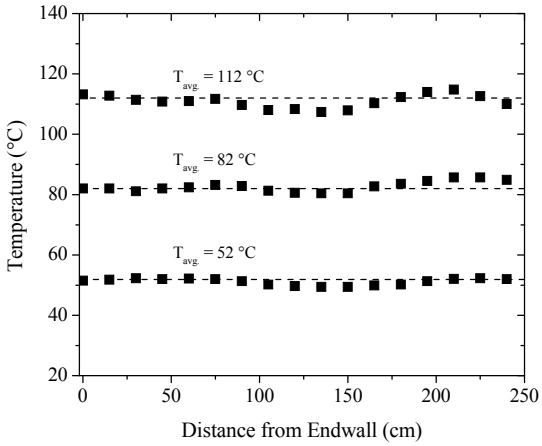

Fig. 3.3. Shock-tube centerline temperature as a function of longitudinal distance from the endwall. Peak temperature deviation for 112 °C, 82 °C, and 52 °C average temperatures are +4.9 °C, +3.3 °C, and –2.5 °C, respectively.

3.2.2 Measurement of thermodynamic test conditions

Shock tubes serve an important role in high-temperature chemical kinetics experiments due to the ability to produce controlled and repeatable conditions of temperature and pressure. Temperatures reported herein for shock tube experiments are calculated, rather than intrusively measured, using 1-D shock relations and real-gas (i.e. temperature dependent) thermodynamic properties described by Gaydon and Hurle [122] and are subject to uncertainty resulting from non-ideal gas dynamics. Temperature is of significant importance due to the exponential dependence in rate coefficients of Arrhenius form. The calculated temperature uncertainty for the present facility is approximately 1%. Calculating an arbitrary rate coefficient at the peak temperature of the present study (1675 K), for E_a = 20 kcal/mol, n = 0, A = 1, a 6% error in $k(T)$ is shown from a 1% variation (17 K) in temperature. The error in $k(T)$ increases with increasing activation energy (a 25% error occurs from the 1% variation in temperature for E_a = 72 kcal/mol). Detailed calculations on temperature uncertainty in shock tubes are documented in Petersen et al. [140].

Due to non-ideal viscosity effects between fluid moving behind the incident shock wave and the internal walls of the shock tube, boundary layers are formed behind the incident shock front which itself inherits attenuation resulting from momentum degradation during propagation. These two effects contribute to uncertainty in temperature from the reflected shock wave propagating through an area smaller relative than that of the incident shock front and from uncertainty in shock velocity, respectively. The reduced area through which the reflected shock wave traverses is the result of boundary layer formation. For the reflected shock front the area can be calculated: $A = \left(A_{Shock\ Tube} - 4(h \cdot W)_{Boundary\ Layer}\right)$, where boundary layer width is that of the shock tube and thickness depends on test pressure, temperature, and the time of incident shock passage at a particular location. The theoretical boundary-layer calculations of Petersen [141, 142] extensively cover boundary layer growth in shock-tube experiments for both laminar and turbulent conditions. Using a shock velocity of 0.8385 mm/μs, a representative reflected-shock front velocity for the present experiments, boundary layer thickness at the diagnostic plane 3.18 cm from the endwall (Section 3.2.3) for the present experiments conducted near pressure and temperature of 1 atm and 1650 K, respectively, is approximately 1 mm, causing an area reduction for the reflected shock front of less than 1%.

Rates of shock attenuation increase as the reflected shock wave passes through a higher-temperature gas and has to interact with the boundary layer formed by the flow behind the incident shock wave. Shock velocity is known within the bounds of the calculated rate of attenuation, which for the present series of experiments is less than 1% per meter, imposing a maximum uncertainty in the calculation of temperature of approximately ±15 K. The consequence of shock velocity attenuation is shown in Fig. 3.4 (velocity decreases towards the endwall). Attenuation is quantified by considering the change in shock front velocity over a given distance (Eqn. 3.10). The degradation of shock velocity translates to a decrease in momentum, which is measured using velocity measurements from pressure transducers. Uncertainty arises in definition of the reflected-shock temperature due to physical limitations of measuring shock velocity

immediately adjacent to the endwall and the required linear extrapolation of velocity from the last measurement point 3.18 cm from the endwall to the face of the endwall.

$$Percent\ Attenuation\ per\ Meter = \frac{\left(\frac{\mathcal{V}_{Final} - \mathcal{V}_{Initial}}{\mathcal{V}_{Initial}}\right) \cdot 100}{Length\ of\ Measurement\ Region\ (m)} \qquad (3.10)$$

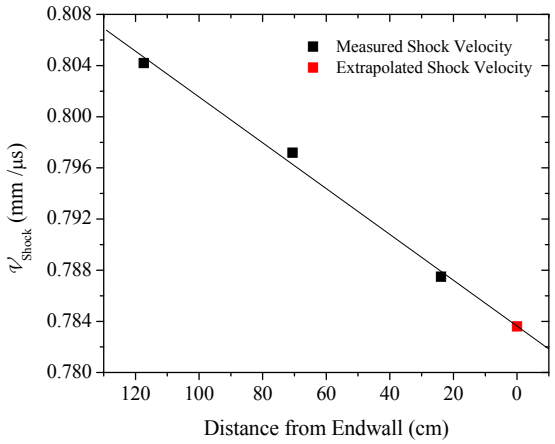

Fig. 3.4. Incident-shock velocity measurements. Linear extrapolation is used to calculate velocity at the endwall. The 0 cm position on the abscissa indicates the endwall location. R^2 = 0.99. Representative attenuation rate for the experiments herein → 1%/m. Solid line indicates experimental fit.

Computation of shock velocity serves as one of two input variables, the other of which being the initial pressure of the driven gas (P_1), to arrive at a characteristic solution of the *Rankine-Hugoniot shock relations*, which are derived from energy and momentum equations. The shock relations are solved iteratively using real-gas thermodynamics, employing $c_P(T)$, s(T), and h(T) data from Sandia National Laboratories to define conditions within the reflected-shock region pertinent to a given experiment. The temperature dependence of the thermodynamic properties is characterized using the NASA polynomials [143]. Appendix D provides the NASA equations for specific heats, entropy and enthalpy as a function of temperature.

In order to predict the thermodynamic conditions within the shock tube, the waves are assumed planar which is a valid approximation past a distance of several diameters of length after the diaphragm station. From the planar-wave assumption, a one-dimensional (1D) simplification of the fundamental equations of motion and energy describing shock-gas interaction is employed (Rankine-Hugoniot equations). From the solution of these equations, one can determine with high accuracy (within 1%) the conditions of temperature and pressure to which the test variable is subjected. These equations require two input variables to reach a characteristic solution, a Mach number and a specific heat ratio. Detailed and highly comprehensive work is performed by M. D. Salas [144] on the history of shock wave theory, dealing with the works of William John Macquorn Rankine [145] and Pierre Henri Hugoniot [146].

Embedded assumptions include propagation of the shock through an ideal gas with variable specific heats (c_P and c_V). The shock process is considered adiabatic as there is both insufficient time and insufficient area for appreciable quantities of heat to transfer. In terms of incident-shock Mach number M_1, pressure and temperature conditions behind the reflected shock wave (P_5 and T_5, respectively) relative to initial conditions are given in Eqns. 3.11 and 3.12, respectively.

$$\frac{P_5}{P_1} = \left\{\frac{2\gamma M_1^2 - (\gamma - 1)}{\gamma + 1}\right\}\left\{\frac{(3\gamma - 1)M_1^2 - 2(\gamma - 1)}{(\gamma - 1)M_1^2 + 2}\right\} \tag{3.11}$$

$$\frac{T_5}{T_1} = \frac{\{2(\gamma - 1)M_1^2 + (3 - \gamma)\}\{(3\gamma - 1)M_1^2 - 2(\gamma - 1)\}}{(\gamma + 1)^2 M_1^2} \tag{3.12}$$

Mach number M (ratio of the speed of an object (shock wave) relative to the characteristic sound speed of the medium through which the object travels) is defined in Eqn. 3.13.

$$M = \frac{\mathcal{V}}{a} \tag{3.13}$$

or, using the ideal gas equation of state and shock velocity,

$$M = \frac{\mathcal{V}_{Shock\ Wave}}{a_{Test\ Gas}} = \frac{\mathcal{V}_{Shock\ Wave}}{(\gamma(T)RT)^{0.5}} \qquad (3.14)$$

As observed from the above 1D shock relations, the thermodynamic conditions within the shock tube are dictated strictly by the specific heat ratio γ and the Mach number M. *Bath gases* can range widely in composition to match experimental goals. Table 3.8 shows several solutions for the Rankine-Hugoniot shock relations for commonly used bath gases using helium as a driver gas. The term bath gas implies a nonreactive gas (Ar, Xe, Kr) or air, differing from test gas which contains reactive fuel with O_2 or air.

Table 3.8. Variance of thermodynamic condition for changing bath gas composition using helium as driver gas. Lower acoustic speeds imply that the fluid has a lower response time to react to oncoming pressure perturbations resulting in a larger Mach number (for fixed-velocity shock) and correspondingly larger step-changes in both pressure and temperature.

Species	γ_1	γ_5	P_5/P_1	T_5/T_1	$M_{Incident\ Shock}$	a_1 (m/s)	a_5 (m/s)
Ar	1.67	1.67	29.03	5.15	2.50	320	726
79/21 Ar/O_2	1.58	1.53	30.01	4.53	2.51	318	667
Air	1.40	1.34	24.25	3.00	2.32	345	586
N_2	1.40	1.35	23.05	2.96	2.29	350	593

3.2.3 Diagnostics

Optical and spectroscopic measurements frequently involve differential laser diagnostic techniques whereby a single laser beam of certain wavelength or multiplexed array of wavelengths is passed through the shock tube to interrogate the formation/depletion of certain species, probe for temperature, or to

measure velocities. Additionally, emission spectroscopy measured from the exiting of electromagnetic radiation from the reacting fuel and oxidizer provides pertinent insight into the underlying chemical kinetics due to the dependence of excited-state species on ground-state chemistry. For these and other measurements, optical access is required in shock tubes which are routinely employed for experiments which utilize such techniques. In the facilities employed in the present work, a sidewall diagnostic station positioned close to the endwall monitors reaction progress using chemiluminescence and pressure time histories.

Pressure measurements at the sidewall provide time-of-arrival information for both incident and reflected shock waves. Sidewall pressure is recorded using a 500-kHz quartz pressure transducer (Kistler 603B1). Sidewall emission of photons from excited species during combustion is tracked using a detector which employs a photomultiplier tube (Hamamatsu Type 1P21), the output signal from which undergoes amplification using a low-noise pre-amplifier (SRS SR560). UV-filtering is employed to observe emission at two specific wavelengths, λ_{OH^*} and λ_{CH^*}. One narrowband filter (10 nm FWHM) centered at 430.0 nm is utilized to capture the ultra-violet CH* chemiluminescence while a separate, 40-nm FWHM filter centered at 300 nm passes emission near the emission band of the OH* species (307.1 nm). The sidewall-positioned window and centerline of the sidewall pressure transducer form a diagnostic plane (field of view) which is positioned 3.18 cm from the endwall. The distance between the sidewall diagnostic plane and the endwall is minimized to reduce the uncertainty in shock speed and resulting uncertainty in thermodynamic state of the reflected-shock gas. Experimental data for pressure and optical diagnostics appended to the sidewall are recorded using two 16-bit, 25-MHz Gage Applied Sciences data acquisition boards (CS8482).

Careful attention is paid to the set up and optical alignment of the photomultiplier (PMT) detector to maximize signal-to-noise (S /N) ratio, force the detector to see a thin plane inside of the test section of the shock tube, and avoid interference emission. A visible Helium-Neon (HeNe) laser (632 nm) is centered with and passed through a window on one side the shock tube directly into a medium placed inside of the

test region which causes the light to disperse, simulating the multi-directional emission that occurs during combustion. The dispersed light is then transmitted through an identical window on the opposite side of the shock tube and collected onto a concave mirror of focal length f = 10 cm. The concavity of the mirror reforms the collected, yet still dispersed light emitting from the shock-tube window into a single, focused point positioned directly onto the detector. Minor adjustments are then made to maximize the S/N while monitoring signal output. During alignment, the PMT detector is unfiltered so that it may see the visible 632 nm light. After optimal alignment is achieved, a bandpass filter is appended to the PMT viewport. The window from which emission exits is unobstructed during alignment, however throughout the experiment, emission from combustion exits a single CaF_2 window through the 400 μm slit. The other (opposing) window is covered so that peak intensity is observed through a single window on the side of the shock tube the detector is positioned. Purposely obstructing the window using a 400-μm slit reduces the field of view of the detector, ensuring minimal interference from wall reflections is incurred. The slit also acts to restrict the detector to a narrow plane (ideally infinitesimally thin) which is representative of a chemically reacting cross-section within the volume of the test region. To further restrict the viewing area of the detector inside of the shock-tube test region, the sidewall PMT detector is positioned at an angle approximately 60° from the sidewall-mounted optical window. The converse to this approach, aligning the detector face normal to the window, results in an enlarged conical-like viewing area as opposed to the intended narrow plane which then artificially increases signal intensity. An optical schematic of the PMT system with which OH* and CH* profiles are measured is shown in Fig. 3.5. A detailed description on the formation of the reflected-shock (test) conditions is given in Appendix E.

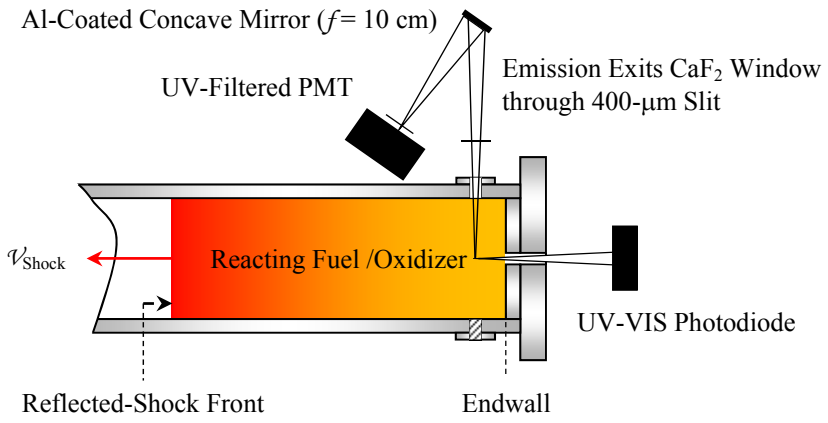

Fig. 3.5. Emission from reacting fuel and oxidizer behind reflected-shock is measured at a sidewall location 1.25 in. (3.18 cm) from the endwall using a UV-filtered photomultiplier tube.

Combustion reactions, driven from the breaking of chemical bonds and formation of new bonds, proceed through an array of hundreds to thousands of elementary reactions depending on the size of the parent fuel. The production of radicals (short-lived species with unpaired valence electrons) occurring during the initial stages of combustion instigates oxidation through branching and propagation reactions prior to the onset of ignition. In cases where energy is absorbed by certain species through collisions with surrounding molecules/atoms (third-body inert species, stable and unstable species) or through highly exothermic reactions, molecules can become excited and reach a higher electronic state. Shortly after excitation, a relaxation period ensues during which the radical tends toward a lower energy (ground) electronic state and in the process the emission of energy in the form of light occurs proportional to the product of the Planck constant and frequency of light by hc/λ (chemluminescence). Temporal measurement of species-specific emission of radiation (λ_{OH*}, λ_{CH*}) resulting from the release of photons during relaxation are obtained behind reflected-shock waves in the present work using a high-sensitivity detector coupled with a filter which excludes wavelengths other than the given wavelength of interest (bandpass filter), yielding species-time histories.

Specific transitions measured in the present study for excited-state OH and CH were $A^2\Sigma^+ \rightarrow X^2\Pi$ and $A^2\Delta \rightarrow X^2\Pi$, respectively, where the numerical superscripts indicate constant quantum number during transition (n = 2) and wave function symmetry (+) about the vertical mirror plane (σ_v). Electronic state designation Σ indicates zero orbital angular momentum (Λ) along the z axis of the molecule ($\Lambda = 0$). Similarly, for Π and Δ electronic states, $\Lambda = 1$ and $\Lambda = 2$, respectively. Figure 3.6 shows schematically a Morse potential energy curve of OH transition from the first electronic excited state (A) to the ground state (X). The expression P + Energy $\rightarrow$ P* is generalized to include energy imparted by collision and from highly exothermic reactions.

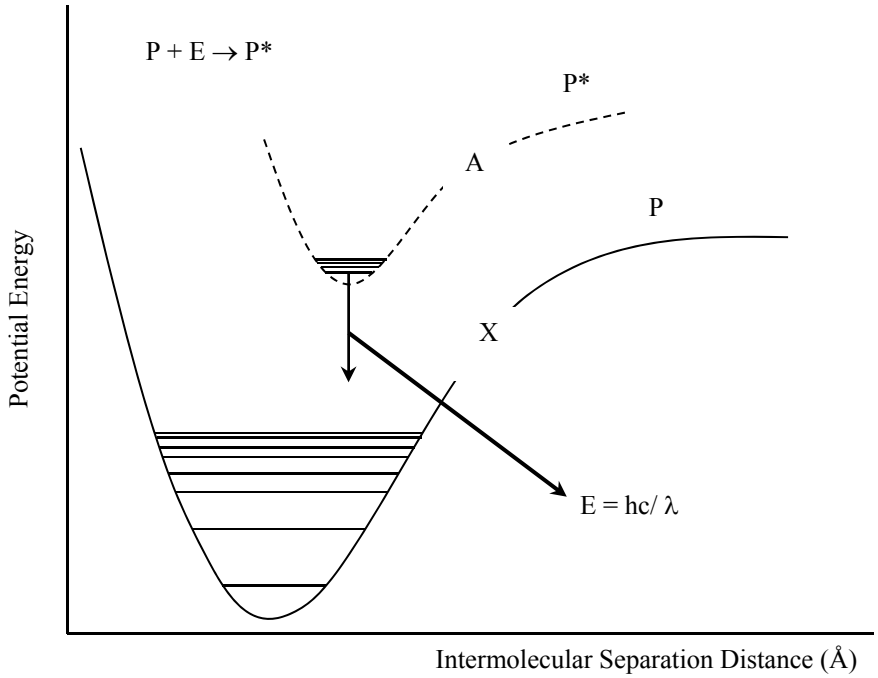

Fig. 3.6. Morse potential energy curves for electronically-excited and equilibrated product species (P) of a chemical reaction or collision. Relaxation brings the species from an elevated electronic level (A) to the ground-state electronic level (X). From the transition of an excited radical (P*) to the ground-state (P), photons of energy E = hc /λ are emitted and measured for intensity according to wavelength λ. For OH* and CH*, $\lambda \approx 307.1$ nm and ≈ 430.0 nm, respectively.

Optical bandpass filters possess a specific bandwidth comprised of a center wavelength bound by a minimum wavelength and a maximum wavelength the filter is capable of passing, defined by the FWHM, forming a near-Gaussian distribution of intensity as a function of wavelength. In the measurements of excited-state species profiles in the present work, the bandwidth for the CH* filter was 10 nm. For the OH*, a bandwidth of 40 nm was used. The two principal measurements reported herein, ignition delay times and species time-histories, were obtained from chemiluminescence measurements of excited hydroxyl radicals (OH*). Experiments were performed to determine the impact on measured OH* profiles from the use of more-narrow bandpass filter (i.e 10 nm FWHM) compared to a filter broader with broader bandwidth (i.e. 40 nm FWHM). Transmission curves as a function of wavelength for the two OH* filters are given in Fig. 3.7. OH* profiles from oxidation of fuel-rich Blend 3 (Table 3.7) were obtained under 1.5 atm pressure at 1627 K and 1630 K for the 40-nm FWHM and 10-nm FWHM filters, respectively. No difference in profile shape is shown from the use of the two filters differing in allowable wavelength transmission (Fig. 3.8). For completion, the transmission curve of the CH* optical filter is provided in Fig. 3.9.

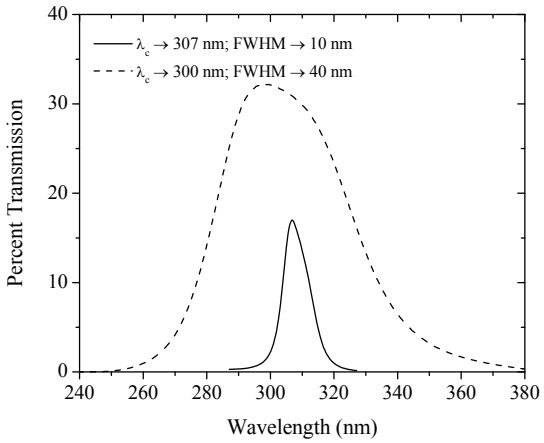

Fig. 3.7. Transmission profiles for optical filters used to measure OH* species (Andover Corporation).

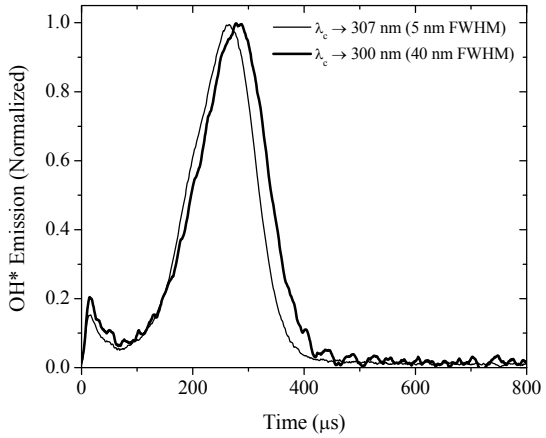

Fig. 3.8. Comparison of OH* time history measurements using two bandpass filters differing in center wavelength and FWHM. The 40-nm FWHM optical filter employed in the present work yields time histories identical to those measured using the narrow filter with the 307-nm center wavelength, therefore no additional interference is detected relative to the more-narrow bandwidth filter.

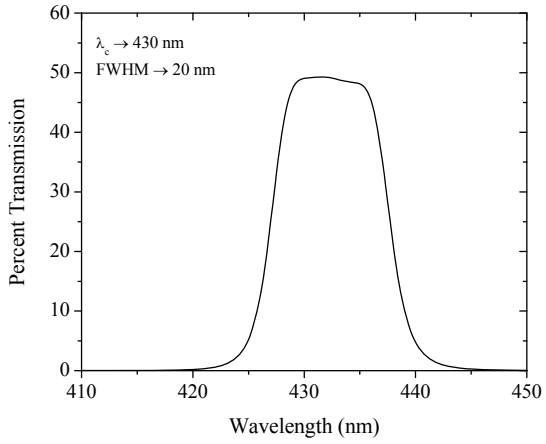

Fig. 3.9. Transmission profile for optical filter used to measure CH* species (Andover Corporation).

3.2.4 Definition of test time and ignition delay time

The test time begins upon arrival of the reflected shock wave at the measurement station, which in the present work is the sidewall positioned 3.18 cm (1.25 in) from the face of the endwall. High temperatures generated behind the reflected shock wave initiate the ignition process by raising the temperature of the

gas within a few microseconds. After a period of time, coupled with rapid collisions between atoms and molecules, thermal energy from the shock process is subsequently absorbed in respective energy storage modes (translation, rotation, vibration, electronic) leading towards chemical bond rupture. Radical species are generated from these processes which then incite oxidation of other species, and the process continues up to a point where radical pools have sufficiently populated leading to the onset of primary ignition (marked by abrupt rise in pressure rise and/or the emission of light). The period of time over which this process occurs is the *ignition delay time*.

In the present work, shock-tube measurements of OH* or CH* chemiluminescence profiles and ignition delay times are conducted behind the reflected shock wave under highly dilute conditions (99% Ar by volume) to minimize unsteady thermodynamic conditions from reaction exothermicity. Species profiles and ignition delay times extracted during fuel oxidation serve as validation targets for a chemical kinetics model compiled from individual mechanisms for each species, the impetus of which is the need for a robust mechanism to predict characteristic combustion properties and reaction pathways.

Ignition delay times are defined herein using the method of steepest ascent as applied to OH* chemiluminescence measurements (Fig. 3.10). The method entails constructing a horizontal line representing zero-concentration of the intermediate species being measured. The line is extended from time-zero throughout the length of the profile to establish a reference (zero) concentration from which changes with time are measured. A second line is then drawn along the slope with the steepest ascent in the profile, indicative of rapid population of the intermediate radical pool, to intersect with the reference line. The difference in time between time-zero (arrival of reflected shock wave at sidewall location) and the intersection point is the ignition delay time, $\tau_{Ignition}$, measured in microseconds (μs).

Although shown below to have negligible impact in the present work, existing in all shock-tube facilities due to non-ideal gas dynamic effects are pressure increases over time which depend highly on shock-tube-specific geometry, test temperature and pressure, and diluent species (Ar, N_2). Figure 3.10 displays time-

dependent OH* formation measured experimentally from methyl octanoate oxidation and compares it to the model prediction of Dayma et al. [42]. To capture the effect of non-ideal gas dynamics (i.e. pressure rise) behind the reflected shock wave, pressure time histories were integrated into the model solutions to account for the slight increase in pressure with time. Three model-predicted OH* profiles are calculated in Fig. 3.10: one under isobaric conditions, one using a linear fit to the characteristic dP/dt trend in the experiment (ca. 2.5% per ms), and an exaggerated dP/dt trend of 10% per ms. Incorporation of the pressure variation behind the reflected shock wave at a rate of 2.5%/ms relative to reflected-shock pressure shows no significant impact on ignition delay times or time-dependent profile behavior within the timeframe of the measurement. In contrast, higher rates of pressure increase, such as those present in smaller-diameter shock tubes, could accelerate ignition kinetics to an appreciable degree due to boundary layer effects as described in detail by Petersen and Hanson [141]. The typical test duration up to and including the main chemical reactions in the present study is on the order of 1-2 ms, which does not allow enough time for dP/dt and dT/dt effects to impact appreciably the results herein, as implied in Fig. 3.10.

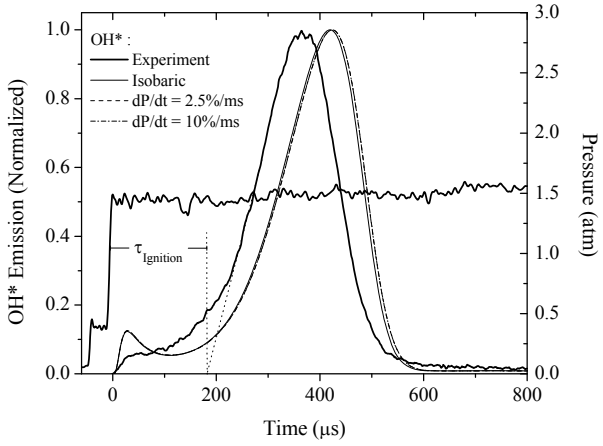

Fig. 3.10. Sidewall pressure and OH* time histories for ϕ = 0.5 $C_9H_{18}O_2$ oxidation (380 ppmv). $\tau_{Ignition}$ = 181 μs, 1378 K, 1.44 atm. dP/dt = 2.5%/ms relative to reflected-shock conditions. Model [42] calculations incorporating isobaric conditions, dP/dt behavior observed in the current work (2.5%/ms), and an exaggerated 10%/ms are shown and indicate no appreciable difference in predicted OH* profiles, justifying that the dP/dt behavior of the shock-tube facility has an insubstantial effect on the thermodynamic conditions and, by extension, ignition delay time measurements.

Calculations were performed to quantify the effect of time-dependent pressure behavior on temperature behind reflected shock waves. The slight compression process post-reflected shock can be modeled as adiabatic, adhering to Eqn. 3.15, due to insufficient time present for appreciable heat transfer to occur. Assuming a linear rate of pressure increase with time (dP/dt) relative to the initial, reflected-shock pressure of 2.5%/ms and 10%/ms, the corresponding rates of temperature increase (relative to the reflected-shock temperature) are 1.5%/ms and 6%/ms using the assumption of an isentropic relationship between temperature and pressure. For a test temperature of 1600 K (the higher range herein), the 2.5%/ms increase in pressure corresponds to a 15-K temperature increase after 1 ms, while the higher 6%/ms rate corresponds to a 60-K temperature increase after 1 ms.

$$\frac{T_{5,s}}{T_5} = \left(\frac{P_5^{'}}{P_5}\right)^{\frac{\gamma-1}{\gamma}} \qquad (3.15)$$

where,

$T_{5,s}$ ≡ Isentropic temperature behind reflected shock at time t (K)

T_5 ≡ Initial reflected-shock temperature (K)

$P_5^{'}$ ≡ Isentropic pressure behind reflected shock at time t (atm)

P_5 ≡ Initial reflected-shock pressure (atm)

γ ≡ Specific heat ratio within reflected-shock region

3.2.5 Correlation equations for ignition delay time measurements

Ignition delay times are plotted using a logarithmic scale (ordinate) as a function of inverse temperature (abscissa), thus increasing temperature occurs from the right to left. Logarithmic scales are routinely used to report ignition delay time data such that the behavior can be described using a linear relation, constructed using empirical equations of Arrhenius form. In the physical sense, ignition delay times

commonly form an exponential dependence on inverse temperature. The activation energy of a mixture is defined qualitatively as the energy required for chemical reaction to take place or, in a quantum mechanical sense the energy required to bring species in the reactive mixture above respective potential energy barriers. Recall the form of the Arrhenius expression for the temperature dependence of reaction rate constants:

$$k = Aexp\left(\frac{-E_a}{R_u T}\right) \tag{3.16}$$

or,

$$\ln k = -\frac{E_a}{R_u}\left(\frac{1}{T}\right) + \ Constant \tag{3.17}$$

where,

$k \equiv$ Rate constant (s^{-1})

$E_a \equiv$ Activation energy (kcal /mol)

$R_u \equiv$ Universal gas constant (kcal /mol · K)

$T \equiv$ Temperature (K)

In terms of an ignition delay time, noting the inversion of the natural log parameter the natural log of the Arrhenius equation can be expressed:

$$\ln \tau = \frac{E_a}{R_u}\left(\frac{1}{T}\right) + \ Constant \tag{3.18}$$

Using the ignition delay time data distributed over inverse temperature (ln $\tau_{Ignition}$ – 1 /T), the above equation takes on a linear form (y = mx + b), where E_a/R_u is the slope and inverse temperature is the abscissa. From this expression, a numeric value for the slope (m) of the linear trend is determined, from

which then the activation energy is calculated through multiplication by the universal gas constant R_u = 1986 kcal /mol·K. In a similar manner to that shown for the Arrhenius expression in Eqns. 3.16 and 3.17, ignition activation energies for a given fuel blend, which can vary with blend composition, equivalence ratio, pressure, and dilution level, are characterized by a linear dependence on inverse temperature when plotted logarithmically and can be determined using the method of least squares. The procedure is applied to Eqn. 3.18 for a complete data set over a specified set of conditions to calculate statistics describing a common linear trend. Ignition delay time dependence with inverse temperature takes the linear form of Eqn. 3.19 with species concentration dependence introduced.

$$\ln(\tau) = \ln(A) + \ xln[Fuel] + yln[Oxidizer] + zln[Inert] + \ (E_a/R_u)T \qquad (3.19)$$

The pre-multipliers x, y, z, and E_A/R_u represent respective slopes for each term, and the $\ln(A)$ term represents the constant (y-intercept). Solution of these parameters is reached using the method of least squares and after taking the exponential of the relation, an equation describing the complete ignition data set as a function of species concentration (mol /m^3) and temperature is defined. A similar expression to that of the Arrhenius equation of $k(T)$ can be formed with ignition delay times plotted in the same manner as reaction rates ($\log_{10}$ – 1 /T), where A represents a fitting parameter rather than a frequency factor (Eqn. 3.16). For large variation in dilution level, inert-gas concentration may be included (Eqn. 3.20). In the present study, Ar concentration remains fixed at 99% (vol.). Empirical correlations are then defined using fuel and oxidizer concentrations (Eqn. 3.21).

$$\tau(\mu s) = A[Fuel]^x[Oxidizer]^y[Third\ Body\ /Inert]^z exp(E_a/R_uT) \qquad (3.20)$$

$$\tau(\mu s) = A[Fuel]^x[Oxidizer]^y exp(E_a/R_uT) \qquad (3.21)$$

3.3 Description of laminar flame speed facility

A cylindrical, heated laminar-flame-speed vessel capable of pre-ignition temperature of 300 °C equipped with a high frame rate camera (up to 20,000 frames per second) is employed for measurements of laminar flame speed as a function of equivalence ratio and initial pressure and described in detail by Krejci [132]. Only a brief description of the flame speed facility is provided herein. Flame speed facility dimensions include an inner diameter of 31.75 cm, internal length of 35.6 cm, resulting in an internal volume of 28.2 L. Measurements of the flame velocity are made using a Z-type schlieren optical diagnostic (Fig. 3.11) which magnifies density gradients within its line of sight. In the experiment, the steepest gradient occurs at the interface between the reacting fuel-oxidizer and the unburned fuel-air mixture.

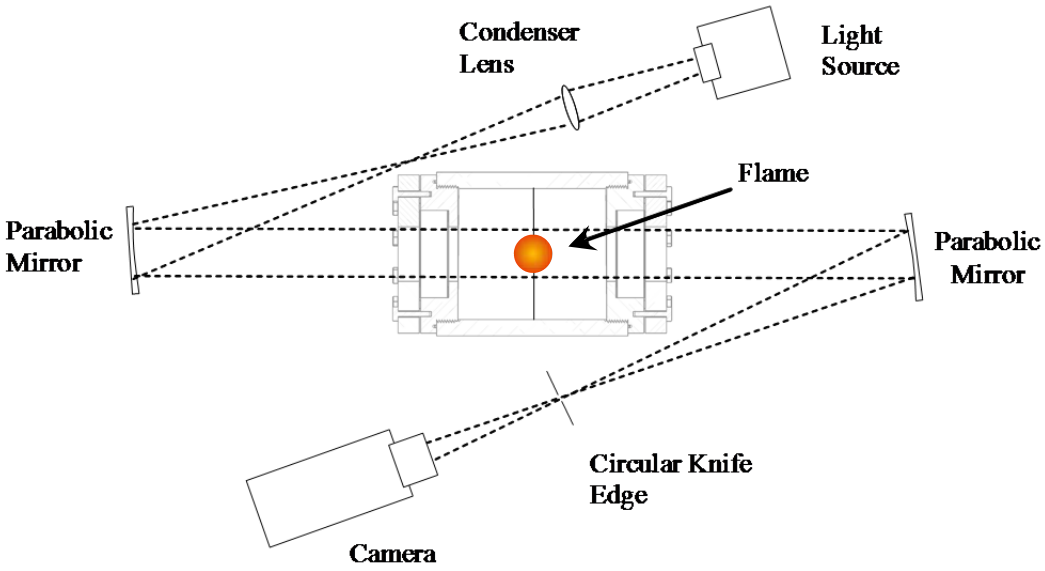

Fig. 3.11. Z-type schlieren optical setup for measurement of flame speed. Flame initiation controlled by centered spark electrodes [132].

Similar precautions to those in the shock-tube experiments, with regards to fuel condensation, were taken to ensure mixture composition. Due to the low vapor pressures of the fuels studied in the present work, heating of the flame speed facility is required and is dependent on the saturation temperature of the least volatile species in the ternary fuel blend (Section 3.1). Temperature measurements were made at five locations: two radial measurements, two axial measurements, and a measurement at the center (Fig. 3.12). Thermocouple measurements at these locations show that temperature within the heated vessel is highly uniform (Fig. 3.13). Maximum deviation from the average measured temperature for the 100 °C, 150 °C, and 200 °C temperature settings were determined to be -0.5 °C, 0.9 °C, and 0.9 °C, respectively.

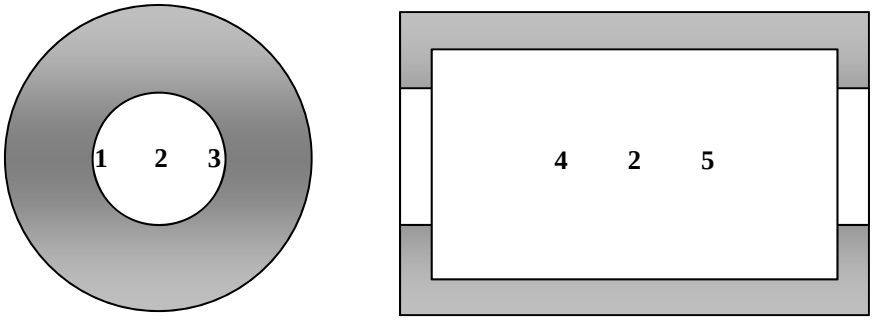

Fig. 3.12. Front and profile views of flame speed vessel showing radial (Left) and axial (Right) location of thermocouples for temperature profile measurement. Thermocouples are positioned 6.35-cm apart.

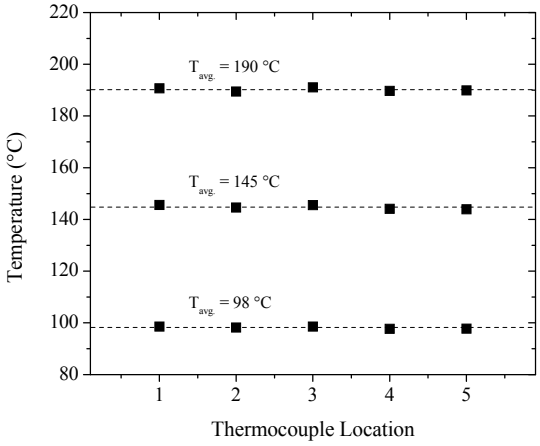

Fig. 3.13. Axial and lateral temperature profiles of stainless steel flame facility (set temperatures 100 °C, 150 °C, and 200 °C).

3.3.1 Procedure for injection of liquid fuel in laminar flame speed experiments

In these experiments, the liquid fuel blend was injected into the flame speed vessel using the same high-vacuum septum apparatus as that appended to the shock-tube mixing chamber. After injection of the fuel, a waiting period of 30 min was implemented to ensure the fuel blend had appropriately evaporated and reached a steady-state pressure. Once the gaseous fuel pressure stabilized, the appropriate amount of UHP air (79/21 N_2/O_2) was introduced into the flame speed vessel. Upon introducing the UHP air and reaching the initial test pressure, a waiting period of 30 min was maintained for all flame speed experiments to ensure homogeneity was reached. Assurance in a uniform mixture was provided by varying the amount of waiting time the fuel/air mixture experienced. No difference in the flame speed results was observed using either a 120 min or 180 min waiting period.

3.3.2 Determination of laminar flame speed

The laminar flame speed is determined from an analytical treatment of the Markstein relation (Eqn. 3.22) which is valid in the limit of weakly stretched flames and relates the measured (burned) velocity (S_b), which intrinsically contains flame stretch, to the burned, unstretched flame velocity (S_b°) by means of the Markstein length (L_b) and the rate of flame stretch (α):

$$S_b = S_b^\circ - L_b\alpha \tag{3.22}$$

where the rate of flame stretch, determined experimentally, is defined:

$$\alpha = (2/R)(dR/dt) \tag{3.23}$$

and the rate of change in flame radius is measured using schlieren imaging of the propagating flame. Regression analysis is performed on an integrated form of Eqn. 3.23:

$$r_i = S_b^\circ t_i - 2L_b \ln(r_i) + c \tag{3.24}$$

The unburned, unstretched flame velocity is then calculated iteratively from the burned, unstretched flame velocity by the density ratio across the flame. This density ratio comes from the equilibrium solver in the ChemKin computer package which is used to calculate the burned-gas density. Conservation of mass applied at the boundary of the flame (where reacting flow meets unburned fuel-air) yields the relation:

$$S_u^\circ = S_b^\circ/\sigma \tag{3.25}$$

where σ is the ratio of unburned- to burned-gas density (Eqn. 3.26)

$$\sigma = \rho_u/\rho_b \tag{3.26}$$

4. BLENDED-FUEL CHEMICAL KINETICS MECHANISM DEVELOPMENT AND CHEMISTRY MODELING

A detailed chemical kinetics model was compiled to study the reaction chemistry pertaining to ignition of the ternary fuel blends (methyl ester/ linear alkane/ cycloalkane) studied herein. The development of a chemistry model for blended biofuels is imperative since the ignition behavior of fuel blends cannot be studied in detail using the individual trends of the pure fuels. The model compiled in the present work serves as an initial version of such a model. Sub-mechanisms were extracted from two well-validated models and integrated into a base mechanism for n-nonane. Described in the sections below are details for the sub-mechanisms for methyl octanoate (Section 4.2) and methylcyclohexane (Section 4.4) and details of the base mechanism (Section 4.3) for the present model. The reaction mechanism is utilized for calculations of time-dependent species profiles, time-dependent sensitivity coefficients, and rate-of-production of species, and to assess the influence of blending effects on ignition. Details on these analyses and solution procedures are discussed in Sections 4.5 – 4.7.

4.1 Reaction mechanism for methyl octanoate/n-nonane/methylcyclohexane blends

The ternary fuel blends studied herein include components of interest as blended biofuel components. The linear alkane and cycloalkane serve as a conventional, petroleum-based fuel species and the methyl ester serves as the bio-derived compound. The supporting chemical kinetics mechanism compiled in the present work to model the experiments integrates two sub-mechanisms into a base mechanism describing the chemical kinetics. Three chemical kinetics mechanisms were utilized to model species profiles and ignition delay times for the pure fuels to serve as a basis for comparison for the present model. The mechanisms of Dayma et al. [42], Rotavera et al. [48], and Pitz et al. [25] were chosen for methyl octanoate, n-nonane, and methylcyclohexane (MCH), respectively. A single mechanism combining the chemistry of the three separate fuels was needed to model the ignition chemistry of the fuel blends. The base chemistry of Dagaut [147] is used for both [42] and [48]. Therefore, the $C_9H_{18}O_2$ and MCH sub-mechanisms were chosen as sub-mechanisms to integrate into the model of Rotavera et al. [48] since this latter mechanism and that in [42] share base reaction sets. Table 4.1 provides details on the base model

and integrated sub-mechanisms. To enable modeling of shock-tube ignition delay times and OH* profiles, the chemiluminescence subset proposed by Hall and Petersen [148] is included in the present model from integration into the base n-nonane mechanism [48].

Table 4.1. Components of the reaction mechanism compiled for blended-fuel ignition analysis in the present study.

Mechanism	Species	Reactions	Role
$C_9H_{18}O_2$ /Dayma et al. [42]	144	1080	Sub-Mechanism
n-C_9H_{20} /Rotavera et al. [48]	729	3445	Base Mechanism
MCH /Pitz et al. [25]	209	260	Sub-Mechanism
Compiled Mechanism (Present Study)	1082	4785	

4.2 Sub-mechanism: methyl octanoate

The methyl octanoate sub-mechanism integrated into the ternary fuel blend model utilizes 144 species and 1080 reactions from the work of Dayma et al. [42]. The base model for methyl octanoate from [42] was validated using jet-stirred reactor (JSR) measurements of stable species from oxidation of 1000 ppmv $C_9H_{18}O_2$ in O_2/N_2. Concentration profiles as a function of temperature ($800 < T\ (K) < 1350$) at 1 atm from lean ($\phi = 0.5$) to rich ($\phi = 2.0$) equivalence ratios were obtained using a 70 ms residence time in the reactor. Species profiles from JSR experiments for 1-olefins, C_2H_2, CH_4, C_2H_6, H, CO, CO_2, H_2O, and stable decomposition products of methyl octanoate were well-predicted. Under stoichiometric conditions, no low-temperature (< 800 K) fuel reactivity was observed in the 1-atm experiments. Reaction pathway analysis (RPA) was performed under stoichiometric conditions at the temperature (1050 K) where 50% (vol.) consumption of the fuel was measured. Under these conditions, approximately 50% of the fuel is consumed by H-atom abstraction by H or OH. Supporting measurements of species profiles from opposed-flow diffusion flames were also used in the work to further constrain model predictions. The same species were measured in the diffusion flame experiments with model agreement exhibited for CO, CO_2, $C_9H_{18}O_2$, CH_4, C_2H_6, 1-butene, 1-heptene. Under-predicted species profiles were noted for C_2H_4, propene,

formaldehyde, 1-pentene, and 1-hexene. Temperature profiles were also calculated with high accuracy. Discrepancies in the model predictions are to some extent attributable to the experimental correction applied to the results of the diffusion flame experiment due to thermal radiation losses causing uncertainty in temperature, as described in Sinha et al. [149].

Jet-stirred reactor experiments on methyl octanoate blends with ethanol (C_2H_5OH) and bio-butanol (C_4H_9OH) at 10 atm were performed in the work of Togbé et al. [41, 36]. Similar to the 1-atm work of [42], species concentration profiles for stable intermediates were measured as a function of temperature from lean ($\phi = 0.5$) to rich ($\phi = 2.0$) equivalence ratios. A 700-ms residence time in the reactor was used in the study due to the elevated pressure. Fuel concentrations of blends were kept below 1000 ppmv to mitigate temperature gradients within the reactor during chemical reaction of the fuel. Table 4.2 provides the base mechanism from which the methyl octanoate model is derived and the conditions over which it has been validated.

Table 4.2. Valid regimes for the methyl octanoate model.

Base Model	P (atm)	T (K)	ϕ	Dilution Level	Apparatus
[42]	1 – 10	800 – 1350	0.5 – 2.0	97% – 99%	Jet-Stirred Reactor, Diffusion Flames

4.3 Base mechanism: n-nonane

The n-nonane mechanism of Rotavera et al. [48] serves as the base mechanism for the present model to which the methyl octanoate and methylcyclohexane chemistry sets were integrated. The n-nonane model is comprised of 729 species and 3446 reactions, including the chemiluminescence mechanism (29 reactions) from Hall and Petersen [148]. The initial version of the mechanism, developed around experimental results covering from low- to intermediate-temperature JSR experiments (species concentration profiles), and intermediate- to high-temperature shock-tube experiments (ignition delay times, excited-state species

profiles), utilizing constant fuel concentration (1000 ppmv) and spanned 1 atm and 10 atm pressures and lean ($\phi = 0.5$) to rich ($\phi = 2.0$) equivalence ratios.

A brief overview of the JSR facility experiments performed for the n-nonane study is provided herein. Complete details of the JSR facility are discussed in Dagaut et al. [150]. Temperature and pressure dependence of product-species concentration produced from the oxidation of n-$C_9H_{20}/O_2/N_2$ mixtures were measured using a fused-silica jet-stirred reactor with an internal volume of 30 cm^3. The fuel/O_2 mixture was preheated to a given initial temperature (> 100 °C) to set reaction temperature and avoid condensation of the low-vapor-pressure alkane and then injected into the reactor body using four nozzles (i.d. = 1 mm). Turbulence was induced prior to entry into the reactor body, thus homogeneity of conditions through enhanced mixing (jet-stirring) of the already turbulent gases is attained. The high dilution level (> 97% diluent) reduces temperature gradients and the release of energy from oxidation reactions. Residence times within the reactor remained fixed at 70 ms and 700 ms for 1-atm and 10-atm conditions, respectively. A vertically adjustable probe positioned along the centerline of the reactor provided assurance of temperature uniformity (~ 1 K/cm) and uniformity of the gaseous mixture. Fourier-transform infrared spectroscopy (FTIR), flame ionization detection (FID), and thermal conductivity detection (TCD) were employed to measure species concentrations. Concentration analysis of select product species was performed during the experiment using FTIR in a 413-K, temperature-controlled gas cell after which combustion products (~ 40 mtorr) were captured using a quartz probe and collected in Pyrex bulbs for immediate analysis using gas chromatography in concert with either FID or TCD.

The base n-nonane kinetics mechanism, derived from a mechanism previously developed for n-decane oxidation in the work of Diévart [151], has a strong hierarchical structure and was designed to model both low- and high-temperature oxidation. The low-temperature n-nonane subset involves the formation of nonylperoxy radicals and derived reactions (isomerization, cyclization, peroxidation, etc., to form cyclic ethers, ketohydroperoxides, and aldehydes). Rate coefficients mainly come from Buda et al. [152]. The high-temperature reactions primarily consist of C–C and C–H bond scissions from n-nonane and nonyl

radicals. Thermodynamic data were taken from the Burcat and Ruscic database [153] when available, or were estimated using the THERGAS software [154] based on group additivity methods proposed by Benson [155]. Rate coefficients for reverse reactions were computed from the corresponding forward rate coefficients and the appropriate equilibrium constant, $K_c = k_{Forward}/k_{Reverse}$, calculated from thermochemical data. Table 4.3 provides the conditions over which the n-nonane model has been validated.

The first version of the n-nonane model used as the base model in the present work was developed by the author in a previous study [16]. Improvement in the low- and intermediate-temperature region was made to the initial version using rate parameters for the formation of cyclic ethers from Wijaya et al. [156]. Several improvements were additionally made in the high-temperature regime using sensitivity and reaction pathway analyses, the specific results and impact of which are described in Section 6. The numerical details for the modified reactions are presented in Table 4.3. The modified reactions (MR) and associated rate parameters responsible for the high-temperature improvements are provided in Table 4.3. Initial changes involved the homolysis rates for n-nonane which in the initial version of the model were those of n-decane from the mechanism of Zeppieri et al. [157]. In the present model, n-nonane homolysis rates (MR1 – MR4) were reduced by decreasing the frequency factor from $2.0 \cdot 10^{17}$ to $3.0 \cdot 10^{16}$ s^{-1}.

The rate of H-abstraction by H from C_2H_4 forming vinyl and H_2 (MR5), H-abstraction from formaldehyde by H, yielding formyl + H_2 (MR8), and thermal decomposition of 1-hexyl were increased. The rate of the latter reaction was increased by multiplying the frequency factor by 10^2 (arrived at parametrically) over the Tsang et al. value [158] used in the initial version. The thermal decomposition rate of propene (MR6) forming vinyl + methyl was reduced.

Rate parameters for MR5 – MR8 were taken from the literature. Parameters for MR5 were obtained from transition state theory (TST) results of Weissman and Benson [159], MR6 from Dean [160], MR7 from JetSurF v2.0 [15], and MR8 from the RRKM extrapolation of Irdam et al. [161]. The H-abstraction

reaction by H_2 on CH was written as $CH_2 + H \rightarrow CH + H_2$ in the initial version of the model. The corresponding rate coefficient depended only on A (i.e. no temperature dependence or activation energy was assigned to the reaction. The reaction was replaced using the reverse reaction from [15] which includes both a dependence on temperature and on activation energy (MR7).

Table 4.3. Modified reactions (MR) and associated rate parameters (units: cal, mol, cm^3, K). Rate coefficients are of modified Arrhenius form: $k(T) = A(T/298\ K)^n exp(-E_a/R_u T)$.

Reaction	A	n	E_a (kcal /mol)	Reference
MR1: n-$C_9H_{20} \rightarrow pC_4H_9 + AC_5H_{11}$	$3.000 \cdot 10^{16}$	0.00	83180.0	Present Work
	$2.000 \cdot 10^{17}$	0.00	83180.0	Initial Parameters
MR2: n-$C_9H_{20} \rightarrow nC_3H_7 + AC_6H_{13}$	$3.000 \cdot 10^{16}$	0.00	83400.0	Present Work
	$2.000 \cdot 10^{17}$	0.00	83400.0	Initial Parameters
MR3: n-$C_9H_{20} \rightarrow C_2H_5 + AC_7H_{15}$	$3.000 \cdot 10^{16}$	0.00	83680.0	Present Work
	$2.000 \cdot 10^{17}$	0.00	83680.0	Initial Parameters
MR4: n-$C_9H_{20} \rightarrow CH_3 + AC_8H_{17}$	$3.000 \cdot 10^{16}$	0.00	85570.0	Present Work
	$2.000 \cdot 10^{17}$	0.00	85570.0	Initial Parameters
MR5: $C_2H_4 + H \rightarrow C_2H_3 + H_2$	$1.710 \cdot 10^{13}$	0.70	8003.3	[159]
	$1.000 \cdot 10^{14}$	0.00	15009.0	Initial Parameters
MR6: $C_3H_6 \rightarrow C_2H_3 + CH_3$	$7.940 \cdot 10^{16}$	0.00	99594.0	[160]
	$1.100 \cdot 10^{21}$	–1.20	97720.0	Initial Parameters
MR7: $CH + H_2 \rightarrow CH_2 + H$ (Reversed)	$1.107 \cdot 10^{8}$	1.79	1670.0	[15]
	$3.500 \cdot 10^{14}$	0.00	0.00	Initial Parameters
MR8: $CH_2O + H \rightarrow HCO + H_2$	$2.879 \cdot 10^{12}$	1.90	2740.4	[161]
	$1.100 \cdot 10^{8}$	1.80	3000.0	Initial Parameters
MR9: $AC_6H_{13} \rightarrow pC_4H_9 + C_2H_4$	$1.020 \cdot 10^{14}$	0.30	27276.0	Present Work
	$1.020 \cdot 10^{16}$	0.30	27276.0	Initial Parameters

Table 4.4. Valid regimes for the n-nonane model of Rotavera et al. [16].

Base Model	P (atm)	T (K)	ϕ	Dilution Level	Apparatus
[151]	1 – 10	550 – 1600	0.5 – 2.0	95.4% – 99.2%	Jet-Stirred Reactor, Shock Tube

4.4 Sub-mechanism: methylcyclohexane

The methylcyclohexane mechanism from the experimental and modeling study of Pitz et al. [25], consisting of 1011 species 4436 reactions, was chosen as the model from which to extract the MCH sub-mechanism implemented into the ternary kinetics model for the present study. The construction of the MCH model involved the integration of the high-temperature Orme et al. mechanism [24] into the iso-octane model of Curran et al. [22]. Table 4.4 provides the mechanisms from which the Pitz et al. MCH model is derived and the conditions over which the model has been validated. Only reactions involving MCH were utilized in the sub-mechanism in the present model. The development of the MCH mechanism in [25] stemmed from the interest in identifying reaction pathways pertaining to the negative temperature coefficient (NTC) behavior which have been studied previously for linear and branched alkanes. For both linear and branched alkanes, RO_2 formation and subsequent isomerization leads to QOOH formation. Hydroperoxyalkyl radicals (QOOH) then proceed through one of several reaction pathways during the low-temperature ignition process: (i) conversion into RO_2 from isomerization; (ii) cyclization to form epoxide + OH; (iii) C–O bond fission to yield an olefin and hydroperoxy (HO_2); or (iv) β-scission reaction. In the Pitz et al. study, for which the impetus was accurate prediction of low- and intermediate-temperature hydrocarbon ignition, detailed chemical kinetics analyses were performed to identify whether analogies could be made among linear and branched alkanes and cycloalkanes, specifically with regards to RO_2 isomerization rates and relative rates of branching and propagation reactions. It was concluded in the study that isomerization rates of RO_2 which are accepted for linear- and branched-alkane systems produced modeled ignition delay times longer than those observed in the rapid compression machine (RCM) experiments. Consequently, the mechanism developed from the study utilized rate constant

estimates for methylcyclohexylperoxy radical isomerization in place of the previous RO_2 isomerization rates employed in the base mechanism [22] formulated for iso-octane.

Table 4.5. Valid regimes for the MCH model of Pitz et al. [25].

Base Model	P (atm)	T (K)	ϕ	Dilution Level	Apparatus
[25]	1 – 45	550 – 1700	0.3 – 1.5	70% – 99%	RCM

4.5 Modeling of chemiluminescence profiles

Species time histories (OH*, CH*) were calculated with the ternary chemical kinetics model in the present work using the time-dependent 0-D homogeneous reactor module in ChemKin v10101 which is void of fluid mechanic implications and considers only the reaction chemistry for the specified set of initial conditions. Absolute and relative tolerances for solution convergence for all calculations performed herein were set to $1 \cdot 10^{-20}$ and $1 \cdot 10^{-8}$, respectively. Settings for solver integration steps and maximum time step of 20 and 1 μs, respectively, were used. The constrained pressure/solution of energy equation setting was chosen as the setting (problem type) within the ChemKin module since pressure time histories are well-characterized for the shock-tube experiments. Shock tubes afford the ability to generate controllable and repeatable conditions of temperature and pressure behind the reflected shock. In the present shock-tube work the high level of dilution (99% Ar by volume) renders the thermodynamic conditions behind the reflected shock effectively constant within the timeframe of the experiment (ca. 1.6 ms). Unless specifically stated, due to the nature of highly dilute shock-tube experiments, conditions in the homogeneous reactor module were modeled as isobaric. In addition to ignition delay times full-width half-maximum (FWHM) values were determined and utilized as a model constraint to compare with model calculations in assessing accuracy (Fig. 4.1).

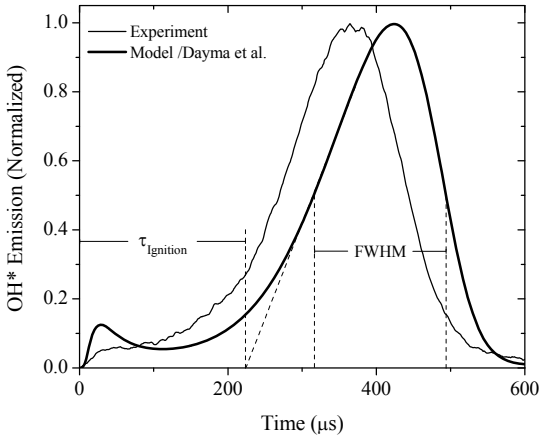

Fig. 4.1. OH* time history showing model definition of ignition delay time and FWHM. Measurement and model calculation performed of $C_9H_{18}O_2$ oxidation (ϕ = 0.5/380 ppmv). 1378 K; 1.44 atm. Model: [42].

4.6 Modeling of rate of production of species and reaction pathways

Rates of production/consumption of species (mol/cm^3·s) are calculated using post-processing of the solution data from the 0-D homogeneous reactor module in ChemKin v10101. The analysis provides a time-dependent indication of the most dominant production and consumption channels of the species of interest. H-atom production/consumption from stoichiometric oxidation of $C_9H_{18}O_2$ in O_2 is shown in Fig. 4.2. Reaction pathway analysis (RPA) is performed using ChemKin PRO v15101 and provides specific pathways from an initial species (e.g. methyl octanoate) to any terminal species of interest (CO_2, OH…). RPA includes rate of production results in conjunction with skeletal diagrams to quantitatively compare which paths are responsible for higher absolute and relative rates of species formation and/or consumption.

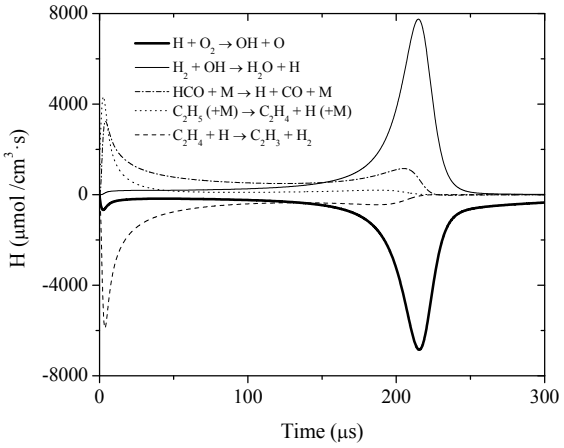

Fig. 4.2. Dominant reactions and corresponding rates of atomic hydrogen production/consumption during ϕ = 1.0 oxidation of n-C_9H_{20} (667 ppmv) calculated using the present model. 1460 K; 9.0 atm; 99% Ar.

4.7 Sensitivity analysis (0-D homogeneous batch reactor simulation)

Sensitivity analysis is a means by which influential reactions within a chemical kinetics model which drive a process of interest (ignition, CO_2 formation…) can be elucidated for a given set of thermodynamic conditions. The identified reactions may then be isolated for further study or replacement using literature parameters, leading ultimately to improvements in the chemistry model. Sensitivity coefficients (S_i), defined for illustrative purposes for OH* in Eqn. 4.1, are produced from the analysis for a given species of interest from perturbation of all of the reaction rate coefficients of all reactions in the model. The change in concentration of the selected species, as a result of individual and isolated perturbations of the reactions in the mechanism, is quantified over the specified period of time. In the present work, only the ten most influential reactions were considered for model improvement. Time-dependent numerical values of S_i are calculated for the selected number of reactions and the results are normalized to the maximum value of S_i within the specified time range for the conditions. Figure 4.2 shows representative normalized results for sensitivity coefficients of OH* from oxidation of ϕ = 2.0 n-nonane (1000 ppmv) at 1555 K, 1.5 atm, calculated using the model from Rotavera et al. [16]. Under the conditions, the chain branching H + O_2

reaction was the reaction to which OH* is most sensitive over the 200 μs time interval. Correspondingly, the peak sensitivity coefficient for this reaction within the 200-μs calculation became the normalization parameter for the entire set of S_i.

$$S_i = \partial ln[OH^*]/\partial lnk_i(T) \qquad (4.1)$$

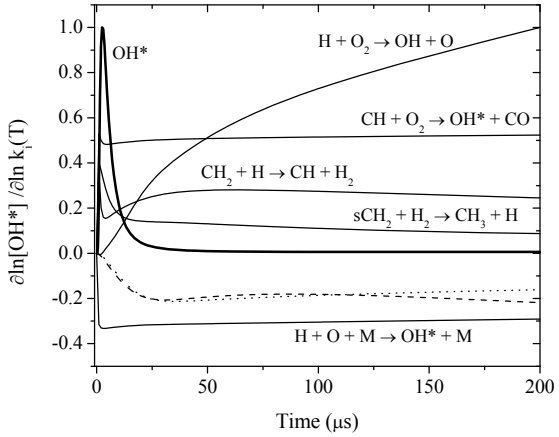

Fig. 4.3. Normalized OH* mole fraction and sensitivity coefficients describing pertinent OH*-sensitive reactions during incipient oxidation of n-C_9H_{20}/O_2 calculated using [16]. 1555 K; 1.5 atm; ϕ = 2.0; 99.2% Ar. $C_3H_6 + H \rightarrow aC_3H_5 + H_2$ (dotted line), $C_2H_4 + H \rightarrow C_2H_3 + H_2$ (dashed line).

Sensitivity coefficients of OH* formation to the 3881 reactions comprising the reaction mechanism compiled in the present work are calculated using the SENKIN module in ChemKin v10101. Sensitivity analysis was used extensively to improve the base (n-nonane) model prior to the synthesis of the present reaction mechanism. Sensitivity of OH* formation to individual rate coefficients $k_i(T)$ in the model are evaluated by perturbation of respective frequency factors A_i of the individual reactions. Rate coefficients $k_i(T)$ are of modified Arrhenius form (Eqn. 4.2). The analysis is performed using a Jacobian matrix calculated for the modified Newton iteration utilized to find a converged solution. The perturbation of A_i is related to absolute and relative tolerances for solution convergence, which for all calculations performed herein were set to $1 \cdot 10^{-6}$ and $1 \cdot 10^{-4}$, respectively, and is not explicitly specified in the output. The

threshold for S_i was set to 0.001. Calculated sensitivity coefficients below 0.001 were disregarded in the solution procedure. Detailed theory and development of the solution procedures are given in Lutz et al. [162].

$$k_i(T) = A_i(T/298\ K)^n exp(-E_a/R_u\ T) \qquad (4.2)$$

where,

A_i: frequency factor for reaction i n: temperature coefficient (nonlinear temperature behavior)

T: temperature E_a: activation energy

5. MEASUREMENTS AND MODELING OF OH* TIME HISTORIES AND IGNITION DELAY TIMES OF METHYL OCTANOATE

Excited-state hydroxyl radical time histories were measured behind reflected shock waves during oxidation of methyl octanoate, and ignition delay times were extracted using the method described in Section 3.2.4 over a broad range of thermodynamic conditions (Table 5.1). Provided in the sections below are species time history and ignition delay time results for methyl octanoate oxidation under fuel lean (Section 5.1), stoichiometric (Section 5.2), and fuel-rich (Section 5.3) conditions. Ignition delay times for methyl octanoate are provided in Appendix F. Species profiles and ignition delay times were calculated using the model compiled in the present study and with the parent model from which the methyl octanoate sub-mechanism came are compared to the measurements. Sharp differences in model predictions from the Dayma et al. model [42] and the model compiled in the present study were observed relative to one another and with the experimental results. The relative difference in the modeling results indicates that the blending of the mechanisms has an adverse effect on the reproducibility of pure fuel results for methyl octanoate. Experimental dependencies of methyl octanoate ignition on equivalence ratio and pressure, $\tau_{Ignition,\ OH^*}$(Constant P, ϕ) and $\tau_{Ignition,\ OH^*}$(P, Constant ϕ), are compared in Section 5.4. In total, 72 shock-tube measurements of $C_9H_{18}O_2$ oxidation were obtained, and an empirical ignition delay time equation was developed (Section 5.5) by correlating the data as a function of concentration (mol /cm^3) and temperature using linear regression as discussed in Section 3.2.5.

Table 5.1. Experimental ranges for fuel and oxygen volume percentages and reflected shock wave conditions.

%n-C_9H_{20}	%O_2	%Ar	P (atm)	T (K)	ϕ
0.038 – 0.138	0.862 – 0.926	99	1.3 – 9.7	1243 – 1559	0.5 – 2.0

5.1 Fuel-lean condition

The fuel mole fraction of methyl octanoate for lean measurements was maintained at $3.8 \cdot 10^{-4}$ and measurements were taken under near-atmospheric pressure (1.5 atm) spanning a temperature range of 216 K (1263 K – 1479 K). Figure 5.1 shows a comparison of a measured OH* profile to model calculations. Under fuel-lean conditions, incipient formation of OH* is evident near time-zero, and this behavior is captured by both the present model and that of Dayma et al. [42]. The incipient oxidation is attributed to rapid fuel decomposition and subsequent formation of CH which then supplies the dominant OH* formation channel: $CH + O_2 \rightarrow OH^* + CO$. Discussed in Section 6 are detailed mechanisms of incipient OH* formation at high temperatures. At 1.5 atm pressure, the time-dependence of OH* is well-predicted by both models over the range of temperature covered. For the compiled model, the FWHM is calculated within 20 μs of the experiment (90 μs) at the high-temperature extreme. The difference in FWHM between measured and model-predicted values became larger with decreasing temperatures; experimental profiles increased in FWHM from 1263 K – 1479 K from 110 μs to 345 μs, respectively, while model predictions show 130 μs – 80 μs over this temperature range. (i.e. model-predicted behavior of FWHM is inverse to that shown in the experiment, with profiles becoming increasingly small with decreasing temperature).

Fuel-lean ignition delay times (Fig. 5.1) are shown with error bars representing an uncertainty of ±10%. The uncertainty, discussed in Section 3.2.6, is systematic and therefore the same for all ignition delay time measurements herein. The experimental results of ignition are predicted well by the Dayma et al. model, yet are overpredicted over the entire temperature range using the compiled model of the present study. Ignition delay times at both the low-temperature extreme (1263 K) and the high-temperature extreme (1479 K) differ by a factor of two. The ignition activation energy of the experimental trend is calculated to be 51.7 kcal/mol, while model predictions are 59.3 kcal/mol and 53.3 kcal/mol for [42] and the present model, respectively.

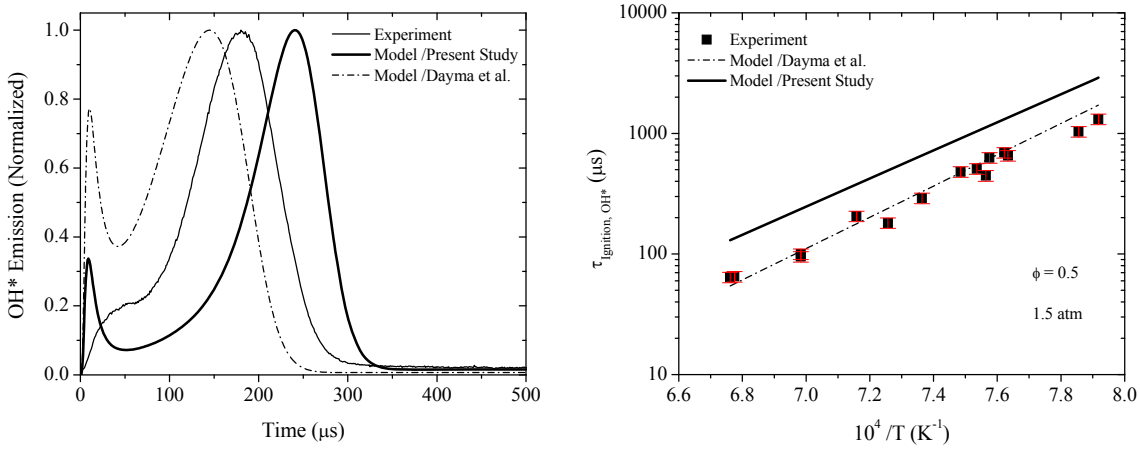

Fig. 5.1. (Left): Measured and model-predicted OH* time history during oxidation of 385 ppmv $C_9H_{18}O_2$ (ϕ = 0.5) in 99% Ar. 1.4 atm, 1479 K, $\tau_{Ignition,\ OH^*}$: 75 μs (Experiment). 4.8-kΩ PMT resistance. (Right): Measured and model-predicted ignition delay times of $C_9H_{18}O_2$ (ϕ = 0.5) in 99% Ar at 1.5 atm. Calculations were performed using Dayma et al. [42] and the present chemical kinetics model. $3.850 \cdot 10^{-4} C_9H_{18}O_2 + 9.615 \cdot 10^{-3} O_2 + 0.99Ar$. Error bars reflect an uncertainty of ±10%.

Measurements taken at a nominal elevated pressure of 9.5 atm spanned a temperature range of 118 K (1272 K – 1390 K). Figure 5.2 shows a comparison of a measured OH* profile to model calculations. The FWHM of the modeled OH* profile in Fig. 5.2 (40 μs) is smaller than that indicated in the measurement (135 μs). Differences in FWHM between modeled and experimental OH* time histories increase with decreasing temperature. The temperature dependence of the model-predicted trend in FWHM is in agreement with that of the experiment, however differences at the high- and low-temperature extremes of 75 μs and 205 μs exist, with FWHM of modeled profiles under-predicting the measurements. Increased pressure suppressed incipient formation of OH* under the fuel-lean condition experimentally and in the model predictions.

Fuel-lean ignition delay times at 9.5 atm are accurately predicted by the compiled model over the entire range of temperatures (within ~ 15%), capturing the ignition activation energy within ~ 20% (52.2 kcal/mol compared to 42.7 kcal/mol). The Dayma et al. mechanism [42] overpredicts the ignition activation energy of the experimental trend by ~ 50% (64.4 kcal/mol compared to 42.7 kcal/mol). As a

result of the overprediction, ignition delay times predicted at higher temperatures are in closer agreement than those at lower temperatures. At 1390 K, ignition delay times are slightly underpredicted (within 15%) and are overpredicted by 50% at the low-temperature extreme.

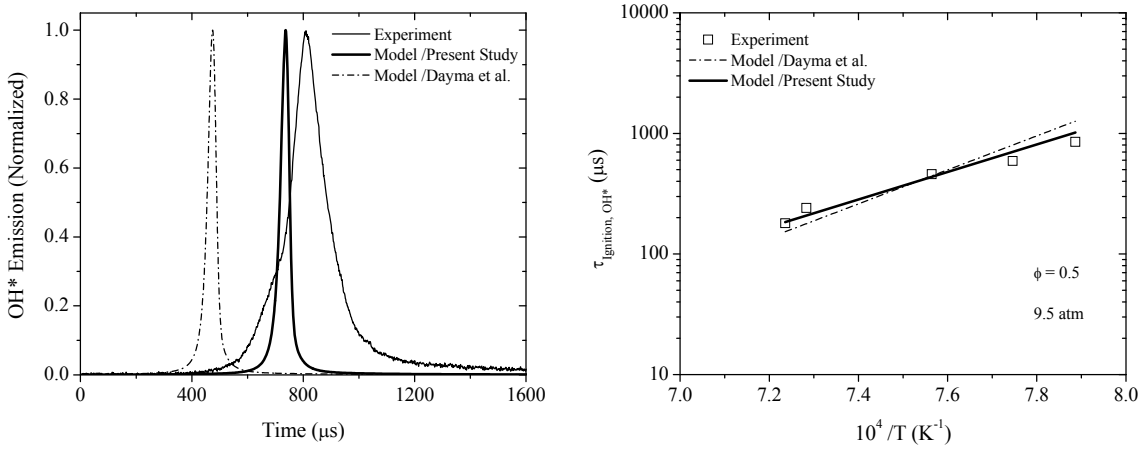

Fig. 5.2. (Left): Measured and model-predicted OH* time history during oxidation of 385 ppmv $C_9H_{18}O_2$ (ϕ = 0.5) in 99% Ar. 9.5 atm, 1322 K, $\tau_{Ignition,\ OH^*}$: 459 μs (Experiment). 4.8-kΩ PMT resistance. (Right): Measured and model-predicted ignition delay times of $C_9H_{18}O_2$ (ϕ = 0.5) in 99% Ar at 9.5 atm. Calculations were performed using Dayma et al. [42] and the present chemical kinetics model. $3.850 \cdot 10^{-4} C_9H_{18}O_2 + 9.615 \cdot 10^{-3} O_2 + 0.99Ar$.

5.2 Stoichiometric condition

The fuel mole fraction of methyl octanoate in stoichiometric experiments was maintained at $7.41 \cdot 10^{-4}$ and measurements were obtained under near-atmospheric pressure (1.5 atm) over a temperature range of 175 K (1269 K – 1444 K). Figure 5.3 shows a comparison of a measured OH* profile to model calculations. The time dependence of OH* is captured well by the Dayma et al. model. Comparing FWHM between OH* measurements and model predictions, overlap is shown at the high-temperature extreme (1444 K) below which the deviations become apparent, with model predictions showing a difference in FWHM of 65 μs at 1333 K. Measured FWHM at these temperatures are 90 μs and 195 μs, respectively.

Ignition activation energy is largely overpredicted the Dayma et al. model and within 10% from calculations using the compiled model in the present work. The experimental results yield an ignition activation energy of 44.0 kcal/mol, while the Dayma et al. model and present model predict 58.6 kcal/mol and 40.8 kcal/mol, respectively. Although the compiled mechanism predicts the temperature trend of ignition reasonably well, ignition delay times are highly overpredicted (by a factor of 3 at higher temperatures and a factor of 2.5 at lower temperatures). While neither models perform with high fidelity for $C_9H_{18}O_2$, this overprediction is similar to that shown for $\phi = 0.5$, 1.5 atm and buttresses the observation that integration of the mechanisms does not, in turn, reproduce methyl octanoate ignition behavior well.

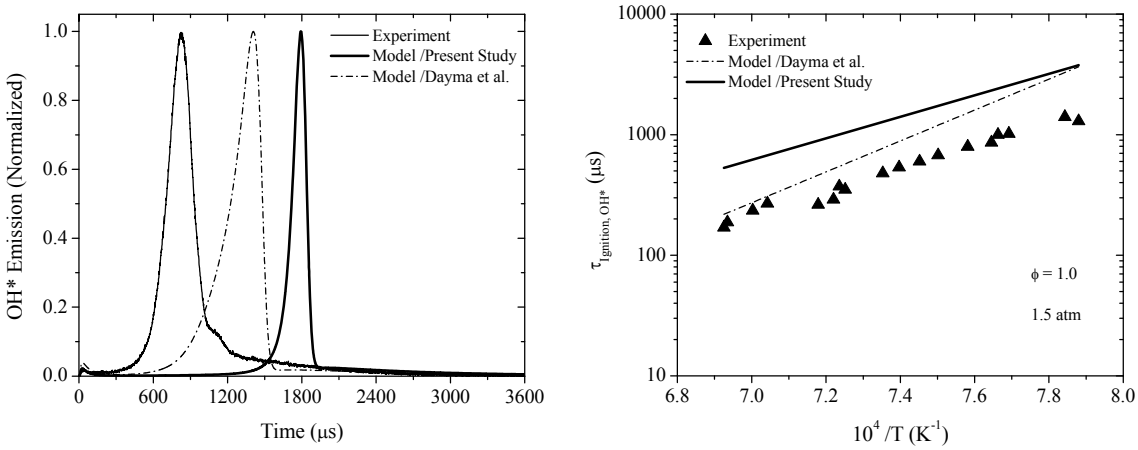

Fig. 5.3. (Left): Measured and model-predicted OH* time history during oxidation of 741 ppmv $C_9H_{18}O_2$ ($\phi = 1.0$) in 99% Ar. 1.5 atm, 1342 K, $\tau_{Ignition, OH^*}$: 600 μs (Experiment). 4.8-kΩ PMT resistance. (Right): Measured and model-predicted ignition delay times of $C_9H_{18}O_2$ ($\phi = 1.0$) in 99% Ar at 1.5 atm. Calculations were performed using Dayma et al. [42] and the present chemical kinetics model. $7.410 \cdot 10^{-4} C_9H_{18}O_2 + 9.260 \cdot 10^{-3} O_2 + 0.99Ar$.

Measurements were obtained at an elevated nominal pressure of 9.3 atm over a temperature range of 256 K (1243 K – 1499 K). Figure 5.4 shows a comparison of a measured OH* profile to model calculations. Resulting from integration of the methyl octanoate model into the compiled mechanism of the present work, the FWHM of model-predicted OH* profiles became smaller relative to those calculated using the Dayma model. Relative to the experimental value of 50 μs at 1499 K, model calculations predict a FWHM

of 20 μs. With decreasing temperature this difference becomes highly exaggerated. At 1243 K, the model differs from the experimental value of 740 μs by 680 μs.

The temperature dependence of the model predictions of ignition delay time trends are in disagreement relative to the experimental trend of 49.5 kcal/mol. The Dayma et al. model predicts an activation energy of 56.4 kcal/mol, a difference of ~ 15% while the compiled mechanism predicts an activation energy of 43.6 kcal/mol, differing by approximately 10%. Ignition delay times using the Dayma et al. model differ by a factor of 1.4 at lower temperatures and approximately 40% at higher temperatures. Ignition delay times using the compiled model are overpredicted by a factor of 2 at the high-temperature extreme and by approximately 40% at the low-temperature extreme, over the range of temperatures covered.

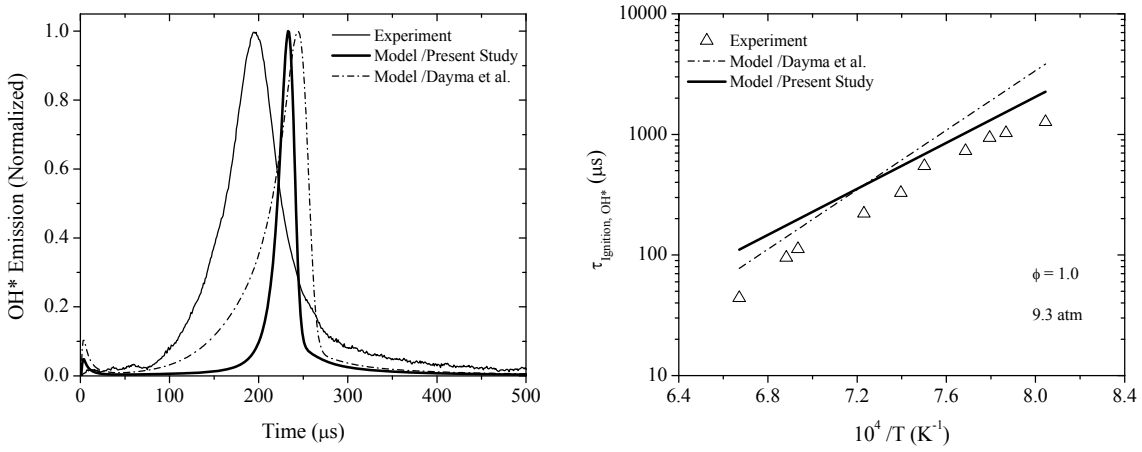

Fig. 5.4. (Left): Measured and model-predicted OH* time history during oxidation of 741 ppmv $C_9H_{18}O_2$ (ϕ = 1.0) in 99% Ar. 9.2 atm, 1436 K, $\tau_{Ignition,\ OH^*}$: 112 μs (Experiment). 4.8-kΩ PMT resistance. (Right): Measured and model-predicted ignition delay times of $C_9H_{18}O_2$ (ϕ = 1.0) in 99% Ar at 9.3 atm. Calculations were performed using Dayma et al. [42] and the present chemical kinetics model. $7.410 \cdot 10^{-4} C_9H_{18}O_2 + 9.260 \cdot 10^{-3} O_2 + 0.99Ar$.

5.3 Fuel-rich condition

The fuel mole fraction of methyl octanoate for lean measurements was maintained at $13.8 \cdot 10^{-4}$ and measurements were taken under near-atmospheric pressure (1.5 atm) spanning a temperature range of 189

K (1370 K – 1559 K). Figure 5.5 shows a comparison of a measured OH* profile to model calculations. Both models largely overpredict the incipient OH* formation observed near time-zero in the experiment. The causes for OH* formation immediately upon formation of the reflected-shock conditions are discussed in detail in Section 6. Integration of the Dayma et al. sub-mechanism as part of the model in the present study resulted in calculations of FWHM values in closer agreement with experimental values relative to the base methyl octanoate model. Using the compiled model, in contrast to previous conditions (both lean and stoichiometric), FWHM values are overpredicted in the calculations. At the high-temperature extreme (1559 K), the experimental value (100 μs) is calculated to be 80 μs longer using the compiled model. At the lower temperature extreme (1370 K), a difference of 210 μs is shown (210 μs experimentally, 420 μs computationally).

The experimental ignition activation energy of 57.0 kcal/mol measured at ϕ = 2.0, 1.5 atm is highly overpredicted using the base methyl octanoate model of Dayma et al. by nearly 30% (72.6 kcal/mol). The compiled model calculates an ignition activation energy of 42.6 kcal/mol, significantly below the experimental value by 25%. With all pure fuels, the fuel-rich conditions posed the most disagreement.

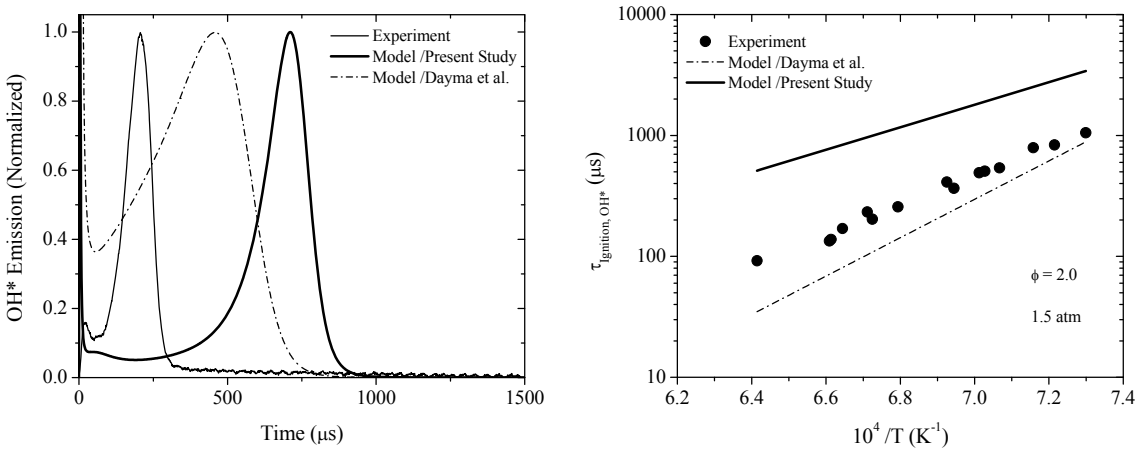

Fig. 5.5. (Left): Measured and model-predicted OH* time history during oxidation of 1380 ppmv $C_9H_{18}O_2$ (ϕ = 2.0) in 99% Ar. 1.4 atm, 1559 K, $\tau_{Ignition,\ OH^*}$: 92 μs (Experiment). 4.8-kΩ PMT resistance. (Right): Measured and model-predicted ignition delay times of $C_9H_{18}O_2$ (ϕ = 2.0) in 99% Ar at 1.5 atm. Calculations were performed using Dayma et al. [42] and the present chemical kinetics model. $13.80 \cdot 10^{-4} C_9H_{18}O_2 + 8.620 \cdot 10^{-3} O_2 + 0.99Ar$.

Ignition delay time measurements at $\phi = 2.0$ were obtained at an elevated (nominal) pressure of 9.2 atm over a temperature range of 208 K (1327 K – 1530 K). Figure 5.6 shows a comparison of a measured OH* profile to model calculations. Evident in Fig. 5.6 is the significant overprediction in FWHM of the measure OH* profile. Using the mechanism compiled in the present work, calculations differ by 160 μs at the high-temperature extreme (1530 K) and by 1230 μs at the low-temperature extreme (1327 K). This corresponds to an increase in FWHM of over 1 ms from the nearly 200-K temperature decrease–the largest increase shown by the calculations.

Ignition delay times measure at $\phi = 2.0$, 9.2 atm yielded a temperature dependence (ignition activation energy) of 47.4 kcal/mol. Both models are highly inaccurate for this condition. Dayma et al. model predicts 71.2 kcal/mol, while the compiled model calculates 21.8 kcal/mol. Considering the substantial temperature dependence of the calculated FWHM results and the large error in activation, the model requires significant improvement at the fuel-rich, high-pressure condition.

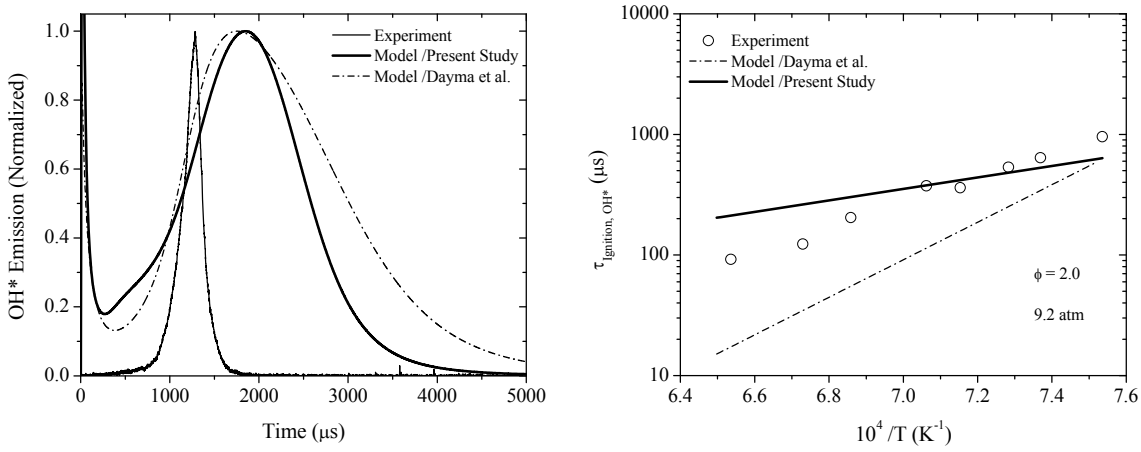

Fig. 5.6. (Left): Measured and model-predicted OH* time history during oxidation of 1380 ppmv $C_9H_{18}O_2$ ($\phi = 2.0$) in 99% Ar. 9.6 atm, 1327 K, $\tau_{Ignition,\ OH^*}$: 957 μs (Experiment). 4.8-kΩ PMT resistance. (Right): Measured and model-predicted ignition delay times of $C_9H_{18}O_2$ ($\phi = 2.0$) in 99% Ar at 9.2 atm. Calculations were performed using Dayma et al. [42] and the present chemical kinetics model. $13.80 \cdot 10^{-4} C_9H_{18}O_2 + 8.620 \cdot 10^{-3} O_2 + 0.99Ar$.

5.4 Pressure and equivalence ratio effects on methyl octanoate ignition

Figure 5.7 shows the effect of equivalence ratio (from 0.5 to 2.0) under conditions of fixed pressure. Comparison of ignition delay times at 1.5 atm show similar ignition activation energies for the fuel-lean and fuel-rich conditions, 51.7 kcal/mol and 57.0 kcal/mol, respectively, and a lower value for stoichiometric measurements (44.0 kcal/mol). Quantifying the effect of equivalence ratio at a given temperature between $\phi = 2.0$ and $\phi = 0.5$, using 1500 K, ignition delay times were approximately a factor of 3.5 shorter for the lean condition on average over the range of comparable temperatures. With decreasing temperature, stoichiometric ignition delay times at 1.5 atm approach the fuel-lean trend.

Increasing pressures reduced the relative differences in ignition delay times trends. At the increased pressure of 9.5 atm (nominal), ignition activation energies were also brought to more similar values: 42.7 kcal/mol ($\phi = 0.5$); 49.5 kcal/mol ($\phi = 1.0$), 47.4 kcal/mol ($\phi = 2.0$). Stoichiometric ignition delay times displayed ignition behavior similar to that for the fuel-lean measurements. Above 1380 K, the trends completely overlap and deviate beyond the experimental uncertainty below 1340 K. Comparing the fuel-lean and fuel-rich trends over the range of comparable temperature, fuel-rich ignition delay times are approximately a factor of 2.5 longer than those measured under fuel-lean conditions.

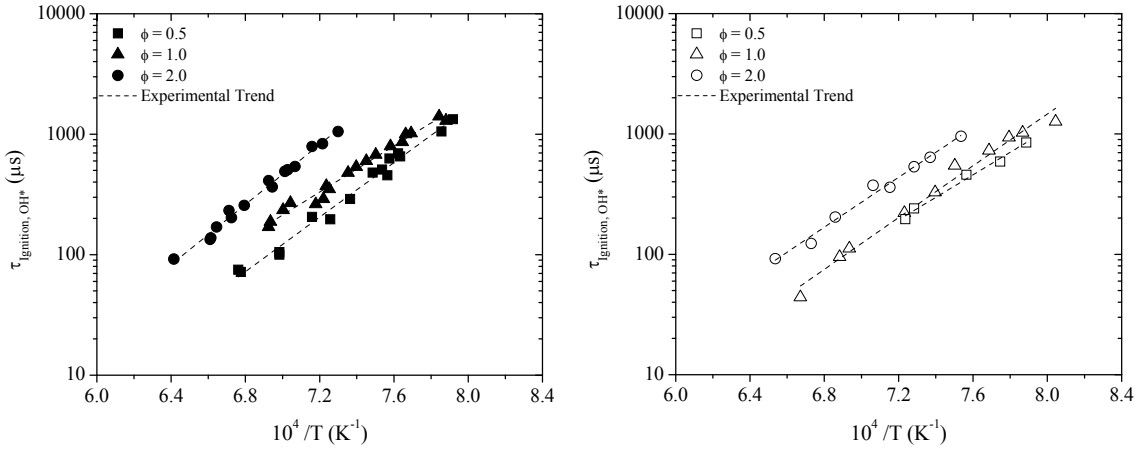

Fig. 5.7. Effect of equivalence ratio on ignition delay times of $C_9H_{18}O_2$ in 99% Ar at 1.5 atm (Left) and 9.5 atm (Right).

The effects of increased pressure from 1.5 atm to 9.5 atm (nominal) under conditions of fixed equivalence ratio on ignition delay times are shown in Figs. 5.8 – 5.10. For fuel-lean measurements, the ignition trends at 1.5 atm and 9.5 atm overlap near 1340 K and deviate to shorter times with decreasing temperature. At the lowest comparable temperature, the higher-pressure trend differs from that of the 1.5 atm trend by 45%. The increase in pressure of approximately 8 atm lowered the ignition activation energy by 20% (from 51.7 kcal/mol to 42.7 kcal/mol).

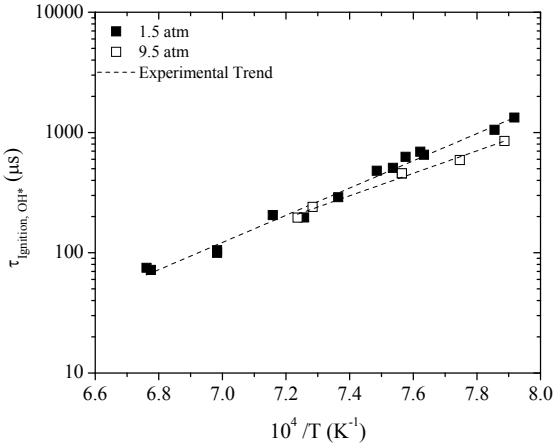

Fig. 5.8. Effect of pressure on ignition delay times of methyl octanoate at $\phi = 0.5$ (99% Ar).

Stoichiometric ignition delay time measurements at 1.5 atm and 9.3 atm are shown in Fig. 5.10. No overlap in the ignition trends was exhibited. The increase in pressure resulted in a ~ 10% increase in ignition activation energy (44.0 kcal/mol to 49.5 kcal/mol). Over the range of comparable temperatures, ignition delay times were shortened by 40% at the high-temperature extreme for the 1.5 atm measurements (1440 K) and by 25% at the low-temperature extreme (ca. 1270 K).

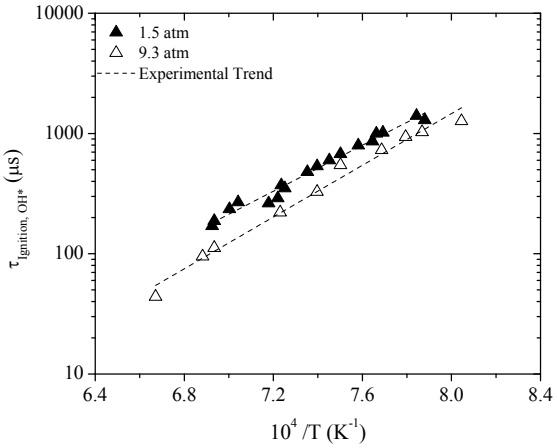

Fig. 5.9. Effect of pressure on ignition delay times of methyl octanoate at $\phi = 1.0$ (99% Ar).

Temperature-dependent ignition trends for $\phi = 2.0$ at 1.5 atm and 9.2 atm are shown in Fig. 5.10. Similar to the stoichiometric trend and in contrast to the fuel-lean trend, no overlap in the ignition behavior of fuel-rich trends was shown. The increase in pressure resulted in a ~ 15% increase in ignition activation energy from 57.0 kcal/mol to 47.4 kcal/mol. Ignition delay times were shortened by 30% at the highest temperature for the 1.5 atm measurements (1530 K) and 50% at the low-temperature extreme (~ 1370 K).

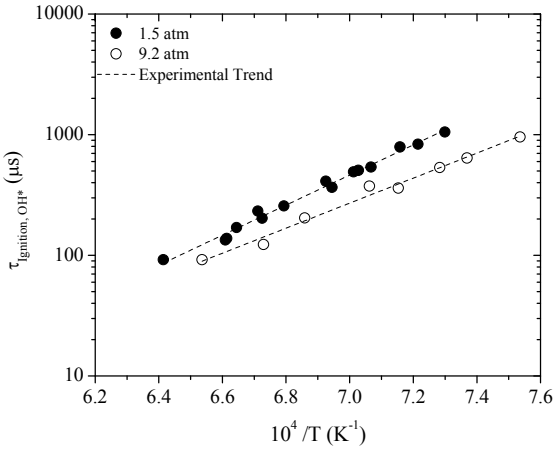

Fig. 5.10. Effect of pressure on ignition delay times of methyl octanoate at $\phi = 2.0$ (99% Ar).

5.5 Empirical ignition delay time correlation

Using linear regression analysis, an experimental correlation was developed from 72 experiments measuring methyl octanoate ignition (Eqn. 5.1), yielding an overall ignition activation energy of 48.7 kcal/mol. Error bars representing 10% uncertainty in measured ignition delay time are shown. The linear fitting procedure resulted in an R^2 of 0.95. In previous temperature-dependent plots of ignition delay times logarithmic ordinates were used, therefore the 10% error is less apparent. In Fig. 5.12 both the ordinate and abscissa are on linear scales, giving the 10% uncertainty a seemingly larger effect. Pressure dependence for the species was calculated to be n = –0.19. Units in Eqn. 5.1 consist of mol/cm^3, kcal, and K for species concentration, activation energy, and temperature, respectively. Conditions over which the equation is valid are given in Table 5.1. The difference in appearance of the ignition delay time plot of Fig. 5.11 compared to those shown previously is due to linear scaling of the abscissa ($\log_{10}$ scaling is used for $\tau_{Ignition,\ OH^*}$ – 1/T ignition delay times plots).

$$\tau(\mu s) = 3.09 \cdot 10^{-6}[C_9H_{18}O_2]^{0.84}[O_2]^{-1.03}exp(48.7/R_uT) \qquad (5.1)$$

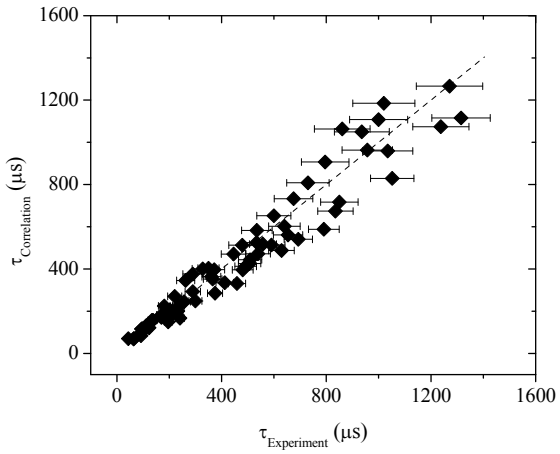

Fig. 5.11. Prediction of experimentally measured ignition delay times of methyl octanoate in 99% using Eqn. 5.1.

5.6 Concluding remarks on oxidation experiments and modeling of $C_9H_{18}O_2$

The first measurements of methyl octanoate ignition delay times were obtained. OH* profiles were measured over ranges of pressure and temperature $1.5 < P\ (atm) < 9.7$ and $1243 < T\ (K) < 1559$, respectively, under highly dilute conditions behind reflected shock waves. Measurements and model-predictions of OH* time histories and ignition delay times were discussed for all pressure/equivalence ratios studied, where both the base methyl octanoate mechanism and the compiled mechanism were used in the calculations for purposes of comparison to one another. The dependence of the ignition trends on pressure for fixed equivalence ratio and on equivalence ratio for fixed pressure was delineated. The order of ignition delay times at both pressures was identical to that for typical hydrocarbon fuels: lean < stoichiometric < rich. Some overlap at high pressure was exhibited by methyl octanoate at high pressure. Under stoichiometric conditions, increased pressure converged ignition times at lower temperatures. In contrast, at $\phi = 2.0$, ignition times tended toward convergence with increasing temperature.

From the ignition delay times measured, 72 in total, an empirical concentration- and temperature-dependent trend was calculated using linear regression. The empirical equation can be used to reproduce ignition delay times of methyl octanoate within the range of experimental conditions covered herein. The pressure dependence for $C_9H_{18}O_2$ ($n = -0.19$) is notably lower than that which is typical for conventional hydrocarbon fuels. The overall ignition activation energy (48.7 kcal/mol), however, is similar to other higher-order hydrocarbons (ca. 50 kcal/mol).

The base mechanism from which the methyl octanoate sub-mechanism in the present work was derived predicts fuel-lean ignition trends well at both 1.5 and 9.5 atm, yet for other conditions the model overpredicts ($\phi = 1.0$) and underpredicts ($\phi = 2.0$) the measured ignition delay times. The compiled model in the present work only predicts ignition delay times accurately at fuel-lean high-pressure conditions. Therefore since the base model is not well-validated for shock tube measurements the compiled model does not, in turn, reproduce pure methyl octanoate ignition behavior well. However, the present model is

intended to serve as a first generation mechanisms for blended fuel study. Refinement is required over all of the conditions in the present section, yet is beyond the scope of the present work.

6. MEASUREMENTS AND MODELING OF OH* AND CH* TIME HISTORIES AND IGNITION DELAY TIMES OF n-NONANE

The linear alkane chosen in the present work, n-C_9H_{20}, serves as both the main constituent in the majority of the fuel blends studied herein, and as the species around which the base model for the compiled chemical kinetics mechanism in the present work was constructed. The initial version of what is used in the present work as the base model was developed around the jet-stirred reactor (JSR) and shock-tube experiments of Rotavera et al. [16]. Improvements were made over the initial version using emission spectroscopy measurements of the $A^2\Sigma^+ \rightarrow X^2\Pi$ transition of OH. More specifically, the characteristic shapes of the time histories of OH* were utilized to refine the high-temperature predictive capability of the model in [16]. The conditions over which 230 experiments on n-nonane were taken are given in Table 6.1.

Table 6.1. Summary of conditions for dilute (99% Ar) shock tube experiments on n-nonane.

%n-C_9H_{20}	%O_2	%Ar	P (atm)	T (K)	ϕ
0.1 – 0.6	0.7 – 4.0	95.4 – 99.2	1.3 – 10.8	1176 – 1653	0.5 – 2.0

In the initial version of the n-nonane model [16], strongly under fuel-rich conditions at elevated temperatures, oxidation occurred immediately upon formation of the reflected-shock conditions (referred to herein as time-zero). While ignition delay times and OH* time histories were reproduced well for lean (ϕ = 0.5) and stoichiometric equivalence ratios, model predictions of OH* time histories at ϕ = 2.0 presented difficulty in defining ignition delay times. The difficulty arose from unclear ignition peaks due to an overprediction, relative to the measurements, of OH* within the first 10 – 20 μs post reflected-shock (referred to herein as incipient OH*). The principle issue with modeling of the incipient OH* was a substantial overprediction in peak OH* within the first 5 – 10 μs.

The present section (Section 6) is broken into two primary parts. The first part (Section 6.1) discusses the details concerning the improvement of the n-nonane mechanism from [16] as it pertains to OH* time history and ignition delay time predictions. Analysis on the underlying mechanisms responsible for incipient OH* formation under the two equivalence ratio extremes covered in the experiments (ϕ = 0.5 and ϕ = 2.0) then ensues. The second part (Sections 6.2 – 6.7) focuses on experimental and modeling trends in n-nonane oxidation at high temperature (> 1100 K) in 99% Ar dilution using both the improved base n-nonane model and the compiled model in the present work. Section 6.2 – 6.4 are separated according to equivalence ratio, from ϕ = 0.5 (Section 6.2) to ϕ = 2.0 (Section 6.4) and present measured OH* time histories and ignition delay times compared to model predictions. Section 6.5 discusses experimental and modeling differences observed in OH* and CH* and the remaining sections present pressure and equivalence ratio dependence of n-nonane ignition delay times (Section 6.6) and details on the empirical ignition delay time equation developed for the dilute (> 97% Ar) experiments of the present work (Section 6.7). Correlated n-nonane ignition delay times presented in Sections 6.2 – 6.4 are provided in Appendix F.

6.1 Development of base n-nonane chemical kinetics model using OH chemiluminescence profiles*

Ground-state chemistry governs excited-state species formation. Therefore, for well-characterized chemiluminescence reaction rates, OH* profiles, when used as an ignition diagnostic, can serve as a basis for identifying influential ground-state reactions which are important to processes such as ignition delay time. With emphasis placed on high-temperature chemistry, improvements were made in a detailed chemical kinetics mechanism for n-nonane oxidation developed previously [16]. Using characteristic features of time-dependent OH* species profiles measured in shock tube experiments as the primary metric for assessing the predictive capability of the model at elevated temperatures, calculations were performed over the following range of conditions: T > 1000 K, 1.5 < P (atm) < 10.5, ϕ = 0.5, 1.0, 2.0.

The base model in the present work is the result of the improvements made to the n-nonane model in Rotavera et al. [16]. The sections below primarily include details of the complications in modeling OH*

profiles using the first version of the model [16], detailed analysis on the root of the complications, and the modification steps taken to improve the model. The impact of experimental parameters on characteristics OH* time histories, which were employed in the model development is also discussed. Resulting from the modifications to the initial version of the mechanism are definable ignition delay times under fuel-rich conditions and improved ignition delay time predictions for lean and stoichiometric equivalence ratios.

6.1.1 Definition of problem

In the initial version of the mechanism, oxidation processes at fuel-rich conditions taking place immediately behind reflected shock waves (time-zero) interrupted the main ignition event as observed in modeled OH* profiles such that ignition times were indefinable. The objective of reaching definable model-predicted ignition times at this condition ($\phi = 2.0$) led to improvements being sought after in three principle areas: (1) accurate prediction of incipient oxidation processes near time-zero (quantified by the ratio of the incipient OH* peak to the main ignition peak), (2) improved OH* time-dependence/profile shape, and (3) definable ignition delay times. In moving towards better agreement in the fuel-rich profiles, improvements were also for both $\phi = 0.5$ and $\phi = 1.0$ conditions, both in terms of OH* profile shape and ignition delay times, the latter of which were captured well with the initial version of the mechanism.

In dilute shock-tube experiments of n-nonane, occurring strongly under fuel-rich conditions at elevated temperatures, OH* formation occurred immediately upon formation of the reflected-shock conditions (time-zero) resulting in formation of two distinct peaks: an incipient peak near time zero and a main ignition peak feature (Fig. 6.1). While ignition delay times and OH* time histories were reproduced accurately for lean ($\phi = 0.5$) and stoichiometric equivalence ratios, model predictions of the incipient OH* behavior at $\phi = 2.0$ were considerably longer in duration and larger in magnitude than those observed experimentally. The overprediction of the modeled incipient OH* peak being substantially greater than the peak resulting from ignition served as an impediment to ignition time definition due to unclear ignition peaks. Model-produced time histories were also significantly longer in duration relative to those measured

experimentally under ϕ = 2.0 conditions (Fig. 6.2). Model-calculated OH* profiles are shown in Fig. 6.2 normalized to the main OH* peak (occurring shortly after primary ignition). As a result of the normalization, since the incipient OH* peaks were predicted to exceed the main ignition peaks in both cases, the modeled profiles take on values greater than unity within the first 100 μs. The overprediction in the stoichiometric case is a factor of 5, while the fuel-rich case is considerably higher (by a factor of 135).

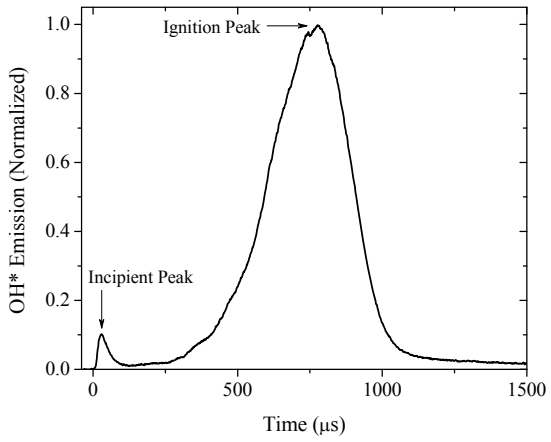

Fig. 6.1. Representative OH* time history from Rotavera et al. [16] showing incipient OH* peak near time-zero over a period of ~ 65 μs relative to the main ignition peak. 0.10%n-C_9H_{20} + 0.70%O_2 + 99.2%Ar (ϕ = 2.0), 1472 K, 1.5 atm. The magnitude of the incipient peak is ~ 11% of the main peak marking ignition.

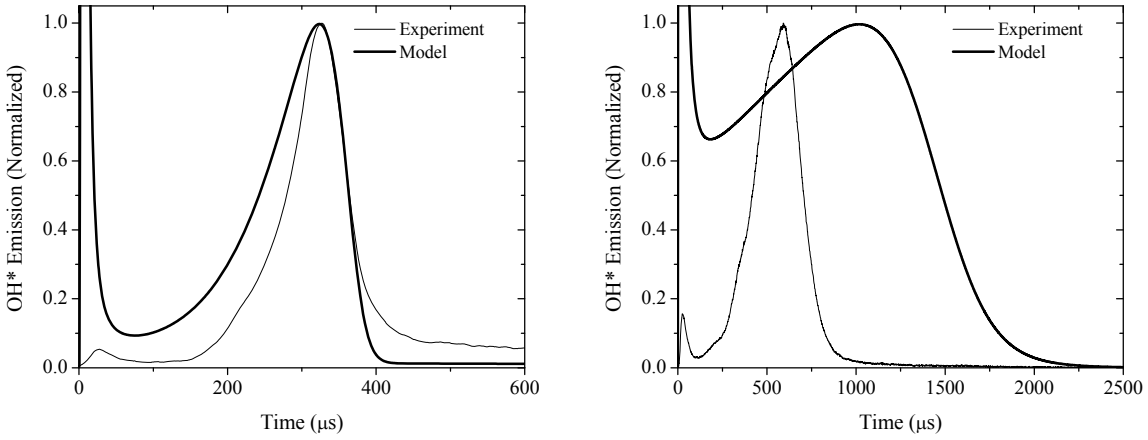

Fig. 6.2. Initial model prediction of OH* time history using [16], normalized to the main ignition peak, during oxidation of 1000 ppmv of n-nonane. ϕ = 1.0, 1487 K, 1.5 atm (Left); ϕ = 2.0, 1525 K, 1.5 atm (Right).

Despite definable ignition delay times at other conditions, the initial version of the n-nonane mechanism [16] did not permit definition of ignition delay time for $\phi = 2.0$ cases using the steepest ascent approach due to unclear ignition peak. Extrapolation of a line from the steepest ascent in the $\phi = 2.0$ profile yields negative time for ignition.

Figure 6.3 compares peak ratios for $\phi = 2.0$ at three temperatures determined from experimental measurements and model predictions using the initial n-nonane mechanism [16]. Noting the axis break, evident in Fig. 6.3 is the overprediction of the relative OH* peaks (incipient-to-ignition peaks) from initial version of the model by almost 3 orders of magnitude. Moreover, experimental measurements of OH* showed that the incipient oxidation behavior displayed a proportional dependence on temperature (increasing with increasing temperature), yet the initial model calculations displayed an inverse relationship between the incipient behavior and temperature.

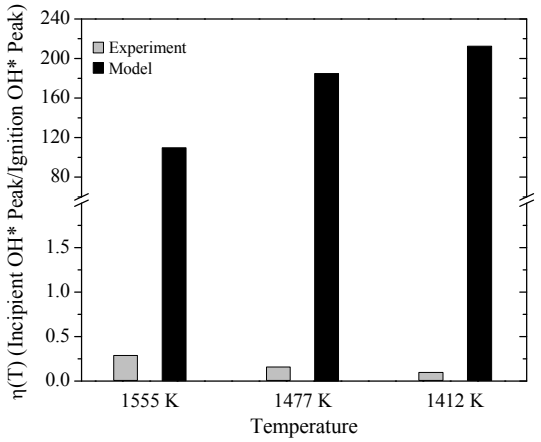

Fig. 6.3. Temperature trends for measured and modeled [16] incipient-to-ignition peak OH* ratios. $\phi = 2.0$, 1000 ppmv n-C_9H_{20}, 1.5 atm.

Resulting from the abovementioned discrepancies between model and experiment, three primary issues were identified as targets for improving the chemical kinetics mechanism using excited-state OH measurements: (1) overprediction of the incipient-to-ignition peak OH* ratio; (2) time-dependent prediction of OH* (profile shapes); and (3) the inability to define ignition delay times for conditions of fuel-rich equivalence ratio at either 1.5- or 10.5-atm reflected-shock pressure. Observations made on the ratio of the incipient OH* peak relative to peak OH* formation resulting from ignition (defined herein as η, shown in Fig. 6.4), led to the conclusion that the phenomenon showed strong dependence on several experimental parameters (in descending order of impact): equivalence ratio, temperature, fuel concentration, and pressure. Experimentally, the individual influences of these parameters on η were elucidated by holding all other experimental conditions constant. The ratio η serves as a characteristic feature of the chemiluminescence profiles which is then used to study the influence of ground-state reactions on its value.

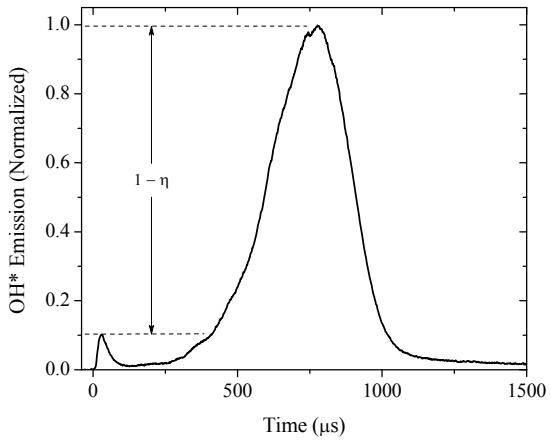

Fig. 6.4. Definition of incipient-to-ignition OH* ratio, η. 0.10%n-C_9H_{20} + 0.70%O_2 + 99.2%Ar (ϕ = 2.0), 1472 K, 1.5 atm, η = 0.11.

Prior to any detailed analysis or modification to any reaction rates within the model, a series of time-response experiments were performed to ensure the incipient OH* behavior measured experimentally did not suffer from inadequate time response. The photomultiplier tube (PMT) detector electronics, to control the output voltage level, incorporate an externally applied resistance integrated into the signal output channel; an artifact of this control implementation is a characteristic time response that depends on the level of applied resistance. The added resistance increases the output voltage signal, yet increases the RC time constant of the output signal. For the majority of the experimental data presented herein, the PMT was equipped with a signal output resistance of 4.8 kΩ. The time constant for this resistance in prior calculations is less than 5 μs. Further, to maintain optical measurements within the region of linearity of the PMT detector, the output voltage was limited to levels less than 500 mV (from previous calibration). To ensure that the entire process leading to the formation of incipient OH* was captured, in terms of peak level of OH* near time-zero, the resistance applied to the PMT was altered from the 4.8-kΩ level used in the experiments herein to 470-Ω, 1-kΩ, or 10-kΩ where lower resistance decreases time response and higher resistance increases signal output. Employing the different resistors, ϕ = 2.0 n-nonane ignition experiments were performed using 99.2% Ar dilution (1000 ppmv n-nonane). Qualitatively, from a series of measurements made near 1600 K, lower levels of resistance led to higher magnitudes of incipient OH* due to the more rapid time response (Fig. 6.5). The change in resistance also had a quantifiable impact on the time constant and, by extension, the incipient OH* magnitude. Incipient OH* magnitude increased by a factor of nearly 2 as a result of decreasing the resistance from 10 kΩ to 470 Ω ($\eta_{470\ \Omega}$ = 0.48; $\eta_{10\ k\Omega}$ = 0.27). Of importance to note is the slower time response exhibited by higher-resistance measurements of chemiluminescence impacts only the first ~30 μs of the experiment and the overall profile shape during the main ignition event is unaffected.

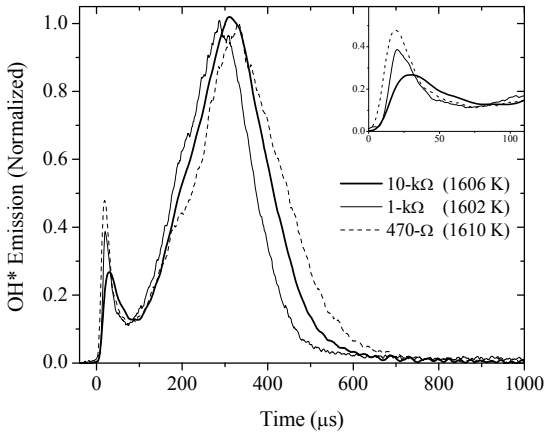

Fig. 6.5. OH* profiles from n-nonane oxidation experiments near 1600 K, 1.5 atm in 99.2% Ar. using three values of output resistance: 470-Ω, 1-kΩ, and 10-kΩ PMT resistance.

For all equivalence ratios, η strongly increased with increasing temperature. Figure 6.6 shows a juxtaposition of two OH* measurements taken under fuel-rich conditions at 1412 K and 1555 K in 99.2% Ar near 1.5 atm. The 140-K increase in temperature led to an increase in incipient OH* formation relative to the ignition peak OH* by a factor of 3.5. While the chemistry differs between the formations of OH and OH*, this phenomenon mirrors the incipient oxidation behavior observed in the ground-state hydroxyl measurements in Vasu et al. [103] during n-dodecane oxidation. The laser absorption measurements of ground-state OH indicated incipient oxidation immediately behind the reflected shock (time-zero) were marked by an appreciable increase in OH absorption in both fuel-lean and stoichiometric mixtures. Similar to the present work, an initial n-dodecane concentration of 1000 ppmv was used. Near 1420 K and 15.5 atm, a 20-ppmv level of incipient OH was measured and sustained for approximately 20 μs.

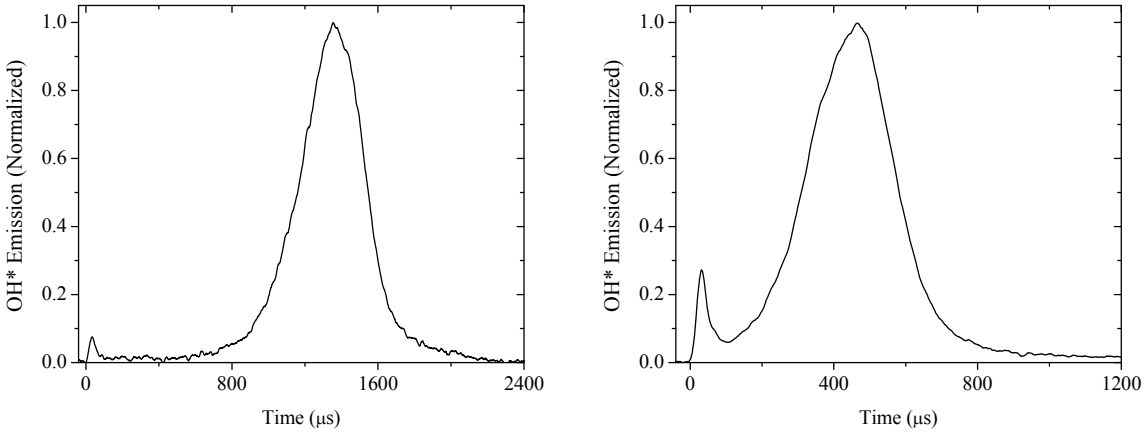

Fig. 6.6. Effect of temperature on incipient OH* at ϕ = 2.0, 1.5 atm; 1412 K (Left), 1555 K (Right).

The effect of equivalence ratio at fixed conditions of temperature (1450 K), pressure (1.5 atm), and dilution concentration (99.2% Ar) is shown in Fig. 6.7. Fuel-lean and fuel-rich equivalence ratios show similar values for η (~ 0.12) at 1450 K. However, the ignition delay times are substantially different between the two profiles. Since temperature has the strongest influence on η, the OH* peak ratios were compared at similar ignition times holding the other parameters constant (Fig. 6.8).

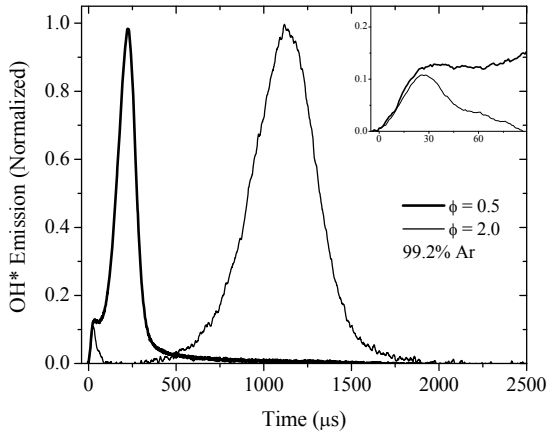

Fig. 6.7. Comparison of OH* time histories at two equivalence ratios (ϕ = 0.5, 2.0) in 99.2% Ar near 1450 K and 1.5 atm. Ignition delay times: ϕ = 0.5, 89 μs; ϕ = 2.0, 761 μs.

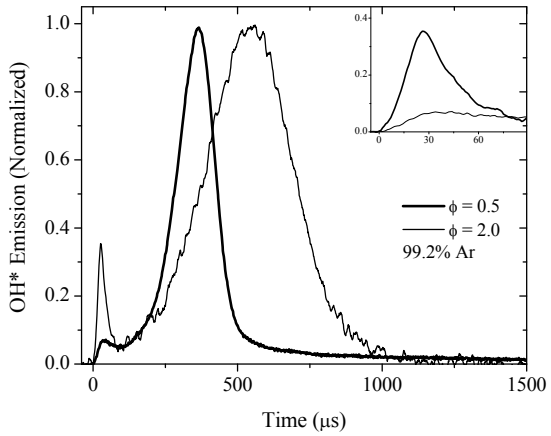

Fig. 6.8. Comparison of OH* time histories near 200-μs ignition time for two equivalence ratios (ϕ = 0.5, 2.0) in 99.2% Ar at 1.5 atm (ϕ = 0.5, 1408 K; ϕ = 2.0 1543 K). η(T) is more pronounced at higher equivalence ratios. The incipient OH* formation for similar ignition delay time is greater for ϕ = 2.0 than for the leaner cases by a factor of 5.

Over the range of experimental conditions covered, the most salient effect on incipient OH* was the growth of the incipient OH* peaks with increasing equivalence ratio. Comparison of three OH* measurements at 1478 K near 1.5 atm shows the dependence of incipient OH* on equivalence ratio for a fixed fuel concentration of 1000 ppmv (Fig. 6.9). Relative to the height indicating peak OH* yield from ignition, formation of early OH* occurs with the least magnitude for lower equivalence ratio (i.e. η increases with ϕ). The inset in Fig. 6.9 details more closely the behavior for the duration of the first peaks. Also noteworthy in Fig. 6.9 is the increase in the duration of OH* time history with increasing equivalence ratio. Comparing the trend with equivalence ratio, FWHM values increase substantially with increasing equivalence ratio: 50 μs (ϕ = 0.5), 100 μs (ϕ = 1.0), 315 μs (ϕ = 2.0).

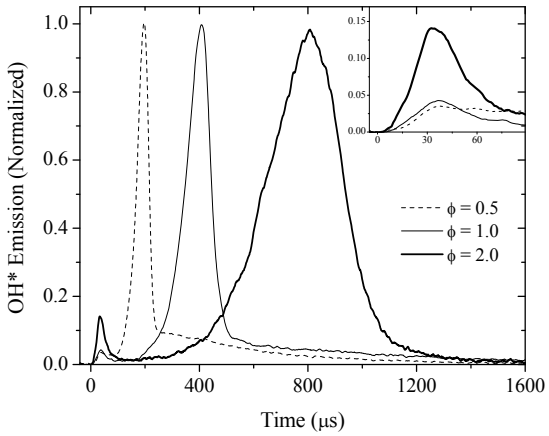

Fig. 6.9. Comparison of experimental OH* profiles at 1478 K near 1.5 atm for three equivalence ratios at a fuel concentration of 1000 ppmv showing the dependence of incipient oxidation on stoichiometry. Relative incipient-peak-to-ignition-peak percentages were quantified: ϕ = 0.5 (η = 3.5%), ϕ = 1.0 (η = 4.5%), ϕ = 2.0 (η = 15.0%).

The effect of fuel concentration on η, which is coupled to a change in diluent concentration for the same equivalence ratio, was investigated by selecting conditions where the incipient phenomenon was most pronounced: fuel-rich, high-temperature, low-pressure conditions. The effect of n-nonane concentration on incipient OH* was determined using ϕ = 2.0 experiments conducted at 1.5 atm at 1515 K in 95.4% Ar and 99.2% Ar using a 10-kΩ PMT resistance (Fig. 6.10). In contrast to comparisons of profiles under conditions of similar dilution, the more dilute profile (99.2% Ar) displays a larger η. One plausible explanation for the smaller amount of incipient behavior in the profile measured in 95.4% Ar could be the higher concentration of OH* formed during chemical reaction and consequently overshadowing the smaller, incipient profile. Calculations were performed using the two different levels of dilution for the fuel-rich case, employing the base n-nonane model in the present work (the model of Rotavera et. al [16] is unable to produce usable fuel-rich profiles) and show an increase in mole fraction of OH* with decreasing dilution level (from increase oxygen concentration) by nearly an order of magnitude ($5.3 \cdot 10^{-10}$ for the 99.2% Ar case compared to $3.4 \cdot 10^{-9}$ for the 95.4% Ar case). It is likely, then, that with increased

fuel concentration the incipient OH* is present in the experiment yet eclipsed within the noise of the diagnostic.

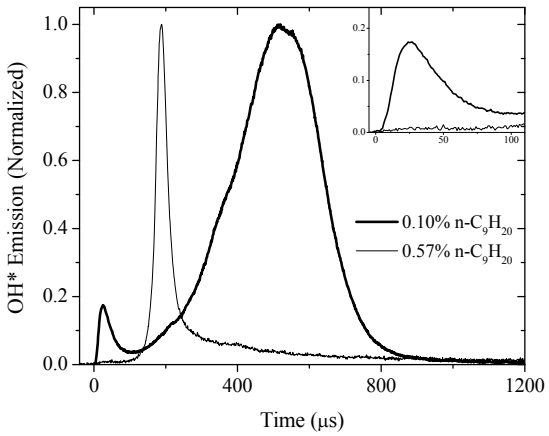

Fig. 6.10. Effect of increased fuel concentration on incipient formation of OH* at fixed equivalence ratio (ϕ = 2.0) and temperature (1515 K) near 1.5 atm. At 99.2% and 95.4% Ar dilution, fuel concentration is 1000 and 5700 ppmv.

To further illustrate the effect of equivalence ratio on η under conditions of fixed fuel concentration, Fig. 6.11 delineates the temperature dependence of η for ϕ = 0.5, 1.0, and 2.0 from oxidation of 1000 ppm of n-nonane. Measurements shown in Fig. 6.11 were obtained using a 10-kΩ PMT resistance. While the specific quantities are not significant, the experimental trends indicate that η is strongly dependent on equivalence ratio for a given temperature. With increasing temperature the fuel-rich trend deviates sharply from those of either the stoichiometric or lean trends. At 1400 K, incipient-to-ignition OH* peak ratios were 0.022, 0.031, and 0.051 for ϕ = 0.5, 1.0, and 2.0. At 1555 K the differences became more exaggerated: η = 0.045 (ϕ = 0.5); η = 0.087 (ϕ = 1.0); η = 0.267 (ϕ = 2.0).

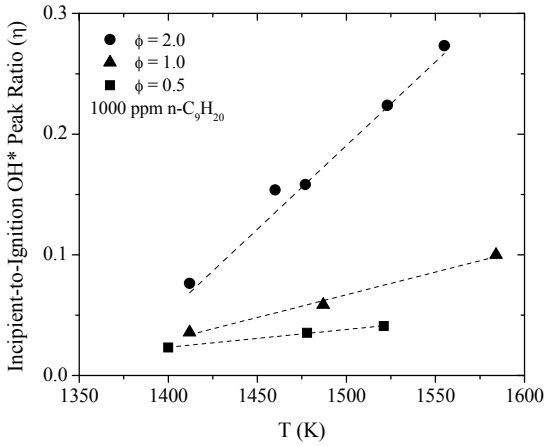

Fig. 6.11. Experimental trends of incipient-to-ignition peak OH* ratios produced from oxidation of 1000 ppm of n-nonane (1.5-atm); Resistance applied PMT $\rightarrow$ 10 kΩ.

Table 6.2 provides a summary of the experimental observations on incipient OH* formation from oxidation of n-nonane. Note that since [Ar] is inversely proportional to both [Fuel] and [O_2], a decrease in diluent concentration simultaneously corresponds to an increase in the concentration of these constituents. The effect of pressure holding other conditions constant was observed only to slightly decrease η within a reasonable amount of uncertainty for assessing the magnitude of the incipient peaks. Conditions 1, 2, 3, and 4 in Table 6.2 correspond to Figs. 6.9, 6.6, 6.10, and 6.7/6.8, respectively.

Table 6.2. Summary of the impact of experimental parameters on the ratio of OH* peaks (η). Parentheses indicate a coupled effect (e.g. Condition 1: increased equivalence ratio at fixed temperature, pressure, and fuel concentration is coupled by a slight increase in Ar concentration and leads to an increase in η).

Condition	ϕ	Temperature	Pressure	[Fuel]	[Ar]	Effect
1	Increase	*Fixed*	*Fixed*	*Fixed*	(Increase)	Increased η
2	*Fixed*	Increase	*Fixed*	*Fixed*	*Fixed*	Increased η
3	*Fixed*	*Fixed*	*Fixed*	Increase	(Decrease)	Decreased η
4	Increase	*Fixed*	*Fixed*	(Increase)	*Fixed*	Increased η

Utilizing the measured incipient-to-ignition OH* peak ratio (η) as a tuning parameter for model improvements in time-dependent kinetics and ignition delay times, detailed analysis on the chemical kinetics model was performed. The impact of chemiluminescence rates on model predictions of species time histories were varied by multiplying/dividing k(T) for the dominant production channels in order to assess the level of influence of chemiluminescence rates on η. Rates of reactions responsible for producing or consuming OH chemiluminescence were examined to elucidate any impact on the over-predicted incipient OH*. The rates of dominant OH* production channels, Eqns. R1 and R2, respectively, were varied to determine the effect of the tuning parameter (i.e. peak ratio).

$$CH + O_2 \rightarrow OH^* + CO \qquad R1$$

$$H + O + M \rightarrow OH^* + M \qquad R2$$

Figure 6.12 shows the effect of varying the frequency factor in the Arrhenius expression of the rate coefficient k(T) of the primary OH* production channel (R1) by factors of 10. The chemiluminescence profiles of OH* were unchanged by the order-of-magnitude increase or decrease in R1. The same non-impacting result on η using multiplying/dividing R2 is observed in Fig. 6.13. Calculations were performed

using increased rates of collisional de-excitation by Ar and O_2 and did not result in any influence on the OH* profile shape. The lack of impact of the chemiluminescence rates leads to the conclusion that overprediction of OH* near time-zero cannot be attributed to any uncertainty in the chemiluminescence mechanism.

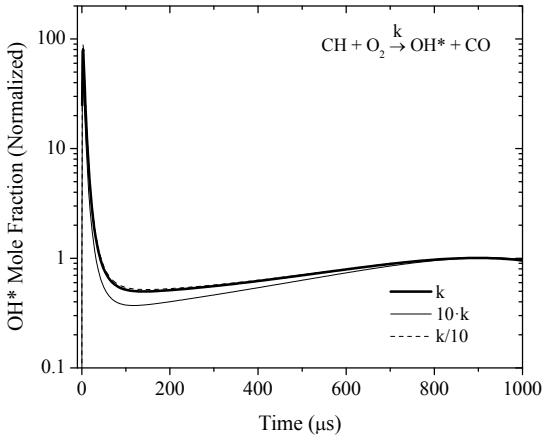

Fig. 6.12. Calculated OH* mole fraction normalized to the primary ignition peak (near 900 μs), showing highly overpredicted OH* near time-zero. Variation in the rate coefficient of R1 shows no impact on OH* production near time zero. 0.10% n-C_9H_{20} + 0.70% O_2 + 99.2% Ar (ϕ = 2.0), 1555 K, 1.5 atm.

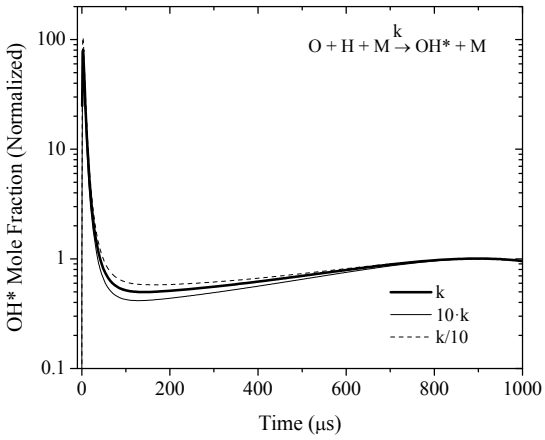

Fig. 6.13. Calculated OH* mole fraction normalized to the primary ignition peak (near 900 μs), showing highly overpredicted OH* near time-zero. Variation in the rate coefficient of R2 shows no impact on OH* production near time zero. 0.10% n-C_9H_{20} + 0.70% O_2 + 99.2% Ar (ϕ = 2.0), 1555 K, 1.5 atm.

Reactions leading to improvement of ignition delay time predictions can be assessed using OH* profiles due to the independence of profile shape from chemiluminescence rates shown in Figs. 6.12 and 6.13. Since ground-state species furnish radicals and intermediates which are involved copious other reactions and in the reactions leading to formation of OH*, as a result of the chemiluminescence reactions having no impact on the tuning parameter η, the experimental OH* time histories were then employed as targets for improving the high-temperature chemistry of the mechanism. To this end, sensitivity, rate-of-production, and reaction pathway analyses were applied to the conditions covered in the experiment to identify ground-state reactions which impact the production/consumption of OH*. Calculations were focused initially at the conditions where incipient OH* formation was most pronounced (fuel-rich, high-temperature, 1.5 atm). The identified reactions are then considered in closer detail with respect to ranges of conditions over which the rates are calculated and/or measured. The majority of the modifications came from utilizing literature results for the various rate coefficients.

6.1.2 Source for incipient OH formation*

The chemiluminescence mechanism [148] contains 14 reactions involving OH*. Under all of the conditions in the present study, reactions R1 and R2 ($CH + O_2 \rightarrow OH^* + CO$ and $H + O + M \rightarrow OH^* + M$, respectively) are the dominant reactions responsible for the formation of OH*. Improvement of the initial n-nonane model [16] relied in part on calculations of OH* rate of production and consumption. Figure 6.14 shows the five most influential reactions involving OH* calculated for ϕ = 2.0, 1555 K, 1.5 atm, 1000 ppmv n-C_9H_{20}. Dominant consumption reactions involve collisional de-excitation by O_2 and Ar (occurring more strongly for O_2 collisions) and unimolecular de-excitation (releasing of hν). The trend of R1 reaches a maximum within the first 5 μs. This is coincident in the OH* profiles with the incipient peaks also reaching a maximum within 5 μs. The rate calculations of OH* emphasize the significance of CH in the formation of OH*.

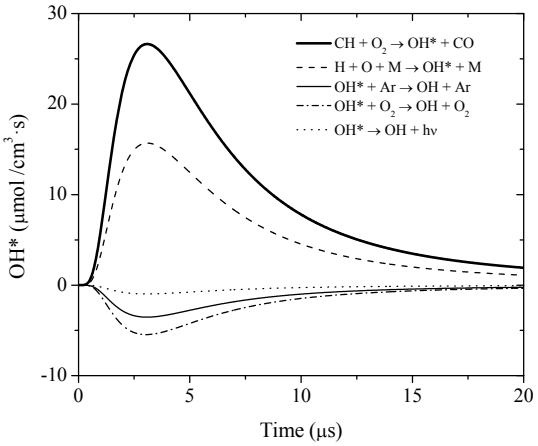

Fig. 6.14. Rates of formation and consumption of OH* calculated using [16]. ϕ = 2.0, 1555 K, 1.5 atm, 1000 ppmv n-C_9H_{20}.

Reactions to which OH* formation shows the highest sensitivity (at the conditions selected for detailed analysis of incipient OH* formation) are shown in Fig. 6.15 using sensitivity analysis to calculate respective sensitivity coefficients. Although the ten most influential reactions were determined, only seven reactions are shown in Fig. 6.15 for clarity. The other three reactions were n-nonane homolysis:

$$n\text{-}C_9H_{20} \rightarrow pC_4H_9 + AC_5H_{11}$$

$$n\text{-}C_9H_{20} \rightarrow nC_3H_7 + AC_6H_{13}$$

$$n\text{-}C_9H_{20} \rightarrow C_2H_5 + AC_7H_{15}$$

The fourth homolysis reaction of n-nonane (formation of methyl and octyl radicals) did not appear in the results. CH is involved explicitly in two of the reactions and other species yielding CH (shown in the ensuing section from reaction pathway analysis) are also indicated. Reactions R1 and R2 appeared in the sensitivity analysis results. Noteworthy in Fig. 6.15 is the nature of the time histories of R1 and R2, specifically the time-independence after the first 2 μs. The insensitivity to time for these reactions explains the results obtained previously on the impact of OH* profile shape by varying the respective rate

coefficients for the dominant OH* production reactions. Time-independence shown in the sensitivity analysis plots points to a change only in magnitude, and not the time dependence, of a particular species. As a result, the variation in k(T) for reactions R1 and R2 (Figs. 6.12 and 6.13), resulted only in a change in the absolute value of OH* and not a change in η. The ground-state reactions shown in Fig. 6.15 served as the initial set which were modified using literature values for respective rate parameters.

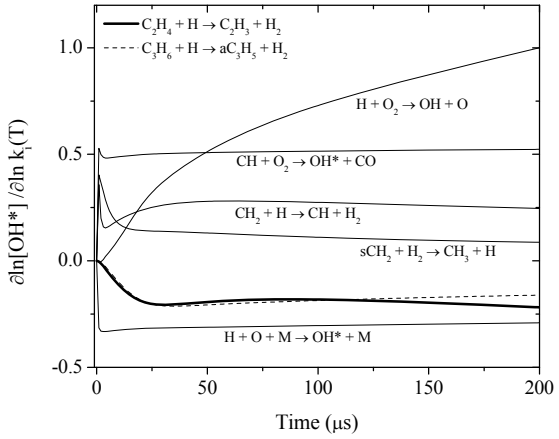

Fig. 6.15. Time-dependent sensitivity coefficients for OH* calculated using [16] at a time-step of 1 μs. ϕ = 2.0, 1555 K, 1.5 atm, 1000 ppmv n-C_9H_{20}.

6.1.3 Analysis of incipient OH formation mechanisms*

Calculations on dilute (99.2% Ar) oxidation of n-nonane under fuel-rich conditions (ϕ = 2.0) were performed at an arbitrary high temperature of 1525 K at a pressure 1.5 atm using reaction pathway analysis (RPA) to identify the mechanisms of incipient OH* formation up to the time of the incipient peak (5 μs) using the model of Rotavera et. al [16]. The analysis, conducted on 1-μs intervals over the first 5 μs of reaction shows that initial fuel decomposition leads immediately to alkyl radicals which then proceed through a series of elementary reactions ultimately leading to the formation of CH. Figure 6.16 shows the unimolecular decomposition steps of n-nonane.

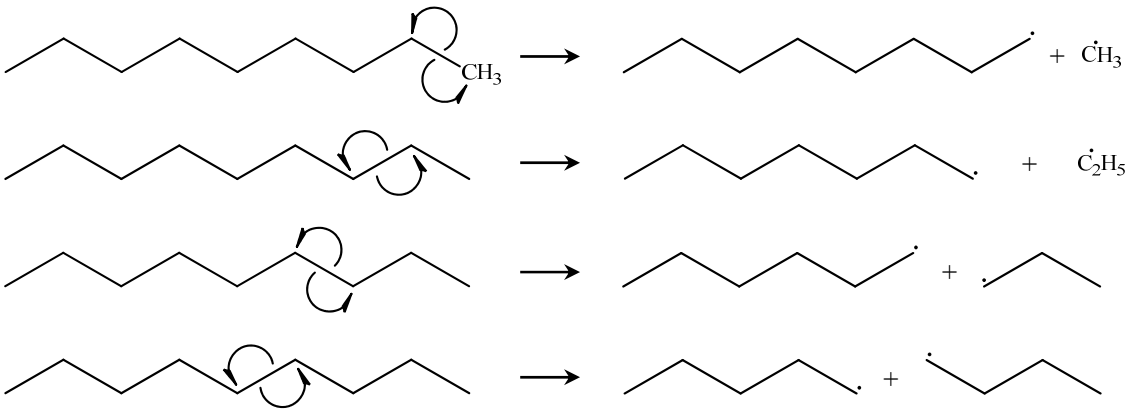

Fig. 6.16. Primary decomposition reactions of n-nonane (ϕ = 2.0, 1525 K, 1.5 atm, 1000 ppmv n-C_9H_{20}).

Due to the conditions of elevated temperatures (> 1400 K), where unimolecular decomposition competes with H-abstraction reactions for parent fuel consumption, calculations of fuel decomposition under the conditions selected show that homolysis of n-nonane yields alkyl radicals preferentially. Decomposition into 1-butyl + 1-pentyl consumes 31% of the parent molecule. The n-Propyl + 1-hexyl and ethyl + 1-heptyl pathways consume 29% and 26% of n-nonane, respectively, and the least preferred decomposition pathway is methyl + 1-octyl (14% of n-nonane consumption). After the initial fuel decomposition step, the fragmented fuel components (alkyl radicals) react in a series of steps which lead the formation of CH_3 after which the pathway to OH* remains independent of time. Figure 6.17 outlines the time history of formation mechanisms of incipient OH* up to the peak incipient yield time of 5 μs. The mechanisms shown in Fig. 6.17, ordered from 6.17a – 6.17c, progress forward in time from 1 μs (Fig. 6.17a, to 3 μs (Fig. 6.17b), ending at the time observed in the calculations to be the peak incipient OH* yield time, 5 μs (Fig. 6.17c). The slowing of incipient OH* production comes as a result of a propagation reaction between two methyl radicals yielding ethyl + H. The consumption of methyl radicals through this channel slows the formation of singlet-state methylene by ~ 30% which then ultimately slows the rate of OH* formation.

The mechanism of incipient OH* can be generalized into six steps:

Step 1: Homolysis of n-nonane (formation of 1-pentyl, 1-butyl, 1-propyl, ethyl, methyl radicals)

Step 2: Alkyl radicals form methyl

Step 3: Methyl radical reacts with H or OH to produce singlet-state methylene (sCH_2)

Step 4: Singlet-state methyl radical undergoes collision with M to form methylene (CH_2)

Step 5: H-abstraction from methylene by H produces CH

Step 6: CH reacts with O_2 to form OH*

Incipient OH* Retardation Step: Propagation reaction of two methyl radicals into ethyl + H

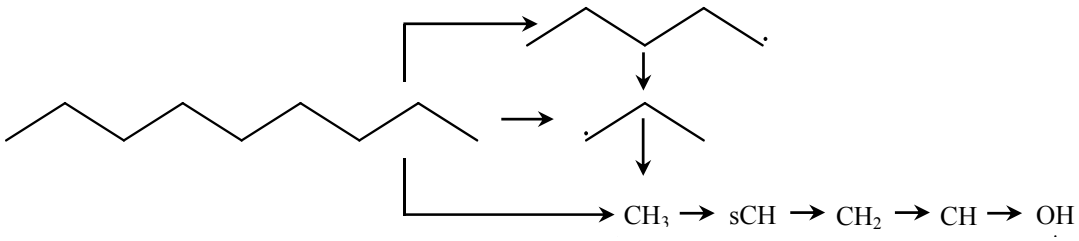

Fig. 6.17a. Dominant reaction pathway of OH* formation at 1 μs using [16]; ϕ = 2.0, 1525 K, 1.5 atm, 1000 ppmv n-C_9H_{20}. Of the dominant channels of methyl production, 83% comes from decomposition of 1-propyl and 17% comes from fuel decomposition.

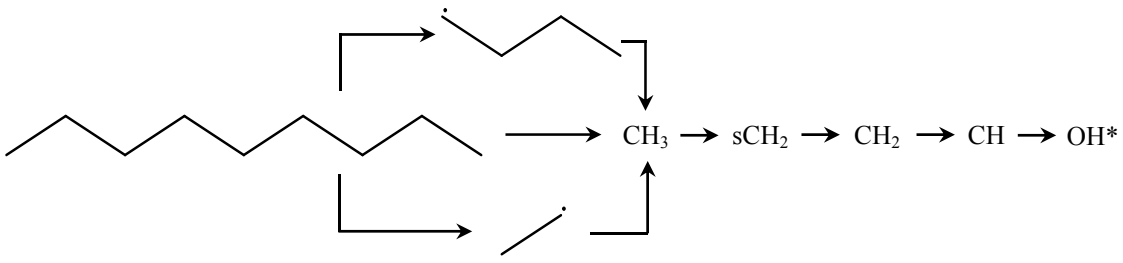

Fig. 6.17b. Dominant reaction pathway of OH* formation at 3 μs using [16]; ϕ = 2.0, 1525 K, 1.5 atm, 1000 ppmv n-C_9H_{20}. Of the dominant channels of methyl production, 68% comes from ethyl + H, 22% comes from fuel decomposition, and 10% comes from decomposition of 1-butyl.

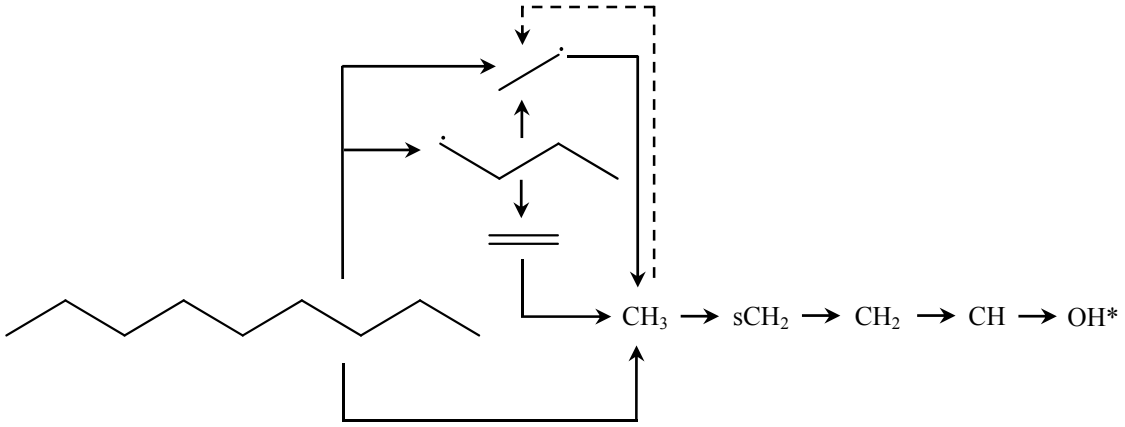

Fig. 6.17c. Dominant reaction pathway of OH* formation at 5 μs (time of peak incipient OH* yield) using [16]; ϕ = 2.0, 1525 K, 1.5 atm, 1000 ppmv n-C_9H_{20}. Rate of singlet-state methylene production slowed by preferential formation of ethyl radicals ($CH_3 + CH_3 \rightarrow C_2H_5 + H$). Of the dominant channels of methyl production, 65% comes from ethyl + H, 20% comes from ethylene + O, and 15% comes from fuel decomposition.

6.1.4 Model improvement using incipient/ignition peak OH ratios*

Detailed below are the specific impacts of the individual modifications which were made to the initial version of the mechanism [16]. Experimental conditions of 1477 K and 1.5 atm at ϕ = 2.0 were arbitrarily chosen to compare measured and modeled profiles of OH* during oxidation of 1000 ppm n-C_9H_{20}. Noting the importance of fuel decomposition, the n-nonane homolysis rates were altered first. The initial model for n-nonane made use of rate parameters for n-decane, the species to which the model is rooted. Using gas kinetic theory equations, Appendix G, first-order approximations as to the magnitude of reduction in collision number were made, due to the slightly smaller collision diameter of n-nonane (14.52 Å) compared to n-decane (16.06 Å), to determine an initial estimate for the reduction in frequency factors relative to those contained initially contained in the model. Collision with Ar atoms was used in the calculations due to the relative abundance (99.2% Ar) of the species. The reduction in collision number led to an approximated decrease in A of 50%, changing the initial values of $2.0 \cdot 10^{17}$ to $1.0 \cdot 10^{17}$. Continued iterations were made in the interest of reducing the incipient OH* peak. Frequency factors for the homolysis rates of n-nonane were ultimately reduced from $2.0 \cdot 10^{17}$ to $5.0 \cdot 10^{16}$ mol/cm^3·s, which are the

values in the present model. The iteration ceased at $5.0 \cdot 10^{16}$ mol/cm^3·s due to a practical limit in the effect of fuel decomposition rates on incipient OH* production, pointing to the need to examine ground-state oxidation reactions. While the overall profile shape of OH* did not change, the incipient OH* peak was reduced by a factor of nearly 10 as a result of decreasing the fuel decomposition rate (inset of Fig. 6.18).

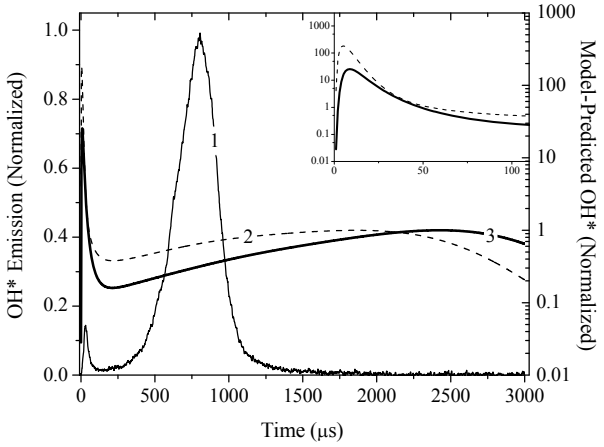

Fig. 6.18. Effect of decreased fuel decomposition rates through homolysis pathways. Rates were initially based on n-decane and reduced for n-nonane from $2.0 \cdot 10^{17}$ to $5.0 \cdot 10^{16}$ mol/cm^3·s. (1): experiment; (2) initial model [16]; (3) OH* profile modeled with modified rate. 1000 ppmv n-C_9H_{20}; $\phi = 2.0$; 1477 K; 1.5 atm.

Modifications continued using the reduced fuel decomposition rates. Transition state theory calculations of Weissman and Benson [159] for the rate of $C_2H_4 + H \rightarrow H_2 + C_2H_3$ over the temperature range $300 < T$ (K) < 1500 K were chosen to replace the initial rate parameters in the model. Figure 6.19 shows the effect of the (increased) rate of H-abstraction from ethylene (including the previous modification) on the modeled OH* profile compared to the experiment, and a comparison of k(T) for the initial and modified sets of rate parameters. The incipient OH* peak was decreased further, relative to the previous modification, by a factor of nearly 18. Note that Fig. 19 shows the effect of the modification relative to the initial OH* peak calculated using the initial model. The reaction rate for the abstraction reaction increased substantially relative to the initial rate (by a factor of nearly 4 at 1600 K).

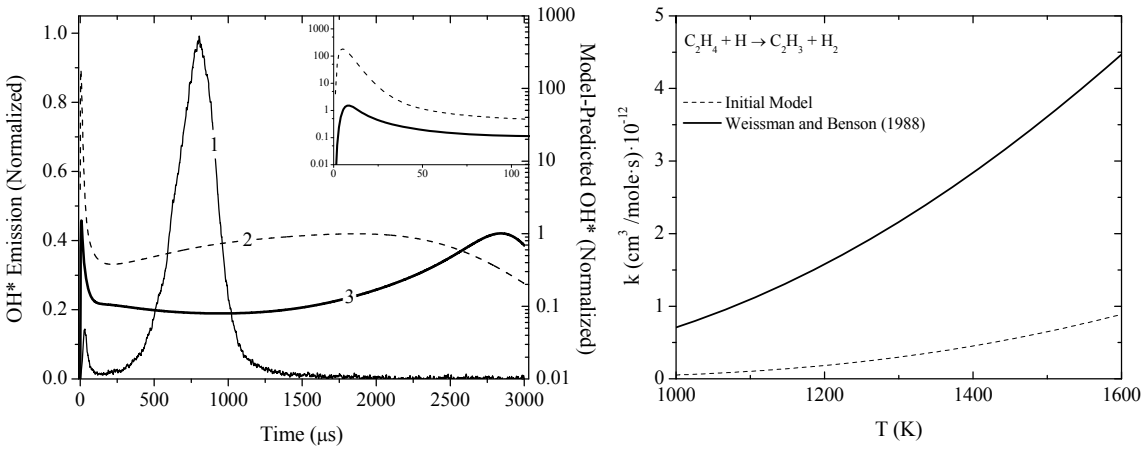

Fig. 6.19. (Left): Effect of increase in rate of H abstraction from ethylene, forming vinyl + H_2 using parameters of Weissman and Benson [159] on OH* profile. (Right): Comparison of rate coefficients from [16] and [159]. (1): experiment; (2) initial model [16]; (3) OH* profile modeled with modified rate. 1000 ppmv n-C_9H_{20}; ϕ = 2.0; 1477 K; 1.5 atm.

The third modification resulted in continued decrease in incipient behavior (by a factor of 5 relative to the previous modifications), OH* profiles more representative of those measured experimentally and, for the first time, definable ignition delay times at ϕ = 2.0. Figure 6.20 shows the effect of the (decreased) rate of addition of $C_2H_3 + CH_3$ (including the previous modifications) on the modeled OH* profile compared to the experiment, and a comparison of k(T) for the initial and modified sets of rate parameters, where the modified rate parameters are those of Dean [160]. Dean employed quantum RRK (QRRK) methods, accounting for pressure and temperature effects, to determine rate coefficient parameters for the radical vinyl + methyl addition reaction over the temperature range 300 < T (K) 2500. The rate coefficient, over the entire range of temperature of interest in the present study, is substantially lower than that of the initial rate from Tsang [163]. The improvement in the OH* profiles, visible in comparing Fig. 6.19 and Fig. 6.20, can be quantified by considering the FWHM. The initial prediction of the model calculated a FWHM of 2 ms. No significant improvement in this value resulted from the first two modifications. The decrease in the rate of propene decomposition into vinyl and methyl led a decrease in the FWHM of the modeled OH* by

over a factor of 5 (370 μs compared to 2 ms.). For the conditions at which the calculations were performed, the experiment is characterized by a FWHM of 315 μs.

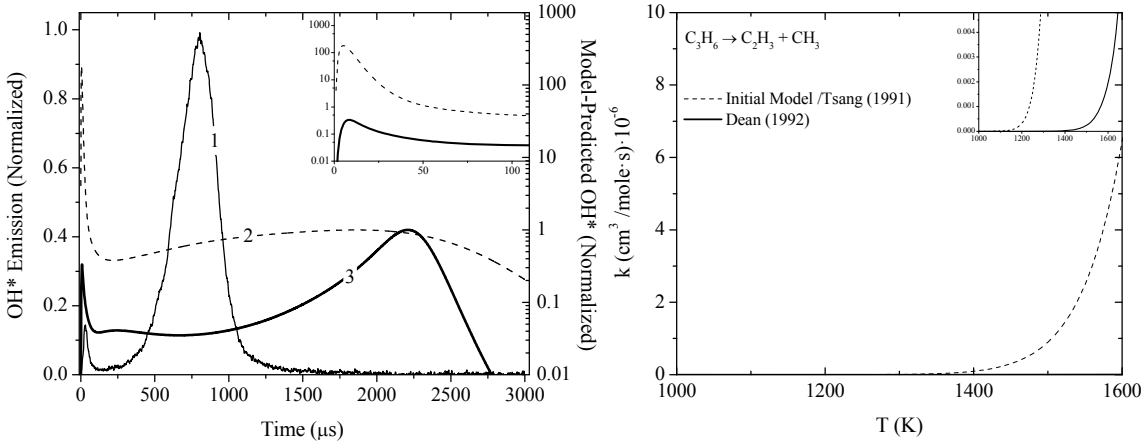

Fig. 6.20. (Left): Effect of decreased rate of $C_3H_6 \rightarrow C_2H_3 + CH_3$ on OH* profile using Dean parameters [160]. (Right): Comparison of rate coefficient from [163] to [160]. (1): experiment; (2) initial model [16]; (3) OH* profile modeled with modified rate. 1000 ppmv n-C_9H_{20}; ϕ = 2.0; 1477 K; 1.5 atm.

The fourth modification to the initial n-nonane model resulted in improved profile shape and ignition delay times in closer agreement with experimental values (Fig. 6.21). The reaction of CH_2 + H forming CH + H_2 appeared as highly sensitive to OH* formation (Fig. 6.15) in the first 10 μs of n-nonane oxidation under fuel-rich, high-temperature conditions. Further, due to the formation of CH, this reaction holds significant importance to OH* formation for all times and conditions. Several studies have focused on this reaction [164 – 167], however rate parameters from these studies did not lead to better agreement with the measured OH* profiles.

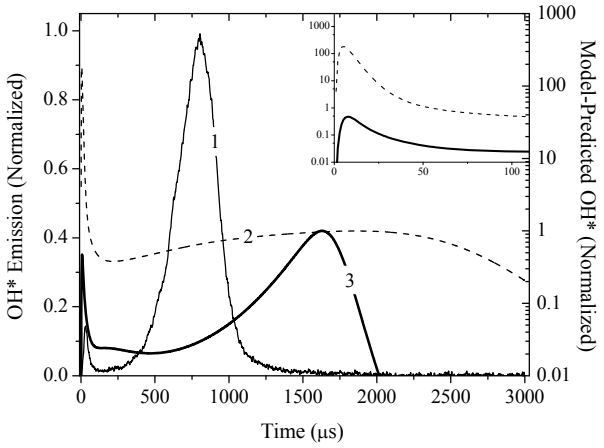

Fig. 6.21. Effect of rate of modified rate for H-abstraction from H_2 by CH. The initial rate, written $CH_2 + H \rightarrow CH + H_2$, did not include either a temperature dependence or an activation energy. The rate obtained from [15] employs a temperature dependence of 1.79 and an activation energy of 1670 cal/mol. (1): experiment; (2) initial model [16]; (3) OH* profile modeled with modified rate. 1000 ppmv n-C_9H_{20}; ϕ = 2.0; 1477 K; 1.5 atm.

A comparison was made to OH* profiles modeled using JetSurF v2.0 [15], which produced an OH* profile more close to the experiment. The JetSurF model employs the reaction written in the reverse direction, with temperature dependence and an activation energy (two parameters which were set to zero in the initial n-nonane model). The reverse reaction and associated parameters from JetSurF v2.0 replaced those of the initial $CH_2 + H$ reaction. Since the two reactions are written in opposing directions, a comparison of rate coefficients is therefore not possible. A FWHM of the modeled OH* of 300 μs resulted from the fourth modification. This is in strong agreement with the experiment, characterized by a FWHM of 315 μs for the conditions at which the calculations were performed.

With the four modifications discussed above, strong agreement in the FWHM between experimental and model-predicted OH* profiles became evident, yet the modeled profiles from the initial model and from the model with the inclusion of the four modifications above did not re-attain a level close to zero-concentration prior to ignition as in the experimental profiles which affects ignition delay times definition.

Modifications were continued to bring the model-predicted ignition delay times in closer agreement with the experimental values. Sensitivity analysis conducted over all conditions (ϕ = 0.5, 1.0, 2.0; 1.5 atm, 10.0 atm) and expanded out beyond the modeled ignition delay times, revealed a plethora of reactions to which OH* formation showed sensitivity. Out of the nearly 160 iterations of model modifications, two reactions led to better ignition delay time predictions across the abovementioned broad range of conditions. The fifth modification made to the initial n-nonane model involved an increase in the rate of H-abstraction from formaldehyde by atomic hydrogen using the rate parameters of Irdam et al. [161]. The effect of the increase on modeled the representative OH* profile and a comparison of the magnitude in the rate change are shown in Fig. 6.22. For this reaction modification, OH* concentration between incipient formation and ignition reached a zero level which improved the agreement relative to the experimental profile.

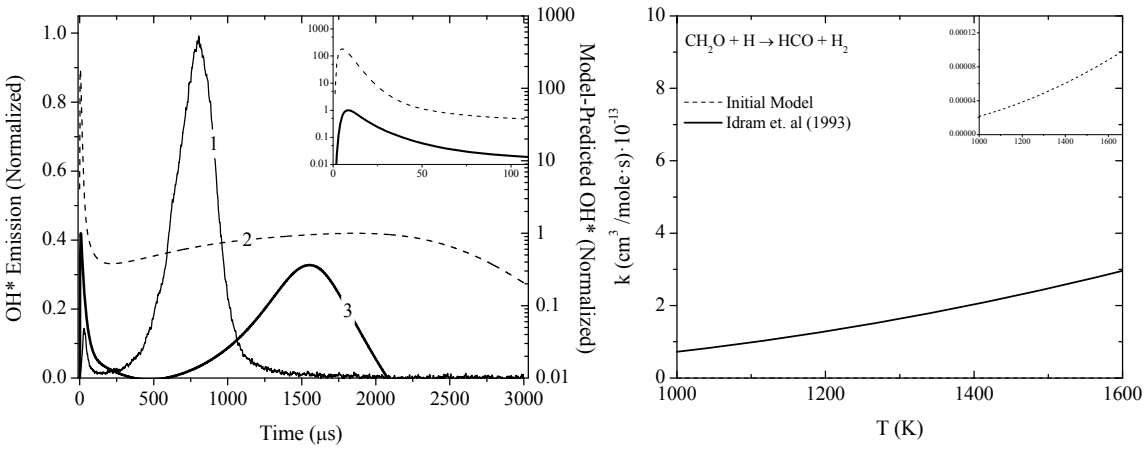

Fig. 6.22. (Left): Effect of increased rate of $CH_2O + H \rightarrow HCO + H_2$ on OH* profiles using Irdam et al. parameters [161]. (Right): Comparison of rate coefficient from [16] to [161]. (1): experiment; (2) initial model [16]; (3) OH* profile modeled with modified rate. 1000 ppmv n-C_9H_{20}; ϕ = 2.0; 1477 K; 1.5 atm.

The sixth modification to the initial mechanism led to improved ignition delay times at the other conditions outside of those of interest in improving OH* time histories. While no significant impact on the time history of OH* at the fuel-rich condition resulted, an increase in the frequency factor of $AC_6H_{13} \rightarrow pC_4H_9 + C_2H_4$ by 10^2 led to improved ignition delay times over the complete range of conditions in the

study. Figure 6.23 shows the (non-impacting) effect of the increased rate on modeled fuel-rich OH* profiles and a comparison of the rate coefficients between the initial and present versions of the model. Outside of the study by Tsang et al. [158], 1-Hexyl decomposition is not well-studied and the change to the frequency factor resulted from parametric alteration. Substantial improvements in the model-predicted OH* were made at the condition of interest (1477 K, 1.5 atm, $\phi = 2.0$) using the six modifications.

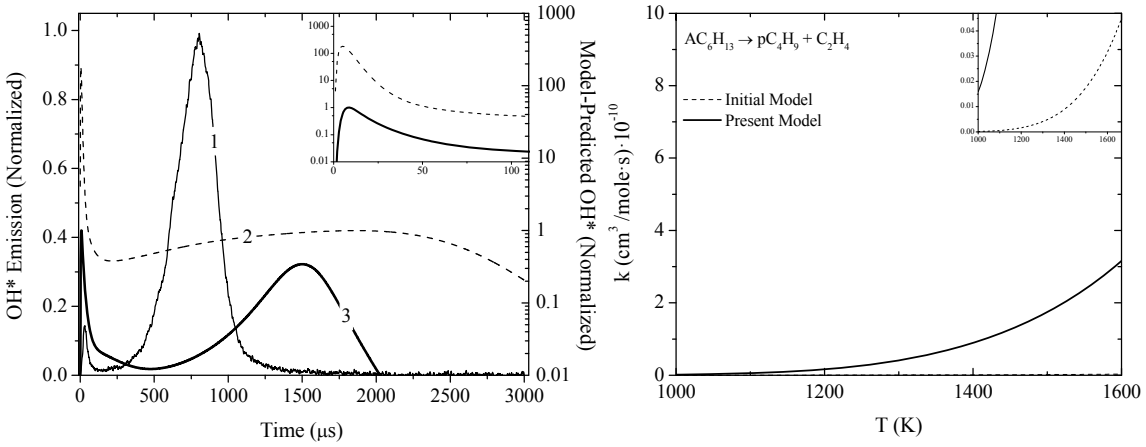

Fig. 6.23. (Left): Effect of increased rate of $AC_6H_{13} \rightarrow pC_4H_9 + C_2H_4$ on OH* profile from 10^2 increase in the frequency factor. (Right): Comparison of rate coefficients. (1): experiment; (2) initial model [16]; (3) OH* profile modeled with modified rate. 1000 ppmv n-C_9H_{20}; $\phi = 2.0$; 1477 K; 1.5 atm.

Figure 6.24 juxtaposes modeled OH* profiles peak-shifted to overlap with the time of the experimental OH* peak. From the shifting, the time dependence predicted by the initial and modified models is contrasted. Strong improvements were made in the prediction of OH* time histories resulting from modifications to ground-state reactions. Table 6.3 summarizes the reactions which were employed in improvement of the predictions of OH* time histories and ignition delay times, including the modified rate parameters and specific impact of the modifications. The effects of the first four reactions (n-nonane homolysis), modified collectively, were shown in Fig. 6.18. For the subsequent reactions, the effects were shown in Figs. 6.19 – 6.23.

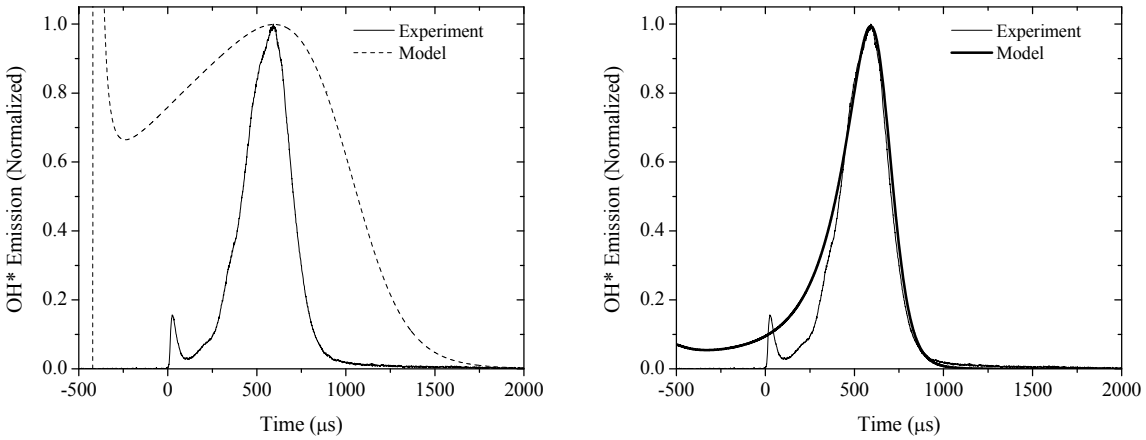

Fig. 6.24. Comparison of experimental model-predicted OH* profiles at ϕ = 2.0, 1477 K, 1.5 atm. (Left) n-Nonane model of [16]. (Right) Base n-nonane model in the present work. 1000 ppmv n-C_9H_{20}; ϕ = 2.0; 1477 K; 1.5 atm.

Table 6.3. Summary of reaction rates changed in the present n-nonane mechanism. Units of $E_a \rightarrow$ cal/mol.

Reaction	A	n	E_a	Impact on OH* Profiles
n-$C_9H_{20} \rightarrow pC_4H_9 + AC_5H_{11}$	$3.0 \cdot 10^{16}$	0	83180.0	
n-$C_9H_{20} \rightarrow C_3H_7 + AC_6H_{13}$	$3.0 \cdot 10^{16}$	0	83400.0	Decreased η by ~ 10^1
n-$C_9H_{20} \rightarrow C_2H_5 + AC_7H_{15}$	$3.0 \cdot 10^{16}$	0	83680.0	
n-$C_9H_{20} \rightarrow CH_3 + AC_8H_{17}$	$3.0 \cdot 10^{16}$	0	85570.0	
$C_2H_4 + H \rightarrow C_2H_3 + H_2$	$1.71 \cdot 10^{13}$	0.70	8003.3	Decreased η further by ~ $2 \cdot 10^1$

(Table 6.3 continued)

Reaction	A	n	E_a	Impact on OH* Profiles
$C_3H_6 \rightarrow C_2H_3 + CH_3$	$7.94 \cdot 10^{16}$	0	99594	(1) Improved OH* profile shape; (2) Decreased η further by 500%; (3) Definable ignition at ϕ = 2.0
$CH + H_2 \rightarrow CH_2 + H$	$1.11 \cdot 10^{8}$	1.79	1670	(1) Improved OH* profile shape; (2) Improved ignition times
$CH_2O + H \rightarrow HCO + H_2$	$2.88 \cdot 10^{12}$	1.9	2740.4	Improved OH* profile shape
$AC_6H_{13} \rightarrow pC_4H_9 + C_2H_4$	$1.02 \cdot 10^{14}$	0.3	27276	Improved ignition times

The incipient-to-ignition OH* peak ratio (η), defined previously as one of the primary points of improvement sought after in the modifications, improved substantially relative to the initial model as a result of the modifications. Figure 6.25 compares the temperature-dependent trend of η among the values obtained from experiments, the initial model [16], and the base n-nonane model in the present study. Noting the break in the vertical axis, a substantial reduction in η is evident. Qualitatively, the temperature trend of η is in agreement with that observed in the OH* profile measurements (i.e. the incipient-to-ignition peak ratio decreases with decreasing temperature). Differences exist between the improved n-nonane model and the experiment, however the primary interest in performing the modifications was to reach agreeable temperature trends. Accurate quantification of incipient OH* is not of specific interest

since it holds no practical significance. In contrast, accuracy in modeling of the temperature dependence and magnitude of η is vital due to the interference with ignition delay time definition.

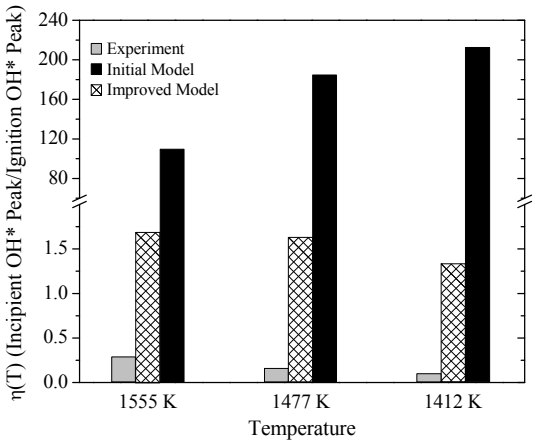

Fig. 6.25. Measured and modeled η(T) trends for 1000 ppmv n-C_9H_{20}. ϕ = 2.0, 1.5 atm. Calculations were performed using the initial n-nonane model of Rotavera et al. [16] and the base n-nonane mechanism of the present work [48]. Improvements in ground-state chemical reactions significantly improved the ability of the model to capture unimolecular fuel decomposition and subsequent oxidation reactions leading to OH* formation near time-zero.

The abovementioned improvements to the initial n-nonane mechanism [16] also made use of two other modifications. Increases in the rates of $CH_4 \rightarrow CH_3 + H$ using the RRKM calculation of Golden et al. [168] and $H_2 + O \rightarrow OH + H$ from [164] were returned to the initial values. Removal of these modifications did not alter OH* profiles and resulted in improvements outside of the fuel-rich condition. To illustrate the improvement in OH* profile predictions at conditions other than ϕ = 2.0, Figure 6.26 compares model-based predictions of experimental OH* profile ϕ = 1.0, 1487 K, 1.5 atm using the initial model and the improved model. The incipient OH* is in close agreement with the measurement. Ignition delay time predictions using the improved n-nonane model (i.e. the base model in the present study) are shown in Fig. 6.27 for ϕ = 1.0 in 4% oxygen, where measurements were made in the present work to compare with the results in the study by Davidson et al. [49] on n-alkane ignition delay times.

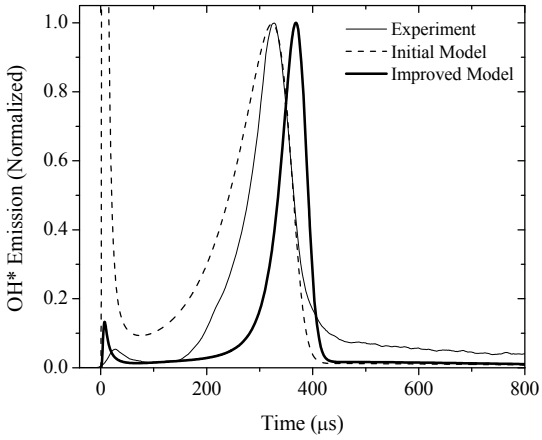

Fig. 6.26. Model predictions of OH* time history using the initial n-nonane model [16] and the improved n-nonane model [48]. The latter model serves as the base chemical kinetics mechanism for the compiled model in the present study. Improvements in ground-state chemistry led to proper determination of time-dependent profiles of OH*. 1000 ppmv n-C_9H_{20}; ϕ = 1.0; 1487 K; 1.5 atm.

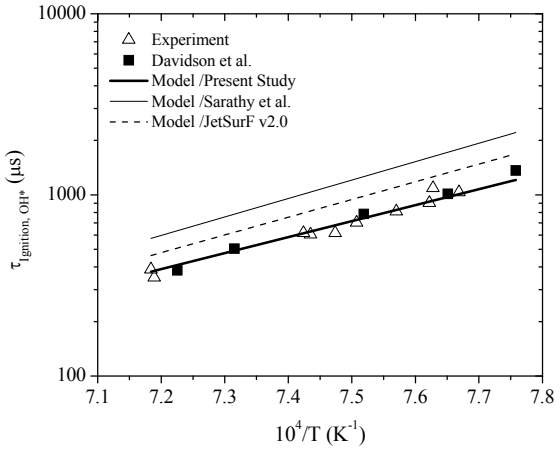

Fig. 6.27. Comparison of ignition delay times of n-nonane in 4% oxygen at 1.5 atm. Measurements: (1) Present Study; (2) Davidson et al. [49]. Models: (1) Present Study; (2) Sarathy et al. [14]; (3) JetSurF v2.0 [15].

6.2 n-Nonane ignition delay times in 99% Ar

Discussed in the sections below are ignition delay times of n-nonane in Ar using a dilution level of 99%.

Comparisons of correlated ignition trends are drawn against model predictions using the base n-nonane

chemical kinetics mechanism [48] and the compiled chemical kinetics mechanism in the present work. OH* profiles are not shown for comparison since correlated ignition times were used in the present study. No measurements of OH* profiles or ignition delay times of n-nonane were taken using 99% Ar. The ignition delay times presented are calculated from the ignition correlation (Eqn. 6.1) of Rotavera et al. [16], wherein the ignition delay time expression correlates 160 measurements of 1000 ppmv n-nonane:

$$\tau(\mu s) = 2.71 \cdot 10^{-8}[n\text{-}C_9H_{20}]^{0.73}[O_2]^{-1.21}exp(51.0/R_uT) \qquad (6.1)$$

For lean ($\phi = 0.5$), stoichiometric, and rich ($\phi = 2.0$) conditions, using 1000 ppmv n-nonane, dilution levels of Ar were 97.1%, 98.5%, and 99.2%, respectively. Since 99% Ar (and the fuel/oxygen concentrations used herein to calculate ignition times) is covered in the range of the correlation, the correlated ignition delay times are nearly identical to measurements at the 99% level of dilution. Figure 6.28 compares calculated relative to measured ignition delay times at the same condition (ϕ, temperature, pressure). Strong agreement is shown from the fitting parameter ($R^2 = 0.95$). Uncertainty bands of ±10% (Section 3) are placed on the calculated times.

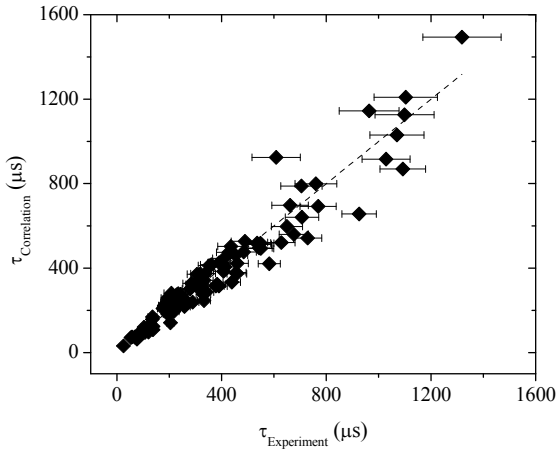

Fig. 6.28. Comparison of measured and correlated ignition delay times (Eqn. 6.1) of n-nonane [16]. Error bars reflect uncertainty of ±10%. $R^2 = 0.95$.

6.2.1 Fuel-lean condition

Fuel-lean (ϕ = 0.5) ignition delay times correlated to 99% Ar at 1.5 and 10.0 atm are shown in Fig. 6.29. The correlated ignition times are compared to the base n-nonane model and the compiled model in the present work which both show strong agreement with the empirical trends. Complete overlap in model predictions is shown at 1.5 atm, over the entire temperature range covered. At 10.0 atm the two modeling trends diverge from one another outside of the ±10% uncertainty bands of the experiment at temperatures higher than 1300 K; a difference in the compiled model prediction, relative to the base n-nonane model, of 25% is present at the high temperature extreme (1440 K). Considering the overlap of trends at 1.5 atm and only a slight amount of deviation relative to the empirical trend at 10.0 atm (~ 15% at 1440 K), the compiled model performs well for lean n-nonane ignition.

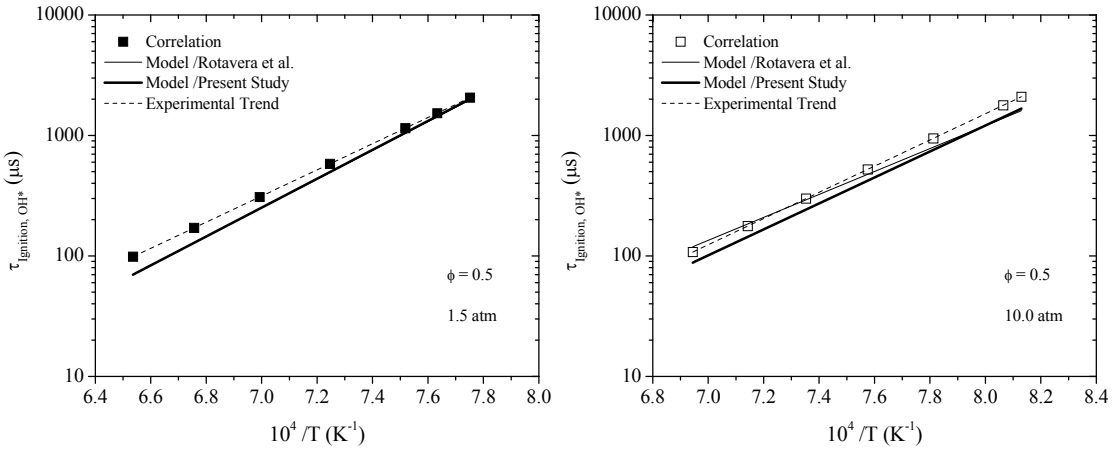

Fig. 6.29. Correlated and model-predicted ignition delay times of n-nonane (ϕ = 0.5) in 99% Ar at 1.5 atm (Left) and 10.0 atm (Right). Calculations were performed using Rotavera et al. [48] and the present chemical kinetics model. $3.4 \cdot 10^{-4}$n-C_9H_{20} + $9.66 \cdot 10^{-3}O_2$ + 0.99Ar.

6.2.2 Stoichiometric condition

Correlated ignition times for stoichiometric n-nonane in 99% Ar at 1.5 and 10.0 atm are shown in Fig. 6.30 compared against model predictions. Identical to the lean behavior at 1.5 atm, complete overlap is shown between the base n-nonane model and the compiled mechanism in the present study. Similar

behavior is exhibited at 10.0 atm. Peak deviation for ignition at 1.5 atm of the model relative to the empirical trend of 35% is shown by the model at the high-temperature extreme (1600 K). Agreement is closer at the low-temperature extreme of 1340 K (< 10%). At 10.0 atm, ~ 30% and ~ 20% are the differences at 1520 K and 1280 K, respectively.

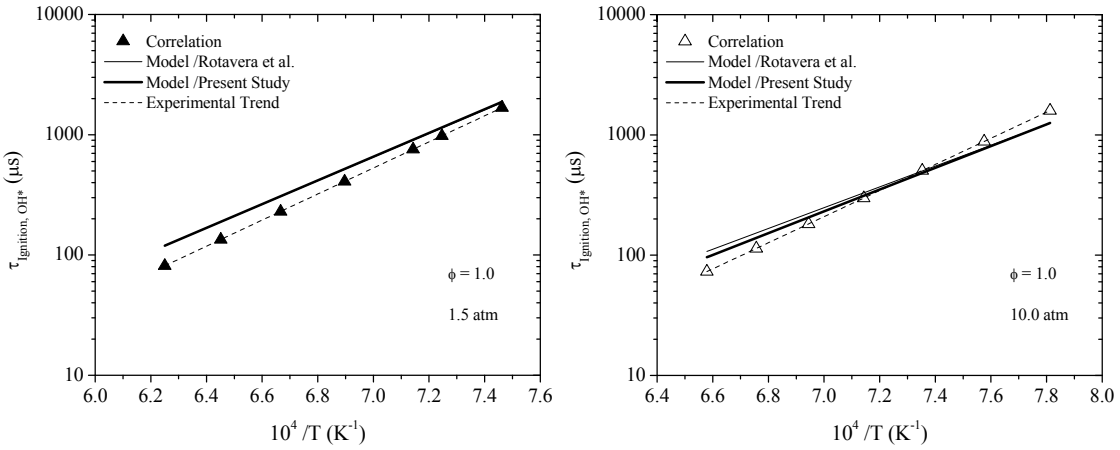

Fig. 6.30. Correlated and model-predicted ignition delay times of n-nonane (ϕ = 1.0) in 99% Ar at 1.5 atm (Left) and 10.0 atm (Right). Calculations were performed using Rotavera et al. [48] and the present chemical kinetics model. $6.7 \cdot 10^{-4}$n-C_9H_{20} + $9.33 \cdot 10^{-3}O_2$ + 0.99Ar.

6.2.3 Fuel-rich condition

Definable fuel-rich ignition delay times were obtainable using the base n-nonane mechanism as a result of the improvements described in Section 6.1, however the predictions differ from the experimental (and correlated) ignition delay times by a factor of approximately 3. Figure 6.31 shows comparisons of correlated fuel-rich n-nonane ignition delay times in 99% Ar against the base n-nonane mechanism and the compiled mechanism in the present work. Identical to the 1.5-atm behavior at lean and stoichiometric conditions, the ignition trends of both models overlap one another. Ignition delay times using the base n-nonane model were definable, yet in stark contrast to the empirical trend. Using the compiled chemical kinetics mechanism, ignition delay times are not definable due to the incipient OH* being predicted on longer timescales than those observed in the experiment or calculated using the base n-nonane model.

Resulting from the integration of the sub-mechanisms for methyl octanoate and methylcyclohexane, the higher-pressure OH* profiles predicted using the compiled mechanism became unusable, exhibiting similar behavior to that discussed in Section 6.1, yet with the larger issue of profile distortion as compared to the previous issue which centered around a severe overprediction of incipient OH*. Overprediction of OH* within the first 50 μs returned as an issue when the three mechanisms were compiled. The problem becomes more exaggerated with decreased temperature. Figure 6.32 compares calculations of OH* profiles from $\phi = 2.0$ n-nonane/O_2 at 1305 K, 10.0 atm performed using the base n-nonane model [48] and the compiled chemical kinetics model in the present work.

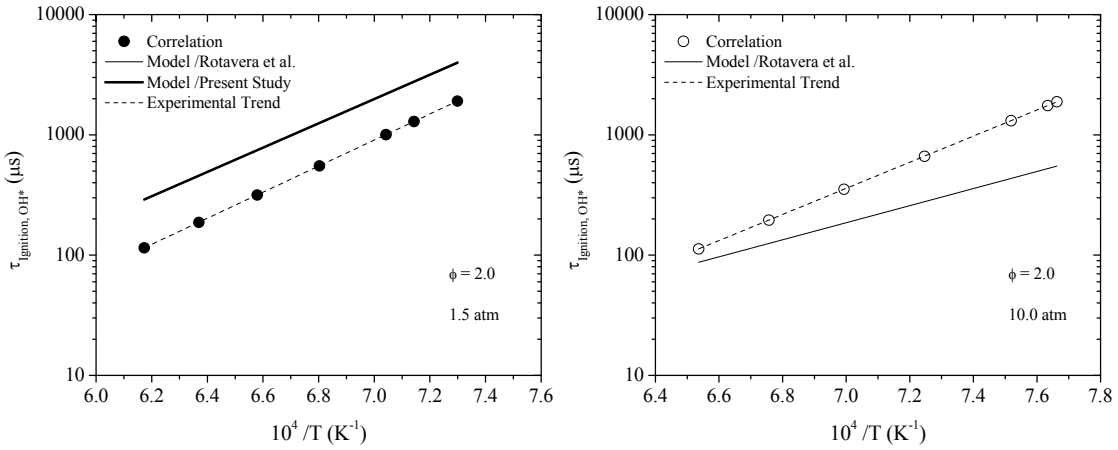

Fig. 6.31. Correlated and model-predicted ignition delay times of n-nonane ($\phi = 2.0$) in 99% Ar at 1.5 atm (Left) and 10.0 atm (Right). Calculations were performed using Rotavera et al. [48] and the present chemical kinetics model. Ignition delay times are indefinable using the model compiled in the present study due to unclear ignition peaks similar to the behavior exhibited in Fig. 6.2.1.25·10^{-3}n-C_9H_{20} + 8.75·$10^{-3}O_2$ + 0.99Ar.

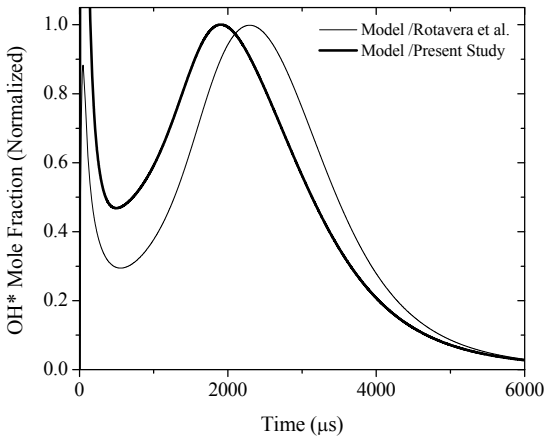

Fig. 6.32. Comparison of model-predicted OH* profiles during oxidation of n-nonane (ϕ = 2.0) in 99% Ar at 1305 K and 10.0 atm. Calculations were performed using Rotavera et al. [48] and the present chemical kinetics model. Extrapolation of a line along the steepest ascent in OH* in the profile calculated using the present model yields negative ignition delay time. $1.25 \cdot 10^{-3}$n-C_9H_{20} + $8.75 \cdot 10^{-3}O_2$ + 0.99Ar.

6.3 Behavior of CH time histories*

Measurements of the excited-state CH radical transition $A^2\Delta \rightarrow X^2\Pi$ were obtained during the OH* measurements in Rotavera et al. [16] to compare the incipient reactivity behavior of n-nonane. Figure 6.33 compares OH* and CH* profiles obtained at 1598 K and 1.5 atm under fuel-rich (ϕ = 2.0) conditions. Despite the favorable conditions for incipient oxidation shown in OH* profiles, no formation of CH* prior to the ignition delay time occurred in the experiments. Further, the incipient oxidation peaks observed in the OH* profiles were not observed under any conditions in the present work in CH* measurements which spanned the same set of equivalence ratio, dilution level, temperature, and pressure as the OH* measurements.

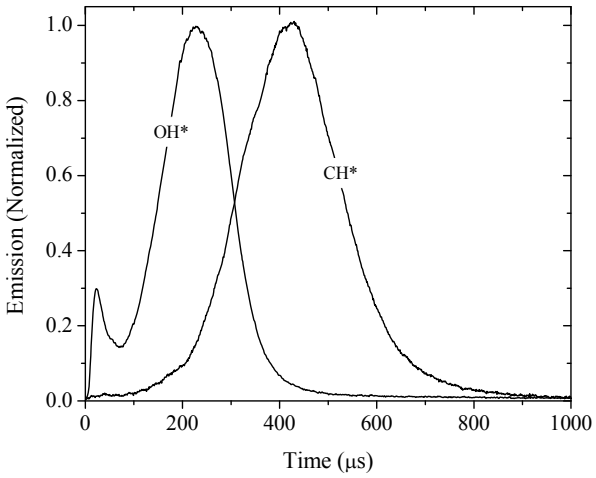

Fig. 6.33. Comparison of OH* and CH* time histories at ϕ = 2.0, 1598 K, 1.5 atm. Incipient oxidation chemistry leading to OH* formation near time-zero is not observed to yield CH*. 4.8-kΩ PMT resistance.

Rate of production/consumption calculations were performed on CH* using the compiled chemical kinetics mechanism in the present work to explain the absence of observation of the species within the first 40 μs of fuel decomposition and subsequent oxidation. Figure 6.34 shows the primary reactions and respective concentration rates responsible for CH* and the net production rate for the species from 0 – 40 μs. Two points are immediately apparent in the results. First, comparing Fig. 6.34 with Fig. 6.14, the absolute quantities (prior to ignition) are substantially smaller than those for OH* by 10^6. Second, CH* formed principally from the reaction of dicarbon with OH, is consumed at the same rate an nearly the same magnitude primarily by collisional de-excitation. The net quantify of CH* produced from integration of the rate profiles is approximately zero ($18 \cdot 10^{-12}$ moles). The calculations show that collision of CH* and subsequent formation of ground-state CH occurs most strongly with Ar atoms. Collision with M, O_2, and spontaneous relaxation (release of hν) contribute in smaller amounts.

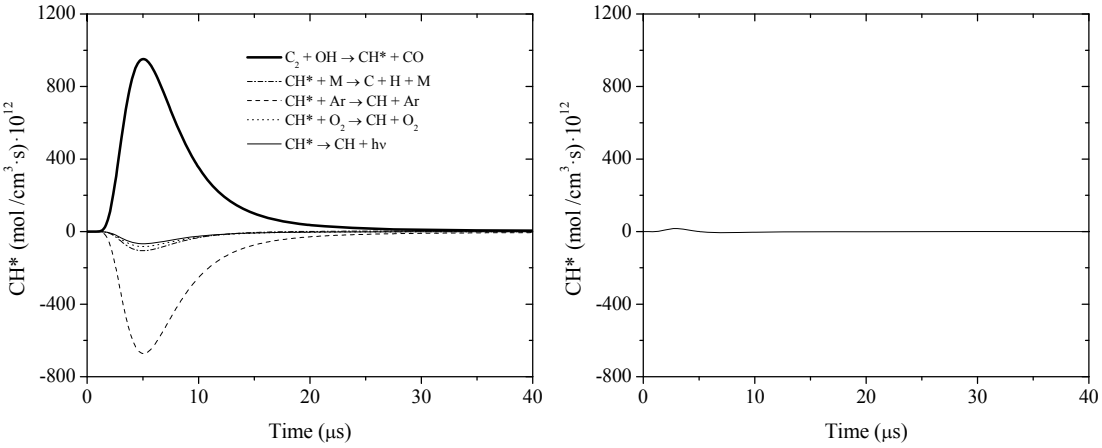

Fig. 6.34. (Left) Rate of CH* production/consumption calculations and corresponding dominant reactions using [16]. (Right) Net rate of CH* production. Production approximately equals consumption of CH*. 1000 ppmv n-C_9H_{20}; ϕ = 2.0; 1525 K; 1.5 atm.

When comparing ignition delay times of n-nonane under dilute conditions defined by OH* and separately by CH*, experiments indicated that ignition delay times determined using measurements of CH* overlap with those measured using OH* under all conditions except the ϕ = 2.0, 1.5-atm condition (Fig. 6.35). For the fuel-rich equivalence ratio tests, 3 different mixtures (of the same molar composition: 1000 ppmv n-C_9H_{20}, 99.2% Ar) were tested and all produced ignition delay times along the trend shown in Fig. 6.35 for CH*. Ignition delay times measured using CH* were approximately 50% longer than those measured from OH* profiles.

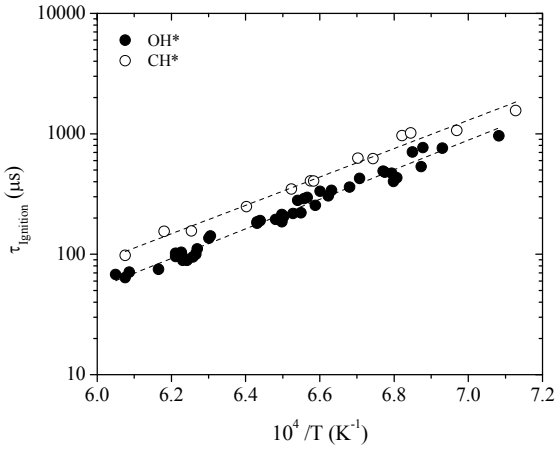

Fig. 6.35. Ignition delay times of ϕ = 2.0 n-nonane/O_2 in 99.2% Ar measured using OH* and CH*. Ignition based on CH* shows identical activation energy (temperature dependence), yet are approximately 50% longer than the OH* trend.

6.4 Concluding remarks on oxidation experiments and modeling of n-C_9H_{20}

Incipient oxidation leading to OH* formation coincident with parent fuel decomposition was improperly modeled using the initial n-nonane model [16] in terms of magnitude (disallowing definition of ignition delay time) and temperature dependence (incipient OH* formation increased with decreasing temperature). It was shown that order-of-magnitude variations in chemiluminescence rates did not impact chemiluminescence time histories (i.e. profile shape). Sensitivity analysis was then performed and revealed reactions important to OH* formation, the majority of which involved ground-state species (all except the two dominant OH* production channels). The mechanism of formation of incipient OH* was investigated and found to center around the formation of methyl radicals. Once CH_3 radicals are produced a series of H-abstraction reactions ensue leading to the formation of CH radicals. The CH radicals react with molecular oxygen (which is in high abundance at incipient timescales) to form OH* directly. The process slows after approximately 5 – 10 μs depending on the temperature due to radical-radical addition reaction of methyl forming ethyl + H.

CH* measurements were also obtained during oxidation experiments of n-nonane. While OH* appreciably formed immediately upon formation of reflected-shock conditions, no experimental observation of CH* formation, under any condition, was noted. This observation is supported by model calculations of CH* rates of production/consumption. Calculations were performed using the compiled chemical kinetics mechanism of the present work and show, at incipient timescales on which OH* forms, CH* (formed from C_2 + OH) is produced at the nearly the same rate it is consumed (primarily by collision with Ar) resulting in a net production of 10^{-12} moles within the first 40 μs.

Improvements in the high-temperature predictive capabilities of the n-nonane mechanism of Rotavera et al. [16] using OH* profiles as a metric for validation. The improved version of the n-nonane model serves as a base model in the present work within which sub-mechanisms for methyl octanoate and methylcyclohexane are integrated. The compiled model reproduces identical n-nonane ignition delay times compared to the base n-nonane model for all conditions except ϕ = 2.0, 10.0 atm. OH* profiles modeled under the latter condition were distorted to a degree such that ignition delay times were for any temperature covered herein. While improvements are needed at these conditions, the integration of the sub-mechanisms did not impact results at other conditions.

7. MEASUREMENTS AND MODELING OF OH* TIME HISTORIES AND IGNITION DELAY TIMES OF METHYLCYCLOHEXANE

Emission spectroscopy measurements of the $A^2\Sigma^+ \rightarrow X^2\Pi$ transition of OH were obtained during oxidation of methylcyclohexane (MCH) behind reflected shock waves. Ignition delay times were extracted from OH* profiles using the method described in Section 3.2.4 over a broad range of thermodynamic conditions (Table 7.1). Provided in the sections below are species time history and ignition delay time results for methylcyclohexane oxidation under fuel lean (Section 7.1), stoichiometric (Section 7.2), and fuel-rich (Section 7.3) equivalence ratios under highly dilute conditions (99% Ar). Ignition delay times for MCH are provided in Appendix F. Species profiles and ignition delay times were calculated using the model compiled in the present study and with the parent model from which the methylcyclohexane sub-mechanism came are compared to the measurements. Integration of the MCH sub-mechanism from [25] resulted in improvements in ignition delay time predictions of MCH under several conditions of equivalence ratio and pressure, yet also caused fuel-rich high-pressure OH* profiles to become distorted relative to those predicted from [25]. Ignition time predictions at ϕ = 1.0, 11.5 atm were also adversely impacted. In general, the relative difference in the modeling results indicates that the integration of the MCH sub-mechanism into the blended mechanism has a neutral effect on the reproducibility of pure-fuel ignition results for methylcyclohexane. Experimental dependencies of MCH ignition on equivalence ratio and pressure, $\tau_{Ignition,\ OH*}$(Constant P, ϕ) and $\tau_{Ignition,\ OH*}$(P, Constant ϕ), are compared in Section 7.4. In total, 65 shock-tube measurements of MCH oxidation were obtained and an empirical ignition delay time equation was developed (Section 7.5) by correlating the data as a function of concentration (in units of mol /cm^3) and temperature using linear regression as discussed in Section 3.2.5.

Table 7.1. Experimental ranges for fuel and oxygen volume percentages and reflected shock wave conditions.

%MCH	$\%O_2$	%Ar	P (atm)	T (K)	ϕ
0.045 – 0.380	0.84 – 4.0	95.6 – 99.6	1.4 – 12.2	1291 – 1672	0.5 – 2.0

Prior to measurements taken to serve as comparative baselines to the blended fuels studied herein, ignition delay time experiments were executed at the same conditions as literature values, namely the recent measurements of Hong et al. [54]. The experiments were performed using a fixed 4% (vol.) oxygen concentration, resulting in a lower dilution (95.6% Ar) than measurements of interest to the current study. The test pressure remained fixed at 1.5 atm (nominal), and temperatures spanned the range $1302 < T\,(K) < 1505$. Figure 7.1 compares the ignition delay time measurements taken using the methodology and facilities described herein to those obtained from Hong et al. compared to model-based predictions using the base MCH mechanism of Pitz et al. [25]. Strong overlap is shown between the two ignition trends. Ignition activation energy of 45.1 kcal/mol for the trend measured herein resulted from linear regression of the temperature dependence. Strong agreement is also present between both experimental datasets and model predictions.

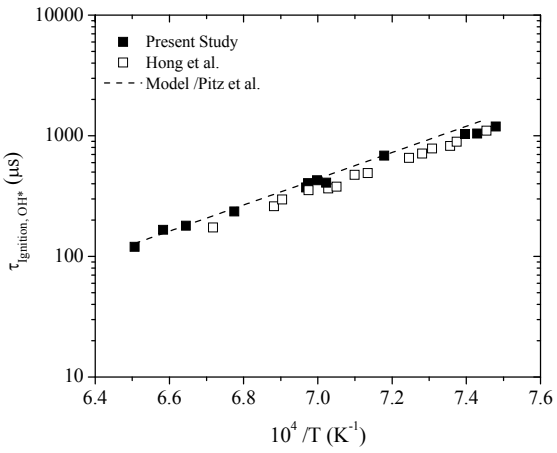

Fig. 7.1. Measured and model-predicted stoichiometric ignition delay times of MCH in 4% O_2 (95.6% Ar) at 1.5 atm compared to Hong et al. [54] and model calculations using Pitz et al. [25]. $3.8 \cdot 10^{-3}$MCH + $4.0 \cdot 10^{-2}O_2$ + 0.956Ar.

7.1 Fuel-lean condition

The fuel mole fraction of methylcyclohexane for lean measurements was maintained at $4.5 \cdot 10^{-4}$, and measurements were taken under near-atmospheric pressure (1.5 atm) spanning a temperature range of 221

K (1314 K – 1535 K). Figure 7.2 shows a comparison of a measured OH* profile to model calculations. Under fuel-lean conditions, incipient formation of OH* is evident near time-zero, and this behavior is captured by both the present model and that of Pitz et al. [25]. The incipient oxidation is attributed to rapid fuel decomposition and subsequent formation of CH which then supplies the dominant OH* formation channel: $CH + O_2 \rightarrow OH^* + CO$. Discussed in Section 6 were detailed mechanisms of incipient OH* formation at high temperatures. At 1.5 atm pressure, the time-dependence of OH* is well-predicted by the compiled model at temperatures higher than ca. 1450 K. For the compiled model, the FWHM is calculated within 10 μs of the experiment (80 μs) at the high temperature extreme. The difference in FWHM between measured and model-predicted values became larger with decreasing temperatures; experimental profiles increased in FWHM from 1314 K – 1535 K from 80 μs to 390 μs, respectively, while model predictions show 90 μs – 220 μs over this temperature range, displaying a consistency to that shown in the experiment, with profiles becoming increasingly wider with decreasing temperature (i.e. longer FWHM).

Fuel-lean ignition delay times (Fig. 7.2) are not shown with the error bars of ±10% as in Fig. 5.1 since the uncertainty, discussed in Section 3.2.6, is the same for all ignition delay time measurements. The experimental results of ignition are predicted well by the Pitz et al. model at lower temperatures, yet are overpredicted at higher temperatures. Above 1475 K, the compiled model of the present study accurately predict ignition delay times within the uncertainty of the experiment. Ignition delay times at the low-temperature extreme (1314 K) predicted using the compiled model differ from the experimental trend by 30%. The ignition activation energy of the experimental trend is calculated to be 57.9 kcal/mol, while model predictions are 69.4 kcal/mol and 51.4 kcal/mol for [25] and the present compiled model, differing by 20% and 10%, respectively.

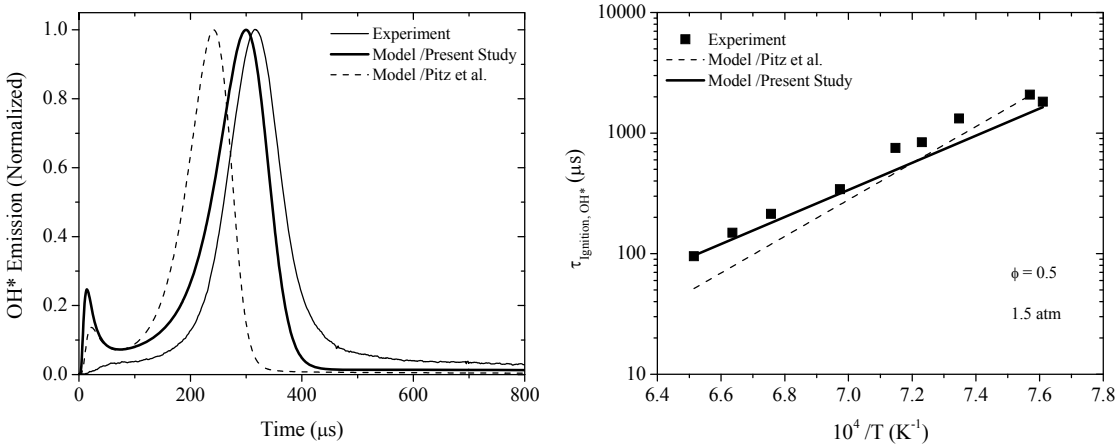

Fig. 7.2. (Left): Measured and model-predicted OH* time history during oxidation of 450 ppmv MCH (ϕ = 0.5) in 99% Ar. 1.5 atm, 1480 K, $\tau_{Ignition,\ OH^*}$: 214 μs (Experiment). 4.8-kΩ PMT resistance. (Right): Measured and model-predicted ignition delay times of MCH (ϕ = 0.5) in 99% Ar at 1.5 atm. Calculations were performed using Pitz et al. [25] and the present chemical kinetics model. $4.5 \cdot 10^{-4}$MCH + $9.55 \cdot 10^{-3}O_2$ + 0.99Ar.

Measurements taken under at nominal elevated pressure of 11.6 atm spanned a temperature range of 201 K (1291 K – 1492 K). Figure 7.3 shows a comparison of a measured OH* profile to model calculations. The FWHM of the modeled OH* profile in Fig. 7.3 (30 μs) is lower than that indicated in the measurement (115 μs). Differences in FWHM between modeled and experimental OH* time histories increase with decreasing temperature. The temperature dependence of the model-predicted trend in FWHM is in agreement with that of the experiment, however differences at the high- and low-temperature extremes of 55 μs and 270 μs exist, with FWHM of modeled profiles under-predicting the measurements. Increased pressure suppressed incipient formation of OH* under the fuel-lean condition experimentally and in the model predictions.

Fuel-lean ignition delay times at 11.6 atm are underpredicted by the compiled model over the entire range of temperatures by approximately 40%, yet the ignition activation energy is captured within ~ 5% relative to the experiment (56.6 kcal/mol compared to 54.1 kcal/mol). The Pitz et al. mechanism [25] accurately

predicts the ignition delay times towards the high-temperature extreme, yet due to an underpredicted activation energy of the experimental trend by ~ 15% (47.1 kcal/mol compared to 54.1 kcal/mol) tends to deviate towards shorter times towards lower temperatures. A peak deviation of 40% is present at 1291 K, the same error as that shown from calculations using the compiled model. The temperature at which deviation beyond the experimental uncertainty begins using the Pitz et al. model is 1440 K.

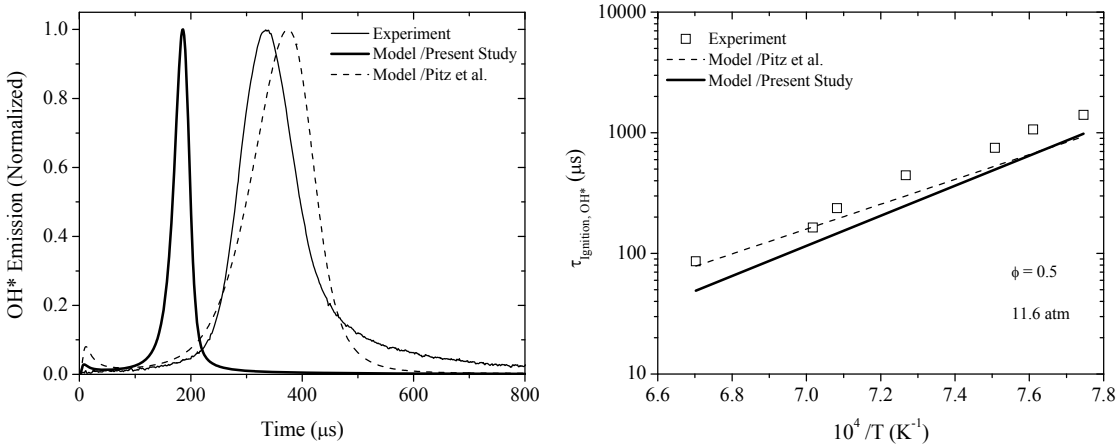

Fig. 7.3. (Left): Measured and model-predicted OH* time history during oxidation of 450 ppmv MCH (ϕ = 0.5) in 99% Ar. 11.5 atm, 1412 K, $\tau_{Ignition,\ OH^*}$: 237 μs (Experiment). 4.8-kΩ PMT resistance. (Right): Measured and model-predicted ignition delay times of MCH (ϕ = 0.5) in 99% Ar at 11.6 atm. Calculations were performed using Pitz et al. [25] and the present chemical kinetics model. $4.5 \cdot 10^{-4}$MCH + $9.55 \cdot 10^{-3}O_2$ + 0.99Ar.

7.2 Stoichiometric condition

The fuel mole fraction of methylcyclohexane in stoichiometric experiments was maintained at $8.70 \cdot 10^{-4}$ and measurements were obtained under near-atmospheric pressure (1.5 atm) over a temperature range of 178 K (1387 K – 1535 K). Figure 7.4 shows a comparison of a measured OH* profile to model calculations. The time dependence of OH* is captured with similar accuracy by the Pitz et al. model. Comparing FWHM between OH* measurements and model predictions, overlap is shown at the high-temperature extreme (1535 K) below which the deviations became stronger, with model predictions showing a difference in FWHM of 275 μs at the low-temperature extreme (1387 K). Measured FWHM at

these temperatures are 90 μs and 420 μs, respectively, with the broader FWHM corresponding to the lower temperature.

Ignition activation energy, relative to the measured value, is predicted with similar deviations between the Pitz et al. model and the compiled model, yet differ with respect to over- and under-prediction. The experimental results yield an ignition activation energy of 56.2 kcal/mol, while the Pitz et al. model and present model predict 64.2 kcal/mol and 47.6 kcal/mol, respectively, corresponding to nearly equal percentage error of 15%. The two models have the highest errors in opposing temperature regions. The Pitz et al. model predicts ignition delay times within 10% below 1450 K. Deviations are stronger at the temperature extrema from calculations using the compiled model in the present work. Predictions of ignition delay times, within the experimental uncertainty, are accurate only over a narrow temperature range (1415 K – 1500 K). At the low- and high-temperature extremes, differences of 25% and 30% are observed.

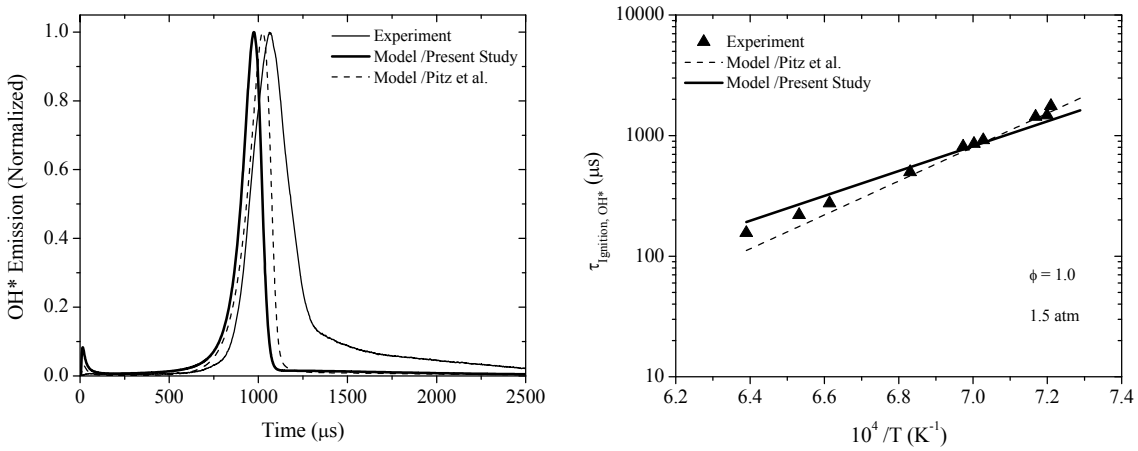

Fig. 7.4. (Left): Measured and model-predicted OH* time history during oxidation of 870 ppmv MCH (ϕ = 1.0) in 99% Ar. 1.5 atm, 1428 K, $\tau_{Ignition,\ OH^*}$: 856 μs (Experiment). 4.8-kΩ PMT resistance. (Right): Measured and model-predicted ignition delay times of MCH (ϕ = 1.0) in 99% Ar at 1.5 atm. Calculations were performed using Pitz et al. [25] and the present chemical kinetics model. $8.7 \cdot 10^{-4}$MCH + $9.13 \cdot 10^{-3}O_2$ + 0.99Ar.

Measurements were obtained at an elevated nominal pressure of 11.3 atm over a temperature range of 178 K (1316 K – 1494 K). Figure 7.5 shows a comparison of a measured OH* profile to model calculations. Resulting from integration of the methylcyclohexane model into the compiled mechanism of the present work, the FWHM of model-predicted OH* profiles became slightly shorter relative to those calculated using the Pitz et al. model. Over the range of temperatures covered, FWHM values predicted using the compiled model are significantly shorter than measured values. Relative to the experimental value of 85 μs at 1494 K, model calculations predict a FWHM of 20 μs. With decreasing temperature, this difference increases. At 1316 K, the model differs from the experimental value of 280 μs by 240 μs. The temperature dependence of the model predictions of ignition delay time trends are in close agreement relative to the experimental trend of 51.1 kcal/mol. The Pitz et al. model predicts an activation energy of 55.2 kcal/mol, a difference of ~ 10%, while the compiled mechanism predicts an activation energy of 49.4 kcal/mol, differing by less than 5%. Ignition delay times using the Pitz et al. model are predicted well relative to the measurements, reaching a maximum deviation at the low-temperature extreme (1316 K) of 20%. Ignition delay times using the compiled model are underpredicted by approximately 30% over the range of temperatures covered due to the similar activation energy values.

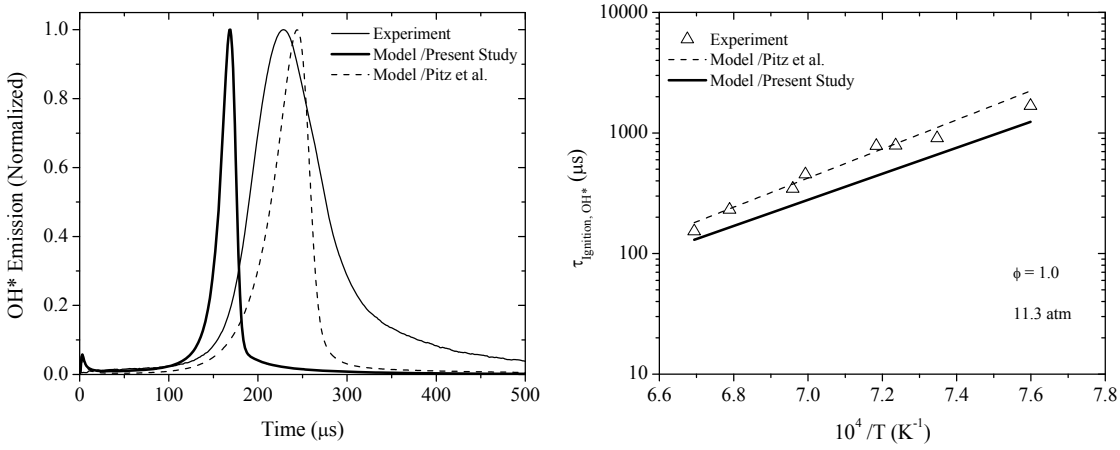

Fig. 7.5. (Left): Measured and model-predicted OH* time history during oxidation of 870 ppmv MCH (ϕ = 1.0) in 99% Ar. 11.0 atm, 1494 K, $\tau_{Ignition,\ OH^*}$: 153 μs (Experiment). 4.8-kΩ PMT resistance. (Right): Measured and model-predicted ignition delay times of MCH (ϕ = 1.0) in 99% Ar at 11.3 atm. Calculations were performed using Pitz et al. [25] and the present chemical kinetics model. $8.7 \cdot 10^{-4}$MCH + $9.13 \cdot 10^{-3}O_2$ + 0.99Ar.

7.3 Fuel-rich condition

The fuel mole fraction of methylcyclohexane for fuel-rich measurements was maintained at $16.0 \cdot 10^{-4}$ and measurements were taken under near-atmospheric pressure (1.5 atm) spanning a temperature range of 241 K (1431 K – 1672 K). Figure 7.6 shows a comparison of a measured OH* profile to model calculations. Both models largely overpredict the incipient OH* formation observed near time-zero in the experiment. The causes for OH* formation immediately upon formation of the reflected-shock conditions are discussed in detail in Section 6. Integration of the Pitz et al. sub-mechanism as part of the model in the present study did not alter calculation of FWHM values. The model-predicted FWHM for both the Pitz et al. model and compiled model were in close agreement with experimental values over the range of temperature covered. At the high-temperature extreme (1672 K), the experimental value (150 μs) is calculated to be only 25 μs longer using the compiled model. At the lower temperature extreme (1431 K), a difference of 125 μs is shown (545 μs experimentally, 670 μs computationally).

The experimental ignition activation energy of 56.1 kcal/mol measured at ϕ = 2.0, 1.5 atm is underpredicted using the base methylcyclohexane model of Pitz et al. by approximately 15% (65.6 kcal/mol). The compiled model calculates an ignition activation energy of 56.9 kcal/mol, in close agreement with the experimental value to within 2%. The compiled mechanism predicts a more accurate ignition activation energy relative to the trend predicted using the Pitz et al. model. The latter model predicts ignition delay times accurately at the low-temperature extreme, yet underpredicts the experimental trend by a factor of 2 at the high-temperature extreme. The ignition trend predicted by the compiled model differs from the experimental trend by 35% over the range of temperature covered.

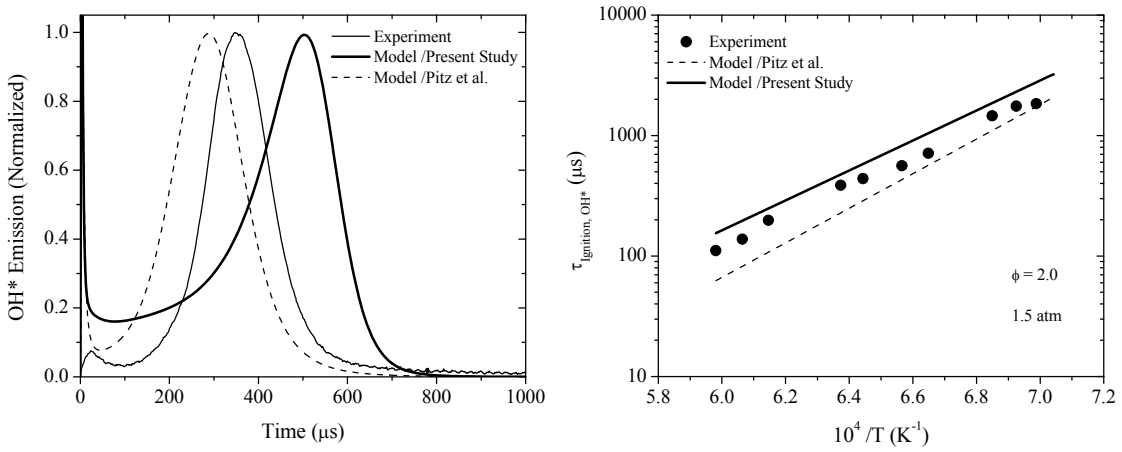

Fig. 7.6. (Left): Measured and model-predicted OH* time history during oxidation of 1600 ppmv MCH (ϕ = 2.0) in 99% Ar. 1.5 atm, 1627 K, $\tau_{Ignition,\ OH^*}$: 198 μs (Experiment). 4.8-kΩ PMT resistance. (Right): Measured and model-predicted ignition delay times of MCH (ϕ = 2.0) in 99% Ar at 1.5 atm. Calculations were performed using Pitz et al. [25] and the present chemical kinetics model. $1.6 \cdot 10^{-3}$MCH + $8.40 \cdot 10^{-3}O_2$ + 0.99Ar.

Ignition delay time measurements at ϕ = 2.0 were obtained at an elevated (nominal) pressure of 11.5 atm over a temperature range of 227 K (1375 K – 1602 K). Figure 7.7 shows a comparison of a measured OH* profile to model calculations. Evident in Fig. 7.7 is a distortion of the measure OH* profile relative to that predicted using the Pitz et al. model. Despite the OH* profile predicted by [25] being in close agreement with the experimental profile, the integration of the sub-mechanism into the compiled model returned the predictions to showing an exaggerated overprediction of incipient OH* formation in fuel-rich high-pressure OH* profiles. Sensitivity analysis is required at this condition to improve the time-dependent OH* profiles. Ignition delay times were indefinable using the compiled model. Measurements of ignition at ϕ = 2.0, 11.5 atm yielded a temperature dependence (ignition activation energy) of 45.3 kcal/mol. The Pitz et al. model reproduces well the temperature trend (50.0 kcal/mol), yet underpredicts the experimental ignition delay times by approximately 25%.

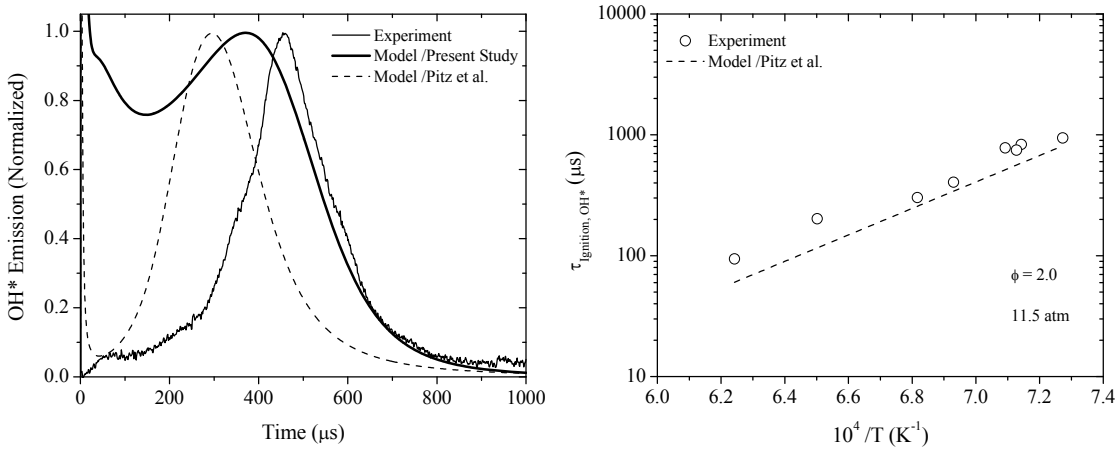

Fig. 7.7. (Left): Measured and model-predicted OH* time history during oxidation of 1600 ppmv MCH (ϕ = 2.0) in 99% Ar. 11.1 atm, 1538 K, $\tau_{Ignition,\ OH^*}$: 202 μs (Experiment). 4.8-kΩ PMT resistance. (Right): Measured and model-predicted ignition delay times of MCH (ϕ = 2.0) in 99% Ar at 11.5 atm. Calculations were performed using Pitz et al. [25]. Ignition delay times using the present chemical kinetics model are indefinable due to distorted OH* profiles. $1.6 \cdot 10^{-3}$MCH + $8.40 \cdot 10^{-3}O_2$ + 0.99Ar.

7.4 Pressure and equivalence ratio effects on MCH ignition

Figure 7.8 shows the effect of equivalence ratio (from 0.5 to 2.0) under conditions of fixed pressure. Comparison of ignition delay times at 1.5 atm show similar ignition activation energies for the fuel-lean, stoichiometric, and fuel-rich conditions: 57.9 kcal/mol, 56.2 kcal/mol, and 56.1 kcal/mol, respectively. Quantifying the effect of equivalence ratio at a given temperature relative to ϕ = 2.0, ϕ = 0.5 and ϕ = 1.0, using 1480 K, ignition delay times were approximately a factor of 2.5 shorter for the stoichiometric conditions and 5 times shorter for the lean condition on average over the range of comparable temperatures.

Increasing pressures reduced the relative differences in ignition delay times trends (Fig. 7.8). At 11.5 atm (nominal), ignition activation energies between lean and stoichiometric equivalence were relatively unaffected: 54.1 kcal/mol (ϕ = 0.5); 51.1 kcal/mol (ϕ = 1.0). The similar ignition behavior between lean and stoichiometric equivalence ratios results in consistent differences in ignition delay times with

temperature. Over the range of temperature covered, fuel-lean ignition delay times were shorter than stoichiometric times by a factor of approximately 2. The activation energy of fuel-rich ignition delay times obtained at 11.5 atm is considerably lower than the other equivalence ratios, and relative to the 1.5 atm value: 45.3 kcal/mol (ϕ = 2.0). Above 1375 K, the fuel-rich trend approaches the stoichiometric trend to within 25%. Comparing the fuel-lean and fuel-rich trends over the range of comparable temperature, fuel-rich ignition delay times are approximately a factor of approximately 2.5 longer than those measured under fuel-lean conditions at the range of comparable temperature between lean and rich conditions.

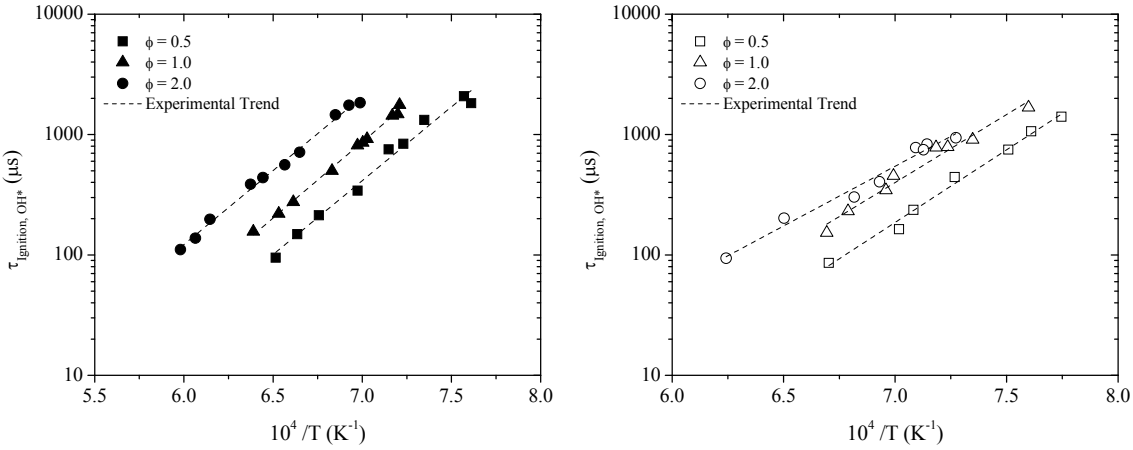

Fig. 7.8. Effect of equivalence ratio on ignition delay times of $C_9H_{18}O_2$ in 99% Ar at 1.5 atm (Left) and 9.5 atm (Right).

The effects of increased pressure from 1.5 atm to 11.5 atm (nominal) under conditions of fixed equivalence ratio on ignition delay times are shown in Figs. 7.9 – 7.11. For fuel-lean measurements, the ignition trends at 1.5 atm and 11.5 atm are similar. The increase in pressure of approximately 10 atm lowered the ignition activation energy by less than 5% (from 57.9 kcal/mol to 54.1 kcal/mol). Ignition delay times at 1.5 atm are approximately a factor of 2.5 longer than those at 11.5 atm (Fig. 7.9).

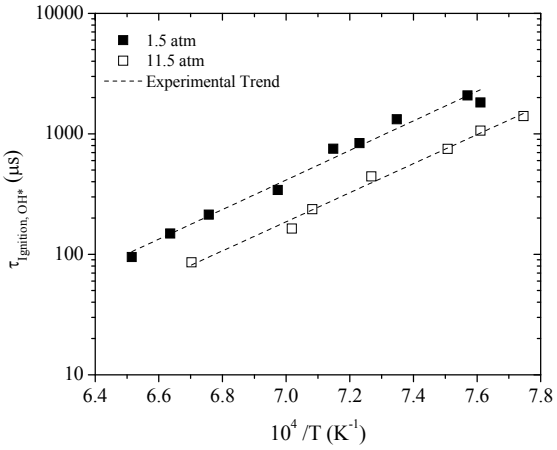

Fig. 7.9. Effect of pressure on ignition delay times of methylcyclohexane (ϕ = 0.5; 99% Ar).

Stoichiometric ignition delay time measurements at 1.5 atm and 11.5 atm are shown in Fig. 7.10. Similar to the trends at lean conditions, no overlap or tendency towards convergence in the ignition trends was exhibited due to similar activation energies. The increase in pressure resulted in a ~ 10% decrease in ignition activation energy (56.2 kcal/mol to 51.1 kcal/mol). Over the range of temperatures covered, using 1240 K as a comparison temperature, ignition delay times were shortened by a factor of 1.1 relative to the 1.5 atm measurements.

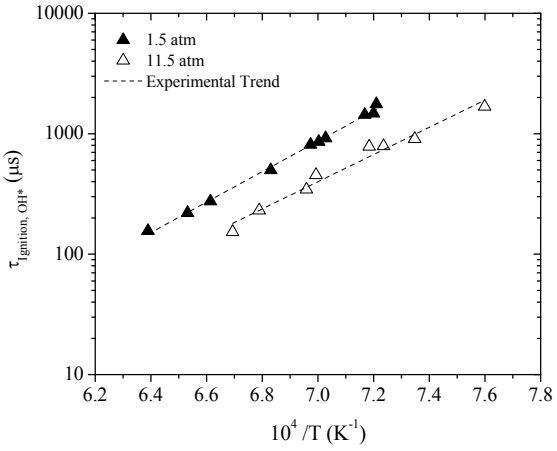

Fig. 7.10. Effect of pressure on ignition delay times of methylcyclohexane (ϕ = 1.0; 99% Ar).

Temperature-dependent ignition trends for ϕ = 2.0 at 1.5 atm and 11.5 atm are shown in Fig. 7.11. No overlap in the ignition behavior of fuel-rich trends is shown. In contrast, the ignition trends tend toward divergence with lower temperatures. The increase in pressure resulted in a ~ 20% increase in ignition activation energy from 56.1 kcal/mol (1.5 atm) to 45.3 kcal/mol (11.5 atm). Over the range of comparable temperatures, ignition delay times were shortened by a factor of approximately 3 at the high-temperature extreme for the 1.5 atm measurements (near 1600 K) and by a factor of 4 at the low-temperature extreme (ca. 1430 K).

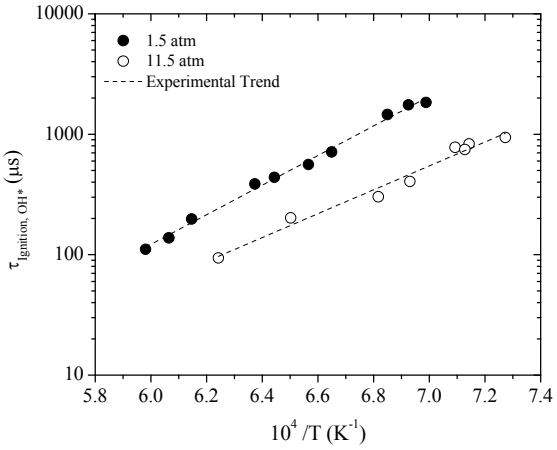

Fig. 7.11. Effect of pressure on ignition delay times of methylcyclohexane (ϕ = 2.0; 99% Ar).

7.5 Empirical ignition delay time correlation

Using linear regression analysis, an experimental correlation was developed from 65 experiments measuring methylcyclohexane ignition (Eqn. 7.1), yielding an overall ignition activation energy of 54.7 kcal/mol. Error bars representing 10% uncertainty in measured ignition delay time are shown. The linear fitting procedure resulted in an R^2 of 0.97. In previous temperature-dependent plots of ignition delay times logarithmic ordinates were used, therefore the 10% error is less apparent. In Fig. 7.12, both the ordinate and abscissa are on linear scales, giving the 10% uncertainty a seemingly larger effect. Pressure dependence for the species was calculated to be n = –0.46. Units in Eqn. 7.1 consist of mol/cm^3, kcal, and

K for species concentration, activation energy, and temperature, respectively. Conditions over which the equation is valid are given in Table 7.1.

$$\tau(\mu s) = 2.15 \cdot 10^{-8}[C_7H_{14}]^{0.91}[O_2]^{-1.36} exp(54.7/R_u T) \qquad (7.1)$$

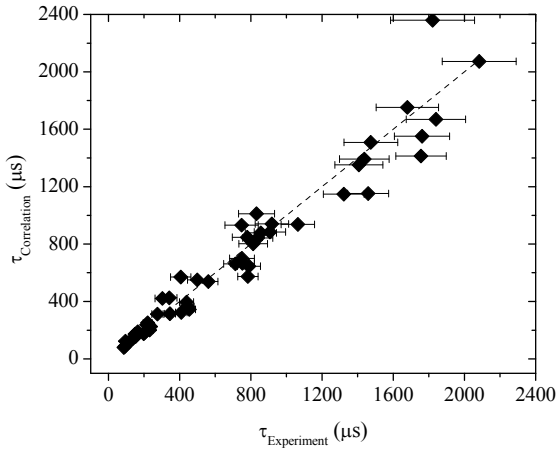

Fig. 7.12. Prediction of experimentally measured ignition delay times of methylcyclohexane in 99% using Eqn. 7.1.

7.6 Concluding remarks on oxidation experiments and modeling of MCH

OH* profiles were measured over ranges of pressure and temperature 1.5 < P (atm) < 11.5 and 1291 < T (K) < 1672, respectively, under highly dilute conditions behind reflected shock waves. Measurements and model-predictions of OH* time histories and ignition delay times were discussed for all pressure/equivalence ratios studied, where both the base methylcyclohexane mechanism and the compiled mechanism were used in the calculations for purposes of comparison to one another. The dependence of the ignition trends on pressure for fixed equivalence ratio and on equivalence ratio for fixed pressure was delineated. Order of ignition delay times at both pressures was identical to that for typical hydrocarbon fuels: lean < stoichiometric < rich. No overlap at either pressure was exhibited by methylcyclohexane. Under fuel-lean and stoichiometric conditions, increased pressure had a negligible effect on ignition

activation energy. In contrast, for the fuel-rich equivalence ratio, experimental and model-predicted ignition times diverged with decreasing temperatures.

From the ignition delay times measured, 65 in total, an empirical concentration- and temperature-dependent trend was calculated. The empirical equation can be used to reproduce ignition delay times of methylcyclohexane within the range of experimental conditions covered herein. The pressure dependence for MCH ($n = -0.46$) is notably lower than that which is typical for conventional hydrocarbon fuels. The overall ignition activation energy (54.7 kcal/mol), however, is similar to other higher-order hydrocarbons (ca. 50 kcal/mol).

The base mechanism from which the methylcyclohexane sub-mechanism in the present work is derived from Pitz et al. [25] and predicts ignition trends well for the high-pressure measurements (11.5 atm). For 1.5 atm pressure, model calculations underpredicts lean ($\phi = 0.5$) and stoichiometric ignition delay times. The compiled model in the present work improves the MCH predictions under certain conditions (e.g. lean equivalence ratios and 1.5-atm fuel-rich measurements), yet improvements are needed. However, the present model is intended to serve as a first generation mechanisms for blended fuel study. Refinement is required over all of the conditions in the present section and is beyond the scope of the present work. The most apparent condition where improvement is needed is the fuel-rich, high-pressure condition.

8. RESULTS OF BLENDED-FUEL MATRIX

OH* time histories and ignition delay times were obtained under dilute conditions (99% Ar) for 10 different ternary fuel blends of $C_9H_{18}O_2$/n-C_9H_{20}/MCH. The ignition behavior of the individual blends cannot be compared directly due to the nature of the multivariable experimental design (i.e. the L9 array); no two blends share the same relative fuel percentages, pressure, or equivalence ratio. Despite the inability for direct comparison, the results from the different blends contribute to the quantification of the effect of these parameters on ignition properties. The utility of the L9 array lies in minimizing the number of experiments required while maximizing the statistical coverage of the parameter space of interest. The Design of Experiments process is described in detail in the literature [133, 134].

Discussed in the ensuing sections (in order from lean to rich equivalence ratios) are experimental trends in ignition behavior of the blends relative to those of the pure fuel constituents, where the ignition behavior of the constituent species is calculated from respective correlation equations. The empirical trends of the blended fuels are also compared to predictions using the chemical kinetics model compiled in the present work. Experimental ignition results of the blends were correlated using linear regression to define an empirical concentration- and temperature-dependent expression that quantifies the individual contributions from the constituent fuel species on ignition properties of the blend resulting in the following dependence on constituent species (in descending order of impact): MCH > n-nonane > methyl octanoate. The section concludes with a computational analysis of the effects of blending on the underlying chemical kinetics. The analysis is conducted at a condition where the compiled mechanism most accurately describes the ignition behavior measured from the experiments in all three blend constituents and several ternary fuel blends: $\phi = 1.0$, 9 atm, 1460 K.

8.1 Fuel-lean condition

Three fuel blends were studied at a fuel-lean equivalence ratio of $\phi = 0.5$: Blends 1, 4, and 7 at nominal pressures of 1.5, 4.7, and 9.3 atm, respectively (Table 3.7). Model calculations capture the ignition

activation energy well for all blends (within 10% of measured values). Incipient formation of OH*, as observed for the pure fuels, occurred in experiments involving the fuel-lean blends. Comparisons below are drawn against experimental results and calculations were performed using the compiled chemical kinetics mechanism of the present study. Ignition trends of the pure fuels are highly disparate under lean ($\phi = 0.5$), 1.5-atm conditions with methyl octanoate igniting more readily at a given temperature relative to either n-nonane or MCH by factors of 2.5 and 4, respectively. With increased pressure, the relative differences in the ignition trends of the pure fuels, while still strong, became smaller. In this respect, the pure-fuel trends, namely those of methyl octanoate and MCH, in effect serve, respectively, as lower and upper bounds of ignition for the fuel blends for all pressures.

The first fuel-lean blend defined in the L9 array is Blend 1. Volumetrically, the blend is defined by 10%/70%/20% $C_9H_{18}O_2$/n-C_9H_{20}/MCH, where the percentages refer to relative fuel volume. Ignition delay times were extracted from OH* time histories at a nominal pressure of 1.5 atm over the range of temperature $1292 < T\,(K) < 1430$. Figure 8.1 shows a representative OH* time history during oxidation of Blend 1 measured near 1400 K and ignition delay times with supporting model calculations.

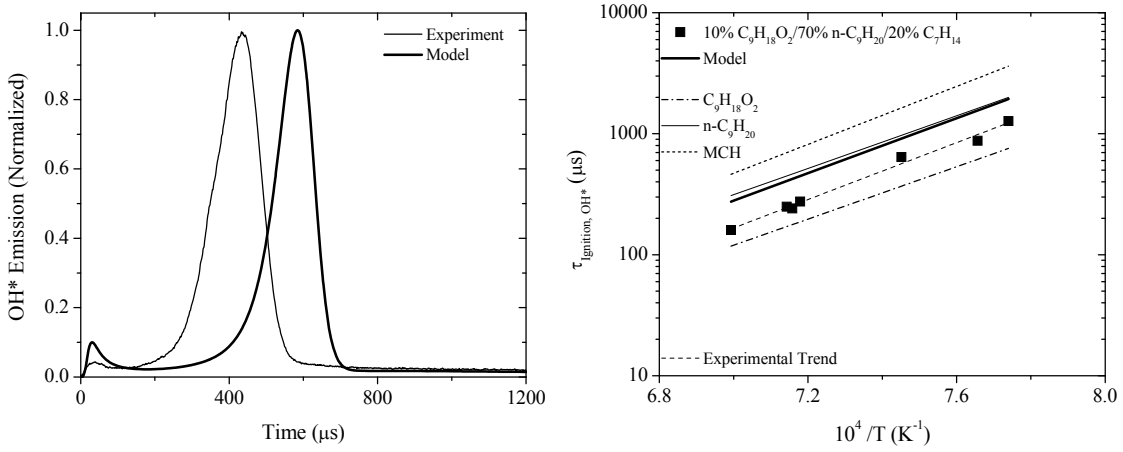

Fig. 8.1. (Left): OH* time history during oxidation of Blend 1. 1.4 atm; 1393 K; $\tau_{Ignition,\ OH^*}$: 275 μs (Experiment), 453 μs (Model). (Right): Measurements and modeling of Blend 1 ignition delay times at 1.5 atm. $3.7\cdot10^{-5}C_9H_{18}O_2 + 25.6\cdot10^{-5}$n-$C_9H_{20} + 7.3\cdot10^{-5}$MCH + $9.63\cdot10^{-3}O_2$ + 0.99Ar (Blend 1 /ϕ = 0.5). Correlated ignition trends of $C_9H_{18}O_2$, n-C_9H_{20}, and MCH are shown for comparison and were calculated using Eqns. 5.1, 6.1, and 7.1, respectively.

The incipient behavior is captured well by the model, as is the overall profile shape (time-dependence of OH*). Model-calculated ignition delay times are over-predicted relative to the experiment by approximately 75%, yet the calculated ignition activation energy (52.0 kcal/mol) for the blend is reproduced within 4% of the experimental value (53.7 kcal/mol). Juxtaposed against the ignition trend of the fuel blend in Fig. 8.1 are those for the pure-fuel constituents. The impact of methyl octanoate on ignition of the ternary blend is apparent in Fig. 8.1. Despite the blend being comprised of 70% n-nonane, the ignition trend is closer to that of $C_9H_{18}O_2$, differing by 40% at the high-temperature extreme (1430 K) and by 70% at the low-temperature extreme (1292 K) compared, respectively, to 90% and 60% for n-nonane at these extremes. In contrast, model calculations of blended fuel ignition predict a trend nearly identical to that of n-nonane, possibly indicative of an insensitivity to the (144 species /1080 reactions) methyl octanoate sub-mechanism. Methylcyclohexane, despite a 2:1 ratio to methyl octanoate, does not impact ignition strongly.

The second fuel-lean blend of the L9 array is Blend 4 which is defined by a ratio of 1:2:2 methyl octanoate:n-nonane:MCH. Ignition delay times were extracted from OH* time histories at a nominal pressure of 4.7 atm over the range of temperature $1258 < T (K) < 1459$. Figure 8.2 shows a representative OH* time history during oxidation of Blend 4 measured at the high-temperature extreme for the blend (1459 K) juxtaposed with ignition delay times with supporting model calculations for both. The slight incipient behavior, expected due to the lean composition of the blend, is captured well by the model. The time-dependence of OH* predicted by the model differs slightly from that observed in the measurement. This is consistent over the range of temperatures studied for Blend 4. Disparity in profile width of OH* between experiment and model predictions became wider with decreasing temperature.

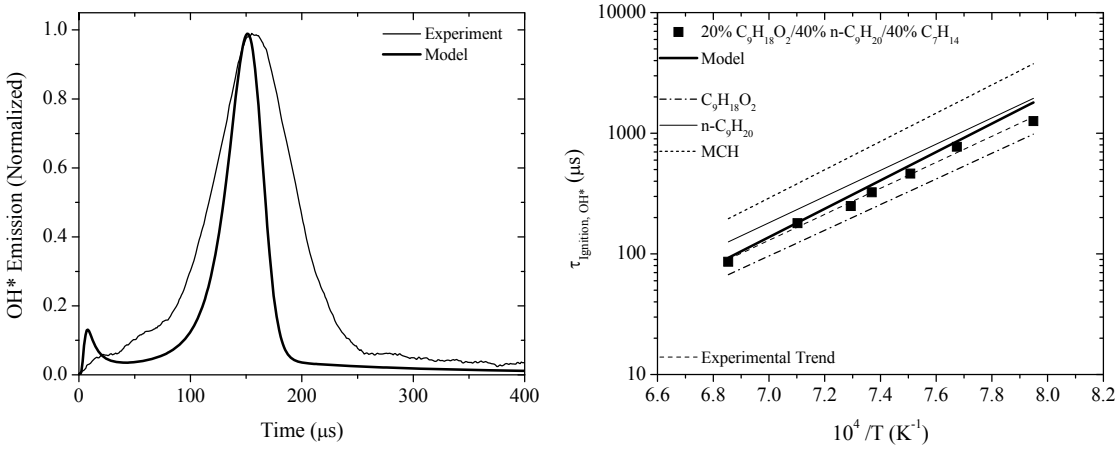

Fig. 8.2. (Left): OH* time history during oxidation of Blend 4. 4.6 atm; 1459 K; $\tau_{Ignition,\ OH^*}$: 86 μs (Experiment), 102 μs (Model). (Right): Measurements and modeling of Blend 4 ignition delay times at 4.7 atm. $7.8 \cdot 10^{-5} C_9H_{18}O_2 + 15.6 \cdot 10^{-5}$ n-$C_9H_{20} + 15.6 \cdot 10^{-5}$MCH + $9.61 \cdot 10^{-3} O_2$ + 0.99Ar (Blend 4 / ϕ = 0.5). Correlated ignition trends of $C_9H_{18}O_2$, n-C_9H_{20}, and MCH are shown for comparison and were calculated using Eqns. 5.1, 6.1, and 7.1, respectively.

The experimental ignition trend of Blend 4 is influenced by methyl octanoate, as evident in Fig. 8.2, positioned nearly equidistant between methyl octanoate and n-nonane. The trend of Blend 4 differs by approximately 40% and 25% at the low- and high-temperature extremes, respectively, relative to both pure fuel trends. Similar to the observation in Blend 1, despite a 2:1 ratio of MCH to $C_9H_{18}O_2$, MCH, which has the slowest ignition delay times, does not inhibit ignition of the blend. Model-calculated ignition activation energy (53.8 kcal/mol) is predicted within 8% of the experimental trend (49.8 kcal/mol). The higher predicted activation energy resulted in accurate modeling near the high-temperature extreme, yet at the low-temperature extreme ignition delay times are overpredicted by approximately 40%. Blend 4, relative to Blend 1, contains a lower percentage of n-nonane (40% relative to 70%), and model calculations deviate from n-nonane trend with increasing temperature.

The third of the three fuel-lean blends covered in the L9 array is Blend 7 which is defined by a ratio of 1:1.33:1 methyl octanoate:n-nonane:MCH, or 30%/40%/30% volumetrically. Ignition delay times were extracted from OH* time histories at a nominal pressure of 9.3 atm over the range of temperature 1277 < T (K) < 1401. Figure 8.3 shows a representative OH* time history during oxidation of Blend 7 measured at the high-temperature extreme for the blend (1401 K) juxtaposed with ignition delay times with supporting model calculations for both. Incipient OH* behavior, experimentally, is suppressed due to the leaner equivalence ratio, yet model calculations indicate the presence of OH* near time-zero. Similar to Blend 4, OH* profile widths, which can be utilized as a metric for model accuracy in ground-state chemistry (Section 6), are predicted on shorter timescales than those observed in the experiment. Deviations become more apparent as temperature is decreased. Using the profile full-width half-max (FWHM), in Fig. 8.3 the model-predicted OH* profile width is approximately 50% shorter than that observed in the experiment. At the low-temperature extreme (1277 K), this difference increases to a factor of 2.6.

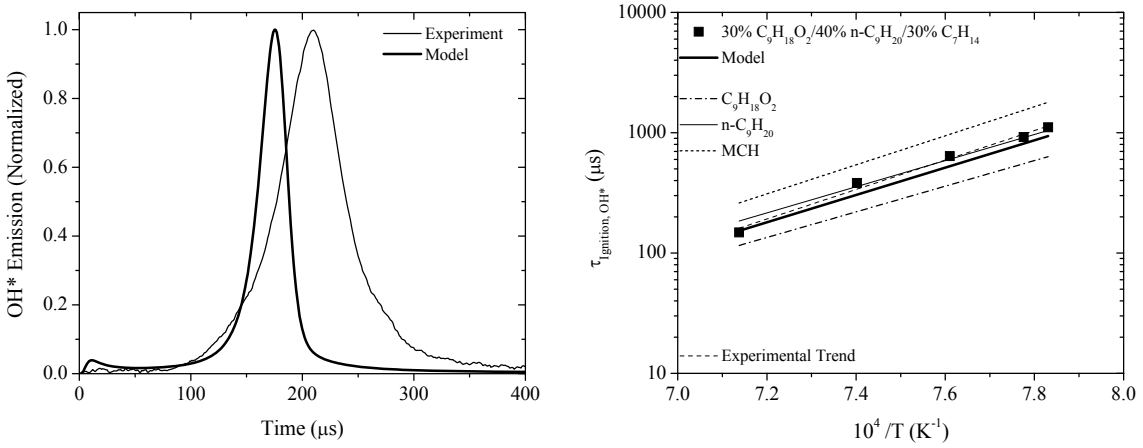

Fig. 8.3. (Left): OH* time history during oxidation of Blend 7. 9.0 atm; 1401 K; $\tau_{Ignition,\ OH^*}$: 148 μs (Experiment), 144 μs (Model). (Right): Measurements and modeling of Blend 7 ignition delay times at 9.3 atm. $11.5 \cdot 10^{-5} C_9H_{18}O_2 + 15.4 \cdot 10^{-5}$n-$C_9H_{20} + 11.5 \cdot 10^{-5}$MCH + $9.62 \cdot 10^{-3} O_2$ + 0.99Ar (Blend 7 /ϕ = 0.5). Correlated ignition trends of $C_9H_{18}O_2$, n-C_9H_{20}, and MCH are shown for comparison and were calculated using Eqns. 5.1, 6.1, and 7.1, respectively.

Both the experimental and model-predicted ignition trends of Blend 7 overlap strongly with that of n-nonane. Neither methyl octanoate or MCH, within the degree of experimental scatter, impacted ignition of the blend. Methyl octanoate has a negligible effect on ignition of the blend only near the high temperature extreme (1401 K). Similar to the previous Blends, MCH does not inhibit ignition delay times of the blend, evidenced in Fig. 8.3 by the ignition trend of Blend 7 overlapping n-nonane. Under these conditions, ignition delay time modeling of Blend 7 can be approximated by n-nonane. The experimental ignition activation energy of the trend (56.0 kcal/mol) is reproduced within 8% by the model (51.9 kcal/mol). Ignition delay times are reproduced accurately towards the high-temperature extreme, yet are slightly underpredicted at the the low-temperature extreme by approximately 20%.

8.2 Stoichiometric condition

Four fuel blends were studied under stoichiometric conditions: Blends 2, 5, 8, and Blend x. Experiments involving Blends 5 and 8 were conducted at nominal pressures 4.6 and 9.3 atm, respectively. Blend 2 and Blend x were both conducted at 1.5 and 9.3 atm nominal pressures. Model calculations capture the ignition activation energy within 2% of measured values for Blends 5, 8, and x. Calculations for Blend 2, for both 1.5-atm and 9.3-atm conditions, underpredict the experimental values by approximately 20%. Incipient formation of OH* did not occur appreciably in the $\phi = 1.0$ experiments, existing only slightly near the high-temperature extremes. Model prediction of the incipient oxidation is in agreement with the experiment, predicting OH* concentrations of less than 5% relative to that at peak concentration after ignition. Comparisons below are drawn against experimental results and calculations were performed using the compiled chemical kinetics mechanism of the present study. Ignition trends of the pure fuels are highly disparate at $\phi = 1.0$, 1.5-atm conditions with methyl octanoate igniting more readily at a given temperature relative to MCH at high- and low-temperature extremes by factors of 3.5 and 4.5, respectively. With increased pressure, the relative differences in the ignition trends of the pure fuels, while still strong, became smaller. Near 9 atm, the correlated ignition delay times of $C_9H_{18}O_2$ are factors of 2.2 and 2.9 shorter than those for MCH at high- and low-temperature extremes, respectively. As in the fuel-

lean case, the pure fuel trends of methyl octanoate and MCH, in effect serve, respectively, as lower and upper bounds of ignition for the fuel blends for all pressures.

Blend x is not part of the L9 array, yet is included in the study to extend the range of methyl octanoate concentration to 5% (the lowest percentage in the L9 array is 10%). Blend x, comprised primarily of n-nonane and MCH, is defined volumetrically by 5%/50%/45% $C_9H_{18}O_2$/n-C_9H_{20}/MCH, where the percentages refer to relative fuel volume. Ignition delay times were extracted from OH* time histories at a nominal pressure of 1.5 atm over the range of temperatures $1354 < T\ (K) < 1553$. Measurements were extended to 9.1 atm, covering $1303 < T\ (K) < 1458$, to capture the pressure effect on the ternary blend. Figure 8.4 shows a representative OH* time history during oxidation of Blend x measured near 1350 K and ignition delay times with supporting model calculations.

OH* time histories of Blend x at 1.5 atm are captured well by the chemical kinetics model over the entire range of temperature covered, with FWHM of experimental and model-based profiles within 15% of one another. The ignition trend of Blend x at 1.5 atm directly overlaps that of the n-nonane correlation (Fig. 8.4). Noting the diminutive amount of methyl octanoate (5%), despite the relatively larger amount of MCH (45%) there is no impact of the latter species on ignition delay times of the fuel blend. Methyl octanoate ignition delay times at $\phi = 1.0$, 1.5 atm are sharply lower than any of the trends compared. Ignition delay times of $C_9H_{18}O_2$ are approximately 2.5 times shorter than those of the n-nonane/Blend x trend.

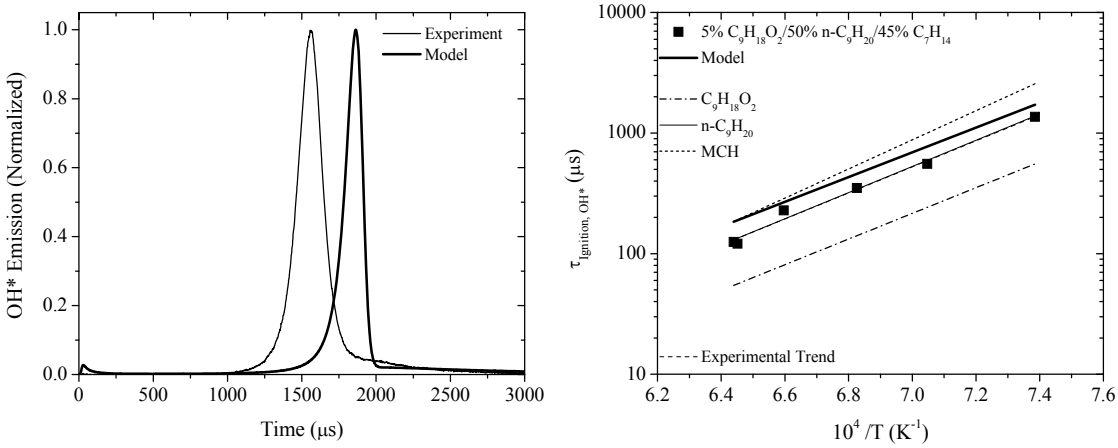

Fig. 8.4. (Left): OH* time history during oxidation of Blend x. 1.4 atm; 1354 K; $\tau_{Ignition,\ OH^*}$: 1363 μs (Experiment), 1611 μs (Model). (Right): Measurements and modeling of Blend x ignition delay times at 1.5 atm. $3.75 \cdot 10^{-5} C_9H_{18}O_2 + 37.45 \cdot 10^{-5}$n-$C_9H_{20} + 33.71 \cdot 10^{-5}$MCH + $9.25 \cdot 10^{-3} O_2$ + 0.99Ar (Blend x /ϕ = 1.0). Correlated ignition trends of $C_9H_{18}O_2$, n-C_9H_{20}, and MCH are shown for comparison and were calculated using Eqns. 5.1, 6.1, and 7.1, respectively.

Model-predicted ignition activation energy of Blend x at 1.5 atm (46.9 kcal/mol) is within 5% of the experimental result of 49.4 kcal/mol. Ignition delay times are overpredicted over the entire temperature range. A larger disparity is present at the low-temperature extreme (1354 K), where modeled ignition times differ from experimental values by 25%. Towards the high-temperature extreme (1553 K), the difference approaches 45%.

Measurements of OH* and ignition delay times for the 5% methyl octanoate blend, Blend x, were extended to higher pressure. While strong agreement in OH* time histories exists between model and experiment OH* time histories at 1.5 atm, at increased pressure modeled profiles became substantially thinner relative to the measurements, as observed in Fig. 8.5 where the FWHM of the modeled OH* profile is approximately 3 times thinner than that of the experiment. With decreasing temperature the increase in pressure led to a continued trend of deviation in OH* time dependence between model and experiment. At the low-temperature extreme (1303 K) the difference in FWHM between model and

experiment increased to a factor of nearly 12, with model-predicted and experimental FWHM of approximately 40 μs and 460 μs, respectively.

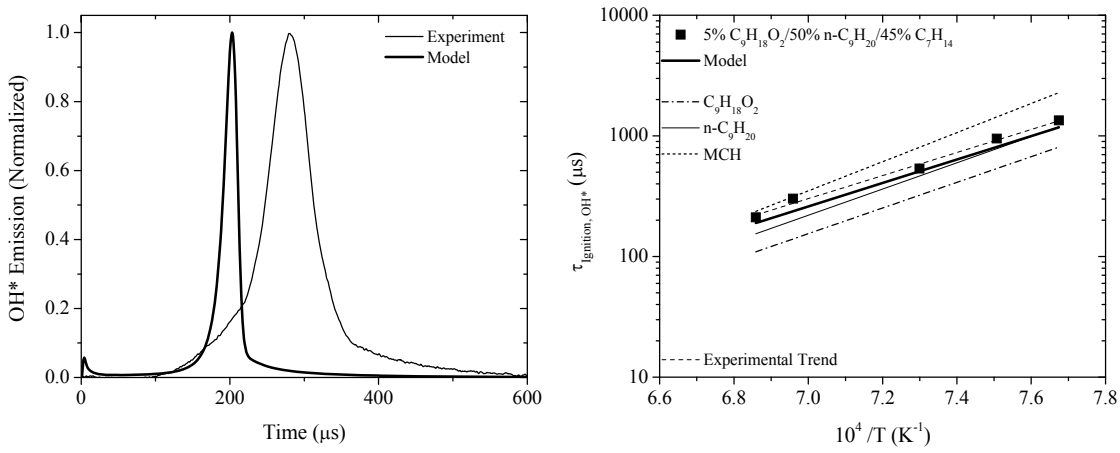

Fig. 8.5. (Left): OH* time history during oxidation of Blend x. 8.6 atm; 1458 K; $\tau_{Ignition,\ OH^*}$: 211 μs (Experiment), 169 μs (Model). (Right): Measurements and modeling of Blend x ignition delay times at 9.1 atm. $3.75 \cdot 10^{-5} C_9H_{18}O_2 + 37.45 \cdot 10^{-5}$n-$C_9H_{20} + 33.71 \cdot 10^{-5}$MCH + $9.25 \cdot 10^{-3} O_2$ + 0.99Ar (Blend x /ϕ = 1.0). Correlated ignition trends of $C_9H_{18}O_2$, n-C_9H_{20}, and MCH are shown for comparison and were calculated using Eqns. 5.1, 6.1, and 7.1, respectively.

Ignition delay times were obtained at a nominal pressure of 9.1 atm (Fig. 8.5). Model calculation of ignition activation energy for the blend (44.3 kcal/mol) shows strong agreement with the experimental value (43.7 kcal/mol), differing negligibly by 1.5%. Blend x is comprised of nearly equimolar amounts of n-nonane and MCH, yet the ignition trend of the blend deviates from n-nonane with increased temperature. In contrast to Blend x at 1.5 atm, measurements obtained at 9.1 atm indicate an influence of MCH on ignition of the ternary blend, specifically towards the high-temperature extreme (1458 K). Relative to n-nonane, ignition delay times of the Blend x deviate by 50% at the high-temperature extreme and then converge towards the low-temperature extreme to within 10%. Due to the position of the trend of Blend x between MCH and n-nonane at 9.1 atm (Fig. 8.5) and overlapping n-nonane at 1.5 atm (Fig. 8.4), methyl octanoate at 5% (vol.) has an insubstantial effect on ϕ = 1.0 ignition of the blend.

The first of the three stoichiometric blends covered in the L9 array is Blend 2 which is defined by a ratio of 1:2.5:1.5 methyl octanoate:n-nonane:MCH, or 30%/40%/30% volumetrically. Ignition delay times were extracted from OH* time histories at nominal pressures of 1.5 and 9.3 atm over the range of temperatures $1344 < T\,(K) < 1515$ and $1320 < T\,(K) < 1477$, respectively. The two pressures produced differing trends in ignition delay times of the blends. At 1.5 atm, differences were observed in the ignition trend of the ternary fuel between model and experiment, both of which deviate from the n-nonane ignition trend. At increased pressure (9.3 atm), the experimental and model-predicted trends of Blend 2 ignition were concurrent with that of n-nonane. This result is consistent experimentally with methyl octanoate which approaches the ignition behavior of n-nonane at elevated pressure (Section 9).

Figure 8.6 shows a representative OH* time history during oxidation of Blend 2 measured at the low-temperature extreme (1344 K) for the blend at 1.5 atm juxtaposed with ignition delay times. Model calculations are shown for both the OH* time history and ignition delay times. Incipient OH* behavior, experimentally is suppressed due to the increased pressure. Model calculations indicate a negligible presence of OH* near time-zero of less than 3% relative to peak OH* concentration (post-ignition). OH* time histories are captured well by the chemical kinetics model. At the high-temperature extreme, a model-predicted 85-μs FWHM compares well with the 115 μs experimental time. At the low-temperature extreme, a model-predicted 137-μs FWHM compares well with the 221 μs experimental time.

Ignition delay times of Blend 2 at 1.5 atm were influenced by the 20% (vol.) methyl ester concentration (Fig. 8.6). Over the range of temperatures covered using Blend 2, ignition delay times for the blend were consistently shorter relative to n-nonane (present in Blend 2 at 50% of the fuel, volumetrically). Despite the blend being composed mostly of n-nonane, the ignition trend deviates towards methyl octanoate with increased temperature by 30% at the high-temperature extreme (1515 K).

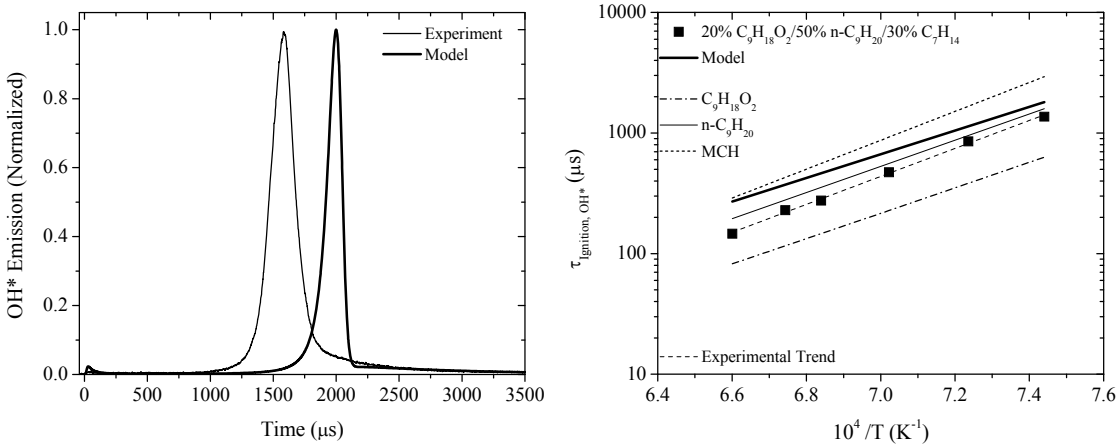

Fig. 8.6. (Left): OH* time history during oxidation of Blend 2. 1.5 atm; 1344 K; $\tau_{Ignition,\ OH^*}$: 1365 μs (Experiment), 1708 μs (Model). (Right): Measurements and modeling of Blend 2 ignition delay times at 1.5 atm. $14.7 \cdot 10^{-5} C_9H_{18}O_2 + 36.6 \cdot 10^{-5}$n-$C_9H_{20} + 22.0 \cdot 10^{-5}$MCH + $9.27 \cdot 10^{-3} O_2$ + 0.99Ar (Blend 2 /ϕ = 1.0). Correlated ignition trends of $C_9H_{18}O_2$, n-C_9H_{20}, and MCH are shown for comparison and were calculated using Eqns. 5.1, 6.1, and 7.1, respectively.

At the low-temperature extreme (1344 K), the ignition trend of Blend 2 at 1.5 atm converges towards the correlated n-nonane trend, differing only by 15%. Noting in Blend 2 the lower concentration of methyl octanoate compared to MCH and the tendency of the ignition trend of the ternary blend towards the former, MCH does not have an appreciable impact on ignition under these conditions. Experimental ignition activation energy of Blend 2 at 1.5 atm (53.0 kcal/mol) is highly underpredicted by the chemical kinetics model (44.8 kcal/mol) by nearly 20%.

Measurements of Blend 2 oxidation were extended to 9.3 atm to capture the influence of pressure on ignition properties of the blend. A representative OH* time history measurement at the high-temperature extreme (1477 K) is shown in Fig. 8.7 with supporting model calculation of OH*. The time-dependent excited-state OH profiles calculated using the chemical kinetics mechanism are in strong disagreement with the experimental profiles indicating the need for improvement in the ground-state chemistry of the model. The FWHM values between experiment and model, at the high-temperature extreme, differs by

approximately 75 μs (92 μs experimentally, 15 μs model-predicted). The disparity in FWHM of the profiles widens at lower temperatures. At the low-temperature extreme (1320 K), the difference increases to 123 μs (168 μs experimentally, 45 μs model-predicted)

Ignition delay time measurements of Blend 2 at 9.3 atm are shown in Fig. 8.7. Relative to the 1.5-atm condition, the ignition trend of the ternary fuel blend coalesces with that of n-nonane over the range of temperatures covered and model calculations reflect this behavior. Peak deviation relative to the n-nonane trend of a negligible 15% exists at the low-temperature extreme. Methyl octanoate ignition delay times are approximately 40% shorter than those of the ternary blend over the entire range of temperature covered. Ignition activation energy of Blend 2 predicted using the chemical kinetics model (43.6 kcal/mol) is lower than the experimentally measured activation energy (51.9 kcal/mol) by nearly 20%, a percentage similar to the predicted lower value at 1.5 atm for Blend 2.

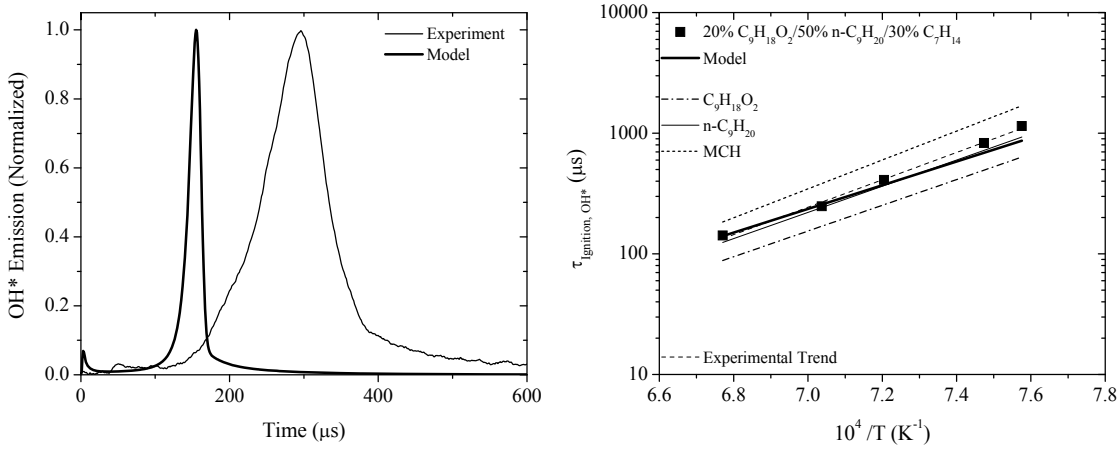

Fig. 8.7. (Left): OH* time history during oxidation of Blend 2. 9.2 atm; 1477 K; $\tau_{Ignition,\ OH^*}$: 142 μs (Experiment), 130 μs (Model). (Right): Measurements and modeling of Blend 2 ignition delay times at 9.3 atm. $14.7 \cdot 10^{-5} C_9H_{18}O_2 + 36.6 \cdot 10^{-5}$n-$C_9H_{20} + 22.0 \cdot 10^{-5}$MCH + $9.27 \cdot 10^{-3} O_2$ + 0.99Ar (Blend 2 /ϕ = 1.0). Correlated ignition trends of $C_9H_{18}O_2$, n-C_9H_{20}, and MCH are shown for comparison and were calculated using Eqns. 5.1, 6.1, and 7.1, respectively.

The effect of pressure on ignition delay times of Blend x and Blend 2, which contain 5% and 20% methyl octanoate, respectively, and an identical amount of n-nonane (50% vol.), is shown in Fig. 8.8. The increase in the relative fuel volume of $C_9H_{18}O_2$ is coupled with a decrease in MCH concentration in the blend. MCH ignition delay times, under all conditions studied herein, are substantially longer than those of methyl octanoate which has the shortest ignition delay time of the three constituents. From the increase in $C_9H_{18}O_2$ between Blend x and Blend 2 of a factor of 3, and the coupled decrease in MCH by a factor of 3, it is indiscernible, empirically, which species causes the shortened ignition delay times observable between the two blends at either pressure.

The increase in methyl octanoate from 5% to 20% (decrease in MCH from 45% to 30%) at 1.5 atm led to shortened ignition delay times by approximately 30% at the high-temperature extreme (1500 K). The two trends converged towards the low-temperature extreme (1350 K) to within 10% of one another. Additionally, ignition activation energy increased with increasing $C_9H_{18}O_2$ content by 15% (43.7 kcal/mol to 51.9 kcal/mol). At an increased pressure of 9.3 atm, the effect of concentration variation became less discernible. Towards the high-temperature extreme (1470 K) the increased methyl ester concentration shortened ignition delay times by 25% relative to the 5% $C_9H_{18}O_2$ blend (Blend x). The two 9.3-atm trends display overlap below 1390 K. As evidenced in Fig. 8.8, which combines Figs. 8.4 – 8.7, respective pressure dependence for the two blends are similar (i.e. the increase in pressure for either blend leads to similar decrease in ignition delay time regardless of blend composition), therefore the addition of the methyl ester does not impact the pressure dependence of the ternary blend. This behavior is supported by the lower pressure dependence calculated for methyl octanoate (n = –0.19, Section 5) compared to the pressure dependence of the other two fuel constituents which have similar dependence ($n_{n\text{-Nonane}}$ = –0.48; n_{MCH} = –0.46). Therefore, the change in MCH concentration does not impact the pressure dependence of the blends.

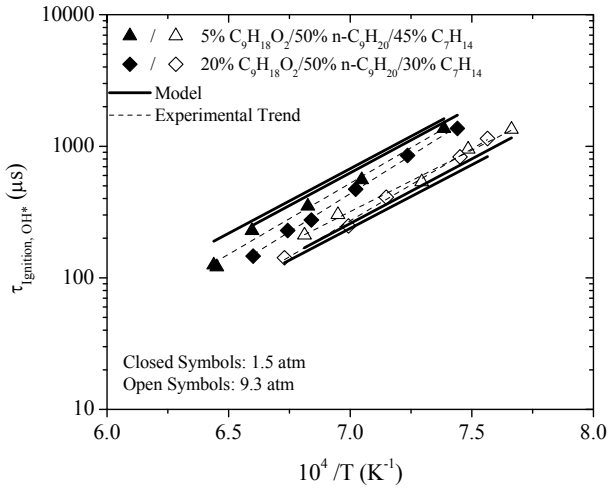

Fig. 8.8. Comparison of the effect of pressure variation from 1.5 atm to approximately 10.0 atm on stoichiometric ignition delay times of Blend x and Blend 2 in 99% Ar.

The second stoichiometric blend of the L9 array is Blend 5, which is defined by a ratio of 1:1.67:0.67 methyl octanoate:n-nonane:MCH, or 30%/50%/20% volumetrically with respect to the partial fuel volume in the experiment. Ignition delay times were extracted from OH* time histories at a nominal pressure of 4.4 atm over the range of temperature 1278 < T (K) < 1487. Figure 8.9 shows a representative OH* time history measurement during oxidation of Blend 5, with supporting model calculation, measured at the high-temperature extreme for the blend (1487 K) juxtaposed with ignition delay times. OH* time histories measured under these conditions predicted shorter timescales relative to those observed in the experiment. At the high-temperature extreme, the difference in FWHM between the experiment and model results is approximately 40 μs (70 μs experimentally, 30 μs model-predicted). Similar to previous conditions, lower temperature causes greater deviation in FWHM times between the experimental value and model calculations. At the low-temperature extreme (1278 K), the difference in FWHM between the experiment and model results is approximately 475 μs (555 μs experimentally, 80 μs model-predicted).

Methyl octanoate displays a slight acceleration effect on ignition delay times, relative to the ignition trend of n-nonane which comprises half of the fuel concentration of the blend. The difference between ignition delay times of the fuel blend and n-nonane at the high-temperature extreme is slightly outside the 10% band of uncertainty in the experiment, measuring 15% shorter relative to n-C_9H_{20}, yet at the low-temperature extreme, the difference increases to over 30% indicating that methyl octanoate impacts ignition of the fuel blend more strongly towards decreased temperature. Observing the position of the ignition trend between those of methyl octanoate and n-nonane, MCH does not impact the ignition behavior of the ternary blend. Ignition activation energy measured in the experiment (45.5 kcal/mol) is predicted within 1% by the chemical kinetics model (45.2 kcal/mol), however model calculations of ignition delay time reproduce the trend of n-nonane ignition and therefore differ similarly with respect to the experimental ignition trend of the blended fuel.

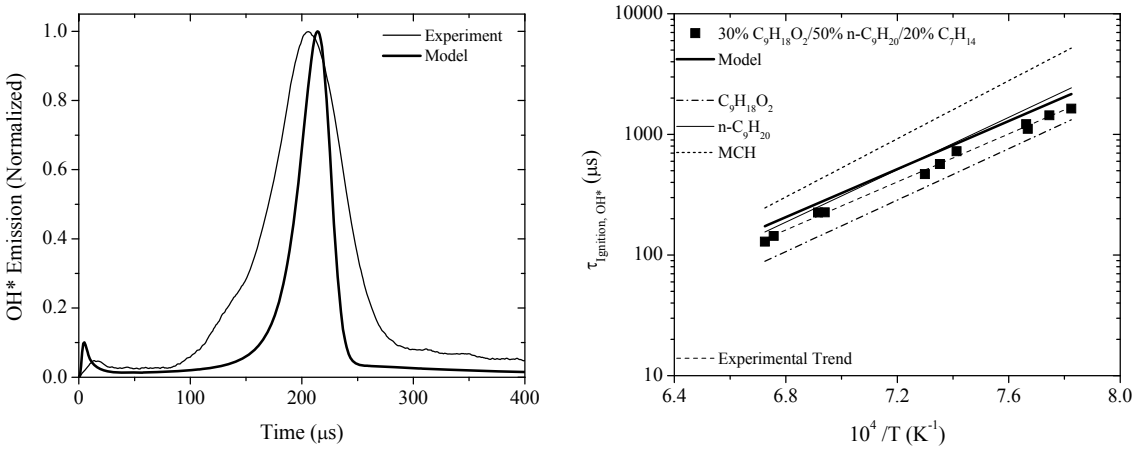

Fig. 8.9. (Left): OH* time history during oxidation of Blend 5. 4.4 atm; 1487 K; $\tau_{Ignition,\ OH^*}$: 129 μs (Experiment), 174 μs (Model). (Right): Measurements and modeling of Blend 5 ignition delay times at 4.6 atm. $21.7 \cdot 10^{-5} C_9H_{18}O_2 + 36.1 \cdot 10^{-5}$n-$C_9H_{20} + 14.4 \cdot 10^{-5}$MCH + $9.28 \cdot 10^{-3} O_2$ + 0.99Ar (Blend 5 /ϕ = 1.0). Correlated ignition trends of $C_9H_{18}O_2$, n-C_9H_{20}, and MCH are shown for comparison and were calculated using Eqns. 5.1, 6.1, and 7.1, respectively.

The third of three stoichiometric blends contained in the L9 array is Blend 8, which is defined by a ratio of 1:5:4 methyl octanoate:n-nonane:MCH, 10%/50%/40% volumetrically with respect to the partial fuel volume in the experiment. Ignition delay times were extracted from OH* time histories at a nominal pressure of 9.3 atm over the range of temperature 1325 < T (K) < 1462. Figure 8.10 shows a representative OH* time history measurement during oxidation of Blend 8 at 1368 K and ignition delay times with supporting model calculation.

OH* profiles predicted from the chemical kinetics model differ sharply with the FWHM observed in the experiment. At the high-temperature extreme (1462 K), the difference is approximately 60 μs (80 μs experimentally, 20 μs model-predicted). The difference increases with decreasing temperature. Model-based prediction of the FWHM increases to 40 μs at the low-temperature extreme (1325 K), while the experimental OH* profile increases 190 μs.

Model prediction of the ignition behavior of Blend 8 reproduces that of pure n-nonane. Ignition delay times for the blend fuel are underpredicted by approximately 25%. Ignition activation energy predicted for the blend using the chemical kinetics model (43.6 kcal/mol) agrees strongly with that measured experimentally (44.4 kcal/mol) to within 2%. Similar to the behavior of Blend x at 9.1 atm, yet to a broader degree with respect to temperature dependence, MCH inhibits ignition delay times of the blend relative to the n-nonane trend which is used as comparative measure of ignition for the blend since the species comprises 50% of the fuel. Ignition trends between Blend 8 and MCH overlap above 1400 K. With decreasing temperature, the ignition trend of the ternary blend deviates to shorter ignition delay times. At the low-temperature extreme, ignition of the ternary blend is 30% shorter relative to the MCH trend. Outside of fuel-rich equivalence ratios, this observed influence of MCH is exhibited only under these two conditions (i.e. relative amounts of fuel species, pressure, temperature, equivalence ratio /ϕ = 1.0); MCH did not impact ignition under fuel-lean conditions.

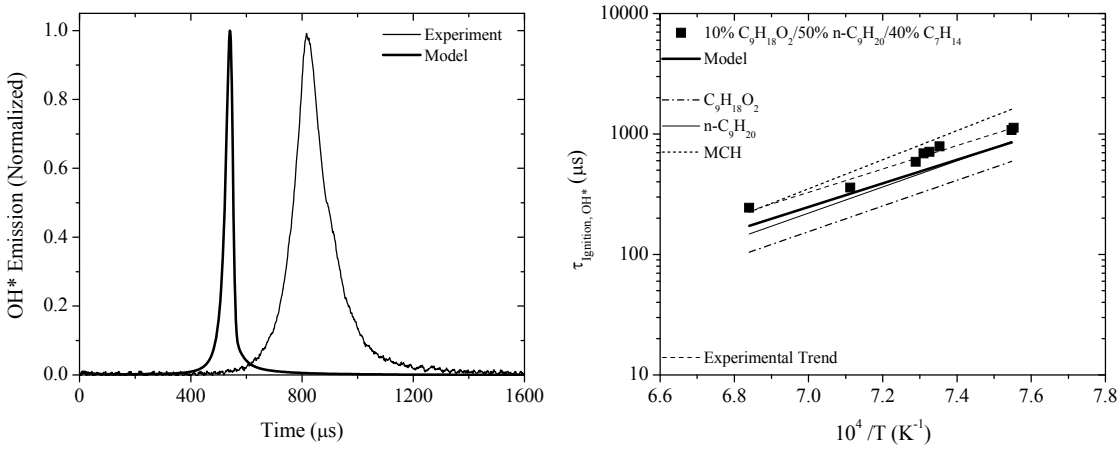

Fig. 8.10. (Left): OH* time history during oxidation of Blend 8. 9.1 atm; 1365 K; $\tau_{Ignition,\ OH^*}$: 711 μs (Experiment), 503 μs (Model). (Right): Measurements and modeling of Blend 8 ignition delay times at 9.3 atm. $7.4 \cdot 10^{-5} C_9H_{18}O_2$ + $37.2 \cdot 10^{-5}$n-C_9H_{20} + $29.7 \cdot 10^{-5}$MCH + $9.26 \cdot 10^{-3} O_2$ + 0.99Ar (Blend 8 /ϕ =1.0). Correlated ignition trends of $C_9H_{18}O_2$, n-C_9H_{20}, and MCH are shown for comparison and were calculated using Eqns. 5.1, 6.1, and 7.1, respectively.

8.3 Fuel-rich condition

Three fuel blends were studied under fuel-rich (ϕ = 2.0) conditions: Blends 3, 6, and 9 at nominal pressures of 1.5, 5.2, and 8.9 atm, respectively. Model calculations capture the ignition activation energy within 3% of the measured value at 1.5 atm. In contrast, with increasing pressure, calculations using the model grossly underpredict ignition trends of the fuel-rich blends. At 5.2 atm, a 50% error in ignition activation energy is reported by the model: 28.5 kcal/mol compared to the experimental value of 43.7 kcal/mol. Further, at 8.9 atm ignition delay times become indefinable below 1500 K. Incipient formation of OH* occurred most strongly under fuel-rich conditions. The effect of ϕ on incipient OH* formation, described in Section 6, is due primarily to the furnishing of CH to $CH + O_2 \rightarrow OH^* + CO$ as a result of immediate parent fuel decomposition and subsequent reaction of the fragmented organic radicals upon formation of the reflected shock wave (i.e. experimental conditions). Under fuel-lean conditions, the greater availability (larger concentration) of O_2 slows the formation of CH. Radicals and intermediates which otherwise, under more fuel-rich conditions, tend to yield CH either directly or indirectly instead oxidize rather than decompose or react in a series which produces CH radicals.

Model calculations largely overpredict the formation of OH* from incipient oxidation which causes profiles to become distorted at elevated pressure and as a result disallows definition of ignition delay times using the model. This overprediction prevented definition of ignition times for ϕ = 2.0 at both 1.5 atm and 10 atm in n-nonane oxidation experiments prior to improvement of ground-state chemistry in the base n-nonane model [48] in a manner similar to that of the initial n-nonane model [16]. The magnitude of the incipient OH* peak, for all fuel-rich conditions, is overpredicted by the model compared to the experimental profile. The 4.8-kΩ resistance imposed on the PMT detector to control voltage output causes a slight increase (several microseconds) in the time constant of the detection system (Sections 3, 6). As described in Section 6, the peak OH* near time-zero in the experiment, under more time-responsive conditions, is higher than that shown in Figs. 8.11 – 8.13 and therefore more closely matched with the model under these conditions. This consideration applies more specifically to the fuel-rich measurements

since, under leaner conditions, the rate and magnitude of incipient OH* formation are smaller. Therefore less of a demand is placed on the time response of the detection system (within ~3 – 5 μs) under leaner conditions to capture incipient oxidation processes which lead to OH*.

Comparisons below are drawn against experimental results and calculations were performed using the compiled chemical kinetics mechanism of the present study. Ignition trends of the pure fuels are disparate with methyl octanoate igniting more readily at a given temperature relative to MCH. The difference in fuel ignition behavior is most prominent at near-atmospheric pressure. Similar to leaner equivalence ratios, with increased pressure the relative differences in the ignition trends of the pure fuels, while still strong, became smaller. The ignition behavior of methyl octanoate and MCH, in effect serve, respectively, as lower and upper bounds of ignition for the fuel blends for all pressure.

The first of three fuel-rich blends contained in the L9 array is Blend 3 which is defined by a ratio of 1:1:1.33 methyl octanoate:n-nonane:MCH, or 30%/30%/40% volumetrically with respect to the partial fuel volume in the experiment. Ignition delay times were extracted from OH* time histories at a nominal pressure of 1.5 atm over the range of temperature $1418 < T\,(K) < 1630$. Figure 8.11 shows a representative OH* time history measurement during oxidation of Blend 3 at 1627 K and ignition delay times with supporting model calculations.

In contrast to leaner equivalence ratios, OH* time histories for Blend 3 are comparatively well-predicted by the compiled chemical kinetics model over the entire range of temperatures. In general, profile widths of fuel-rich OH* exist on longer timescales relative to those at leaner conditions. Near the high-temperature extreme, at 1627 K, the difference between experimental and model-predicted FWHM is 10 μs (135 μs experimentally, 145 μs model-predicted). At the low-temperature extreme (1418 K), the difference is 170 μs (630 μs experimentally, 460 μs model-predicted).

The ignition trend of fuel-rich Blend 3 lies between that of n-nonane and MCH. Noting the high relative volumetric percentage of methyl octanoate and shorter ignition delay times corresponding to this species, no significant impact on ignition chemistry of the blend due to the presence of $C_9H_{18}O_2$ (30% vol.) is apparent. At the high-temperature extreme, the ignition trend of the ternary fuel blend differs negligibly from that of n-nonane (ca. 10% longer ignition delay) and by approximately 30% relative to MCH, with shorter ignition delay times for the blend. At the low-temperature extreme, ignition delay times for the blend were 40% shorter and 40% longer relative to n-nonane and MCH, respectively. Ignition activation energy of the ternary blend is similar to that of MCH with an experimental value of 53.7 kcal/mol. The model-predicted ignition activation energy for Blend 3 of 52.0 kcal/mol is within 3% of the experiment. While the temperature dependence of the fuel blend is captured accurately by the model, the absolute ignition delay times are overpredicted by a factor of 2.

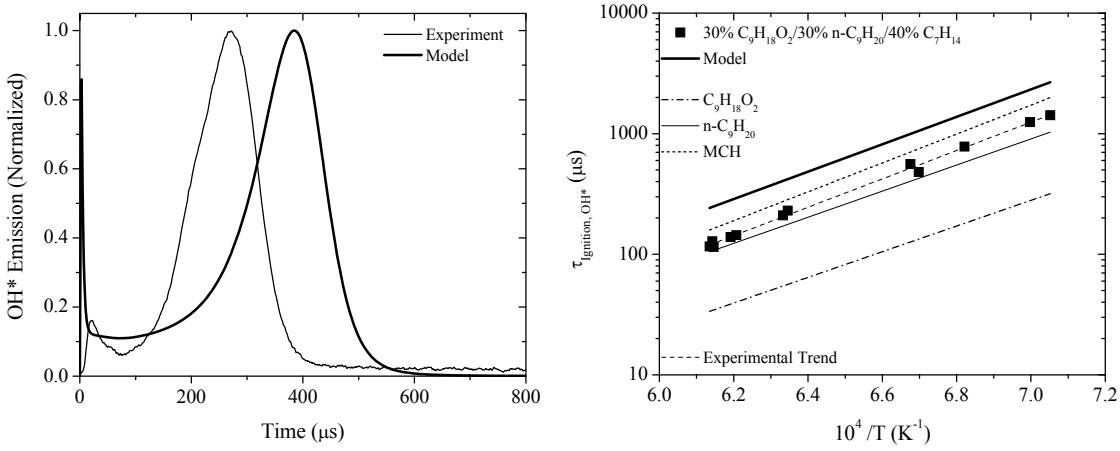

Fig. 8.11. (Left): OH* time history during oxidation of Blend 3. 1.4 atm, 1627 K, $\tau_{Ignition,\ OH^*}$: 115 μs (Experiment), 227 μs (Model). (Right): Measurements and modeling of Blend 3 ignition delay times at 1.5 atm. $42.4 \cdot 10^{-5} C_9H_{18}O_2 + 42.4 \cdot 10^{-5}$ n-$C_9H_{20} + 56.5 \cdot 10^{-5}$MCH + $8.59 \cdot 10^{-3} O_2$ + 0.99Ar (Blend 3 /ϕ = 2.0). Correlated ignition trends of $C_9H_{18}O_2$, n-C_9H_{20}, and MCH are shown for comparison and were calculated using Eqns. 5.1, 6.1, and 7.1, respectively.

The second of three fuel-rich blends contained in the L9 array is Blend 6, which is defined by a ratio of 1:6:3 methyl octanoate:n-nonane:MCH, or 10%/60%/30% volumetrically with respect to the partial fuel

volume in the experiment. Ignition delay times were extracted from OH* time histories at a nominal pressure of 5.2 atm over the range of temperature 1345 < T (K) < 1622. Figure 8.12 shows a representative OH* time history measurement during oxidation of Blend 6 at 1622 K and ignition delay times with supporting model calculations.

OH* profile time histories measured duration oxidation of Blend 6 are predicted well by the chemical kinetics model, however only at high temperatures. The FWHM of the model-calculated OH* profiles increases with decreasing temperature, which agrees with experimental observations, yet relative to the experiment are predicted to be wider. At the high-temperature extreme (1622 K), the difference between experimental and model calculations of FWHM is predicted within 10 μs (120 μs experimentally, 110 μs model-predicted). At the low-temperature extreme (1345 K), the difference is nearly 2 ms (770 μs experimentally, 2110 μs model-predicted). The overprediction of the FWHM of the OH* profile is due to imperfections in the ground-state chemistry in the compiled model. Section 6 discusses the effects of reaction rates of ground-state reactions on OH* profile shape (i.e. time dependence) and incipient OH* formation from modeling of profiles which were obtained from experiments on n-C_9H_{20}/O_2. Reactions controlling OH* profile shape and incipient peak magnitude, as presented in Section 6, can be elucidated quantitatively using sensitivity analysis and the mechanisms of these processes can be revealed from reaction pathway and rate-of-production analyses.

Ignition delay time measurements obtained at 5.2 atm show similarity to those for n-nonane (Fig. 8.12). The ignition trends of Blend 6 and n-nonane differ negligibly. At the high-temperature extreme ignition delay times between the two trends are within the scatter of the experiment. Towards the low-temperature extreme, Blend 6 ignition delay times were shorter than those predicted by the n-nonane correlation by only 20%.

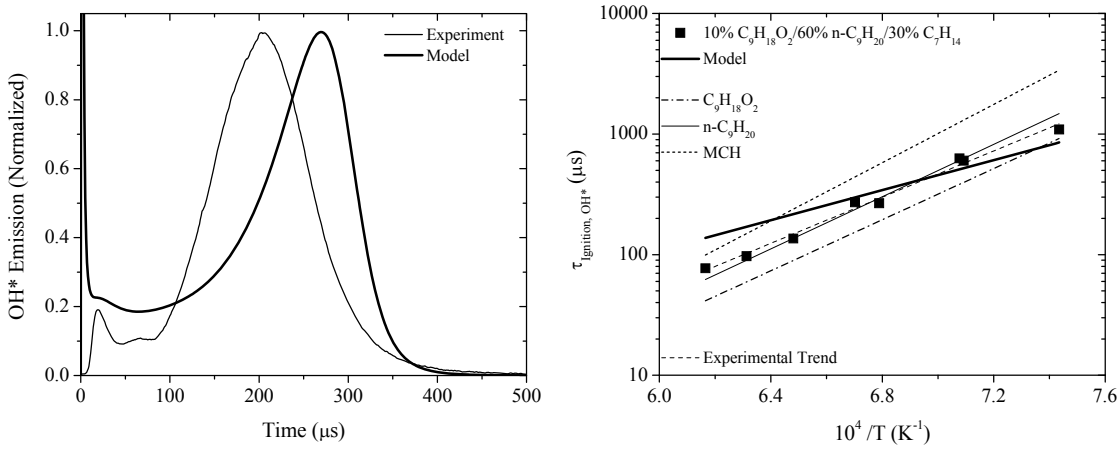

Fig. 8.12. (Left): OH* time history during oxidation of Blend 6. 5.2 atm; 1622 K; $\tau_{Ignition,\ OH^*}$: 77 μs (Experiment), 150 μs (Model). (Right): Measurements and modeling of Blend 6 ignition delay times at 5.2 atm. $13.5 \cdot 10^{-5} C_9H_{18}O_2 + 81.1 \cdot 10^{-5}$ n-$C_9H_{20} + 40.5 \cdot 10^{-5}$MCH + $8.65 \cdot 10^{-3} O_2$ + 0.99Ar (Blend 6 /ϕ = 2.0). Correlated ignition trends of $C_9H_{18}O_2$, n-C_9H_{20}, and MCH are shown for comparison and were calculated using Eqns. 5.1, 6.1, and 7.1, respectively.

With respect to methyl octanoate and MCH trends, ignition delay times of Blend 6 tended towards MCH with increasing temperature (to within 35% at the high-temperature extreme) and towards the $C_9H_{18}O_2$ trend at lower temperatures (to within 20% at the extreme). Ignition activation energy is highly underpredicted by the model; 43.7 kcal/mol (measured), 28.5 kcal/mol (calculated). Under these conditions (> 1 atm, ϕ = 2.0), this behavior is reflected in calculations for pure n-nonane. Noting the higher concentration of n-nonane in Blend 6 (60% vol.) coupled with the model behavior and the overlap of the ignition trend of Blend 6 with that of n-nonane, ignition chemistry under these conditions appears to be dominated by that of n-nonane.

The third of three fuel-rich blends contained in the L9 array is Blend 9, which is defined by a ratio of 1:3:1 methyl octanoate:n-nonane:MCH, or 20%/60%/20% volumetrically with respect to the partial fuel volume in the experiment. Ignition delay times were extracted from OH* time histories at a nominal pressure of

8.9 atm over the range of temperature 1348 < T (K) < 1587. Figure 8.13 shows a representative OH* time history measurement during oxidation of Blend 9 at 1571 K and ignition delay times with supporting model calculations.

OH* profiles modeled at higher pressures become increasingly distorted. Ignition delay times are indefinable using the model below ~1475 K due to unclear ignition peaks. OH* profiles near the high-temperature extreme are closer to those observed in the experiment in terms of ignition delay times and time dependence. At 1571 K (Fig. 8.13) the difference between experimental and model calculations of FWHM is predicted well, within 70 μs (130 μs experimentally, 200 μs model-predicted). Predictions of ignition delay times of Blend 9 agree with those obtained from the measurements, however only above ca. 1475 K. Experimentally, the ignition trend of Blend 9 overlaps that of n-nonane. This behavior was also observed at 5.2 atm (Blend 6), however at 1.5 atm (Blend 3) the ignition trend of the blended fuel deviates from that of n-nonane, particularly at lower temperatures (Figs. 8.11 and 8.12, respectively). The temperature dependence of ignition delay times for Blend 9 yielded an overall (ignition) activation energy of 49.9 kcal/mol.

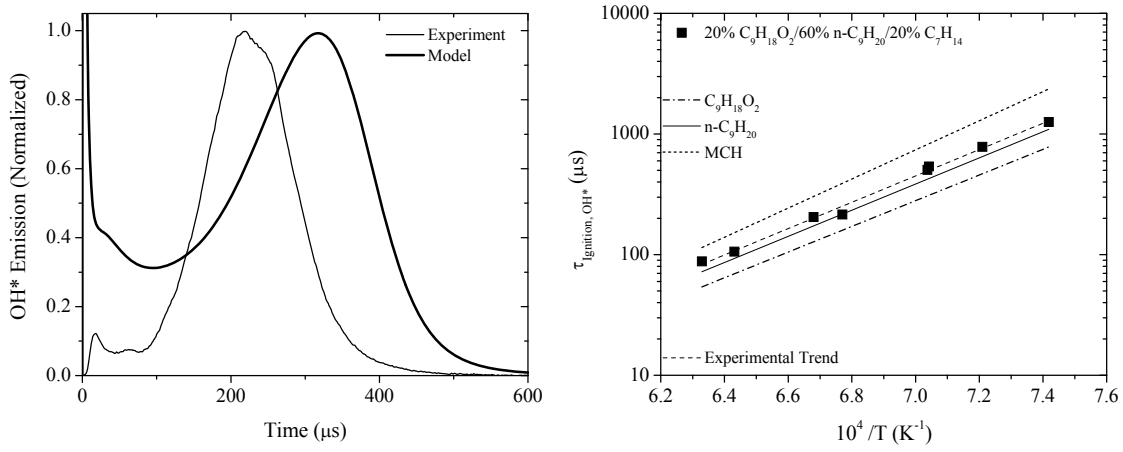

Fig. 8.13. (Left): OH* time history during oxidation of Blend 9. 8.7 atm; 1571 K; $\tau_{Ignition,\ OH^*}$: 106 μs (Experiment), 186 μs (Model). (Right): Measurements and modeling of Blend 9 ignition delay times at 8.9 atm. $26.7 \cdot 10^{-5} C_9H_{18}O_2 + 80.0 \cdot 10^{-5}$ n-C_9H_{20} + $26.7 \cdot 10^{-5}$MCH + $8.67 \cdot 10^{-3} O_2$ + 0.99Ar (Blend 9 /ϕ = 2.0). Correlated ignition trends of $C_9H_{18}O_2$, n-C_9H_{20}, and MCH are shown for comparison and were calculated using Eqns. 5.1, 6.1, and 7.1, respectively.

Figure 8.14 juxtaposes measurements and model predictions of OH* at 1571 K and 1420 K, showing the distortion of the OH* profiles with decreasing temperature. Ignition delay times using OH* profiles are unable to be defined due to extrapolation of the steepest ascent leading to negative times. From the work on improving the high-temperature behavior of the base n-nonane mechanism (Section 6), namely OH* time dependence predictions (i.e. profile shape), the three most impacting reactions were (in no specific order): $C_3H_6 \rightarrow C_2H_3 + CH_3$, $CH + H_2 \rightarrow CH_2 + H$, and $CH_2O + H \rightarrow HCO + H_2$.

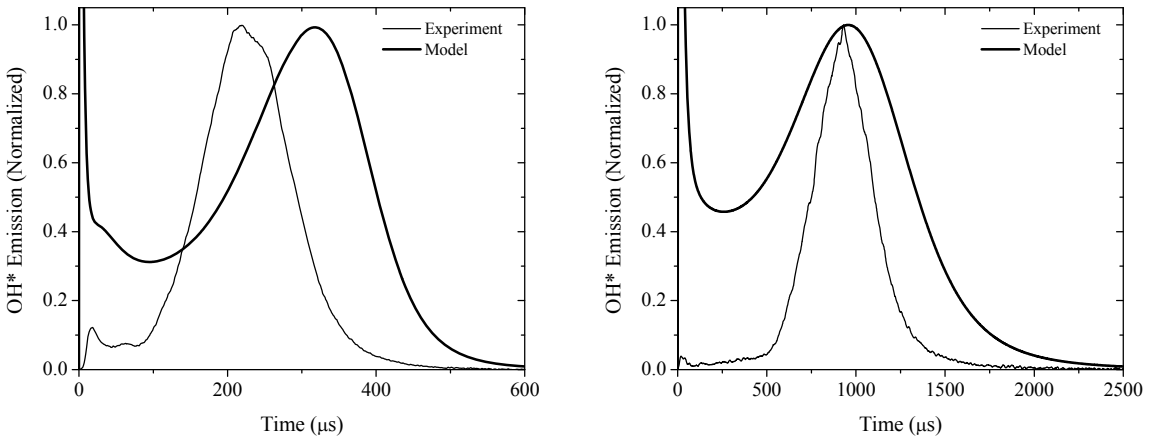

Fig. 8.14. OH* time histories from oxidation of Blend 9. (Left): 1571 K, 8.7 atm. (Right): 1420, 8.9 atm. Model-based ignition delay times are not definable below ~1475 K due to overprediction of incipient OH*. Extrapolation of a line along the steepest ascent in the modeled OH* profile at 1420 K yields an (artificial) ignition delay time of 0 μs as a result of the exaggerated magnitude and duration of OH* near time-zero.

8.4 Empirical ignition delay time correlation

An empirical ignition delay time correlation calculated using linear regression on the results obtained from 89 experiments performed on the blends is given in Eqn. 8.1. The correlation is placed in terms of molar concentrations of the fuel species and oxygen, as these parameters were varied according to fuel blend composition and equivalence ratio, respectively. A dependence on Ar concentration was neglected since this parameter remained effectively constant for a given pressure (from fixing of the mole fraction to 0.99) compared to the larger variation in the other parameters. Units in Eqn. 8.1 consist of mol/cm^3, kcal, and K

for species concentration, activation energy, and temperature, respectively. Conditions over which the equation is valid are given in Table 8.1. Percentage variation of relative fuel volume for methyl octanoate, n-nonane, and MCH ranged from 5% – 30%, 30% – 70%, and 20% – 45%, respectively. Pressure dependence (n) for the blends, n = –0.32, determined from the correlation by summation of the exponents of species concentration (from extraction of the pressure term common among the concentration (P/R_uT) terms), is near the average of that of the constituent species: n = –0.38. From similar analysis for the pure fuel ignition trends yielded pressure the following dependencies: n($C_9H_{18}O_2$) = –0.19, n(n-C_9H_{20}) = –0.48, n(MCH) = –0.46.

Table 8.1. Summary of conditions for dilute (99% Ar) shock tube experiments on ternary fuel blends.

P (atm)	T (K)	ϕ	$y_{C_9H_{18}O_2}$ ($\cdot 10^4$)	$y_{n\text{-}C_9H_{20}}$ ($\cdot 10^4$)	y_{MCH} ($\cdot 10^4$)	y_{O_2} ($\cdot 10^3$)
1 – 10	1258 – 1630	0.5 – 2.0	0.366 – 4.240	1.538 – 8.108	0.733 – 5.654	8.587 – 9.634

$$\tau\,(\mu s) = 2.39 \cdot 10^{-6}[C_9H_{18}O_2]^{0.10}[n\text{-}C_9H_{20}]^{0.32}[C_7H_{14}]^{0.62}[O_2]^{-1.35}exp(50.0/R_uT) \qquad (8.1)$$

The ignition correlation (Eqn. 8.1) was utilized to reproduce measured ignition delay times under the exact conditions at which the measurements were performed. Figure 8.15 compares calculated ignition delay times relative to measured ignition delay times at the same condition (fuel blend, ϕ, temperature, pressure). Strong agreement is shown from the fitting parameter (R^2 = 0.97). Uncertainty bands of ±10% (resulting from the ±1% uncertainty in the calculated reflected-shock temperature as discussed in Section 3) are placed on the calculated times. The difference in appearance of the ignition delay time plot of Fig. 8.15 compared to those shown previously is due to linear scaling of the abscissa ($\log_{10}$ scaling is used for $\tau_{Ignition,\ OH^*}$ – 1/T ignition delay times plots).

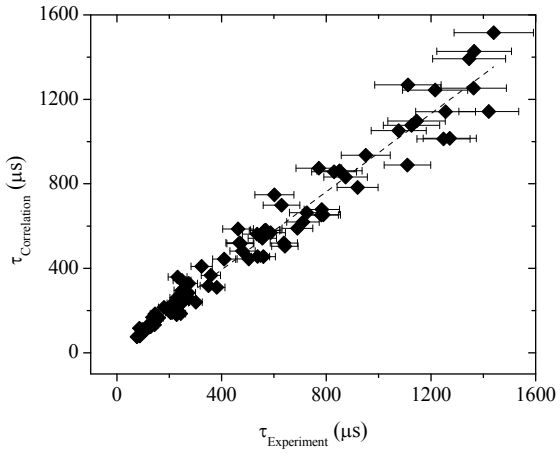

Fig. 8.15. Comparison of measured and correlated ignition delay times (Eqn. 8.1) of blended methyl octanoate/n-nonane/MCH. Error bars reflect uncertainty of ±10%. $R^2 = 0.97$.

8.5 Modeling of blending effects on time histories of stable and radical species

Calculations were performed using the compiled chemical kinetics model with the objective of assessing the influence of increased methyl octanoate concentration on the ignition behavior of two of the ternary fuel blends under conditions where the ignition delay times are well-predicted. Ignition delay times of 20%/50%/30% $C_9H_{18}O_2$/n-C_9H_{20}/MCH (Blend 2) measured approximately 25% shorter than those for the 5%/50%/45% (Blend x) at temperatures above ca. 1500 K (Fig. 8.8). A second, simultaneous objective of the calculations was to determine the ability of the model to capture effects on ignition from blending $C_9H_{18}O_2$/MCH with n-nonane relative to pure n-nonane by considering the time histories of O_2 and radicals H, O, and OH. The ignition trend of Blend x near 9 atm deviated from that of n-nonane with increasing temperature, while that of Blend 2 (near 9 atm) overlapped the ignition trend of n-nonane, within the uncertainty of the experiment, over the range of temperatures covered. The latter objective of determining deviations from n-nonane ignition kinetics is achieved by comparing the two blends selected for computational analysis to results obtained from simulating oxidation of pure n-nonane. Three different cases were considered for the calculations, differing by composition of the parent fuel: (1) n-nonane; (2) Blend x; (3) Blend 2. Under stoichiometric conditions the calculations were performed at 1460 K, 9 atm

which yielded a model-based ignition delay time of 185 μs from modeling of the OH* profile at this condition.

8.5.1 Formation/consumption of O_2, H, O, and OH

Calculations were performed to determine mole fractions of O_2, atomic hydrogen, atomic oxygen, and hydroxyl using the compiled chemical kinetics model which integrates sub-mechanisms for methyl octanoate and methylcyclohexane into a base (n-nonane) mechanism. Calculations using the model were then extended to determine the reactions responsible for the formation and/or consumption of these species and corresponding rates (μmol /cm^3·s).

No appreciable change in the predicted time history of O_2 is shown by the model (Fig. 8.16). A slight acceleration effect is shown to occur with increasing methyl octanoate concentration (note that the increase in [$C_9H_{18}O_2$] is coupled to a decrease in [MCH] by the same proportion). This result is consistent with the shorter ignition delay times shown in the trends of Blends x and 2. Relative to n-nonane, no significant difference in oxygen consumption rates are shown for Blend x and Blend 2. Mole fraction calculations on atomic hydrogen (Fig. 8.17) show a slight increase (~ 10%) in H production with increasing $C_9H_{18}O_2$ concentration (decreasing MCH concentration). The overall time dependence of H-atom consumption among the trends produced from the use of three different parent fuels differs negligibly.

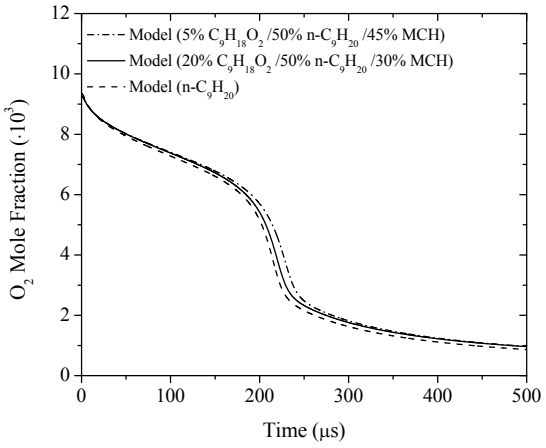

Fig. 8.16. Model prediction of O_2 mole fraction using n-nonane, Blend x, and Blend 2 as parent fuels. 1460 K, 9 atm, ϕ = 1.0, 99% Ar. $\tau_{Ignition,\ OH*}$: 185/Blend x, 167/Blend 2, 172/n-C_9H_{20}.

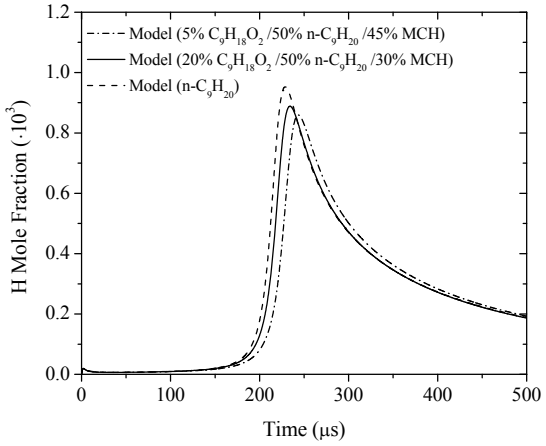

Fig. 8.17. Model prediction of H mole fraction using n-nonane, Blend x, and Blend 2 as parent fuels. 1460 K, 9 atm, ϕ = 1.0, 99% Ar. $\tau_{Ignition,\ OH*}$: 185/Blend x, 167/Blend 2, 172/n-C_9H_{20}.

Noting the importance of atomic oxygen and hydroxyl in chain-branching reactions and other ignition processes, time histories for O (Fig. 8.18) and OH (Fig. 8.19) were calculated for the three parent-fuel cases. In similar form to that for H-atom time histories, the trends indicate only a slight increase in radical production with increasing methyl octanoate (decreasing methylcyclohexane) content in the blended fuel.

Relative to mole fractions produced using n-nonane as the parent fuel, calculations for O and OH mole fractions from blended fuel oxidation shows only negligible changes. Model calculations indicate, using Blend x (5% $C_9H_{18}O_2$) as the parent fuel, a slightly slower rate of formation for both O and OH and only negligibly smaller yields. Using Blend 2 (20% $C_9H_{18}O_2$) as parent fuel, the percentage difference in radical production is the same, yet is slightly increased rather than decreased as in the case for Blend x with a lower concentration of $C_9H_{18}O_2$ (higher concentration of MCH).

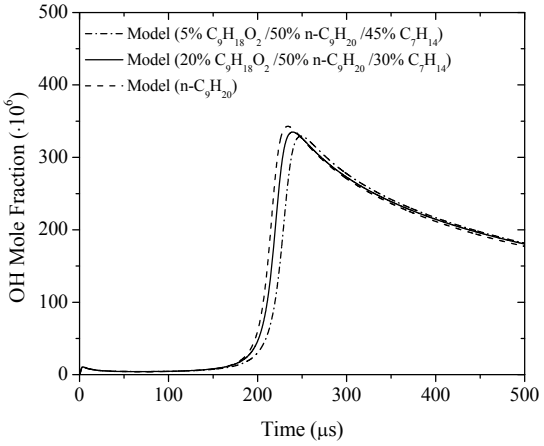

Fig. 8.18. Model prediction of OH mole fraction using n-nonane, Blend x, and Blend 2 as parent fuels. 1460 K, 9 atm, ϕ = 1.0, 99% Ar. $\tau_{Ignition,\ OH^*}$: 185/Blend x, 167/Blend 2, 172/n-C_9H_{20}.

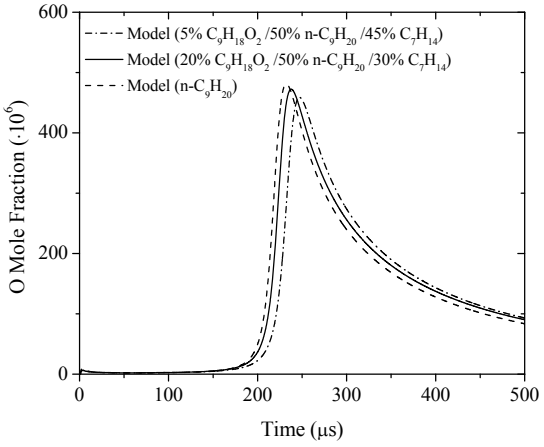

Fig. 8.19. Model prediction of atomic oxygen mole fraction using n-nonane, Blend x, and Blend 2 as parent fuels. 1460 K, 9 atm, ϕ = 1.0, 99% Ar. $\tau_{Ignition,\ OH^*}$ (μs): 185/Blend x, 167/Blend 2, 172/n-C_9H_{20}.

Rate of formation/consumption calculations were performed using only n-nonane and Blend 2 since no significant differences in the quantities of O_2, H, O, or OH being formed and/or depleted were observed in the mole fraction calculations. Since mole fractions indicate concentration for conditions of fixed pressure and temperature from $mol/cm^3 \sim (y_i P/R_u T)$, no differences in the quantities of the species were to be expected in the rate calculations. Rate of formation/consumption calculations, however, report which reactions are specifically responsible for the time history of a species. The five most influential reactions were determined for oxidation of n-nonane and for Blend 2 at 1460 K, 9 atm. Using this comparison, any observed differences in the specific reactions involving the species of interest in the case of Blend 2, relative to the use of n-nonane as a parent fuel, could then be ascribed to the presence of $C_9H_{18}O_2$ and/or MCH. While some small differences were observed in either the rate or quantity of species produced or consumed, the reactions responsible for all species remained the same for both sets of calculations. Therefore, for the conditions at which the calculations were conducted, neither the presence of the methyl ester species nor methylcyclohexane impacts the model prediction of O_2 or the formation and consumption of O, H, or OH radicals.

Reactions primarily responsible for consumption of O_2 are shown in Fig. 8.20 for n-nonane as parent fuel and for Blend 2 as parent fuel. The most prominent reaction for consumption of oxygen is the chain-branching $H + O_2 \rightarrow OH + O$ reaction. The abrupt depletion in oxygen is coincident with the ignition delay time predicted by the model (185 μs) using the steepest ascent in OH* as the marker for ignition. In both cases, initiation reactions involving vinyl consumed oxygen rapidly in the first 30 – 40 μs. Hydroperoxy radical formation with CO from $HCO + O_2$ also contributes to oxygen consumption in the first 20 μs. Neither the main chain-branching mechanism driving ignition, nor the initiation reactions were altered despite 50% of n-nonane being replaced by 20% and 30% methyl octanoate and MCH, respectively, in Blend 2. This result points to either an insensitivity by the model to the presence of these species or the dominance of n-nonane ignition chemistry.

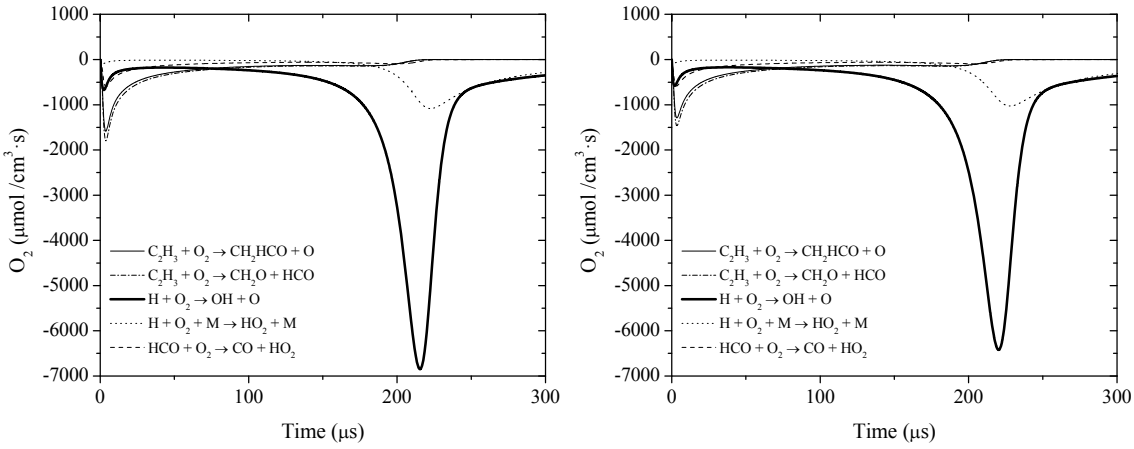

Fig. 8.20. Rate of production/consumption calculations for O_2 using n-nonane (Left) and Blend 2 (Right) as parent fuel. 1460 K, 9 atm, $\phi = 1.0$, 99% Ar. $\tau_{Ignition,\ OH^*}$ (μs): 172/n-C_9H_{20}, 167/Blend 2.

Reactions primarily responsible for the formation and/or depletion of H are shown in Fig. 8.21 for n-nonane as parent fuel and for Blend 2 as parent fuel. The model results indicate no difference in the reactions involved in atomic hydrogen production or consumption. In the first 40 – 50 μs, H atoms are most strongly produced by decomposition of both ethyl and formyl radicals from interaction with third-body colliders. Simultaneously upon incipient formation of H, ethylene is indicated as the primary consumer of H for both cases. Near the point of ignition indicated from the modeled OH* profile (185 μs), atomic hydrogen is produced from the propagation reaction $H_2 + OH \rightarrow H_2O + H$ and is immediately consumed by the chain-branching reaction $H + O_2 \rightarrow OH + O$. Contributions for H-atom production and consumption near ignition also come from $HCO + M \rightarrow H + CO + M$ and $C_2H_4 + H \rightarrow C_2H_3 + H_2$, respectively.

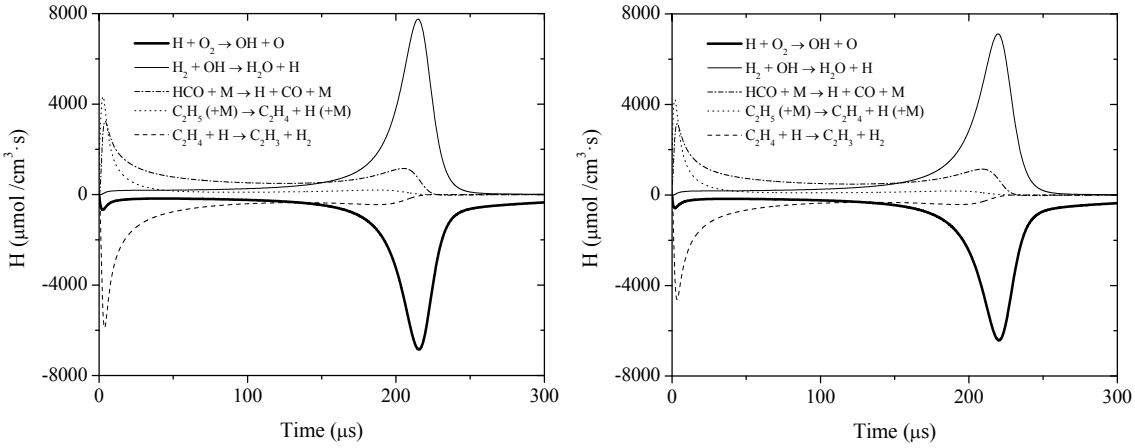

Fig. 8.21. Rate of production/consumption calculations for H using n-nonane (Left) and Blend 2 (Right) as parent fuel. 1460 K, 9 atm, ϕ = 1.0, 99% Ar. $\tau_{Ignition,\ OH^*}$ (μs): 172/n-C_9H_{20}, 167/Blend 2.

Reactions primarily responsible for the formation and/or depletion of atomic oxygen are shown in Fig. 8.22 for n-nonane as parent fuel and for Blend 2 as parent fuel. In-line with the predictions for O_2 consumption and H formation and depletion, the model results indicate no difference in the reactions involved in atomic oxygen production or consumption. For both parent fuels, in the first 20 – 30 μs, O atoms are most strongly produced from consumption of O_2 by vinyl forming $H_2C{-}C(=O)H$ and O radicals, followed by $H + O_2 \rightarrow OH + O$. No other contribution to the formation of O atoms is indicated in the results. Near the point of ignition, oxygen atoms are formed solely by $H + O_2 \rightarrow OH + O$ and consumed primarily by $O + H_2 \rightarrow OH + H$ with minor contributions from oxidation of acetylene leading to ethynyloxy ($HC{\equiv}C{=}O$) and H radicals and from $CH_3 + O \rightarrow H + CH_2O$.

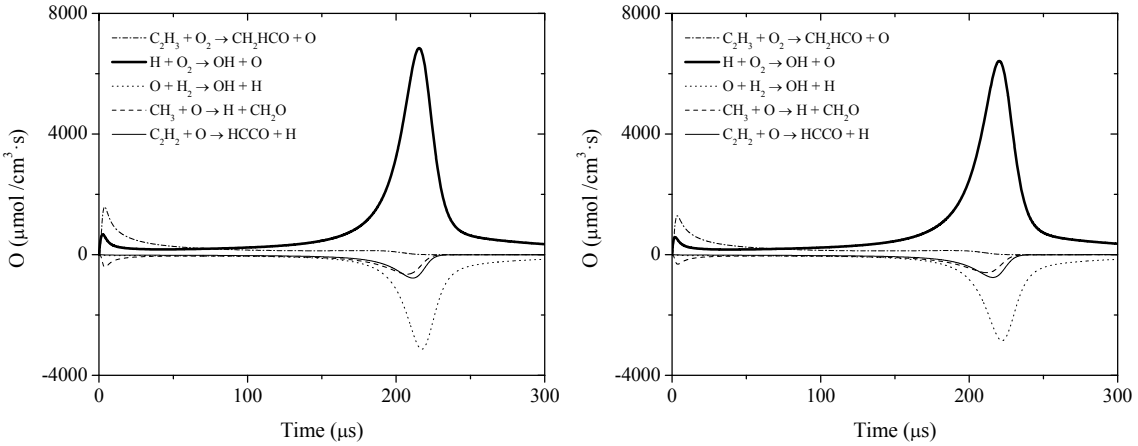

Fig. 8.22. Rate of production/consumption calculations for atomic oxygen using n-nonane (Left) and Blend 2 (Right) as parent fuel. 1460 K, 9 atm, $\phi = 1.0$, 99% Ar. $\tau_{Ignition,\ OH^*}$ (μs): 172/n-C_9H_{20}, 167/Blend 2.

Identical to the results for O_2 consumption, H and O formation and consumption, dominant reactions responsible for the formation and/or depletion of OH, shown in Fig. 8.23 for n-nonane oxidation and Blend 2 oxidation, are independent of parent fuel composition with only negligible (~ 10%) differences observed in peak rates of OH formation: 7780 μmol /cm^3·s for n-nonane as parent fuel, 7145 μmol /cm^3·s for Blend x as parent fuel. Similar difference is noted for OH production by H + O_2. Hydroxyl is formed primarily near the point of ignition by the following reactions (in descending order of OH production): H + $O_2 \rightarrow$ OH + O, O + $H_2 \rightarrow$ OH + H, H + $HO_2 \rightarrow$ OH + OH. Consumption of OH comes predominantly from H_2 + OH $\rightarrow$ H_2O + H with secondary contribution from CO + OH $\rightarrow$ CO_2 + H.

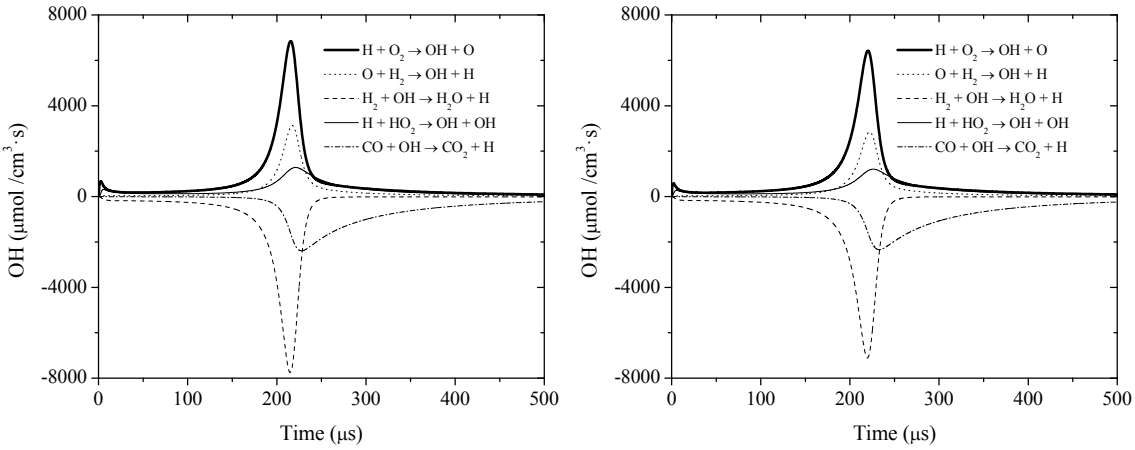

Fig. 8.23. Rate of production/consumption calculations for OH using n-nonane (Left) and Blend 2 (Right) as parent fuel. 1460 K, 9 atm, ϕ = 1.0, 99% Ar. $\tau_{Ignition,\ OH^*}$ (μs): 172/n-C_9H_{20}, 167/Blend 2.

8.5.2 Sensitivity analysis of OH formation*

In order to assess the sensitivity of the compiled chemical kinetics model to methyl octanoate and MCH species, time-dependent sensitivity coefficients were calculated for the 10 most influential reactions involved in the production and/or consumption of excited-state OH under stoichiometric conditions at 1460 K and 9 atm for two cases: (1) n-nonane as parent fuel, (2) Blend 2 as parent fuel. Calculations were performed relative to the case where pure n-nonane is the parent fuel species since the mechanism of the present work is based on a model for n-nonane oxidation and due to the species occupying the largest volumetric percentage in Blend 2. For clarity, results are presented in two separate figures. Sensitivity analysis results for pure n-nonane oxidation using the present model are shown in Figs. 8.24a and 8.24b with the calculated OH* mole fraction shown for correspondence of ignition delay time with abrupt changes in sensitivity coefficients. H + O_2 forming OH + O is the reaction to which OH* formation, and through utilization of OH* profiles for ignition delay time definition, the reaction most controlling of ignition. The next most influential reactions controlling OH* (in descending order) are $C_2H_3 + O_2 \rightarrow CH_2HCO + O$, $H_2 + OH \rightarrow H_2O + H$, and $HCO + M \rightarrow H + CO + M$. In Fig. 8.24b, sensitivity coefficients for OH* for reactions $CH_2CO + H \rightarrow HCCO + H_2$ and $C_3H_6 + O \rightarrow CH_3CHCO + H + H$ take on the same

behavior. Calculation of sensitivity coefficients and corresponding dominant reactions controlling OH* using Blend 2 as the parent fuel species identifies the same set of reactions produced from analysis using n-nonane as the parent fuel. The time dependencies of the sensitivity coefficients for respective reactions using Blend 2 are also identical. For brevity, only the results of n-nonane as parent fuel are shown. Notable in the results of sensitive reactions to OH* formation is the absence of any reactions directly involving OH*. This is in contrast to previous calculations involving pure n-nonane, presented in Section 6, where the two dominant OH* formation reactions ($CH + O_2 \rightarrow OH^* + CO$ and $H + O + M \rightarrow OH^* + M$) were present and emphasizes the impact of ground-state chemistry on OH* profiles.

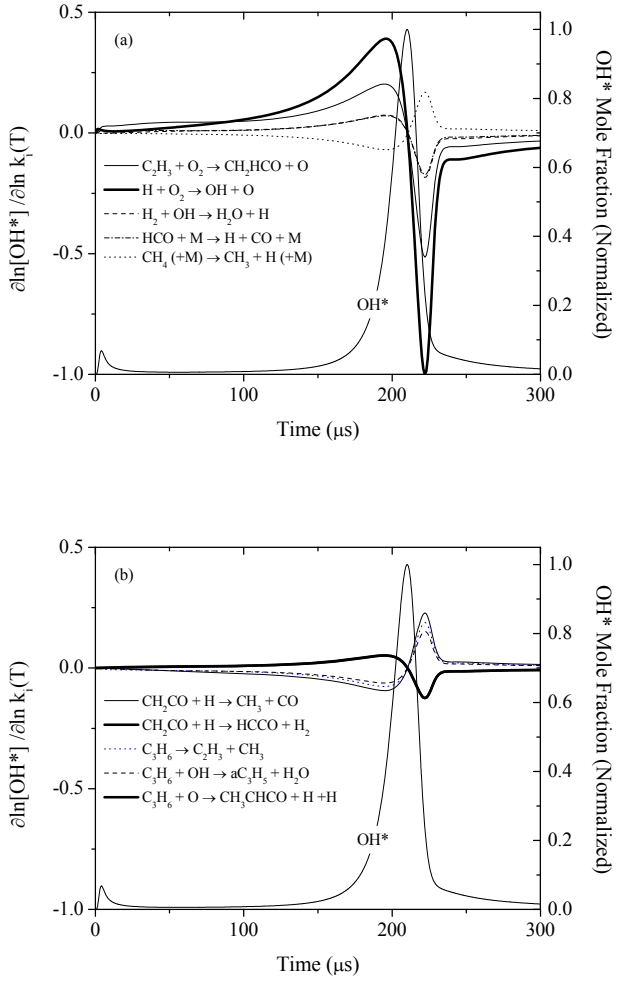

Fig. 8.24. Normalized OH* sensitivity coefficients and mole fraction using n-nonane as parent fuel. 1460 K, 9 atm, $\phi = 1.0$, 99% Ar. (a): Top five dominant reactions; (b): Bottom five dominant reactions.

8.6 Concluding remarks on oxidation experiments and modeling of ternary fuel blends

Experiments were performed on a series of blended ternary fuels of methyl octanoate/n-nonane/methylcyclohexane using a Design of Experiments approach, namely a 3-level L9 array. Four sets of test variables (equivalence ratio, pressure, and fuel-volume percentages of methyl octanoate and MCH) were selected to define the array with each variable having three levels. Levels of equivalence ratio, pressure, and relative fuel-volume percentages of methyl octanoate and MCH of 0.5, 1.0, and 2.0, 1.5 atm, 5.0 atm, and 9.0 atm, 10% – 30%, and 20% – 40% were chosen, respectively. From measurements of ignition delay times under these conditions, an empirical ignition delay time correlation was developed. The equation also included a tenth ternary fuel blend not incorporated into the L9 array (Blend x: 5%/50%/45% $C_9H_{18}O_2$/n-C_9H_{20}/MCH) which extended the lower and upper limits of methyl octanoate and MCH to 5% and 45%, respectively.

The chemical kinetics model compiled from integration of sub-mechanisms for methyl octanoate [42] and MCH [25] into the base n-nonane mechanism of Rotavera et al. [48] performed well under certain conditions and poorly for other conditions. For the following blends and specific equivalence ratio and pressure conditions, ignition trends overlap with both the model and with empirical trends of n-nonane: (Blend 7, ϕ = 0.5, 9.3 atm), (Blend 2, ϕ = 1.0, 9.3 atm). Blend x (ϕ = 1.0, 1.4 atm) overlapped the ignition trend of n-nonane without model agreement. Other blends deviated from both model predictions of ignition and the n-nonane trend: (Blend 1, ϕ = 0.5, 1.4 atm), (Blend 4, ϕ = 0.5, 4.7 atm), (Blend x, ϕ = 1.0, 9.1 atm), (Blend 2, ϕ = 1.0, 1.5 atm), (Blend 5, ϕ = 1.0, 4.6 atm), (Blend 8, ϕ = 1.0, 9.3 atm), and (Blend 3, ϕ = 2.0, 1.5 atm). Temperature dependence of the trends (i.e. ignition activation energies) were calculated to within 10% with the exception of Blend 2 (ϕ = 1.0) under both 1.5-atm and 9.3-atm pressure and Blend 6 (ϕ = 2.0, 5.2 atm). Table 8.2 summarizes model performance in predicting ignition activation energy for the 10 ternary fuel blends.

Table 8.2. Comparison of measured and model-predicted ignition activation energies for ternary fuel blends.

Blend	P (atm)	ϕ	$E_{a,\ Experiment}$ (kcal/mol)	$E_{a,\ Model}$ (kcal/mol)	% Difference
1	1.5	0.5	53.7	52.0	–3.3
2	1.5	1.0	53.0	44.8	–18.3
2	9.3	1.0	51.9	43.6	–19.0
3	1.5	2.0	53.7	52.0	–3.3
4	4.7	0.5	49.8	53.8	7.4
5	4.6	1.0	45.5	45.2	–0.7
6	5.2	2.0	43.7	28.5	–53.3
7	9.3	0.5	56.0	51.9	–7.9
8	9.3	1.0	44.4	43.6	–1.8
9	8.9	2.0	49.9	-	-
x	1.5	1.0	49.4	46.9	–5.3
x	9.1	1.0	43.7	44.3	1.4

Model-based FWHM values of OH* profiles relative to the experiments are well characterized only for the following blends and corresponding conditions of equivalence ratio and pressure: (Blend 1, ϕ = 0.5, 1.5 atm), (Blend x, ϕ = 1.0, 1.5 atm), (Blend 2, ϕ = 1.0, 1.5 atm), (Blend 3, ϕ = 2.0, 1.5 atm). The consistent parameter at which accurate predictions of OH* FWHM are made is a pressure of 1.5 atm. At elevated pressures, the FWHM of calculated OH* profiles became smaller than those observed in the experiment. Noting that chemiluminescence rates do not impact OH* profile time histories (Section 6), the discrepancy in the modeled OH* profiles relative to the measured profiles is ascribed to imperfections in the ground-state chemistry of the model. Moreover, with increased-pressure OH* profiles modeled under fuel-rich conditions became increasingly distorted, and calculations near 10 atm were unusable below 1475 K for purposes of defining ignition delay times.

Due to the importance of O_2, H, O, and OH to combustion phenomena, calculations of mole fractions (time histories) and rates of formation/consumption were performed using the model, where either n-nonane, Blend x, or Blend 2 served as parent fuel. No significant differences in mole fractions or reactions responsible for consumption and/or production of these species were observed. Noting the constant 50% fuel volume in the Blends x and 2, the absence of any blending effect indicates that either n-nonane kinetics govern ignition processes of these two fuel blends or an insensitivity of the model to the presence of either methyl octanoate or MCH. Given the number of reactions contained in the sub-mechanisms specific to $C_9H_{18}O_2$ and MCH (1080 and 260, respectively) it is more plausible that the 50% concentration contained in the fuel blends (Blend x and Blend 2) dominates ignition chemistry.

9. EMPIRICAL COMPARISON OF IGNITION BEHAVIOR OF PURE AND BLENDED FUELS

The sections below concern the empirical characterization of the constituent fuels in terms of relative equivalence ratio and pressure dependence for the pure fuels (Section 9.1). Analysis is then extended to compare the ignition behavior of the ternary fuel blends relative to those of the pure-fuel constituents by employing the ignition correlation for the blended fuel (Eqn. 8.1). Calculations using the correlations utilize concentration extrema over which the correlations are valid to assess the effect of relative fuel percentage on ignition delay times (Section 9.2). Calculations were performed for ϕ = 0.5, 1.0, and 2.0 at a pressure of 1.5 atm. Comparisons at 9.5 atm were made to include the effect of increased pressure on the relative ignition trends between the fuel blends and constituent species. The utility of the ignition delay time correlations defined previously for the ternary fuel blend and three constituent fuels (Eqns. 5.1, 6.1, 7.1) lies in the ability to compare ignition trends over the range of conditions which were not directly measured, yet are within the limits of the correlation boundaries.

Experimental ignition trends of methyl octanoate, n-nonane, and methylcyclohexane were compared over the range of thermodynamic conditions: 1175 K – 1670 K, 1.5 – 10 atm, ϕ = 0.5 – 2.0. Under near-atmospheric pressure (1.5 atm), ignition delay times were of the following order for the pure fuels: methyl octanoate < n-nonane < methylcyclohexane. Experimental results also indicate that the ignition behavior of the higher-order methyl ester approaches that of the higher-order linear alkane with increased pressure and nearly overlaps n-nonane ignition trends for ϕ = 0.5 and ϕ = 2.0. Methyl octanoate displayed significantly lower pressure dependence relative to the linear alkane and cycloalkane. Table 9.1 provides the correlation parameters for the study as extracted from linear regression analysis which yields the generic equation describing ignition:

$$\tau(\mu s) = A[Fuel]^x[O_2]^y exp(E_a/R_u T) \qquad (9.1)$$

Table 9.1. Ignition delay time correlation parameters and corresponding pressure dependence. Fuel exponents for the blends are in the order $C_9H_{18}O_2$/n-C_9H_{20}/MCH. Pressure dependence determined from: x + y = n. The pressure dependence of the blended fuels (n = –0.32) is 15% lower relative to that calculated using an averaging of the pure fuel pressure dependencies ($n_{Average}$ = –0.38).

Species	A	x	y	n	E_a (kcal/mol)
$C_9H_{18}O_2$	$3.09 \cdot 10^{-6}$	0.84	–1.03	–0.19	48.7
n-C_9H_{20}	$2.71 \cdot 10^{-8}$	0.73	–1.21	–0.48	51.0
C_7H_{14}	$2.15 \cdot 10^{-8}$	0.91	–1.36	–0.46	54.7
Blends	$2.38 \cdot 10^{-6}$	0.10/0.32/0.62	–1.36	–0.32	50.1

9.1 Comparison of ignition behavior of pure fuels at fixed equivalence ratio and pressure

Comparison of ignition delay time measurements for methyl octanoate, n-nonane, and methylcyclohexane are shown in Fig. 9.1 at a fuel-lean equivalence ratio of ϕ = 0.5 for 1.5 atm and 10.0 atm (nominal) pressure. Results are compared over the temperature range 1263 < T (K) < 1535 for 1.5 atm and 1268 < T (K) < 1492 for 10.0 atm. Average experimental pressures for $C_9H_{18}O_2$ and MCH were 9.5 atm and 11.6 atm, respectively for elevated-pressure measurements. n-Nonane ignition delay times were correlated using Eqn. 6.1 using the average experimental pressure from [16] of 10.4 atm.

Ignition trends at 1.5 atm were of the following order: methyl octanoate < n-nonane < methylcyclohexane. Methyl octanoate exhibited more-rapid ignition relative to both the linear alkane and the cycloalkane. Methylcyclohexane and n-nonane are slower by factors of 4 and 3, respectively. The methyl ester and cycloalkane species were observed to have similar temperature dependence. Ignition activation energies (E_a) for $C_9H_{18}O_2$ and MCH of 53.0 and 57.9 kcal/mol, respectively, were measured, differing by approximately 10%. Due to a 2% difference in dilution between the present results and the n-nonane measurements of [16] (ignition measurements of n-nonane were made using 97.1% dilution), a direct comparison of ignition activation energy to n-nonane is not feasible.

At increased pressure (~10.0 atm), ignition trends for n-nonane and methyl octanoate were observed to overlap strongly above 1300 K, below which the trends diverged with methyl octanoate again showing increased reactivity relative to the alkane. Methylcyclohexane ignition delay times were longer than the other two species, diverging with decreasing temperature to times 45% and 60% longer than n-nonane and methyl octanoate, respectively. Ignition activation energy at 10.5 atm decreased for $C_9H_{18}O_2$ by approximately 10 kcal/mol and 3 kcal/mol for MCH (E_a of 43.8 and 54.1 kcal/mol, respectively) relative to results at 1.5 atm.

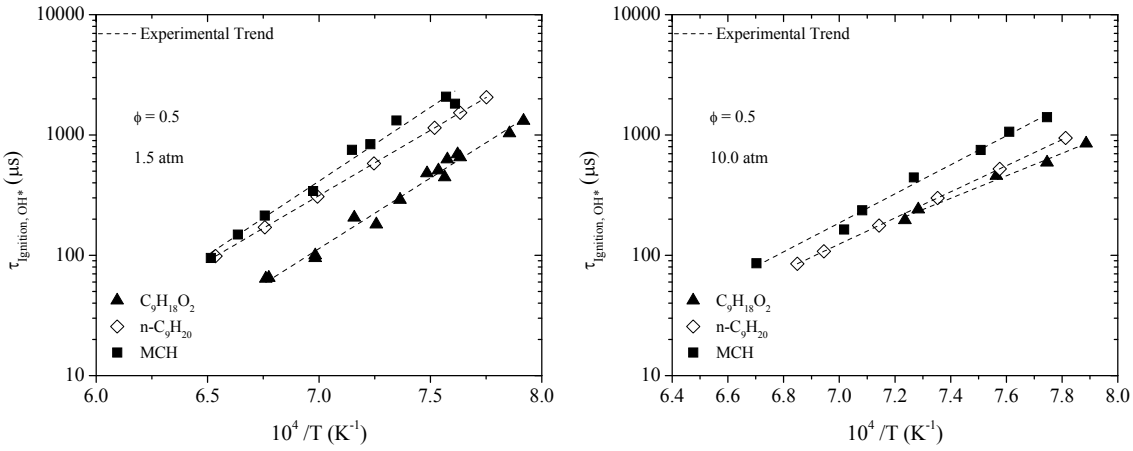

Fig. 9.1. Comparison of lean (ϕ = 0.5) ignition trends of methyl octanoate, n-nonane, and methylcyclohexane at 1.5 atm (Left) and 10.0 atm (Right) in 99% Ar.

Comparison of stoichiometric ignition delay time measurements for methyl octanoate, n-nonane, and methylcyclohexane are shown in Fig. 9.2. Temperature and pressure conditions for the comparison are 1269 < T (K) < 1565 for 1.5 atm and 1243 < T (K) < 1494 for 10.0 atm (nominal). Average experimental pressures for $C_9H_{18}O_2$ and MCH were 9.3 atm and 11.3 atm, respectively for elevated-pressure measurements. n-Nonane ignition delay times were correlated using Eqn. 6.1 using the average experimental pressure from [16] of 10.4 atm.

Stoichiometric ignition trends at 1.5 atm follow the same order as those for the lean condition: methyl octanoate < n-nonane < methylcyclohexane. Similarly, methyl octanoate exhibited more-rapid ignition relative both the linear alkane and the cycloalkane. Methylcyclohexane and n-nonane were slower by factors of 4 and 2, respectively. Ignition activation energies for the linear alkane and cycloalkane were similar, yet closer than those of the lean condition: 59.0 and 56.2 kcal/mol for n-C_9H_{20} and MCH, respectively, differing by less than 5%. The temperature trend for $C_9H_{18}O_2$ is considerably lower (44.6 kcal/mol). Stoichiometric measurements of n-nonane from [16] were made at 98.5% (negligibly lower than the level of dilution herein, thereby allowing for close comparison). Although to a lesser extent relative to the ϕ = 0.5 condition, stoichiometric ignition behavior of methyl octanoate and of n-nonane approach one another as a result of the increase in pressure. Ignition activation energies at elevated pressure for $C_9H_{18}O_2$ and MCH of 51.2 and 49.5 kcal/mol, respectively, were measured. Stoichiometric measurements of n-nonane at 10.4 atm from [16] yielded E_a of 44.9 kcal/mol.

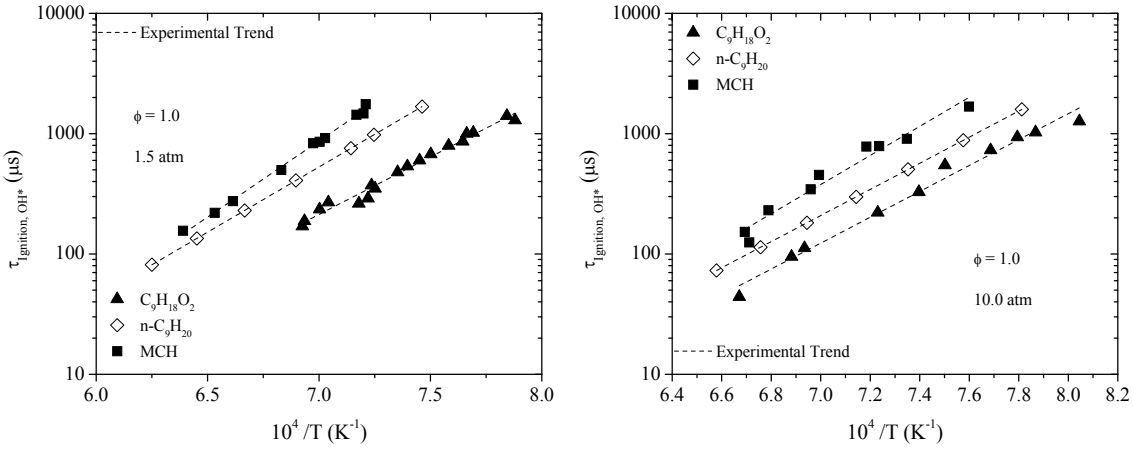

Fig. 9.2. Comparison of lean (ϕ = 1.0) ignition trends of methyl octanoate, n-nonane, and methylcyclohexane at 1.5 atm (Left) and 10.0 atm (Right) in 99% Ar.

Ignition delay time comparisons of measurements for methyl octanoate, n-nonane, and methylcyclohexane are shown in Fig. 9.3 at a fuel-rich equivalence ratio of ϕ = 2.0 for 1.5 atm and 10.0 atm (nominal) pressure. Results are compared over the temperature range 1370 < T (K) < 1672 for 1.5 atm and 1327 < T

(K) < 1602 for 10.0 atm. Average experimental pressures for $C_9H_{18}O_2$ and MCH were 9.2 atm and 11.5 atm, respectively for the elevated-pressure measurements. n-Nonane ignition delay times were correlated using Eqn. 6.1 using the average experimental pressure from [16] of 10.3 atm.

Ignition activation energies at ϕ = 2.0, 1.5 atm for $C_9H_{18}O_2$ and MCH of 56.9 and 56.1 kcal/mol, respectively, were measured from the temperature dependence of the ignition delay times. Measurements of n-nonane at ϕ = 2.0 from [16], which were obtained at 99.2% dilution in Ar, revealed an E_a of 54.1 kcal/mol. Ignition trends at 1.5 atm were of the following order: methyl octanoate < n-nonane < methylcyclohexane. In similar manner, as observed under the previous conditions, the ignition trends of methyl octanoate and n-nonane again approach one another resulting from the increase in pressure. Ignition activation energies at 10.0 atm for $C_9H_{18}O_2$ and MCH of 46.3 and 45.3 kcal/mol, respectively, were measured. Fuel-rich measurements of n-nonane ignition from [16] yielded an E_a of 52.8 kcal/mol.

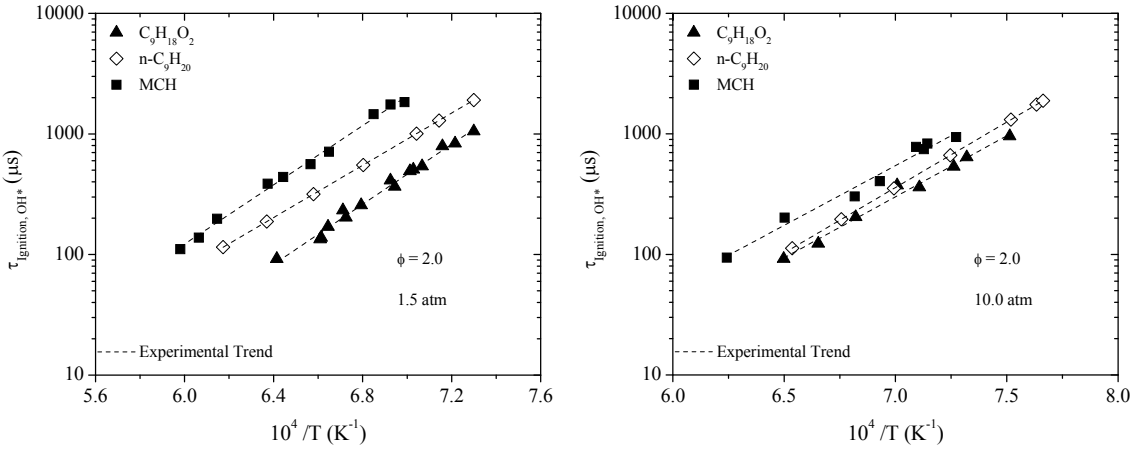

Fig. 9.3. Comparison of lean (ϕ = 2.0) ignition trends of methyl octanoate, n-nonane, and methylcyclohexane at 1.5 atm (Left) and 10.0 atm (Right) in 99% Ar.

9.2 Empirical analysis of blending effects on ignition of $C_9H_{18}O_2$/n-C_9H_{20}/MCH

Due to the nature of the L9 array assembled for the study, direct comparison of ignition delay times for all conditions is not possible. However, in the work of Rotavera and Petersen [135], ternary blends of methyl octanoate/n-nonane/MCH were studied under identical conditions as in the present study. Holding n-nonane concentration constant at 50%, methyl octanoate concentrations of 5% and 20% were used under stoichiometric conditions near 10 atm. Figure 9.4 shows a direct comparison of the effect of blending the three fuels on global ignition including the two blends from [135] and the 10/50/40 blend from the L9 array. The three blends lie between the trends of n-nonane and methylcyclohexane. Notable in the trends is the decreased ignition activation energy of the blends with the lower concentrations of methyl octanoate (5% and 10% vol.), yet at 20% (vol.) the activation energy of the trend increases by 15% to 51.9 kcal/mol relative to the average of the 5% and 10% trends which are within the scatter of one another and therefore share nearly identical activation energies (5% blend: 43.7 kcal/mol; 10% blend: 44.4 kcal/mol).

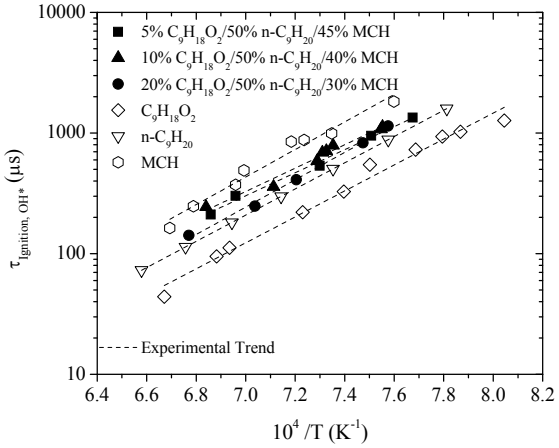

Fig. 9.4. Measured stoichiometric ignition delay time trends for three ternary blends compared to constituent species at 9.5 atm (MCH ignition times are pressure corrected to 9.5 atm from 11.5 atm using n = –0.45). 5% $C_9H_{18}O_2$: Blend x; 10% $C_9H_{18}O_2$: Blend 8; 20% $C_9H_{18}O_2$: Blend 2.

The utility of the ignition delay time correlations employed herein to assess the effects of blending ratios of the ternary fuel on ignition lies in the ability to compare ignition trends over the range of conditions which were not directly measured, yet are within the limits of the correlation boundaries. To this end, concentrations and relative proportions measured experimentally can be replicated using the correlation to verify accuracy. Ignition delay times calculated using the correlation equation for the ternary fuel blend (Eqn. 8.1), compared to measured ignition delay times for respective fuel blends are shown in Fig. 9.5. Blends 1, 2, and 3 covering lean, stoichiometric, and rich conditions, respectively, and 1.5 – 9.3 atm are correlated well. The blends also span the full range of fuel volume percentages for the constituent species, as defined in the L9 array.

The ensuing sections discuss empirical ignition trends of $C_9H_{18}O_2$/n-C_9H_{20}/MCH fuel blends over the range of concentration extrema covered experimentally in the present study. Ignition trends for lean (ϕ = 0.5), stoichiometric, and fuel-rich (ϕ = 2.0) equivalence ratios were calculated and compared to the ignition trends of the pure fuels over the same conditions of temperature and pressure for a given equivalence ratio. For each equivalence ratio, calculations were performed using fixed fuel concentration for one constituent (e.g. 5% $C_9H_{18}O_2$, Fig. 9.6) while varying the percentages of the other two over the maximum and minimum percentages allowable given the percentage level of the fixed fuel. The percentage of the fixed fuel in the blend is then increased to its maximum in the present work (e.g. 30% $C_9H_{18}O_2$, Fig. 9.6) and adjustments to the remaining two constituents are made accordingly within the bounds of concentration covered experimentally. These effects are juxtaposed to compare the effects of blending on ignition delay time.

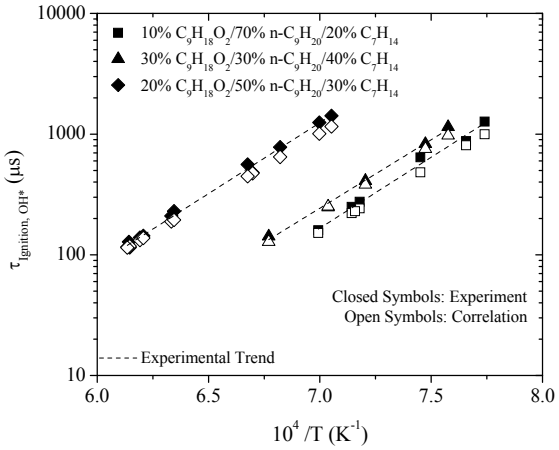

Fig. 9.5. Comparison of measured and correlated ignition delay times for Blends 1 (ϕ = 0.5, 1.5 atm), 2 (ϕ = 1.0, 4.5 atm), and 3 (ϕ = 2.0, 9.5 atm). Strong agreement between measured and correlated ignition delay times from ternary fuel blend experiments permits parametric study of blending effects.

An experimental sensitivity analysis was performed to identify the individual influence of the four parameters defining the L9 array with respect to ignition delay times of the blended fuels. Experimental sensitivity coefficients were determined by taking the difference of the averages of ignition delay times measured at the extrema of the four L9 parameters (e.g. difference in ignition delay times between averaged ϕ = 2.0 blends and averaged ϕ = 0.5 blends; similarly for pressure, %$C_9H_{18}O_2$, and %MCH) at a comparable temperature were the correlation overlaps with the temperature ranges at which measurements were obtained (1375 K). Since ignition delay times were not obtained for all blends at the specific temperature used for comparison (1375 K), the blended correlation (Eqn. 8.1) was used to determine the ignition delay time for all blends at this temperature. The results indicate that equivalence ratio is the most influential parameter on ignition delay times. The next most impacting parameter (pressure) was a factor of 2 less influential than ϕ over the range of conditions studied. Of the two fuels included in the L9 array, MCH had nearly twice the impact on ignition delay times compared to methyl octanoate. Since n-nonane is not considered as part of the L9 array (the mole fraction of n-nonane is dictated by the ratio of $C_9H_{18}O_2$/MCH), experimental sensitivity was not calculated since it did not have 3 values to average.

Figure 9.6 shows the results of the experimental sensitivity analysis normalized to the equivalence ratio effect. Appendix H contains the details of the calculation.

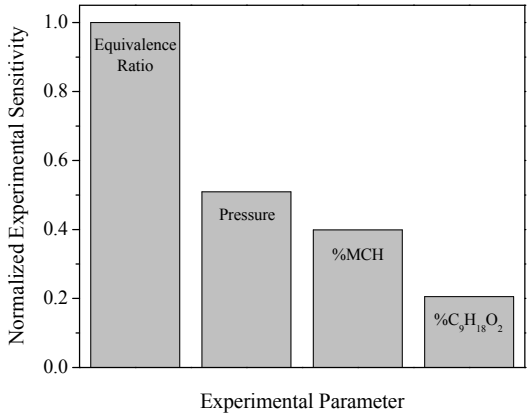

Fig. 9.6. Comparison of experimental sensitivity coefficients (normalized) determined using average values of ignition delay times at the extrema of the L9 array parameters. Equivalence ratio is shown to most strongly influence ignition delay times of the ternary fuel blends.

9.2.1 Blending effects on fuel-lean ignition of $C_9H_{18}O_2$/n-C_9H_{20}/MCH

Ignition delay time trends under fuel-lean (ϕ = 0.5) conditions were calculated for 5% and 30% methyl octanoate blends at 1.5 atm over the temperature range 1300 < T (K) < 1600 (Fig. 9.6). Calculations using the 5% $C_9H_{18}O_2$ concentration included variation in n-nonane and MCH from 55% – 70% and 25 – 40%, respectively. For the 30% $C_9H_{18}O_2$ blend, n-nonane and MCH concentrations were varied from 30% – 50% and 20% – 40%. Under lean conditions, the blended-fuel ignition trends lie below that of n-nonane and above that of methyl octanoate. Ignition delay times of the 5%/55%/40% blend were 30% shorter than the n-nonane trend and 90% longer than the methyl octanoate trend. For the 5%/70%/25% blend, ignition delay times were closer to those of pure methyl octanoate, to within 45%, and shorter by an equivalent amount relative to n-nonane. Relative differences to methyl octanoate and n-nonane for the 30% methyl octanoate blends are nearly identical to those of the 5% methyl octanoate blend.

Comparing the ignition delay times of the 5%/55%/40% blend with those of the 30%/30%/40% blend at 1400 K, noting the only change between the two being the 25% change in methyl octanoate and n-nonane volumes, ignition delay times of 310 μs are predicted for both, indicating no dependence on the $C_9H_{18}O_2$/n-C_9H_{20} ratio. Noting the nearly identical ignition activation energies of the trends, this similarity is consistent over the range of temperatures covered. From this comparison, the shortened ignition delay times observed between the two trends can then be ascribed to the reduction in MCH concentration. At 1400 K, ignition delay times of the lower-MCH concentration blends were nearly identical: 225 μs and 240 μs for the 5%/70%/25% and 30%/50%/20% blends, respectively. Quantitatively, the ~ 40% reduction in MCH concentration in the fuel blend shortened ignition delay times of the blend by ~ 25%. The reduction in MCH may therefore be considered responsible for the reduced ignition delay times in the blends at this condition, an effect which is consistent for both the 5% and 30% blends.

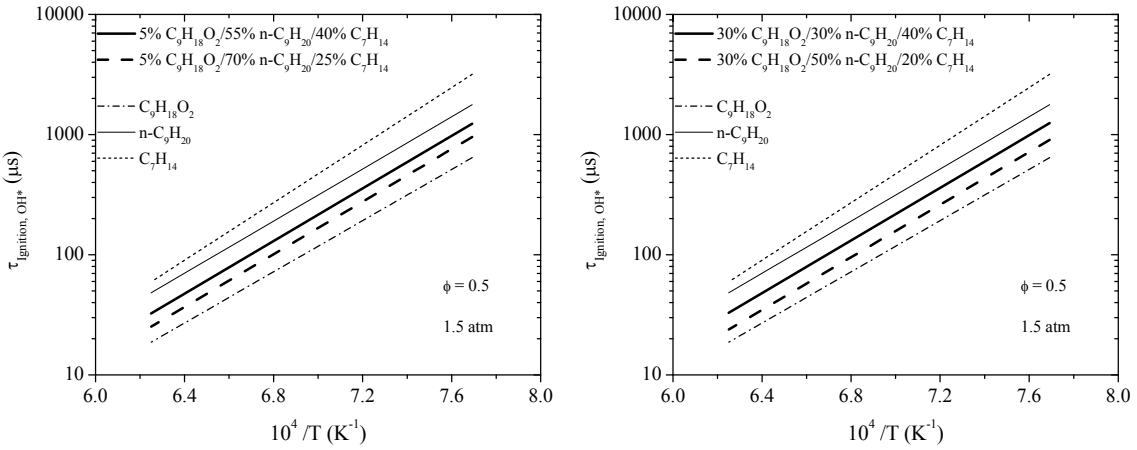

Fig. 9.7. Comparison of correlated ignition delay times of methyl octanoate/n-nonane/MCH blends holding methyl octanoate constant at 5% (Left) and 30% (Right) with ignition trends of the pure-fuel constituents. 1.5 atm; ϕ = 0.5. Correlated ignition times for $C_9H_{18}O_2$, n-C_9H_{20}, MCH, and ternary blends were calculated using Eqns. 5.1, 6.1, 7.1, and 8.1, respectively.

Ignition delay time trends under fuel-lean ($\phi = 0.5$) conditions were calculated for 40% and 60% n-nonane blends at 1.5 atm over the temperature range $1300 < T\ (K) < 1600$ (Fig. 9.7). Calculations using the 40% n-C_9H_{20} concentration included variation in methyl octanoate and MCH from 20% – 30% and 30% – 40%, respectively. For the 60% n-C_9H_{20}, methyl octanoate and MCH concentrations were varied from 5% – 20% and 20% – 35% in the calculations, respectively. Under lean conditions, the ternary fuel blend ignition trends lie below that of n-nonane and above that of methyl octanoate. Ignition delay times of the 20%/40%/40% blend were 35% shorter than the n-nonane trend and 70% longer than the methyl octanoate trend. For the 30%/40%/30% blend, ignition delay times were closer to those of pure methyl octanoate, to within 30%, and shorter relative to n-nonane by 50%. The ignition trends differed only slightly between the 40% and 60% n-nonane blends. No differences in ignition delay times are shown in the calculations between the 20%/40%/40% blend and the 5%/60%/35% blend. Using 1450 K as a comparative temperature, calculations predict ignition times of 160 μs for both.

Comparing the ignition delay times of the 20%/40%/40% blend with those of the 20%/60%/20% blend at 1450 K, noting the only change between the two being the 20% change in n-nonane and MCH volumes, ignition delay times are predicted with a difference of 30% (175 μs for the former, at 1450 K, compared to 120 μs for the latter), indicating a slight dependence on the n-nonane/MCH fuel ratio at fixed methyl octanoate concentration. Noting the nearly identical ignition activation energies of the trends, this similarity is consistent over the range of temperatures covered. Since the trends in ignition delay times with temperature between the 20%/40%/40% blend and the 5%/60%/35% blend are identical, the difference in ignition delay times between these blends and those of the 30%/40%/30% blend, approximately 15% over the range of temperature covered, is the same.

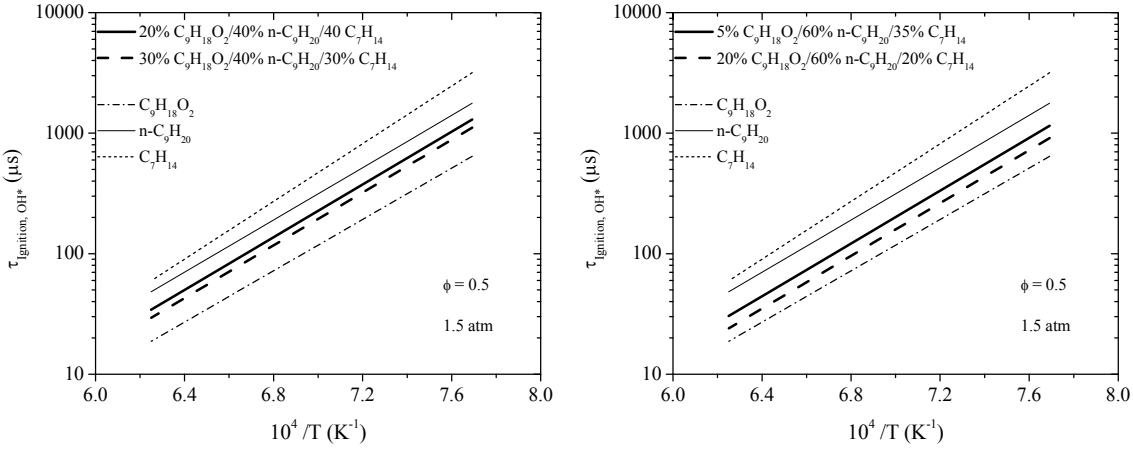

Fig. 9.8. Comparison of correlated ignition delay times of methyl octanoate/n-nonane/MCH blends holding n-nonane constant at 40% (Left) and 60% (Right) with ignition trends of the pure-fuel constituents. 1.5 atm; $\phi = 0.5$. Correlated ignition times for $C_9H_{18}O_2$, n-C_9H_{20}, MCH, and ternary blends were calculated using Eqns. 5.1, 6.1, 7.1, and 8.1, respectively.

Ignition delay time trends under fuel-lean ($\phi = 0.5$) conditions were calculated for 20% and 40% MCH blends at 1.5 atm over the temperature range $1300 < T\ (K) < 1600$ (Fig. 9.8). Calculations using the 20% MCH concentration included variation in methyl octanoate and n-nonane from 10% – 30% and 50% – 70%, respectively. For the 40% MCH, methyl octanoate and n-nonane concentrations were varied from 5% – 30% and 30% – 55% in the calculations, respectively. Under the lean conditions, the ternary fuel blend ignition trends lie below that of n-nonane and above that of methyl octanoate. In contrast to the previous blends, no effect on blending is shown from the calculations under conditions of fixed MCH concentration. Over the range of temperatures covered, the variation of methyl octanoate from 10% to 30% and corresponding variation in n-nonane from 50% to 70% has no impact on ignition delay times using 20% MCH. Similarly for 40% MCH with variation in methyl octanoate and n-nonane by 5% – 30% and 30% – 55%, respectively. At 1425 K, trends for both predict an ignition delay time of 160 μs. The 40% MCH blend also displayed independence from variation in the ratio of methyl octanoate to n-nonane, however differs from the 20% MCH ignition trends by 40% comparing the ignition delay time at 1425 K

(225 μs). Since the ignition activation energies are nearly equivalent over the temperature range, the 40% difference in ignition delay times is consistent from 1300 K – 1600 K.

Ignition delay times for both of the 20% MCH blends were 50% shorter than the n-nonane trend and 35% longer than the methyl octanoate trend. For the 40% MCH blends, ignition delay times were closer to those of pure n-nonane, to within 30%, and shorter relative to methyl octanoate by approximately 50%. The ignition delay time trend of methylcyclohexane diverges to longer times with decreasing temperature. Comparing the two fixed-MCH blends to the pure MCH ignition delay times at the temperature extrema, calculations of the 20% MCH blend show that ignition delay times differ from those of MCH at 1600 K by a factor of 3 and at 1300 K by a factor of 3.5. The 40% MCH blend decreases the difference to a factor of 2 at 1600 K and a factor of 2.5 at 1300 K.

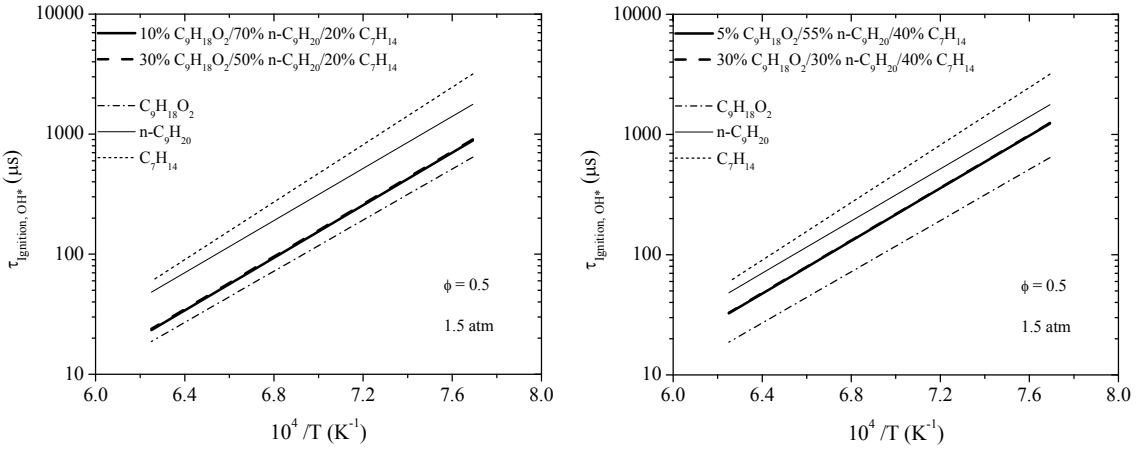

Fig. 9.9. Comparison of correlated ignition delay times of methyl octanoate/n-nonane/MCH blends holding MCH constant at 20% (Left) and 40% (Right) with ignition trends of the pure-fuel constituents. 1.5 atm; ϕ = 0.5. Correlated ignition times for $C_9H_{18}O_2$, n-C_9H_{20}, MCH, and ternary blends were calculated using Eqns. 5.1, 6.1, 7.1, and 8.1, respectively.

9.2.2 Blending effects on stoichiometric ignition of $C_9H_{18}O_2$/n-C_9H_{20}/MCH

Stoichiometric ignition delay time trends were calculated for 5% and 30% methyl octanoate blends at 1.5 atm over the temperature range 1350 < T (K) < 1600 (Fig. 9.9). Calculations using the 5% $C_9H_{18}O_2$ concentration included variation in n-nonane and MCH from 55% – 70% and 25 – 40%, respectively. For the 30% $C_9H_{18}O_2$ blend, n-nonane and MCH concentrations were varied from 30% – 50% and 20% – 40%. Relative to the lean condition, the ternary fuel blend ignition trends using 5% and 30% methyl octanoate lie closer to that of n-nonane, yet between those of n-nonane and methyl octanoate. Ignition delay times of the 5%/55%/40% blend were 15% shorter than the n-nonane trend and longer than the methyl octanoate trend by a factor of nearly 1.2. For the 5%/70%/25% blend, ignition delay times were closer to those of pure n-nonane, to within 35%, and approximately 70% longer relative to methyl octanoate. Relative differences between the 5%/55%/40% and 30%/30%/40% blends are negligible, indicating an insensitivity to variation in the ratio of methyl octanoate to n-nonane for conditions of fixed MCH concentration.

Using 1375 K as a comparison temperature, ignition delay times differ between the 5% methyl octanoate blends by 20%: 890 μs for the 5%/55%/40% blend, 700 μs for the 5%/70%/25% blend. The difference in ignition delay times between the two 30% methyl octanoate blends is slightly less: 890 μs for the 30%/30%/40% blend, 650 μs for the 30%/50%/20% blend. Under stoichiometric conditions at near-atmospheric pressure, no strong effect is shown for blending the three fuels in different proportions within the degree of uncertainty of the ignition delay time measurements (±10%). Both ignition trends for the 5% and 30% methyl octanoate blends, using fixed 40% MCH concentration, lie closely to that of n-nonane.

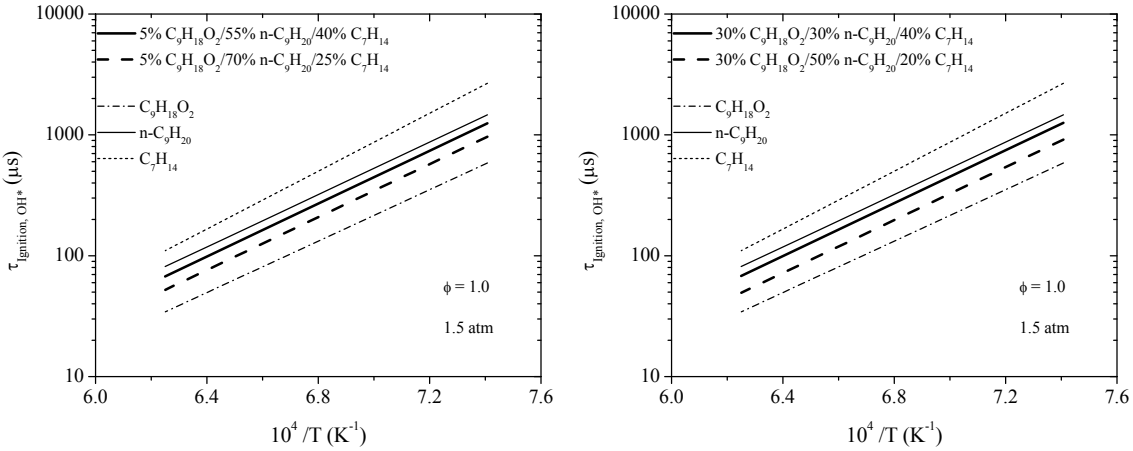

Fig. 9.10. Comparison of correlated ignition delay times of methyl octanoate/n-nonane/MCH blends holding methyl octanoate constant at 5% (Left) and 30% (Right) with ignition trends of the pure-fuel constituents. 1.5 atm; ϕ = 1.0. Correlated ignition times for $C_9H_{18}O_2$, n-C_9H_{20}, MCH, and ternary blends were calculated using Eqns. 5.1, 6.1, 7.1, and 8.1, respectively.

Ignition delay time trends under stoichiometric conditions were calculated for 40% and 60% n-nonane blends at 1.5 atm over the temperature range 1350 < T (K) < 1600 (Fig. 9.10). Calculations using the 40% n-C_9H_{20} concentration included variation in methyl octanoate and MCH from 20% – 30% and 30% – 40%, respectively. For the 60% n-C_9H_{20}, methyl octanoate and MCH concentrations were varied from 5% – 20% and 20% – 35% in the calculations, respectively. The ternary fuel blend ignition trends lie closely to that of n-nonane and above that of $C_9H_{18}O_2$. The trends shown for the case of fixed n-nonane concentration (Fig. 9.10) are nearly identical to those shown in Fig. 9.9 since the fuel percentages in Fig. 9.10 are within the range of those in Fig. 9.9. The 30%/40%/30% blend is in closer agreement with the 20%/40%/40% blend, however these two blends differ in MCH concentration by only 10%.

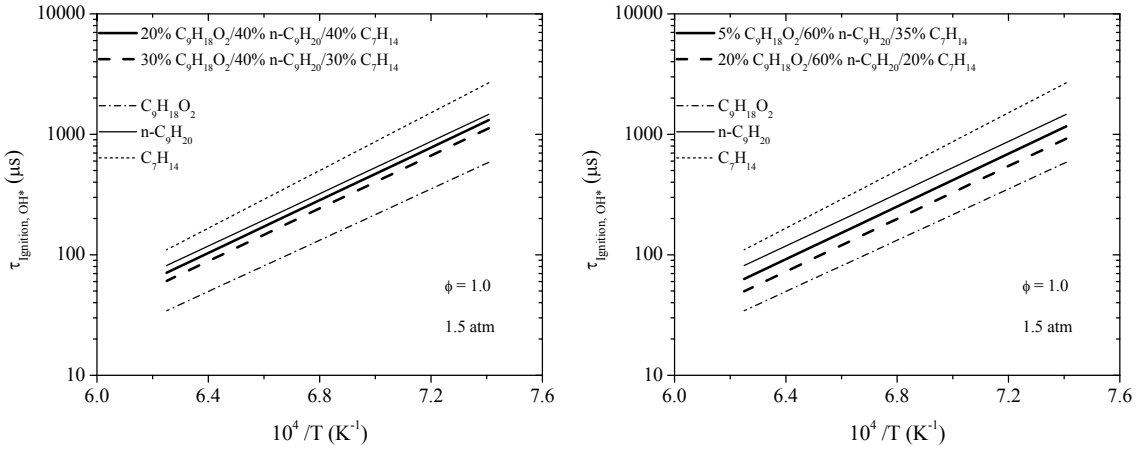

Fig. 9.11. Comparison of correlated ignition delay times of methyl octanoate/n-nonane/MCH blends holding n-nonane constant at 40% (Left) and 60% (Right) with ignition trends of the pure-fuel constituents. 1.5 atm; ϕ = 1.0. Correlated ignition times for $C_9H_{18}O_2$, n-C_9H_{20}, MCH, and ternary blends were calculated using Eqns. 5.1, 6.1, 7.1, and 8.1, respectively.

Stoichiometric ignition delay time trends were calculated for 20% and 40% MCH blends at 1.5 atm over the temperature range 1350 < T (K) < 1600 (Fig. 9.12). Calculations using the 20% MCH concentration included variation in methyl octanoate and n-nonane from 20% – 30% and 50% – 60%, respectively. For the 40% MCH, methyl octanoate and n-nonane concentrations were varied from 5% – 20% and 40% – 55% in the calculations, respectively. Under stoichiometric conditions, as for lean conditions, the ternary fuel blend ignition trends lie below that of n-nonane and above that of methyl octanoate. No effect on blending is shown from the calculations under conditions of fixed MCH concentration. Over the range of temperatures covered, the variation of methyl octanoate corresponding variation in n-nonane for respective MCH concentrations has no impact on ignition delay times. In contrast to the 20% and 40% MCH blends under lean conditions (Fig. 9.8), the stoichiometric condition brings the ignition trend of these blends closer to the behavior exhibited by pure n-nonane, differing by 40% and 15% compared to 50% and 30% at the lean condition for 20% and 40% MCH blends, respectively. Since the ignition activation energies

are nearly identical between the blends and the pure fuels, this percentage difference is consistent over the range of temperatures covered.

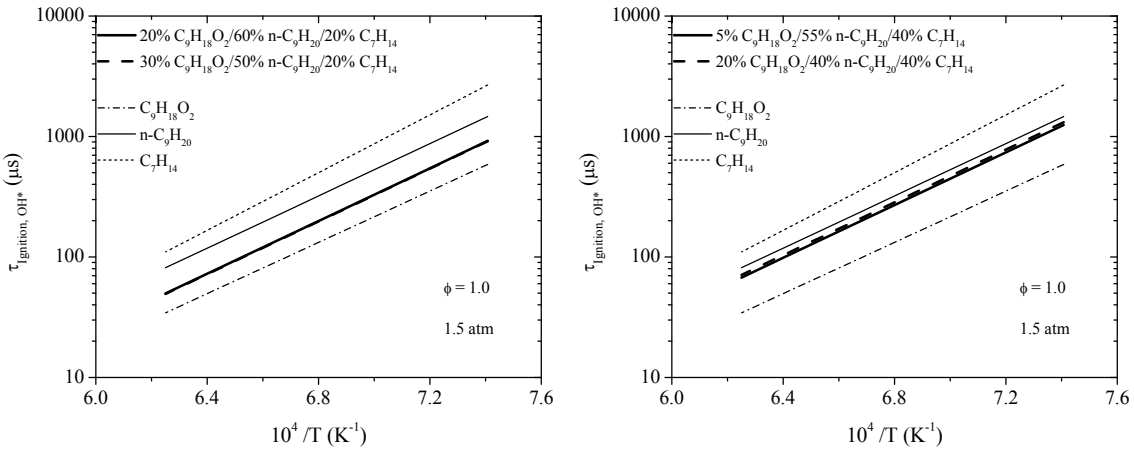

Fig. 9.12. Comparison of correlated ignition delay times of methyl octanoate/n-nonane/MCH blends holding MCH constant at 20% (Left) and 40% (Right) with ignition trends of the pure-fuel constituents. 1.5 atm; ϕ = 1.0. Correlated ignition times for $C_9H_{18}O_2$, n-C_9H_{20}, MCH, and ternary blends were calculated using Eqns. 5.1, 6.1, 7.1, and 8.1, respectively.

9.2.3 Blending effects on fuel-rich ignition of $C_9H_{18}O_2$/n-C_9H_{20}/MCH

Ignition delay time trends under fuel-rich (ϕ = 2.0) conditions were calculated for 5% and 30% methyl octanoate blends at 1.5 atm over the temperature range 1400 < T (K) < 1600 (Fig. 9.13). Calculations using the 5% $C_9H_{18}O_2$ concentration included variation in n-nonane and MCH from 55% – 70% and 25 – 40%, respectively. For the 30% $C_9H_{18}O_2$ blend, n-nonane and MCH concentrations were varied from 30% – 50% and 20% – 40%. Under the rich condition, the blended-fuel ignition trends using 40% MCH concentration completely overlap with that of n-nonane and are 55% longer than the $C_9H_{18}O_2$ trend. The 5%/70%/25% and 30%/50%/20% blends show negligible relative differences. Compared to methyl octanoate and n-nonane, ignition delay times of the lower-MCH concentration blends are 80% longer and 20% shorter, respectively.

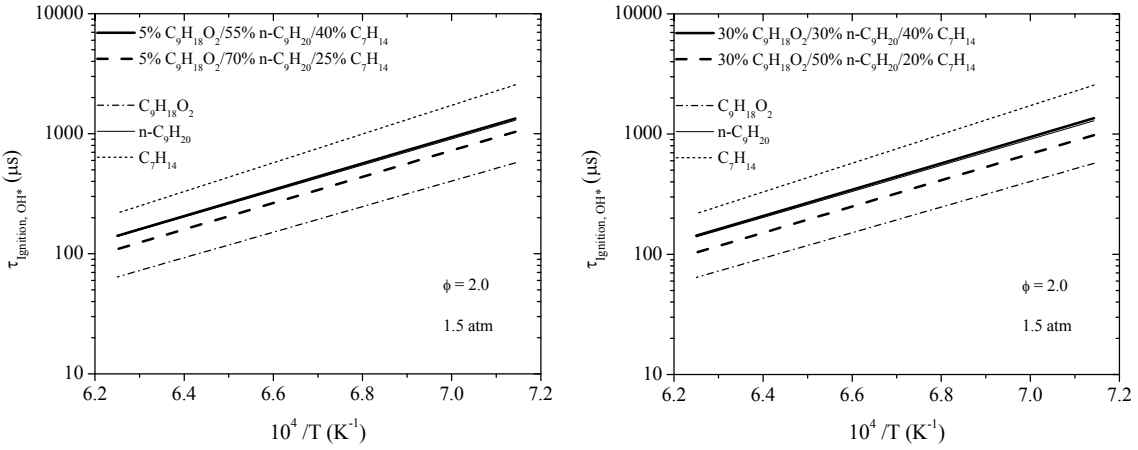

Fig. 9.13. Comparison of correlated ignition delay times of methyl octanoate/n-nonane/MCH blends holding methyl octanoate constant at 5% (Left) and 30% (Right) with ignition trends of the pure-fuel constituents. 1.5 atm; ϕ = 2.0. Ignition trends of 5/55/40 and 30/30/40 $C_9H_{18}O_2$/n-C_9H_{20}/MCH is coincident with n-nonane. Correlated ignition times for $C_9H_{18}O_2$, n-C_9H_{20}, MCH, and ternary blends were calculated using Eqns. 5.1, 6.1, 7.1, and 8.1, respectively.

Ignition delay time trends at ϕ = 2.0 were calculated for 40% and 60% n-nonane blends at 1.5 atm over the temperature range 1400 < T (K) < 1600 (Fig. 9.14). Calculations using the 40% n-C_9H_{20} concentration included variation in methyl octanoate and MCH from 20% – 30% and 30% – 40%, respectively. For the 60% n-C_9H_{20}, methyl octanoate and MCH concentrations were varied from 5% – 20% and 20% – 35% in the calculations, respectively. Immediately apparent is the behavior of the ignition trends of the 40% n-nonane blends being closer to the MCH ignition trend than either the lean or stoichiometric trends for these blends. Moreover, the two 40% n-nonane blends and the 5%/60%/35% blend completely overlap the ignition behavior of n-nonane within the experimental accuracy (±10%). A 15% difference in the 40% n-nonane trends is shown by the calculations.

Percentage differences between MCH and n-nonane (and, by extension, the two 40% n-nonane blends and the 5%/60%/35% blend) of 40% and 50% are shown in the calculations at 1600 K and 1400 K,

respectively. The blend with the lowest MCH concentration (20%/60%/20%) deviates by nearly 25% from the n-nonane trend. Comparing the three trends which show strong similarity to n-nonane, noting MCH concentration ranging from 30% – 40%, the ratio of the three fuels within this concentration range for MCH has no impact on the fuel-rich ignition delay times. Under both the lean and stoichiometric conditions, differences were observed and quantifiable outside of the experimental uncertainty.

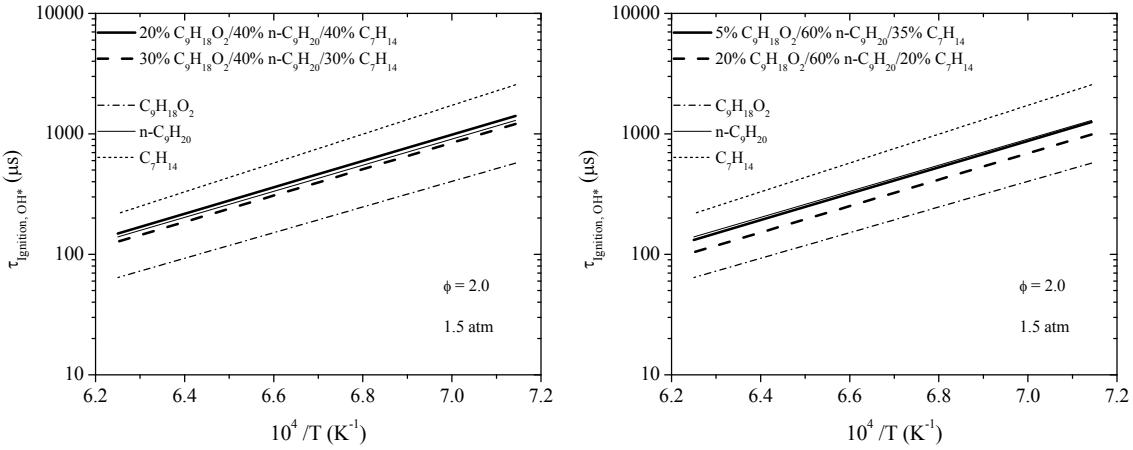

Fig. 9.14. Comparison of correlated ignition delay times of methyl octanoate/n-nonane/MCH blends holding n-nonane constant at 40% (Left) and 60% (Right) with ignition trends of the pure-fuel constituents. 1.5 atm; ϕ = 2.0. Ignition trend of 5/60/35 $C_9H_{18}O_2$/n-C_9H_{20}/MCH is coincident with n-nonane. Correlated ignition times for $C_9H_{18}O_2$, n-C_9H_{20}, MCH, and ternary blends were calculated using Eqns. 5.1, 6.1, 7.1, and 8.1, respectively.

Stoichiometric ignition delay time trends were calculated for 20% and 40% MCH blends at 1.5 atm over the temperature range 1400 < T (K) < 1600. Calculations using the 20% MCH concentration included variation in methyl octanoate and n-nonane from 20% – 30% and 50% – 60%, respectively. For the 40% MCH, methyl octanoate and n-nonane concentrations were varied from 5% – 20% and 40% – 55% in the calculations, respectively. Under fuel-rich conditions, as for lean and stoichiometric conditions, the ignition trend of the 20% MCH ternary fuel blend lies below that of n-nonane and above that of methyl octanoate. At 40% MCH concentration, however, both fuel blends (5%/55% and 30%/30% methyl octanoate/n-nonane) completely overlap the ignition trend of n-nonane over the range of temperatures

covered. In either case, no effect on blending (i.e. the change in methyl octanoate/n-nonane ratio) is shown from the calculations under conditions of fixed MCH concentration.

The difference in ignition delay times between the two 20% MCH blends and the n-nonane trend is smaller relative to the blends at lean and stoichiometric equivalence ratios. At ϕ = 0.5 and 1.0, the overlapping 20% MCH blends were 50% and 40% shorter relative to n-nonane. For the ϕ = 2.0 condition, this difference is reduced to 25%, indicating an equivalence ratio effect on blended fuel ignition for constant MCH concentration. Since the ignition trends are nearly identical, the difference in ignition delay times is consistent over the range of temperatures covered.

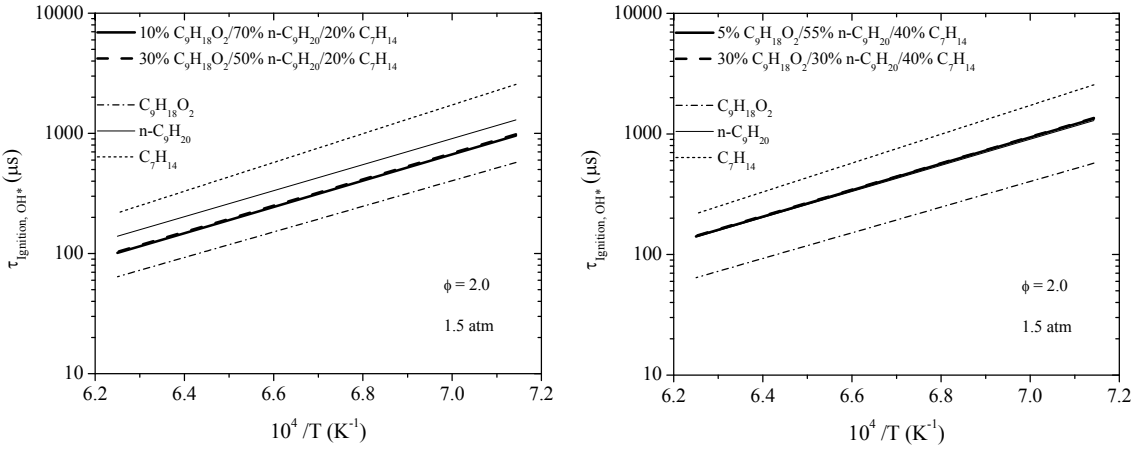

Fig. 9.15. Comparison of correlated ignition delay times of methyl octanoate/n-nonane/MCH blends holding MCH constant at 20% (Left) and 40% (Right) with ignition trends of the pure-fuel constituents. 1.5 atm; ϕ = 2.0. Ignition trends of 5/55/40 and 30/30/40 $C_9H_{18}O_2$/n-C_9H_{20}/MCH are coincident with n-nonane. Correlated ignition times for $C_9H_{18}O_2$, n-C_9H_{20}, MCH, and ternary blends were calculated using Eqns. 5.1, 6.1, 7.1, and 8.1, respectively.

9.3 *Concluding remarks on empirical ignition behavior of pure and blended fuels*

Experimental ignition trends for the pure fuels were compared. The influence of pressure on ignition delay times is higher for both n-nonane and MCH than for methyl octanoate, which is partly responsible for the overlap observed between methyl octanoate and n-nonane near 10 atm. The overlap occurred most

strongly under lean and rich conditions. Ignition delay times for ternary blends of methyl octanoate/n-nonane/MCH were then compared, holding n-nonane concentration constant at 50% and varying methyl octanoate concentrations from 5% to 20% under stoichiometric conditions near 10 atm. The three blends produced ignition trends between those of n-nonane and methylcyclohexane. The ignition activation energy of the blends decreased with lower concentrations of methyl octanoate (5% and 10% vol.), yet at 20% (vol.) the activation energy of the blend increased by 15% to 51.9 kcal/mol relative to the average of the 5% and 10% trends which share nearly identical activation energies (within 2%).

The effects of fuel variation in the ternary blends on ignition behavior were analyzed empirically using ignition delay time correlations. Ignition trends for a wide range of relative fuel percentages were compared to the ignition behavior of the pure fuel constituents at 1.5 atm at three equivalence ratios: ϕ = 0.5, 1.0, and 2.0. Fuel percentages utilized in the calculations for methyl octanoate, n-nonane, and methylcyclohexane of 5% – 30%, 30% – 70%, and 20% – 40%, respectively, were consistent for all equivalence ratios. Temperatures, depending on equivalence ratio, were varied from 1300 K to 1600 K.

Under lean conditions, no dependence of ignition delay times on methyl octanoate/n-nonane ratio for fixed (40%) MCH concentration was shown in the correlation calculations. For fuel blends with only 5% variation in MCH concentration, no difference is shown in the ignition behavior, despite a wide variation in relative fuel percentage of methyl octanoate (5% – 30%) and n-nonane (50% – 70%). The similar ignition delay times between the two blends differing in MCH by 5% were 25% shorter than those measured using 40% MCH, yet the same methyl octanoate concentration (5% and 30%). A slight dependence on n-nonane/MCH ratio for fixed methyl octanoate concentration was shown, where ignition delay times were 30% shorter for a higher ratio.

Relative to the lean condition, stoichiometric fuel blend ignition delay times of the ternary blends using 5% and 30% methyl octanoate lie closer to those of n-nonane. Differences between the 5%/55%/40% and 30%/30%/40% blends for ϕ = 1.0 were negligible, providing another indication as to an insensitivity in

variation of the ratio of methyl octanoate to n-nonane for conditions of fixed MCH concentration. In contrast to the 20% and 40% MCH blends under lean conditions, stoichiometric ignition delay times of the blends were closer to those shown from the calculations of pure n-nonane, differing by 40% and 15% compared to 50% and 30% at the lean condition for 20% and 40% MCH blends, respectively.

At the fuel-rich equivalence ratio (ϕ = 2.0), it was shown that for blends with constant n-nonane concentration, increased equivalence ratio led to ignition trends that approach that of MCH. Under lean conditions, ignition trends of the blends using fixed 40% n-nonane concentration differ from that of MCH by 50%. At ϕ = 1.0, the percentage difference decreased to 40%. For ϕ = 2.0, the difference decreased further to 25% relative to MCH. Within a concentration range for MCH of 30% – 40%, the ratio of the three fuels had no impact on the fuel-rich ignition delay times. At 40% MCH concentration, fuel blends of 5%/55% and 30%/30% methyl octanoate/n-nonane completely overlapped the ignition trend of n-nonane over the range of temperatures covered. In either case, no effect on blending (i.e. the change in methyl octanoate/n-nonane ratio) was shown from the calculations under conditions of fixed MCH concentration.

10. LAMINAR FLAME SPEEDS OF FUEL BLEND CONSTITUENTS

Measurements of laminar flame speeds were obtained for the three constituent fuels of the ternary blends: methyl octanoate, n-nonane, and methylcyclohexane. Due to the low vapor pressures of the three constituent species, the fuels were injected (in separate experiments) directly in liquid form into the heated vessel. The injected fuel volumes for all experiments, to determine the appropriate equivalence ratio, were calculated using liquid densities at 293 K. A nominal uncertainty of 4 cm/s is assigned to all measured values of flame speed. Details on the heated flame speed facility are given in the thesis work of Krejci [132], and discussions one measurement uncertainties are given in de Vries [169], Lowry [170], and Krecji [132]. The experiments were conducted at 1 atm and 170 °C (443 K) using ultra-high purity air. The MCH measurements presented herein are reported using the constant-volume apparatus and compared to results from a similar apparatus [171] and also from counterflow flames [172, 173]. The methyl octanoate results are the first measurements obtained for that species. In addition to measurements of methylcyclohexane at 170 °C (403 K) initial temperature, results were also obtained at 130 °C (403 K) to compare with the available literature values [171 – 173]. Discussed below are experimental and modeling results for laminar flame speeds of the pure fuel species with supporting images of the observed flames. Appendices I and J contain mixture information on flame speed experiments with specific experimental details and numerical values of laminar flame speed, respectively.

10.1 Methyl octanoate

Laminar flame speeds of methyl octanoate were obtained at conditions of atmospheric pressure and 170 °C. Figures 10.1 and 10.2 show images of a $C_9H_{18}O_2$ laminar flame and flame speed measurements as a function of equivalence ratio, respectively. Measurements were taken over the range of equivalence ratio $0.86 < \phi < 1.43$. The experimental trend indicates that the peak laminar flame speed occurs at approximately $\phi = 1.12$. Fuel partial pressures of 10.8 torr and 17.8 torr were used to obtain the fuel-lean and fuel-rich extremes, respectively.

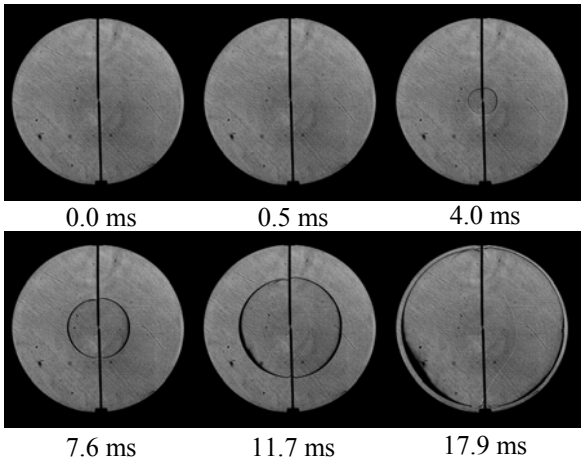

Fig. 10.1. Schlieren images of laminar flame propagation of methyl octanoate ($C_9H_{18}O_2$) in atmospheric air; 170 °C; ϕ = 1.08. $S_{L,u}^{\circ}$ = 64.75 cm/s.

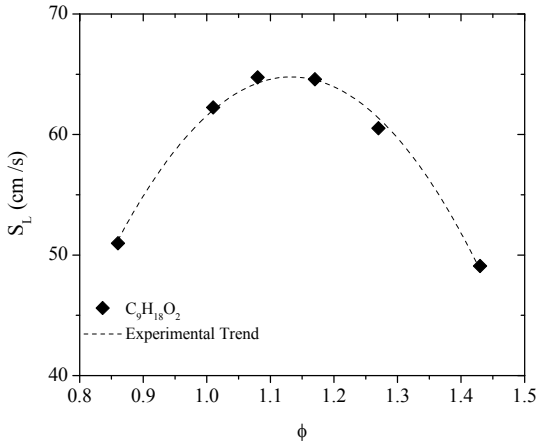

Fig. 10.2. Laminar flame speeds of methyl octanoate ($C_9H_{18}O_2$) in atmospheric air; 170 °C.

10.2 n-Nonane

Laminar flame speeds of methyl octanoate were obtained for conditions of atmospheric pressure and 170 °C. Measurements were taken over the range of equivalence ratio $0.83 < \phi < 1.30$. The fuel-lean and fuel-rich extremes produced flames speeds of 57.0 cm/s and 68.2 cm/s, respectively. The experimental trend for n-nonane indicates that the peak laminar flame speed (ca. 68 cm/s) occurs at approximately $\phi = 1.07$. Fuel partial pressures of 9.4 torr and 14.5 torr were used to obtain the lean and rich extremes, respectively.

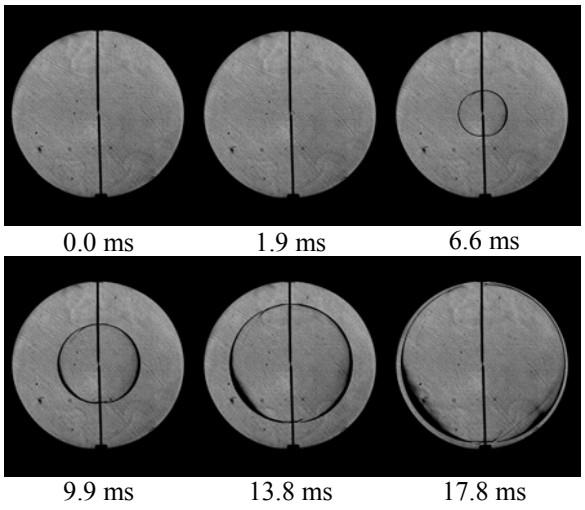

Fig. 10.3. Schlieren images of laminar flame propagation of n-nonane (n-C_9H_{20}) in atmospheric air; 170 °C; $\phi = 1.08$; $S_{L,u}^{\circ} = 68.2$cm/s.

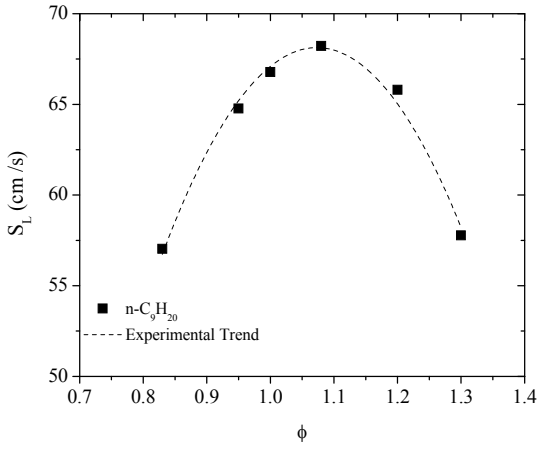

Fig. 10.4. Laminar flame speeds of n-nonane (n-C_9H_{20}) in atmospheric air; 170 °C.

10.3 Methylcyclohexane

Laminar flame speeds of methylcyclohexane were obtained for conditions of atmospheric pressure and 170 °C for comparison to the other fuel constituents in the present study, and at 130 °C for comparison to literature values. Two experimental studies on MCH flame speeds have been conducted using a diffusion flame apparatus [172, 173]. These values are consistently higher than those measured using the constant-volume apparatus herein. Measurements of MCH flame speeds taken at 403 K in the present work are in strong agreement with those from the constant-volume apparatus of Singh et al. [171], differing less than 5% from one another over the range of equivalence ratios.

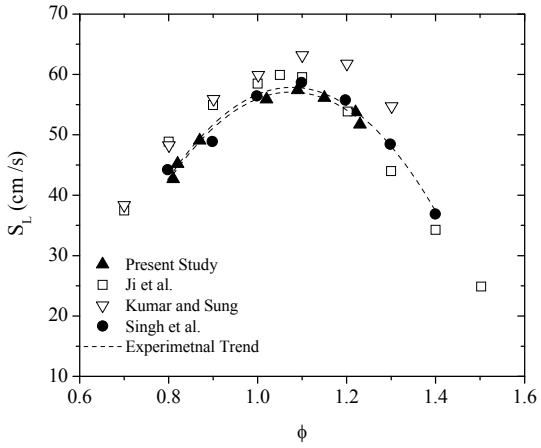

Fig. 10.5. Laminar flame speeds of MCH in atmospheric air (403 K). Symbols: open → counterflow (diffusion) flame apparatus; solid → constant-volume apparatus.

For the 170 °C temperature measurements, flame speeds were obtained over the range of equivalence ratio $0.81 < \phi < 1.30$. The fuel-lean and fuel-rich extremes produced flames speeds of 51.7 cm/s and 53.8 cm/s, respectively. The experimental trend for MCH indicates that the peak laminar flame speed (ca. 67 cm/s) occurs at approximately $\phi = 1.07$. Fuel partial pressures of 12.1 torr and 19.3 torr were used to obtain the fuel-lean and fuel-rich extremes, respectively. Figures 10.6 and 10.7 show images of a MCH laminar flame and flame speed measurements at 170 °C as a function of equivalence ratio, respectively.

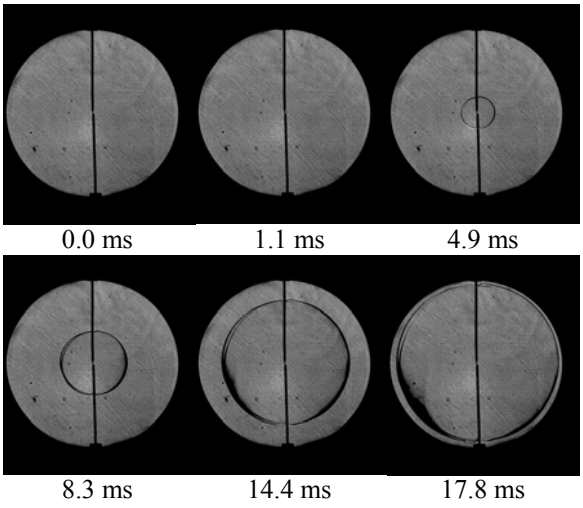

Fig. 10.6. Schlieren images of laminar flame propagation of methylcyclohexane (MCH) in atmospheric air; 170 °C; ϕ = 1.10; $S_{L,u}^{\circ}$ = 66.6 cm/s.

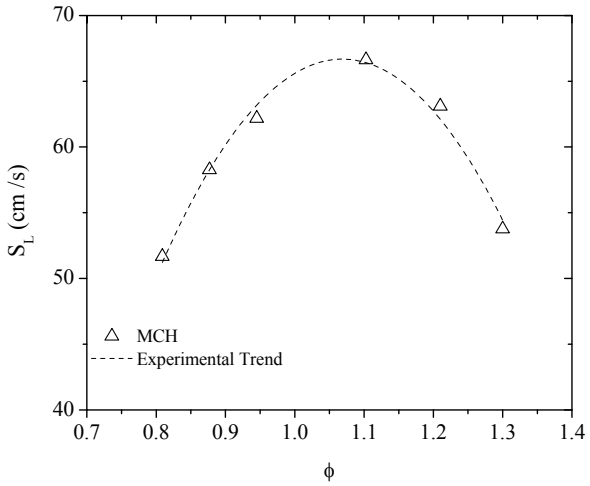

Fig. 10.7. Laminar flame speeds of MCH in atmospheric air; 170 °C.

10.4 Comparison of laminar flame speeds of methyl octanoate, n-nonane, and MCH

Figure 10.8 compares laminar flame speeds trends of the three constituent fuels that comprise the ternary fuel blend studied herein. The peak laminar flame speed occurs at a slightly more fuel-rich equivalence ratio for the oxygenated hydrocarbon relative to the higher-order linear alkane or cycloalkane (ϕ = 1.12 compared to ϕ = 1.07). Flame speeds follow the order below ϕ = 1.0, from highest to lowest of n-nonane > MCH > methyl octanoate. With increasing equivalence ratio, MCH flame speeds became the lowest and methyl octanoate became the highest. Up to ϕ = 1.0, the differences are largely consistent. Relative to n-nonane, MCH and $C_9H_{18}O_2$ have ~ 1.5 cm/s and 5.5 cm/s lower flame speeds (ca. 2% and 8% respectively). Resulting from the slight shift in equivalence ratio for peak flame speed, for equivalence ratios lower than 1.2, methyl octanoate flame speeds were lower than those of the pure hydrocarbons. Above ϕ = 1.2, the trend of $C_9H_{18}O_2$ became higher than that of either n-nonane or MCH.

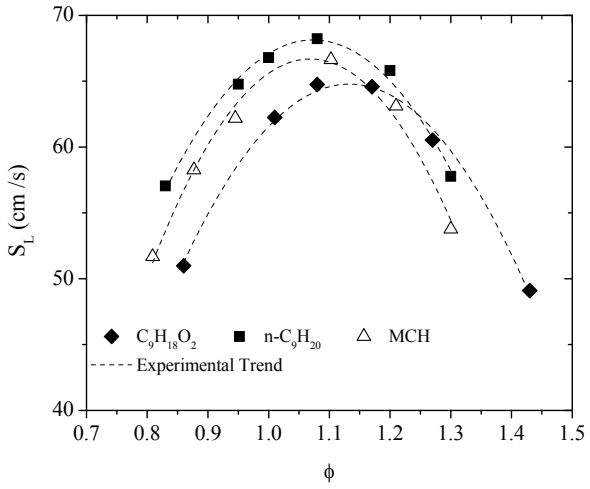

Fig. 10.8. Comparison of laminar flame speed trends for methyl octanoate, n-nonane, and MCH in atmospheric air (443 K).

10.5 Concluding remarks on laminar flame speed measurements

Laminar flame speeds were measured for the first time for a higher-order methyl ester species (methyl octanoate) and were also measured for n-nonane and MCH using a heated flame speed facility. Initial

pressure and temperature of 1 atm and 170 °C were maintained for all comparison experiments. Measurements at higher pressure (10 atm) were attempted, however the resulting flame became highly turbulent immediately upon ignition and the steady-state approximation applied to laminar flame speed measurements therefore became invalid. To increase the stability of the flames, and thereby maintain the 1-D steady-state approximation, the use of He dilution in air should be implemented. The process of He-dilution and corresponding effects on flame stability at high pressure has been covered in the thesis of Lowry [170].

Methylcyclohexane results were also obtained at 130 °C to compare with literature values. The measurements reported herein agree strongly with results reported from the constant-volume apparatus of Singh et al. [171]. The two constant-volume measurement sets are lower than those reported using diffusion flame experiments. Comparing flame speed trends of the three constituent fuels showed two primary observations. The first is the similarity in n-nonane and MCH flame speeds over the range of equivalence ratios tested (< 2% difference). The second is the lower flame speed of methyl octanoate compared to either n-nonane or MCH below $\phi = 1.2$, yet above this equivalence ratio the speeds of $C_9H_{18}O_2$ flames were higher by approximately 10%.

Relative to calculations performed under 0-D homogeneous conditions (i.e. simulation of shock tube experiments) which consider only chemical kinetics, computation of 1-D premixed laminar flame speeds involves more-complex mathematics and solution procedures due to the coupling of conservation equations for species transport processes, continuity (conservation of mass), energy, and equations of state with reaction chemistry. Further, combustion modeling of larger species imposes additional difficulty due to the large number of products and reactions involved in the decomposition and reaction of larger fuel molecules. Calculations of flame speed using either the current chemical kinetics model or the other higher-order-molecular-weight species models were unable to reach convergence at the time of the present work due to memory limitations.

11. CONCLUSIONS AND RECOMMENDATIONS

Shock-tube and laminar flame speed measurements were obtained for species acting as surrogates in biofuel: methyl octanoate, n-nonane, and MCH. Ignition delay time measurements and excited-state OH profiles were measured in a heated shock tube for ternary blends of these fuel species using a statistical Design of Experiments approach, namely an L9 array, using equivalence ratio, pressure, and volume percentages of methyl octanoate and MCH. The statistical approach undertaken, by extension of the representation of the constituent fuels acting as surrogates for the respective hydrocarbon classes, afforded an experimental study on the effects of blend variation in ternary fuels of higher-order n-alkanes. Resulting from the broad range of conditions covered in the L9 array, an empirical ignition delay time correlation was defined for ignition of the ternary blends. Experimental sensitivity calculations using the correlation revealed that the experimental parameter to which ignition delay times of the blends are most was equivalence ratio, followed by pressure and %MCH. The effect of methyl octanoate concentration in the ternary blends, varied by a factor of 12, showed to be the least-impacting variable on ignition delay time measurements for the range of the conditions in the present study.

In order to model ignition delay times of the blended fuels, a detailed chemical kinetics mechanism was compiled using two sub-mechanisms for methyl octanoate and MCH integrated into a base n-nonane mechanism. The ability of the compiled mechanism to reproduce the ignition behavior of the pure fuels needs improvement for pure methyl octanoate ignition, yet predicts n-nonane and MCH ignition delay times well for most conditions covered herein. Model calculations were performed to assess the effects of blending the methyl ester with the linear alkane and cycloalkane under thermodynamic conditions (1460 K, 9.5 atm, $\phi = 1.0$), where agreement was shown by the compiled model for the pure fuels and for a series of blends (5%/20% methyl octanoate concentration, 50% n-nonane concentration, 45%/30% MCH). Only a small effect was shown in model calculations of ignition delay times outside of the uncertainty in the measurement. The small effect was reflected in the predictions using the compiled model using calculations of species time histories, species rate-of-production, and sensitivity analysis.

Recommendations for improvements to the larger study of blended biofuel combustion include: (1) refinement of compiled mechanism presented herein in order to better predict ignition trends of pure methyl octanoate; (2) incorporation of iso-alkanes into blends of conventional and alternative fuels (methyl ester, alcohols, ethers); (3) expansion of a broader number of species within a given study; (4) elementary studies (laser absorption, GC/MS speciation…) to quantify the effects of blending methyl esters and/or other alternative fuels with conventional fuels on stable production formation (CO_2, H_2O); (5) expansion of ignition delay time measurements for blended biofuels to high-pressure and low- and intermediate-temperatures; (6) perform similar studies focusing on blends of conventional fuels of the same ratio as those used herein to experimentally identify the effects of the methyl ester (or other biologically-derived fuel).

REFERENCES

[1] A. Vertès, N. Qureshi, H. Yukawa, H.P. Blaschek (Eds.): Biomass to Biofuels: Strategies for Global Industries, Wiley, 2010.

[2] W. Soetaert, E. Vandamme, Biofuels, Wiley, 2009.

[3] D.M. Mousdale, Introduction to Biofuels, CRC Press, 2010.

[4] M.S. Carolan, A Sociological Look at Biofuels: Understanding the Past/ Prospects for the Future, Nova Science Publishers, 2010.

[5] L. Reijnders, M. Huijbregts, Biofuels for Road Transport – A Seed to Wheel Perspective, Springer, 2010.

[6] A. Demirbas, Biofuels – Securing the Planet's Future Energy Needs, Springer, 2010

[7] A. Demirbas, Biodiesel – A Realistic Fuel Alternative for Diesel Engines, Springer, 2010.

[8] Worldwatch Institute, Biofuels for Transport: Global Potential and Implications for Sustainable Agriculture and Energy in the 21st Century, Earthscan Publishing, 2007.

[9] S.W. Tatum, S.J. Skinner, J.D. Jackson, Energy Econ., 32, 2010, p. 1263.

[10] D. Vedenov, M. Wetzstein, Energy Econ., 30, 2008, p. 2073.

[11] Fuel Economy Report: Fuel Economy Standards for MY2011-2025, http://www.whitehouse.gov/ (2011).

[12] Energy Information Agency, http://eia.gov (2011).

[13] S.M. Sarathy, C. Yeung, C.K. Westbrook, W.J. Pitz, M. Mehl, M.J. Thomson, Combust. Flame 158 (2011) p. 1277.

[14] S.M. Sarathy, C.K. Westbrook, M. Mehl, W.J. Pitz, C. Togbé, P. Dagaut, H. Wang, M.A. Oehlschlaeger, U. Niemann, K. Seshadri, P.S. Veloo, C. Ji, F.N. Egolfopoulos, T. Lu, Combust. Flame 158 (2011) p. 2338.

[15] H. Wang, E. Dames, B. Sirjean, D. A. Sheen, R. Tangko, A. Violi, J. Y. W. Lai, F. N. Egolfopoulos, D.F. Davidson, R.K. Hanson, C.T. Bowman, C.K. Law, W. Tsang, N.P. Cernansky, D.L. Miller, R.P. Lindstedt: JetSurF Version 2.0, September 2010 (http://melchior.usc.edu/JetSurF/JetSurF2.0).

[16] B. Rotavera, P. Diévart, C. Togbé, P. Dagaut, E.L. Petersen, Proc. Comb. Inst. 33 (2011) p. 175.

[17] E. Ranzi, A. Frassoldati, S. Granata, T. Faravelli, Ind. Eng. Chem. Res. 44 (2005) p. 5170.

[18] S.P. Zeppieri, S.D. Klotz, F.L. Dryer, Proc. Comb. Inst. 28 (2000) p. 1587.

[19] H.J. Curran, P. Gaffuri, W.J. Pitz, C.K. Westbrook, Comb. Flame 114 (1998) p. 149.

[20] A. Ristori, P. Dagaut, M. Cathonnet, Comb. Flame (125) 2001 p. 1128.

[21] S. Jahangirian, S. Dooley, F.M. Haas, F.L. and Dryer, Comb. Flame (159) 2012 p. 30.

[22] H.J. Curran, P. Gaffuri, W.J. Pitz, C.K. Westbrook, Comb. Flame 129 (2002) p. 253.

[23] M. Jia, M. Xie, Fuel 85 (2006) p. 2593.

[24] J.P. Orme, H.J. Curran, J.M. Simmie, J. Phys. Chem. A 110 (2006) p. 114.

[25] W.J. Pitz, C.V. Naik, T.N. Mhaoldúin, C.K. Westbrook, H.J. Curran, J.P. Orme, J.M. Simmie, Proc. Comb. Inst. 31 (2007) p. 267.

[26] M.H. Hakka, P.-A. Glaude, O. Herbinet, F. Battin-Leclerc, Comb. Flame 156 (2009) p. 2129.

[27] H.P. Ramirez, K. Hadj-Ali, P. Diévart, G. Dayma, C. Togbé, G. Moréac, P. Dagaut, Proc. Comb. Inst. 33 (2011) p. 375.

[28] O. Herbinet, W.J. Pitz, C.K. Westbrook, Comb. Flame 154 (2008) p. 507.

[29] P. Dagaut, Fuel 89 (2010) p. 280.

[30] Z. Luo, M. Plomer, T. Lu, S. Som, D.E. Longman, Proc. 7th U.S. Natl. Comb. Mtg. (2011) Paper IC18.

[31] S. Garner, K. Brezinsky, Comb. Flame 158 (2011) p. 2289.

[32] S. Garner, T. Dubois, C. Togbé, N. Chaumeix, P. Dagaut, K. Brezinsky, Comb. Flame 158 (2011) p. 2302.

[33] J.J. Hernandez, J. Sanz-Argent, J. Benajes, S. Molina, Fuel 87 (2008) p 655.

[34] C.K. Westbrook, W.J. Pitz, P.R. Westmoreland, F.L. Dryer, M. Chaos, P. Osswald, K. Kohse-Höinghaus, T.A. Cool, J. Wang, B. Yang, N. Hansen, T. Kasper, Proc. Comb. Inst. 32 (2009) p. 221.

[35] S. Gäil, M.J. Thomson, S.M. Sarathy, S.A. Syed, P. Dagaut, P. Diévart, A.J. Marchese, F.L. Dryer, Proc. Comb. Inst. 31 (2007) p. 305.

[36] C. Togbé, G. Dayma, A. Mzé-Ahmed, P. Dagaut, Energy Fuels 24 (2010) p. 3906.

[37] K. Hadj-Ali, M. Crochet, G. Vanhove, M. Ribaucour, R. Minetti, Proc. Comb. Inst. 32 (2009) p. 239.

[38] P.-A. Glaude, O. Herbinet, S. Bax, J.B. Biet, V. Warth, F. Battin-Leclerc, Comb. Flame 157 (2010) p. 2035.

[39] O. Herbinet, J. Biet, M.H. Hakka, V. Warth, P.-A. Glaude, A. Nicolle, F. Battin-Leclerc, Proc. Comb. Inst. 33 (2011) p. 391.

[40] P. Diévart, S. Dooley, S.H. Won, F.L. Dryer, Y. Ju, Proc. 7th U.S. Natl. Comb. Mtg. (2011) Paper 2A15.

[41] C. Togbé, J.B. May-Carle, G. Dayma, P. Dagaut, J. Phys. Chem. A 114 (2010) p. 3896.

[42] G. Dayma, S.M. Sarathy, C. Togbé, C. Yeung, M.J. Thomson, P. Dagaut, Proc. Comb. Inst. 33 (2011) p. 1037.

[43] E.M. Fisher, W.J. Pitz, H.J. Curran, C.K. Westbrook, Proc. Comb. Inst. 28 (2000) p. 1579.

[44] W.J. Pitz, C.J. Mueller, Prog. Energy Comb. Sci. 37 (2010) p. 330.

[45] T. Edwards, L.Q. Maurice, J. Prop. Power 17 (2001) p. 401.

[46] E. Ranzi, Energy & Fuels 20 (2006) p. 1024.

[47] C.K. Westbrook, W.J. Pitz, O., Herbinet, H.J. Curran, E.J. Silke, Comb. Flame 156 (2009) p. 181.

[48] B. Rotavera, P. Dagaut, E.L. Petersen, in preparation.

[49] D.F. Davidson, S.C. Ranganath, K.-Y. Lam, M. Liaw, Z. Hong, R.K. Hanson, J. Prop. Power 26 (2010) p. 280.

[50] R. Pohorecki, J. Bałdyga, W. Moniuk, W. Podgórska, A. Zdrójkowski, P.T. Wierzchowski, Chem. Eng. Sci. 56 (2001) p. 1285.

[51] C. Ji, E. Dames, B. Sirjean, H. Wang, F.N. Egolfopoulos, Proc. Comb. Inst. 33 (2011) p. 971.

[52] B. Sirjean, F. Buda, H. Hakka, P.-A. Glaude, R. Fournet, V. Warth, F. Battin-Leclerc, M. Ruiz-Lopez, Proc. Comb. Inst. 31 (2007) p. 277.

[53] Y. Yang, A.L. Boehman, J.M. Simmie, Comb. Flame 157 (2010) p. 2369.

[54] Z. Hong, K.-Y. Lam, D.F. Davidson, R.K. Hanson, Comb. Flame 158 (2011) p. 1456.

[55] A. El Bakli, M. Braun-Unkhoff, P. Dagaut, P. Frank, M. Cathonnet, Proc. Comb. Inst. 28 **(**2000) p. 1631.

[56] J. Vanderover, M.A. Oehlschlaeger, Int. J. Chem. Kin. 41 (2009) p. 82.

[57] S.S. Vasu, D.F. Davidson, R.K. Hanson, Comb. Flame 156 (2009) p. 736.

[58] G. Mittal, C.-J. Sung, Comb. Flame 156 (2009) p. 1852.

[59] R.D. Hawthorn, A.C. Nixon, AIAA Journal 4 (1966) p. 513.

[60] S. Granata, T. Faravelli, E. Ranzi, Comb. Flame 132 (2003) p. 533.

[61] S. Zeppieri, K. Brezinsky, I. Glassman, Comb. Flame 108 (1997) p. 266.

[62] C. Ji, F.N. Egolfopoulos, Proc. Comb. Inst. 33 (2011) p. 955.

[63] Y. Zhang, A.L. Boehman, Comb. Flame 157 (2010) p. 546.

[64] S.R. Hoffman, J. Abraham, Fuel 88 (2009) p. 1099.

[65] S.M. Sarathy, M.J. Thomson, W.J. Pitz, T. Lu, Proc. Comb. Inst. 33 (2011) p. 399.

[66] K. Seshadri, T. Lu, O. Herbinet, S. Humer, U. Niemann, W.J. Pitz, R. Seiser, C.K. Law, Proc. Comb. Inst. 32 (2009) p. 1067.

[67] W. Wang, M.A. Oehlschlaeger, Comb. Flame 159 (2012) p. 476.

[68] D.R. Haylett, D.F. Davidson, R.K. Hanson, Comb. Flame 159 (2012) p. 552.

[69] A.J. Marchese, T.L. Vaughn, K. Kroenlein, F.L. Dryer, Proc. Comb. Inst. 33 (2011) p. 2021.

[70] O. Herbinet, P.-A. Glaude, V. Warth, F. Battin-Leclerc, Comb. Flame 158 (2011) p. 1288.

[71] E. Alptekin, M. Çanakçi, Fuel 88 (2009) p. 75.

[72] M.S.P. Kahandawala, M.J. DeWitt, E. Corporan, S.S. Sidhu, Energy Fuels 22 (2008) p. 3673.

[73] A. Violi, S. Yan, E.G. Eddings, A.F. Sarofim, S. Granata, T. Faravelli, E. Ranzi, Combust. Sci. Tech. 174 (2002) p. 399.

[74] J.A. Cooke, M. Bellucci, M.D. Smooke, A. Gomez, A. Violi, T. Faravelli, E. Ranzi, Proc. Comb. Inst. 30 (2005) p. 439.

[75] S. Humer, A. Frassoldati, S. Granata, T. Faravelli, E. Ranzi, R. Seiser, K. Seshadri, Proc. Comb. Inst. 31 (2007) p. 393.

[76] A. Agosta, N.P. Cernansky, D.L. Miller, T. Faravelli, E. Ranzi, Exp. Therm. Fluid Sci. 28 (2004) p. 701.

[77] S.S. Vasu, D.F. Davidson, R.K. Hanson, Comb. Flame 152 (2008) p. 125.

[78] K. Schmidt, J. Van Gerpen, SAE Paper 961086 (1996).

[79] A. Farooq, D.F. Davidson, R.K. Hanson, L.K. Huynh, A. Violi, Proc. Comb. Inst. 32 (2009) p. 247.

[80] S.M. Walton, M.S. Wooldridge, C.K. Westbrook, Proc. Comb. Inst. 32 (2009) p. 255.

[81] B. Akih-Kumgeh, J.M. Bergthorson, Comb. Flame 158 (2011) p. 1037.

[82] Y.L. Wang, Q. Feng, F.N. Egolfopoulos, T.T. Tsotsis, Comb. Flame 158 (2011) p. 1507.

[83] C.V. Naik, C.K. Westbrook, O. Herbinet, W.J. Pitz, M. Mehl, Proc. Comb. Inst. 33 **(**2011) p. 383.

[84] J. Biet, V. Warth, O. Herbinet, P.-A. Glaude, F. Battin-Leclerc, Proc. Euro. Comb. Meeting 4 (2009).

[85] C.K. Westbrook, C.V. Naik, O. Herbinet, W.J. Pitz, M. Mehl, S.M. Sarathy, H.J. Curran, Comb. Flame 158 (2011) p. 742.

[86] F. Battin-Leclerc, Prog. Energy Comb. Sci. 34 (2008) p. 440.

[87] L. Sy Tran, B. Sirjean, P.-A. Glaude, R. Fournet, F. Battin-Leclerc, Energy doi: 10.1016/j.energy.2011.11.013.

[88] M.H. Hakka, H. Bennadji, J. Biet, M. Yahyaoui, B. Sirjean, V. Warth, L. Coniglio, O. Herbinet, P.-A. Glaude, F. Billaud, F. Battin-Leclerc, Int. J. Chem. Kin. 42 (2010) p. 226.

[89] J.B. Koffend, N. Cohen, Int. J. Chem. Kin. 28 (1996) p. 79.

[90] P. Zhou, O.L. Hollis, B.L. Crynes, Ind. Eng. Chem. Res. 26 (1987) p. 852.

[91] D. Kunzru, Y.T. Shah, E.B. Stuart, Ind. Eng. Chem. Processing Des. Develop. 11 (1972) p. 605.

[92] F.O. Rice, J. Amer. Chem. Soc. 55 (1933) p. 3035.

[93] A. Kossiakoff, F.O. Rice, J. Amer. Chem. Soc. 65 (1943) p. 580.

[94] J.H. Bae, C.T. Avedisian, Comb. Flame 145 (2006) p. 607.

[95] J.H. Bae, C.T. Avedisian, Comb. Flame 137 (2004) p. 148.

[96] B.J. Callahan, C.T. Avedisian, AIAA Paper 99-1077 (1999).

[97] H. Wang, E. Dames, B. Sirjean, D. A. Sheen, R. Tangko, A. Violi, J. Y. W. Lai, F. N. Egolfopoulos, D.F. Davidson, R.K. Hanson, C.T. Bowman, C.K. Law, W. Tsang, N.P. Cernansky, D.L. Miller, R.P. Lindstedt: JetSurF Version 1.0, September 2009 (http://melchior.usc.edu/JetSurF/JetSurF1.0).

[98] X.Q. You, F.N. Egolfopoulos, H. Wang, Proc. Combust. Inst. 32 (2009) p. 403.

[99] C. Ji, E. Dames, Y.L. Wang, H. Wang, F.N. Egolfopoulos, Comb. Flame 157 (2010) p. 277.

[100] S.G. Davis, C.K. Law, Combust. Sci. Technol. 140 (1998) p. 427.

[101] A. Smallbone, W. Liu, C.K. Law, X. You, H. Wang, Proc. Comb. Inst. 32 (2009) p. 1245.

[102] A.P. Kelley, A.J. Smallbone, D.L. Zhu, C.K. Law, Proc. Comb. Inst. 33 (2010) p.963.

[103] S.S. Vasu, D.F. Davidson, Z. Hong, V. Vasudevan, R.K. Hanson, Proc. Combust. Inst. 32 (2009) p. 173.

[104] D.C. Horning, D.F. Davidson, R.K. Hanson, J. Prop. Power 18 (2002) p. 363.

[105] J.M. Smith, J.M. Simmie, H.J. Curran, Int. J. Chem. Kin. 37 (2005) p. 728.

[106] V.P. Zhukov, V.A. Sechenov, A. Yu. Starikovskii, Comb. Flame 153 (2008) p. 130.

[107] D.F. Davidson, J.T. Herbon, D.C. Horning, R.K. Hanson, Int. J. Chem. Kin. 33 (2001) p. 775.

[108] D.F. Davidson, M.A. Oehlschlaeger, R.K. Hanson, Proc. Combust. Inst. 31 (2007) p. 321.

[109] D.F. Davidson, Z. Hong, G.L. Pilla, A. Farooq, R.D. Cook, R.K. Hanson, Combust. Flame 157 (2010) p. 1899.

[110] D.F. Davidson, Z. Hong, G.L. Pilla, A. Farooq, R.D. Cook, R.K. Hanson, Proc. Combust. Inst. (2011) p. 151.

[111] O. Herbinet, P.-M. Marquaire, F. Battin-Leclerc, R. Fournet, J Anal. App. Pyrolysis. 78 (2007) p. 419.

[112] K.D. Dahm, P.S. Virk, R. Bounaceur, F. Battin-Leclerc, P.-M. Marquaire, R. Fournet, E. Daniau, M.J. Bouchez, J. Anal. Appl. Pyrolysis 71 (2004) p. 865.

[113] M.S. Kurman, R.H. Natelson, N.P. Cernansky, D.L. Miller, 47th AIAA Aerospace Sciences Meeting, Orlando, FL, January 2009.

[114] D.F. Davidson, M. E. MacDonald, G. Pilla, R.K. Hanson, Air Force Research Laboratories Report Number AFRL-RZ-ED-TP-2010-200 (2010).

[115] S.S. Vasu, D.F. Davidson, R.K. Hanson, Comb. Flame 156 (2009) p. 736.

[116] S.S. Vasu, D.F. Davidson, Z. Hong, R.K. Hanson, Energy Fuels 23 (2009) p. 175.

[117] J. Vanderover, M.A. Oehlschlaeger, Int. J. Chem. Kin. 41 (2009) p. 82.

[118] R.D. Hawthorne, A.C. Nixon, AIAA Journal 4 (1966) p. 513.

[119] G. Mittal, C.-J. Sung, Proceedings of the Technical Meeting of the Central States Section of the Combustion Institute (2008).

[120] C.S. McEnally, L.D. Pfefferle, Proc. Comb. Inst. 30 (2005) p. 1425.

[121] E. Ranzi, http://www.chem.polimi.it/CRECKModeling/kinetic.html (2006).

[122] A.G. Gaydon, I.R. Hurle, *The Shock Tube in High-Temperature Chemical Physics*, Chapman and Hall, London, 1963.

[123] J.N.B. Bradley, *Shock Waves in Chemistry and Physics*, Methuen, London, 1962.

[124] J.K. Wright, *Shock Tubes* (Methuen's Monographs on Physical Subjects), Methuen, London, 1961.

[125] J.E. John, T.G. Keith, *Gas Dynamics*, 3rd Ed., Pearson /Prentice Hall, New Jersey, 2006.

[126] Ya.B. Zel´dovich, Yu.P. Raizer, W.D. Hayes, R.F. Probstein (Eds.), *Physics of Shock Waves and High-Temperature Hydrodynamic Phenomena*, Dover Publications, New York, 2002.

[127] I.I. Glass, W.A. Martin, G.N. Patterson, A Theoretical and Experimental Study of the Shock Tube, University of Toronto Institute for Aerospace Studies Report (November 1953).

[128] I.I. Glass, J.P. Sislian, Nonstationary Flows and Shock Waves, Oxford Engineering Science Series, Vol. 39, 1994.

[129] D. Bitondo, R.K. Lobb, Design and Construction of a Shock Tube, University of Toronto Institute for Aerospace Studies Report (May 1950).

[130] R.K. Lobb, On the Length of a Shock Tube, University of Toronto Institute for Aerospace Studies Report (July 1950).

[131] P. Vielle, Comptes Rendus Hebdomadaires des Séances de l'Académie des Sciences 129 (1899) p. 1228.

[132] M.C. Krejci, Development of a New Flame Speed Vessel to Measure the Effect of Steam Dilution on Laminar Flame Speeds of Syngas Fuel Blends at Elevated Pressures and Temperatures, MSME Thesis, Texas A&M University, 2012.

[133] P.J. Ross, *Taguchi Techniques for Quality Engineering*, 2nd Ed., McGraw-Hill Professional, New York, New York, 1995.

[134] R. Roy, *A Primer on the Taguchi Method*, Society of Manufacturing Engineers, Dearborn, Michigan, 1990.

[135] B. Rotavera, E.L. Petersen, Accepted to Proceedings of the 34th International Symposium on Combustion (April 2012).

[136] C. Antoine, Comptes Rendus des Séances de l'Académie des Sciences 107 (1888) p. 681, 778, 836.

[137] A. Rose, W.R. Supina, J. Chem. Eng. Data 6 (1961) p. 173.

[138] B.E. Poling, J.M. Prausnitz, J.P. O'Connell, *The Properties of Liquids and Gases*, 5th Ed., McGraw-Hill Professional, New York, 2000.

[139] B. Rotavera, Chemiluminescence and Ignition Delay Time Measurements of C_9H_{20} Oxidation in O_2-Ar behind Reflected Shock Waves, MSME Thesis, Texas A&M University, 2009.

[140] E.L. Petersen, M.J.A. Rickard, M.W. Crofton, E.D. Abbey, M.J. Traum, D.M. Kalitan, Meas. Sci. Tech. 16 (2005) p. 1716.

[141] E.L. Petersen, R.K. Hanson, Shock Waves 10 (2001) p. 405.

[142] E.L. Petersen, R.K. Hanson, AIAA Journal 41 (2003) p. 1314.

[143] B.J. McBride, S. Gordon, M.A. Reno, Coefficients for Calculating Thermodynamic and Transport Properties of Individual Species, NASA Report TM-4513 (October 1993).

[144] M.D. Salas, 17th Shock Interaction Symposium, Rome, Italy (September 2006) p. 1.

[145] W.J.M. Rankine, Phil. Trans. Royal Soc. 160 (1870) p. 277.

[146] H. Hugoniot, J. l'Ecole Polytech. 57 (1887) p. 3.

[147] P. Dagaut, M. Cathonnet, Prog. Energy Combust. Sci. 32 (2006) p. 48.

[148] J.M. Hall, E.L. Petersen, Int. J. Chem. Kin. 38 (2006) p. 714.

[149] A. Sinha, M.J. Thomson, Comb. Flame 136 (2004) p. 548.

[150] P. Dagaut, M. Cathonnet, J.P. Rouan, R.J.C. Boettner, F. Gaillard, H. James, J. Phys. E.: Sci. Instrum. 19 (1986) p. 207.

[151] P. Diévart, Oxydation et Combustion en Milieu Ultra-Pauvre de Carburants Types Gazoles. Étude Expérimentale en Réacteur Agité et Modélisation, Ph.D. Dissertation, Université d'Lille, 2008.

[152] F. Buda, R. Bounaceur, V. Warth, P.-A. Glaude, R. Fournet, F. Battin-Leclerc, Combust. Flame 142 (2005) p. 170.

[153] A. Burcat, B. Ruscic, http://garfield.chem.elte.hu/Burcat/THERM.DAT (2006).

[154] C. Muller, V. Michel, G. Schacchi, G.M. Côme, J. Chim. Phys. Phys.-Chim. Biol. 92 (1995) p. 1154.

[155] S.W. Benson, *Thermochemical Kinetics: Methods for the Estimation of Thermochemical Data and Rate Parameters*, Wiley, New York, 1976.

[156] C.D. Wijaya, R. Sumathi, W.H. Green Jr., J. Phys. Chem. A. 107 (2003) p. 4908.

[157] S.P. Zeppieri, S.D. Klotz, F.L. Dryer, Proc. Comb. Inst. 28 (2000) p. 1587.

[158] W. Tsang, J.A. Walker, J.A. Manion, Proc. Comb. Inst. 31 (2007) p. 141.

[159] M.A. Weissman, S.W. Benson, J. Phys. Chem. 92 (1988) p. 4080.

[160] A.M. Dean, J. Phys. Chem. 89 (1985) p. 4600.

[161] E.A. Irdam, J.H. Kiefer, L.B. Harding, A.F. Wagner, Int. J. Chem. Kin. 25 (1993) p. 285.

[162] A.E. Lutz, R.J. Kee, J.A. Miller, SenKin: A FORTRAN Program for Predicting Homogeneous Gas Phase Chemical Kinetics with Sensitivity Analysis, Sandia National Labortories Report SAND87-8248 (Revised), 1997.

[163] W. Tsang, J. Phys. Chem. Ref. Data 20 (1991) p. 221.

[164] D.L. Baulch, C.J. Cobos, R.A. Cox, C. Esser, P. Frank, Th. Just, J.A. Kerr, M.J. Pilling, J. Troe, R.W. Walker, J. Warnatz, J. Phys. Chem. Ref. Data 21 (1992) p. 411.

[165] W. Tsang, R.F. Hampson, J. Phys. Chem. Ref. Data 15 (1986).

[166] J. Warnatz: W.C. Gardiner Jr. (Ed.), *Combustion Chemistry*, 1st Ed., Springer-Verlag, New York, 1984.

[167] S. Zabarnick, J.W. Fleming, M.C. Lin, J. Chem. Phys. 85 (1986) p. 4373.

[168] P.H. Stewart, G.P. Smith, D.M. Golden, Int. J. Chem. Kin. 21 (1989) p. 923.

[169] J. de Vries, A Study on Sperical Expanding Flame Speeds of Methane, Ethane, and Methane/Ethane Mixtures at Elevated Pressures, Ph.D. Dissertation, Texas A&M University, 2009.

[170] W.B. Lowry, Effect of Blending on High-Pressure Laminar Flame Speed Measurements, Markstein Lengths, and Flame Stability of Hydrocarbons, MSME Thesis, Texas A&M University, 2010.

[171] D. Singh, T. Nishiie, L. Qiao, Proceedings of the Technical Meeting of the Central States Section of the Combustion Institute (2010).

[172] K. Kumar, C.-J. Sung, Energy Fuels 24 (2010) p. 3840.

[173] C. Ji, F.N. Egolfopoulos, Proc. Comb. Inst. 33 (2011) p. 955.

APPENDIX A

MASS AND VOLUME OF FUEL CONSTITUENTS IN LIQUID TERNARY BLENDS

Blend	$C_9H_{18}O_2$ (g)	$C_9H_{18}O_2$ (cm^3)
1	34.19	39.0
2	62.45	71.3
3	20.47	23.4
4	24.28	27.7
5	15.47	17.7
6	20.97	23.9
7	58.51	66.8
8	32.03	36.6
9	67.59	77.2
x	16.57	18.9

Blend	V_{total} (cm^3)
1	390.4
2	356.5
3	77.9
4	138.6
5	58.9
6	239.4
7	222.7
8	365.7
9	385.8
x	378.4

Blend	n-C_9H_{20} (g)	$V_{ideal,\ n\text{-}Nonane}$ (cm^3)	$V_{actual,\ n\text{-}Nonane}$ (cm^3)	$m_{2,\ ideal}$ (g)	$m_{2,\ actual}$ (g)
1	195.8	273.2	273.2	229.989	229.99
2	127.7	178.2	178.8	190.178	190.55
3	16.7	23.4	23.4	37.217	37.24
4	39.7	55.4	55.4	64.008	64.01
5	21.09	29.4	29.4	36.564	36.57
6	102.9	143.6	143.7	123.905	123.93
7	63.8	89.1	88.7	122.334	122.04
8	131.0	182.8	183.0	163.051	163.19
9	165.9	231.5	231.7	233.479	233.59
x	135.6	189.2	189.4	152.132	152.26

Blend	MCH (g)	$V_{ideal,\ MCH}$ (cm^3)	$V_{actual,\ MCH}$ (cm^3)	$m_{3,\ ideal}$ (g)	$m_{3,\ actual}$ (g)
1	59.9	78.1	78.2	289.936	290.03
2	82.1	106.9	106.9	272.671	272.65
3	23.9	31.2	31.2	61.167	61.17
4	42.6	55.4	55.5	106.581	106.59
5	9.0	11.8	11.8	45.611	45.61
6	55.2	71.8	71.8	179.081	179.09
7	51.3	66.8	67.1	173.333	173.55
8	112.3	146.3	146.3	275.508	275.49
9	59.3	77.2	77.1	292.844	292.77
x	130.7	170.3	170.3	282.996	283.05

APPENDIX B

LIQUID FUEL DENSITIES

Species	T (°C)	ρ (g /cm^3)	M_W (kg /kmol)
$C_9H_{18}O_2$	22	0.876	158.24
n-C_9H_{20}	22	0.717	128.26
MCH (C_7H_{14})	22	0.768	98.19
	T (K)	ρ (kg /m^3)	Uncertainty (kg /m^3)
$C_9H_{18}O_2$	293	877.63	0.63
	294	876.76	0.61
	295	875.88	0.59
	296	875.01	0.57
	297	874.13	0.56
	298	873.26	0.55
	299	872.39	0.54
	300	871.51	0.54
n-C_9H_{20}	293	718.15	0.57
	294	717.36	0.56
	295	716.57	0.55
	296	715.79	0.54
	297	715.00	0.54
	298	714.21	0.53
	299	713.42	0.52
	300	712.63	0.52
MCH (C_7H_{14})	293	769.57	0.52
	294	768.71	0.52
	295	767.85	0.52
	296	766.98	0.52
	297	766.12	0.52
	298	765.26	0.51
	299	764.39	0.51
	300	763.53	0.52

ThermoML, NIST/Thermodynamics Research Center, *Pure Appl. Chem.*, 2006, 78, 541-612; *Pure Appl. Chem.*, 2011, 83, 1937-1967.

http://trc.nist.gov/

APPENDIX C

TEMPLATE FOR CALCULATION OF GAS-PHASE MIXTURE COMPOSITION

Ideal	P_{Fill} (torr)	P_{Fill} (psia)	y_i	$(F/O)_{Actual}$	ϕ
$C_9H_{18}O_2$	0.35	0.01	0.00007		
n-C_9H_{20}	2.43	0.05	0.00049		
MCH	0.69	0.01	0.00014		
O_2	49.13	0.95	0.00929	0.076	1.0
Ar		95.00	**0.99000**		
Σy_i			1.000		

Corrected	P_{Fill} (torr)	P_{Fill} (psia)	y_i	$(F/O)_{Actual}$	ϕ
$C_9H_{18}O_2$	0.5	0.01	0.00007		
n-C_9H_{20}	3.5	0.07	0.00049		
MCH	1.0	0.02	0.00014		
O_2	70.75	1.37	0.00929	0.076	1.0
Ar		136.81	0.99000		
Σy_i			1.000		

Actual	P_{Fill} (torr)	P_{Fill} (psia)	y_i	$(F/O)_{Actual}$	% Error	ϕ
$C_9H_{18}O_2$	0.5	0.01	0.00007		(0.07)	1.0
n-C_9H_{20}	3.5	0.07	0.00049		(0.07)	
MCH	1.0	0.02	0.00014		(0.07)	
O_2	70.8	1.37	0.00929	0.076	0.01	
Ar (Actual)		136.90	0.99000		(0.00)	
Ar (Ideal)		136.90				
Σy_i			1.00			

$$y_1C_9H_{18}O_2 + y_2\text{n-}C_9H_{20} + y_3C_7H_{14} + xO_2 \rightarrow aCO_2 + bH_2O$$

a	8.60
b	9.30
x	13.15

Mixture	**8**	N_{Fuel}	1.00	$(F/O)_{Stoich.}$	0.07605
y_1 ($C_9H_{18}O_2$)	**0.10**	N_{Oxygen}	13.15	$(O:F)_{Stoich.}$	13.15
y_2 (n-C_9H_{20})	**0.70**	N_{Total}	14.15	(O:F)	13.15
y_3 (MCH)	**0.20**	y_{Fuel}	0.0007	ϕ	**1.0**

Step		
1	Input mixture number	**Required Input in Bold**
2	Input fuel mole fractions	
3	Input equivalence ratio	
4	Input Ar mole fraction	
5	Input injected fuel (torr)	

$P_{Fuel, Calc.}$ (torr)	3.5
$P_{Fuel, Inj.}$ (torr)	**5.0**
%Fuel	0.07
ppm of Fuel	707
$P_{Ult.}$ (μtorr)	1.5
P_{Total} (psia)	95

APPENDIX D

NASA POLYNOMIAL EQUATIONS FOR THERMODYNAMIC PROPERTIES

$$c_P/R_u = a_1 + a_2T + a_3T^2 + a_4T^3 + a_5T^4$$

$$H/R_uT = a_1 + a_2T/2 + a_3T^2/3 + a_4T^3/4 + a_5T^4/5 + a_6/T$$

$$S/R_u = a_1 \ln T + a_2T + a_3T^2/2 + a_4T^3/3 + a_5T^4/4 + a_7$$

Numerical coefficients a_i are supplied in NASA thermodynamic files from McBride et al. [1]. The first 7 numbers starting on the second line of each species entry (five of the second line and the first two of the third line) are the seven coefficients (a1 through a7) for the high-temperature range (above 1000 K, the upper boundary is specified on the first line of the species entry). The following seven numbers are the coefficients (a1 through a7) for the low-temperature range (below 1000 K, the lower boundary is specified on the first line of the species entry).

H in the above equation is defined as the sum of formation and sensible enthalpies:

$$H(T) = \Delta H_{f,298\,K} + (H_T - H_{298\,K})$$

[1] McBride, B. J., Gordon S., and Reno, M. A., *Coefficients for Calculating Thermodynamic and Transport Properties of Individual Species*, NASA Report TM-4513, October 1993.

APPENDIX E

FORMATION OF REFLECTED-SHOCK CONDITIONS

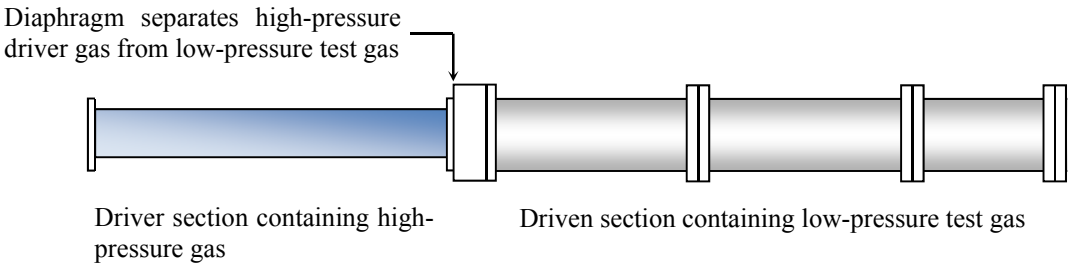

Fig. E.1. The shock-tube driver section is filled at a constant rate with a high-pressure gas. Helium (M_W = 4 kg /kmol, γ = 1.67) is utilized for the present experiments as driver gas. The driver section of the shock tube is filled to yield pressure set by the diaphragm thickness and material. Diaphragms are specifically chosen to produce the desired experimental conditions.

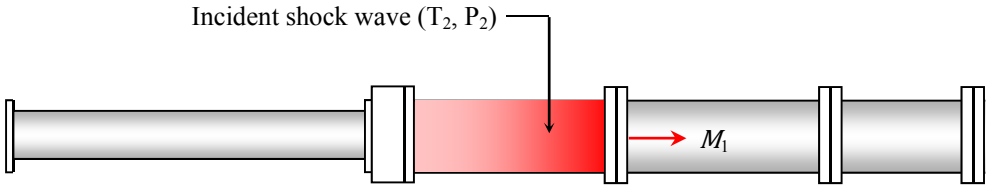

Fig. E.2. The diaphragm is ruptured after a diaphragm-specific critical pressure is surpassed and a shock wave of Mach number M_1 is formed in and propagates through the low-pressure reactive mixture. Diaphragm-bursting transfers high-pressure gas, initially separated from the low-pressure region, into high-velocity gas exiting the driver section. The test-gas response time (acoustic speed, a_1) is insufficient to react to the change in conditions and collide with the entering, high-velocity gas molecules. Resultingly, a shock wave forms and the passage of the shock wave heats and compresses the test gas to State 2. As the shock wave traverses the tube, attenuation from interaction with the shock tube walls and corresponding viscous force decreases its velocity with increasing distance as it approaches the endwall.

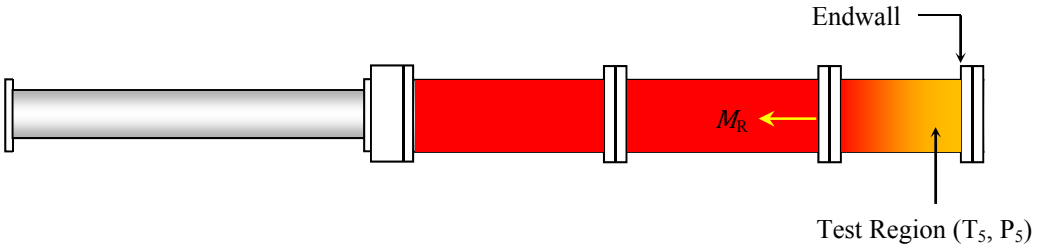

Fig. E.3. The test region of the shock-tube is formed as a result of the reflection of the incident shock wave off of the endwall. Since the gas near the endwall experiences two shock waves, $T_5 > T_2$ and $P_5 > P_2$. The reflected shock wave passes back through the shock tube where it interacts with expansion waves of lesser strength. Shock waves uniformly bring the test region to elevated temperature and pressure near instantaneously, thus (at short times) heat transfer effects to the gas can be neglected and the temperature of the gas is taken to be that created by the shock wave at the instant it forms.

APPENDIX F

TABULATION OF IGNITION DELAY TIMES

Methyl Octanoate Ignition Delay Times –

T (K)	P (atm)	$\tau_{Ignition}$ (μs)	Diagnostic
	$0.0385\%C_9H_{18}O_2 + 0.9615\%O_2 + 99.0\%Ar$ ($\phi = 0.5$)		
1476	1.3	72	
1479	1.4	75	
1432	1.4	100	
1432	1.4	105	
1378	1.4	197	
1397	1.4	206	
1358	1.4	290	
1322	1.5	456	
1336	1.4	481	
1327	1.4	509	OH*
1320	1.4	629	
1310	1.4	654	
1312	1.5	693	
1273	1.5	1054	
1263	1.5	1332	
1382	9.4	180	
1373	9.6	241	
1322	9.5	459	
1291	9.6	591	
1268	10.0	850	

T (K)	P (atm)	$\tau_{Ignition}$ (μs)	Diagnostic
	$0.0741\%C_9H_{18}O_2 + 0.9259\%O_2 + 99.0\%Ar$ ($\phi = 1.0$)		
1444	1.5	179	
1442	1.3	188	
1428	1.3	235	
1393	1.3	263	
1385	1.4	290	
1420	1.3	300	
1379	1.4	350	
1382	1.3	372	
1360	1.5	479	
1352	1.3	535	
1342	1.5	600	
1333	1.5	675	
1319	1.4	796	
1308	1.3	861	
1305	1.4	1000	OH*
1300	1.4	1020	
1307	1.4	1238	
1269	1.5	1296	
1275	1.5	1405	
1499	9.0	44	
1453	9.2	95	
1436	9.2	112	
1383	9.1	221	
1352	9.5	328	
1336	9.5	547	
1301	9.6	730	
1283	9.6	936	
1271	9.2	1027	
1243	9.0	1268	

T (K)	P (atm)	$\tau_{Ignition}$ (μs)	Diagnostic
	$0.1379C_9H_{18}O_2 + 0.8621\%O_2 + 99.0\%Ar$ ($\phi = 2.0$)		
1559	1.4	92	
1513	1.3	134	
1512	1.4	138	
1505	1.3	170	
1487	1.4	203	
1440	1.3	366	
1444	1.4	412	
1423	1.4	507	
1415	1.4	539	
1386	1.4	835	OH*
1370	1.4	1052	
1530	8.7	92	
1486	8.8	123	
1458	9.0	204	
1398	9.1	361	
1416	9.3	375	
1373	9.5	534	
1357	9.7	640	
1327	9.6	957	

n-Nonane Ignition Delay Times (Correlated using Equation 6.1) –

T (K)	P (atm)	$\tau_{Ignition}$ (μs)	Diagnostic
	0.0345%n-C_9H_{20} + 0.9655%O_2 + 99.0%Ar (ϕ = 0.5)		
1530	1.5	99	
1480	1.5	171	
1430	1.5	308	
1380	1.5	581	
1330	1.5	1148	
1310	1.5	1530	
1290	1.5	2058	OH*
1460	10.4	85	
1440	10.4	108	
1400	10.4	177	
1360	10.4	299	
1320	10.4	523	
1280	10.4	946	

T (K)	P (atm)	$\tau_{Ignition}$ (μs)	Diagnostic
	0.0667%n-C_9H_{20} + 0.9333%O_2 + 99.0%Ar (ϕ = 1.0)		
1600	1.5	81	
1550	1.5	135	
1500	1.5	230	
1450	1.5	408	
1400	1.5	756	
1380	1.5	979	
1340	1.5	1682	OH*
1520	10.4	73	
1480	10.4	114	
1440	10.4	182	
1400	10.4	298	
1360	10.4	505	
1320	10.4	881	
1280	10.4	1594	

T (K)	P (atm)	$\tau_{Ignition}$ (μs)	Diagnostic
	0.1250%n-C_9H_{20} + 0.8750%O_2 + 99.0%Ar (ϕ = 2.0)		
1620	1.5	115	OH*
1570	1.5	188	
1520	1.5	316	
1470	1.5	553	
1420	1.5	1006	
1400	1.5	1293	
1370	1.5	1912	
1530	10.4	113	
1480	10.4	195	
1430	10.4	353	
1380	10.4	664	
1330	10.4	1313	
1310	10.4	1751	
1305	10.4	1884	

Methylcyclohexane Ignition Delay Times –

T (K)	P (atm)	$\tau_{Ignition}$ (μs)	Diagnostic
	0.0450%MCH + 0.9550%O_2 + 99.0%Ar (ϕ = 0.5)		
1535	1.5	95	OH*
1507	1.5	149	
1480	1.5	214	
1434	1.5	342	
1399	1.6	753	
1383	1.5	839	
1361	1.5	1322	
1321	1.6	2083	
1314	1.5	1821	
1492	11.8	86	
1425	11.5	164	
1412	11.5	237	
1376	11.8	444	
1332	11.8	750	
1314	11.4	1064	
1291	11.4	1407	

T (K)	P (atm)	$\tau_{Ignition}$ (μs)	Diagnostic
	0.0870%MCH + 0.9130%O_2 + 99.0%Ar (ϕ = 1.0)		
1565	1.5	156	OH*
1531	1.5	220	
1512	1.5	275	
1464	1.6	499	
1434	1.6	813	
1428	1.5	856	
1423	1.5	918	
1395	1.5	1437	
1389	1.5	1474	
1387	1.5	1762	
1494	11.0	153	
1473	11.1	231	
1437	11.3	345	
1430	11.3	454	
1392	11.4	783	
1382	12.0	789	
1361	11.6	907	
1316	11.5	1679	

T (K)	P (atm)	$\tau_{Ignition}$ (μs)	Diagnostic
	0.1600%MCH + 0.8400%O_2 + 99.0%Ar (ϕ = 2.0)		
1672	1.4	111	OH*
1649	1.5	138	
1627	1.5	198	
1569	1.5	387	
1552	1.4	439	
1523	1.5	561	
1504	1.5	713	
1460	1.5	1459	
1444	1.5	1756	
1431	1.5	1840	
1602	11.8	94	
1538	11.1	202	
1467	11.1	303	
1443	11.2	406	
1410	12.2	780	
1403	12.2	748	
1400	11.2	832	
1375	11.4	942	

Blend x Ignition Delay Times –

T (K)	P (atm)	$\tau_{Ignition}$ (μs)	Diagnostic
0.0037%$C_9H_{18}O_2$ + 0.0375%n-C_9H_{20} + 0.0337%MCH + 0.9251%O_2 + 99.0%Ar (ϕ = 1.0)			
1553	1.4	125	
1550	1.4	121	
1516	1.4	228	
1465	1.4	350	
1419	1.4	556	
1354	1.4	1363	OH*
1458	8.6	211	
1437	9.2	302	
1370	8.9	536	
1332	9.1	951	
1303	9.5	1346	

Blend 1 Ignition Delay Times –

T (K)	P (atm)	$\tau_{Ignition}$ (μs)	Diagnostic
0.0037%$C_9H_{18}O_2$ + 0.0256%n-C_9H_{20} + 0.0073%MCH + 0.9634%O_2 + 99.0%Ar (ϕ = 0.5)			
1430	1.4	160	
1400	1.4	250	
1397	1.3	241	
1393	1.4	275	OH*
1342	1.5	642	
1306	1.5	874	
1292	1.5	1272	

Blend 2 Ignition Delay Times –

T (K)	P (atm)	$\tau_{Ignition}$ (μs)	Diagnostic
0.0147%$C_9H_{18}O_2$ + 0.0366%n-C_9H_{20} + 0.0220%MCH + 0.9267%O_2 + 99.0%Ar (ϕ = 1.0)			
1515	1.4	146	
1483	1.4	229	
1462	1.4	275	
1424	1.4	472	
1382	1.5	851	
1344	1.5	1365	OH*
1477	9.2	142	
1421	9.0	248	
1388	9.2	410	
1338	9.5	830	
1320	9.6	1145	

Blend 3 Ignition Delay Times –

T (K)	P (atm)	$\tau_{Ignition}$ (μs)	Diagnostic
0.0424%$C_9H_{18}O_2$ + 0.0424%n-C_9H_{20} + 0.0565%MCH + 0.8587%O_2 + 99.0%Ar (ϕ = 2.0)			
1630	1.4	116	
1628	1.4	128	
1627	1.4	115	
1615	1.3	139	
1611	1.3	144	
1579	1.4	210	OH*
1576	1.4	230	
1498	1.4	560	
1493	1.4	480	
1466	1.4	781	
1429	1.4	1248	
1418	1.5	1421	

Blend 4 Ignition Delay Times –

T (K)	P (atm)	$\tau_{Ignition}$ (μs)	Diagnostic
0.0078%$C_9H_{18}O_2$ + 0.0156%n-C_9H_{20} + 0.0156%MCH + 0.9609%O_2 + 99.0%Ar (ϕ = 0.5)			
1459	4.6	86	OH*
1408	4.7	180	
1371	4.8	249	
1357	4.9	324	
1335	4.3	564	
1332	4.6	463	
1303	4.9	772	
1258	5.1	1262	

Blend 5 Ignition Delay Times –

T (K)	P (atm)	$\tau_{Ignition}$ (μs)	Diagnostic
0.0217%$C_9H_{18}O_2$ + 0.0361%n-C_9H_{20} + 0.0144%MCH + 0.9278%O_2 + 99.0%Ar (ϕ = 1.0)			
1487	4.4	129	OH*
1480	4.6	144	
1446	4.5	225	
1441	4.6	226	
1370	4.2	469	
1360	4.5	569	
1349	4.8	726	
1305	4.6	1216	
1304	4.6	1112	
1291	4.7	1440	
1278	4.7	1636	

Blend 6 Ignition Delay Times –

T (K)	P (atm)	$\tau_{Ignition}$ (μs)	Diagnostic
0.0135%$C_9H_{18}O_2$ + 0.0811%n-C_9H_{20} + 0.0405%MCH + 0.8649%O_2 + 99.0%Ar (ϕ = 2.0)			
1622	5.2	77	OH*
1584	5.1	97	
1543	5.0	136	
1492	5.3	272	
1473	5.0	232	
1413	5.8	629	
1410	5.3	602	
1345	5.6	1091	

Blend 7 Ignition Delay Times –

T (K)	P (atm)	$\tau_{Ignition}$ (μs)	Diagnostic
0.0115%$C_9H_{18}O_2$ + 0.0154%n-C_9H_{20} + 0.0115%MCH + 0.9615%O_2 + 99.0%Ar (ϕ = 0.5)			
1401	9.0	148	OH*
1351	9.3	382	
1314	9.2	638	
1286	9.3	920	
1277	9.5	1110	

Blend 8 Ignition Delay Times –

T (K)	P (atm)	$\tau_{Ignition}$ (μs)	Diagnostic
0.0074%$C_9H_{18}O_2$ + 0.0372%n-C_9H_{20} + 0.0297%MCH + 0.9257%O_2 + 99.0%Ar (ϕ = 1.0)			
1462	9.2	244	OH*
1406	9.0	359	
1372	8.9	587	
1368	9.4	690	
1365	9.1	711	
1360	9.5	789	
1325	9.6	1077	
1324	9.4	1126	

Blend 9 Ignition Delay Times –

T (K)	P (atm)	$\tau_{Ignition}$ (μs)	Diagnostic
0.0267%$C_9H_{18}O_2$ + 0.0800%n-C_9H_{20} + 0.0267%MCH + 0.8667%O_2 + 99.0%Ar (ϕ = 2.0)			
1580	8.4	88	OH*
1555	8.7	106	
1497	8.3	205	
1477	8.8	215	
1421	9.3	504	
1420	9.0	538	
1387	9.5	783	
1348	9.3	1256	

APPENDIX G

COLLISION FREQUENCIES FOR n -NONANE AND n-DECANE (1477 K)

Bond Lengths [1]		d (Å)	M_W (kg/kmol)	μ (Fuel-Ar)	$Z_{1477\,K}$ (Fuel-Ar) [2]
C−C (Å)	n-Nonane	14.44	128	30.48	$8.63 \cdot 10^{-9}$
1.53	n-Decane	15.97	142	31.21	$1.02 \cdot 10^{-8}$
	Ar	1.88	40		
C−H (Å)					
1.10	% Difference	-10.6	-10.9	-2.4	-18.2

$Z_{AB} = (A)(B)\sigma_{AB}^2(8\pi k_B T/\mu)^{0.5}$

[1] Glassman, I. and Yetter, R., *Combustion, 4th Ed.*, London, 2008, p. 46.

[2] Eğe, S. N., *Organic Chemistry: Structure and Reactivity, 4th Ed.*, Boston, 1999, p. 63.

APPENDIX H

CALCULATION OF EXPERIMENTAL SENSITIVITY

Experimental Parameter	Ignition Delay Time (μs)		$\Delta\tau_{Ignition,\ OH^*}$ (μs)	Normalized Sensitivity
	High	Low		
ϕ	1259	278	981	1.00
P (atm)	502	1001	-500	-0.51
$\%C_9H_{18}O_2$	850	649	201	0.21
%MCH	903	512	391	0.40

$\tau_{Ignition,\ OH^*,\ 1375\ K}$ (μs)	Blend
307	1
816	2
1881	3
312	4
454	5
1123	6
215	7
516	8
774	9

	High	Low
ϕ	2.0	0.5
P (atm)	1.5	9.5
$\%C_9H_{18}O_2$	10	30
%MCH	20	40

ϕ = 2.0		9.5 atm	
Blend 3	1881	Blend 7	215
Blend 6	1123	Blend 8	516
Blend 9	774	Blend 9	774
ϕ = 0.5		1.5 atm	
Blend 1	307	Blend 1	307
Blend 4	312	Blend 2	816
Blend 7	215	Blend 3	1881
$30\%C_9H_{18}O_2$		40%MCH	
Blend 3	1881	Blend 3	1881
Blend 5	454	Blend 4	312
Blend 7	215	Blend 8	516
$10\%C_9H_{18}O_2$		20%MCH	
Blend 1	307	Blend 1	307
Blend 6	1123	Blend 5	454
Blend 8	516	Blend 9	774

APPENDIX I

COMPOSOITION AND CONDITIONS OF FLAME SPEED MIXTURES

$C_9H_{18}O_2$

Partial Pressures (torr)

Blend	$C_9H_{18}O_2$	Air	$P_{Initial}$	ϕ	x_{Fuel}	x_{Oxygen}	(F/O)	$(F/O)_{stoich.}$
Pure	10.8	761.8	772.6	0.84	0.014	0.207	0.07	0.08
	14.7	745.4	760.1	1.17	0.019	0.206	0.09	170 °C
	12.7	751.2	763.9	1.01	0.017	0.207	0.08	
	13.5	746.5	760.0	1.08	0.018	0.206	0.09	
	15.9	744.3	760.2	1.27	0.021	0.206	0.10	
	17.8	742.6	760.4	1.43	0.023	0.205	0.11	

$n\text{-}C_9H_{20}$

Partial Pressures (torr)

Blend	$n\text{-}C_9H_{20}$	Air	$P_{Initial}$	ϕ	x_{Fuel}	x_{Oxygen}	(F/O)	$(F/O)_{stoich.}$
Pure	12.1	747.9	760.0	1.08	0.016	0.207	0.08	0.07
	9.4	750.6	760.0	0.83	0.012	0.207	0.06	170 °C
	10.7	749.3	760.0	0.95	0.014	0.207	0.07	
	14.5	745.5	760.0	1.30	0.019	0.206	0.09	
	13.4	746.6	760.0	1.20	0.018	0.206	0.09	
	11.2	748.8	760.0	1.00	0.015	0.207	0.07	

MCH

Partial Pressures (torr)

Blend	MCH	Air	$P_{Initial}$	ϕ	x_{Fuel}	x_{Oxygen}	(F/O)	$(F/O)_{stoich.}$
	12.1	747.9	760.0	0.81	0.016	0.207	0.08	0.10
	14.1	745.9	760.0	0.95	0.019	0.206	0.09	
	13.0	747.0	760.0	0.87	0.017	0.206	0.08	
	18.1	741.9	760.0	1.22	0.024	0.205	0.12	
	12.3	750.2	762.5	0.82	0.016	0.207	0.08	130 °C
	15.2	746.5	761.7	1.02	0.020	0.206	0.10	
	18.3	741.7	760.0	1.23	0.024	0.205	0.12	
Pure	17.1	742.9	760.0	1.15	0.023	0.205	0.11	
	16.2	743.8	760.0	1.09	0.021	0.206	0.10	
	16.4	743.6	760.0	1.10	0.022	0.205	0.11	
	14.1	745.9	760.0	0.95	0.019	0.206	0.09	
	13.1	746.9	760.0	0.88	0.017	0.206	0.08	170 °C
	12.1	747.9	760.0	0.81	0.016	0.207	0.08	
	18.0	742.0	760.0	1.21	0.024	0.205	0.12	
	19.3	740.7	760.0	1.30	0.025	0.205	0.12	

APPENDIX J

NUMERICAL VALUES OF LAMINAR FLAME SPEEDS

Species	ϕ	S_L (cm/s)	$v_{Unburned}$ (cm^3 /g)	v_{Burned} (cm^3 /g)	σ	$T_{Initial}$ (°C)
$C_9H_{18}O_2$	0.86	51.0	1185.6	6290.9	5.306	170
	1.17	64.6	1161.1	6817.5	5.872	170
	1.01	62.2	1170.6	6775.7	5.788	170
	1.08	64.7	1165.9	6822.2	5.851	170
	1.27	60.5	1151.5	6717.6	5.834	170
	1.43	49.1	1142.2	6557.2	5.741	170
n-C_9H_{20}	1.08	68.2	1194.5	6929.2	5.801	170
	0.83	57.0	1210.5	6219.3	5.138	170
	0.95	64.8	1202.4	6692.9	5.566	170
	1.30	57.8	1183.0	6814.0	5.760	170
	1.20	65.8	1186.8	6875.8	5.794	170
	1.00	66.8	1198.5	6847.0	5.713	170
MCH	0.81	42.7	1104.1	6139.4	5.561	130
	0.95	51.8	1096.6	6663.8	6.077	130
	0.87	49.1	1101.7	6343.1	5.758	130
	1.22	53.8	1084.1	6763.6	6.239	130
	0.82	45.2	1104.1	6139.4	5.561	130
	1.02	55.9	1094.0	6770.6	6.189	130
	1.23	51.7	1084.1	6763.6	6.239	130
	1.15	56.1	1086.6	6806.4	6.264	130
	1.09	57.4	1091.5	6832.9	6.260	130
	1.10	66.6	1197.2	6899.9	5.763	170
	0.95	62.2	1205.4	6723.6	5.578	170
	0.88	58.3	1211.0	6412.3	5.295	170
	0.81	51.7	1213.7	6214.0	5.120	170
	1.21	63.1	1191.7	6843.7	5.743	170
	1.30	53.8	1188.9	6795.7	5.716	170

APPENDIX K

GLOSSARY

A

Adiabatic – Thermodynamic process in absence of heat transfer (definite temperature gradient).

Alcohol – Compound in which a hydroxy group, –OH, is attached to a saturated carbon atom; R_3COH.

Aldehyde – Compound in which a carbonyl group is bonded to one hydrogen atom and to one R group; RC(=O)H.

Alkane (Paraffin) – Linear, saturated hydrocarbon with single-bonded carbon atoms; C_nH_{2n+2}.

Alkene (Olefin) – Unsaturated hydrocarbon with at least one double-bonded carbon atom; C_nH_{2n}.

Alkyne – Unsaturated hydrocarbon with at least one triple-bonded carbon atom; C_nH_{2n-2}.

Aromatic – Cyclic, ring-structured hydrocarbon with alternating single and double carbon bonds.

Attenuation – Decrease in energy, intensity, or other intrinsic property of matter as a result of some physical process; shock wave attenuation in internal flows results from viscous interaction with surrounding walls.

Automatic Mechanism Generation – Automated process of generating a chemical kinetics mechanism that constructs models composed of elementary chemical reaction steps using generalized sets of reaction rules.

B

β-scission – Formation of free radicals upon splitting of a carbon-carbon bond.

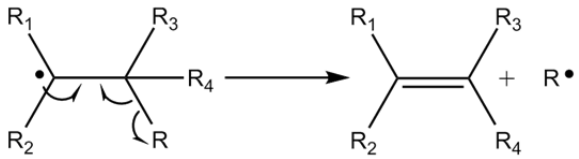

Bandpass Filter – Optical filter designed to allow only a certain wavelength pass through it. Width of allowable bands establishes a center wavelength λ_c and filter bandwidth.

Biofuel – Fuel derived from biological sources (e.g. algae, vegetable oil, tallow).

Boundary Layer – Laminar or turbulent transition layer of fluid between the solid boundary of a body and a moving viscous fluid formed as a consequence of the no-slip condition (requirement that a fluid immediately adjacent to a boundary must move with that boundary, and therefore retain zero-velocity, due to viscosity effects) and within which flow is characterized by velocity and momentum distributions.

C

Chemical Kinetics Model (Reaction Mechanism) – Group(s) of elementary reactions each of which having specific rate parameters A, n, and E_a, designed to interact in concert and simulate real (multi-step) chemical reactions.

Chemiluminescence – Emission from a species at a characteristic wavelength following excitation by chemical reaction or high-energy collision.

Combustion – Chemical reaction during involving the release of heat and/or light.

Conventional Hydrocarbons – Hydrocarbons produced from petroleum distillation.

Cyclization – Formation of a ring compound from a chain by formation of a new bond.

Cycloalkane (Naphthene) – Cyclic hydrocarbon in which carbon atoms are bound to two H atoms; $(CH_2)_n$.

D

Detailed Chemical Kinetics Model – Chemical kinetics model containing all possible elementary reactions.

Driven Gas – Lower pressure gas or mixture of gases under study.

Driver Gas – Higher pressure gas or mixture of gases used to generate large momentum upon diaphragm rupturing and create a shock wave in the driven gas.

E

Elementary Reaction – Single-step chemical reaction defined by rate parameters A, n, and E_a; $H + O_2 \rightarrow OH + O$.

Endothermic Reaction – Chemical reaction for which the overall standard enthalpy change is positive.

Entropy – Thermodynamic state property which quantifies the degree of order within a given system.

Ethanol – Alcohol; oxygenated hydrocarbon presently used as a gasoline supplement; $H_2C(OH)CH_3$.

Ether – Compound with two R-groups ($R \rightarrow$ alkyl or aryl) bound to an oxygen atom; ROR ($R \neq H$)

Exothermic Reaction – Chemical reaction for which the overall standard enthalpy change is negative, therein involving the net liberation of heat.

F

Fischer-Tropsch (FT) Synthetic Fuel – Synthetic fuel tailored to meet specific properties.

Flame Speed – Velocity of unburned gases entering the reaction zone in the direction normal to the combustion zone; measure of the rate of reactant consumption.

Fluid Mechanics – Topic concerning fluid flows and associated changes in pressure, temperature, effects of viscosity, momentum, and energy.

Frequency Factor (Arrhenius Pre-Exponential Factor) – Probability of colliding bodies having the proper orientation and energy to incite chemical reaction.

G

Global Reaction – Chemical reaction which does not consider elementary steps; $CH_4 + O_2 \rightarrow CO_2 + H_2O$.

H

HCCI (Homogeneous Charge Compression Ignition) Engine – A form of an internal combustion engine in which well-mixed fuel and oxidizer (typically air) are compressed to the point of auto-ignition.

Heat of Combustion – The difference between the enthalpy of the products at a specified state and the enthalpy of the reactants at the same state for a complete combustion reaction.

Homolysis Reaction – The cleavage of a bond ('homolytic cleavage' or 'homolytic fission') resulting in the retaining of one of the bonding electrons by each of the molecular fragments between which the bond is broken. A unimolecular reaction involving homolysis of a bond (not forming part of a cyclic structure) in a molecular entity containing an even number of (paired) electrons results in the formation of two radicals.

I

Incident Shock Wave (Shock Tube) – Initial shock wave generated upon diaphragm rupture.

Irreversible – Thermodynamic process which incurs effects from physical processes such as friction and/or heat transfer resulting in degradation of the energy of a system which, as a result, requires work to return to the initial state and thereby leaving a change on the surroundings.

iso-Alkane – Saturated alkane with at least one branched moiety.

Isomerization – A chemical reaction of a species in which the product is of identical atomic composition with different configuration (constitutional/structural, conformational). An intramolecular isomerization that involves the breaking or making of bonds is a special case of a molecular rearrangement. Isomerization does not necessarily imply molecular rearrangement (e.g. in the case of the interconversion of conformational isomers).

K

Kinetic Energy – Energy associated with motion.

L

Laser – Device which utilizes quantum mechanical principals and the physical phenomenon of quantized energy of a species to generate coherent light at a specific wavelength; acronym: Light Amplification by Stimulated Emission of Radiation (LASER).

M

Mach Number – Ratio of the speed V of a disturbance or object through a medium with acoustic speed a.

Mean Free Molecular Path – The average distance λ a particle travels between collisions. For molecules/atoms:

$$\lambda = \left(\sqrt{2}\pi n d_m^2\right)^{-1}$$

n is the number of molecules/atoms per unit volume and d_m is the mean diameter. For O_2 at 760 torr and 298 K, the mean free molecular path is 97 nm; at 7.6 mtorr (10^{-6} atm) the mean free path increases to 9.7 cm.

Methyl Ester – Ester compound in which the R-group forming a single bond with O is CH_3; $R{-}C(=O){-}OCH_3$.

N

Napthene (Cycloalkane) – Cyclic hydrocarbon in which carbon atoms are bound to two H atoms; $(CH_2)_n$.

Negative Temperature Coefficient Behavior/Regime – Refers to the temperature exponent n in the Arrhenius rate coefficient expression. The behavior under certain thermodynamic conditions/regimes (notably high-pressure and low-temperature) where the rate of reaction increases with decreasing temperature.

O

Oxidation – Chemical reaction resulting in the exchange or reconfiguring of electrons.

P

Parent Fuel (Hydrocarbon) – Fuel molecule from which smaller organic radicals are produced.

Petroleum – Naturally occurring fuel source which contains hundreds of hydrocarbon species.

Photodiode Detector – Detector utilizing a two-electrode, radiation-sensitive junction formed in a semiconductive material.

Photon – Particle of zero charge, zero rest mass, spin quantum number of 1, energy $h\nu$ and momentum of $h\nu/c$; carrier of electromagnetic force.

Peroxidation – Chemical reaction in which oxygen atoms are formed leading to the production of peroxides.

PMT (Photomultiplier Tube) – A vacuum tube consisting of an input window, a photocathode, focusing electrodes, an electron multiplier, and an anode, used to measure and amplify photons.

Pyrolysis – Rupture of chemical bonds due to high temperature in absence of an oxidizer.

R

Rate Coefficient – Pre-multiplier of the expression for the rate of a chemical reaction as defined by combination of the law of mass action and law of stoichiometry. The modified Arrhenius form is defined mathematically:

$$k(T) = AT^n exp(E_A/R_u T)$$

Radical – Short-lived, unstable species with unpaired valence electrons.

Reaction Mechanism (Chemical Kinetics Model) – Group(s) of elementary reactions each of which having specific rate parameters A, n, and E_a, designed to interact in concert and simulate real (multi-step) chemical reactions.

Reaction Pathways – Coordinated series of chemical reactions leading to the formation of a particular species

Reduced Chemical Kinetics Mechanism – Group(s) of elementary reactions each of which having specific rate parameters A, n, and E_a, designed to interact in concert and simulate real (multi-step) chemical reactions.

Reflected Shock Wave – (Shock Tube) Shock wave which has reflected from a solid boundary (endwall in shock tube) and as a result possesses diminished strength.

S

Shock Tube – Scientific instrument which makes used of physical laws of gas dynamics and fluid mechanics to create repeatable and controllable conditions of temperature and pressure by producing and controlling shock waves.

Shock Wave – Thermodynamic discontinuity with thickness of on the order of the mean-free path of the constituent molecules/atoms that occurs in a medium due to a disturbance (series of molecular collisions) that transpire on timescales smaller than the acoustic (sound speed) of the medium.

Sound Speed (Acoustic Speed) – Characteristic speed of motion of molecules in a system. For an ideal gas:

$$a = (\gamma RT)^{0.5}$$

Sound Wave – Infinitesimal elastic pressure wave with propagation speed that moves at the speed of sound (acoustic speed) compressive or expansive in nature. In a compressible fluid, the acoustic speed is defined:

$$a^2 = dP/d\rho$$

Spectroscopy – The study of the physical relationships between light and matter.

Surrogate Fuel – Representative fuel comprised of only a few species, made to replicate properties of a multi-component fuel used for experimental study and /or chemical kinetic modeling.

Synthetic Fuel – Fuel derived from alternative sources.

T

Third-body – Particle with which a chemical species collides in the proper orientation and with sufficient energy to promote reaction or de-excitation; denoted M.

V

Vapor Pressure – Temperature- and species-dependent pressure below which a substance transforms from a given phase to the gas phase; pressure at phase equilibrium.

Viscosity – Measure of resistance of a substance /body to fluid flow.

VITA

Name: Brandon Michael Rotavera

Address: 3123 TAMU | Department of Mechanical Engineering | College Station, TX 77840

Email: Rotavera@AggieNetwork.com

Educational Background:

Ph.D., Interdisciplinary Engineering, Texas A&M University, 2012

M.S., Mechanical Engineering, Texas A&M University, 2009

B.S., Mechanical Engineering, University of Central Florida, 2006

Interdisciplinary Graduate Coursework:

- Mechanical Engineering Department, *College of Engineering*
  - Combustion Science
  - Gas Dynamics
  - Aerosol Science
  - Classical Thermodynamics
  - Mathematical Methods in Engineering
  - Internal Combustion Engine Analysis
  - Heat Transfer
  - Inviscid/Viscous Fluid Mechanics
- Chemistry Department, *College of Science*
  - Physical Chemistry I
  - Physical Chemistry II
  - Organic Chemistry
  - Quantum Mechanics
- Aerospace Engineering Department, *College of Engineering*
  - Laser Diagnostics
  - Rocket Propulsion
  - Principles of Fluid Motion
  - Theory of Fluid Mechanics

Honors/Awards:

- **Linda D. and Joe R. Fowler ’68 Graduate Fellowship in Mechanical Engineering**, Department of Mechanical Engineering, Texas A&M University, 2009 – 2010 Recipient
- **Central States Section Student Travel Fellowships**: Technical Meeting of the Central States Section of The Combustion Institute: Dayton, Ohio, April 2012; Urbana, Illinois, March 2010; Tuscaloosa, Alabama, April 2008
- **Student Government Association Travel Award (UCF)**: 26th International Symposium on Shock Waves, Göttingen, Germany, July 2007